Title
The Role of the Tear-Film Lipid Layer in Tear Dynamics and in Dry Eye

Author
Cerretani, Colin

Publication Date
2013

Peer reviewed|Thesis/dissertation

The Role of the Tear-Film Lipid Layer in Tear Dynamics and in Dry Eye

by

Colin Francis Cerretani

A dissertation submitted in partial satisfaction of the

requirements for the degree of

Doctor of Philosophy

in

Chemical Engineering

in the

Graduate Division

of the

University of California, Berkeley

Committee in charge:

Professor Clayton J. Radke, Chair

Professor John Newman

Professor Stephen J. S. Morris

Spring 2013

Abstract

The Role of the Tear-Film Lipid Layer in Tear Dynamics and in Dry Eye

by

Colin Francis Cerretani

Doctor of Philosophy in Chemical Engineering

University of California, Berkeley

Professor Clayton J. Radke, Chair

The increasing global prevalence of dry-eye disease has spurred clinical and research interest in understanding this condition. Most cases of dry eye are attributed to increased tear-evaporation rates. The current paradigm holds that a dysfunctional tear-film lipid layer (TFLL) leads to an increased tear-evaporation rate from the exposed ocular surface, which causes elevated tear salinity (hyperosmolarity). Chronic tear hyperosmolarity then triggers an inflammatory cascade that leads to clinical dry-eye disease. However, a limited fundamental understanding of the role of the TFLL in dry eye impedes progress in developing care strategies. In an effort to advance knowledge in the field, this thesis focuses on tear evaporation in dry eye, on the structure and physical properties of tear lipid, and on the role of duplex-oil films in water-evaporation reduction.

First, a compartmental tear-dynamics model is presented that predicts the role of various tear flows on relevant tear parameters such as tear osmolarity and volume. The tears are compartmentalized based on physiology, and tear physics is described over an entire blink cycle. Coupled water- and salt-conservation equations govern the dynamics within each compartment. Tear-supply and tear-evaporation rates are varied to investigate tear behavior in normal and dry-eye conditions. Model predictions match clinical measurements over a wide range of tear-supply and tear-evaporation rates. The tear-evaporation rate is the strongest driver of tear osmolarity. Inclusion of osmotic water flow through the cornea and conjunctiva enables better matching to clinical data than previous models. Additionally, osmotic water flow is found to contribute significantly to tear flow, especially in dry-eye conditions.

Despite substantial knowledge of the chemical composition of the secreted lipid, called meibum, little is known of its structure or bulk properties. We investigate the physical and structural properties of collected bulk samples of human and bovine meibum utilizing rheology,

calorimetry, and x-ray scattering. Steady and oscillatory shear rheology demonstrate both human and bovine meibum to be remarkably viscoelastic and shear-thinning even at elevated temperatures. Small- and wide-angle x-ray scattering (SAXS and WAXS) confirm the presence of structured crystalline domains at physiological temperature that dissipate with increasing temperature. The melting of crystalline structures near eye temperature measured by SAXS and differential scanning calorimetry (DSC) corresponds to a decrease in meibum viscosity and elasticity over the same temperature range. Meibum viscoelasticity persists even after crystal structures liquefy in SAXS experiments. Thus, our proposed structure for the TFLL at physiologic temperature is a highly viscoelastic, shear-thinning liquid suspension consisting of lipid lamellar-crystallite particulates immersed in a continuous liquid phase. This new paradigm for viewing the lipid layer contrasts with the current picture of several layers of stacked lipids.

Finally, we measure water-evaporation reduction by duplex-oil films at thicknesses from 100 nm and 100 μm. Water-evaporation rates are measured gravimetrically with a newly constructed apparatus under controlled gas-phase mass transfer and environmental conditions. White-light interferometry permits continuous visualization of the deposited oil layers to monitor film uniformity. Duplex-film spreading and dewetting are identified as key challenges to obtaining reliable water-evaporation reduction. Duplex-oil films of oxidized mineral oil, bovine meibum, and human meibum reduce evaporation by a proposed dissolution-diffusion mechanism. The data are fitted to dissolution-diffusion theory to yield the water permeability of the duplex-oil film, *Dk*, which is a material property of the oil. Measured film permeabilities of oxidized mineral oil agree with those reported in literature. Bovine and human meibum, however, do not reduce water-evaporation rates significantly at thicknesses near 100 nm. These findings appear to contradict *in-vivo* tear-evaporation measurements performed clinically. However, clinical evaporation measurements lack calibration and gas-phase mass-transfer characterization. Consequently, more experiments are needed to clear up this apparent contradiction and to discern the true role of the TFLL in evaporation reduction.

Table of Contents

List of Figures

List of Tables

Acknowledgements

I could write an independent dissertation on the individuals and the experiences that have inspired and enabled me to complete this work. I never intended to be a scientist or an engineer. I certainly did not expect to attend graduate school and earn a Ph.D. My desired career path has fluctuated because I have always believed that the ideal route through life is the one that seems right at each turn. At various times, including the present, I have wanted to be an artist, an architect, a stuntman, a wilderness educator, a blues man, a pizza chef, and an adventurer. At the moment, I am a doctor of chemical engineering, and I could not be happier. That I enjoy so much success despite not striving toward any particular goal suggests fate, yet my scientific mind is skeptical. Instead, I believe that, in addition to my own hard work, I owe my accomplishments to a set of special people and circumstances...

...for coaxing me into science,

Science class was never my favorite, but my 6th-grade teacher, Ms. Williams, and later my high-school chemistry and physics teachers, Ms. Hickey and Mr. Mangini, changed. Without these individuals in my life, I doubt that I would be a scientist or an engineer. Ms. Williams kept my interest and let my imagination run wild with science. Who else would let me build for homework a Lego spaceship designed to explore black holes? Ms. Hickey made the mistake of showing me how to make flammable H_2 gas, and even lent us goggles when she realized that my friend, Kevin, and I were going to repeat it at home. When science and explosions became the same thing, Kevin and I became scientists. Mr. Mangini did what every teacher wishes they could do: he made physics and math fun. And, there is John Bast, who convinced me that good things don't occur without math and science.

for helping me complete my PhD,

My experience in chemical engineering at Cornell University laid the foundation for my success in graduate school. Thanh Van Tran catalyzed my switch to ChemE. Prof. Abraham Stroock planted the idea of graduate school in my head, and the skills I developed working under Prof. Paul Steen and Dr. Mike Vogel ensured that I was prepared to begin graduate-school research.

My research here at Berkeley has progressed thanks to the hard work and generosity of a number of wonderful people. Friends in the Newman, Segalman, Kumar, and Clark labs at UC Berkeley have been kind enough lend me their equipment and their expertise. John Newman and Stephen Morris sat down and talked theory with me on more than one occasion. Danielle Leiske and Liat Rosenfeld from the Fuller lab in Stanford adopted me into their lab and co-wrote Chapter 3 with me. Without their help, meibum characterization would have been impossible. Tom Millar and Shiwani Raju at the University of Western Sydney helped immerse me in the vision-science community. They were generous hosts in Sydney and lots of fun in Florence. The guys in the machine, electronics, wood, and glass shops make research possible. Not only did they help me design almost everything I built, but they shared their expertise along the way. I am a better machinist thanks to Eric Granlund and Phil Simon, and I can cut glass thanks to Jim Breen. The guys in the wood shop just rule, especially Jadz. Rocio Sanchez is the best graduate

advisor ever, and she is also a friend. I thank Alcon Laboratories for funding my research. I hope I was worth the investment!

The people – the characters, really – in the Radke Lab made grad school enjoyable. I cannot imagine remaining happy while working in any other lab for six years. Thanks, everyone! The senior members, Vicky Tran, Elisa Rodriguez-Porcel, and Mahendra Chhabra showed me the ropes and got me off on the right foot. That Sam Maurer and I are friends after sharing a cubicle, GSI duties, and too many drunken nights and afternoons says what a great guy he is. Tom Dursch and Cheng-Chun Peng have taken on an impressive workload to help the lab chug along. I know I leave the lab in their good hands. If Clay is the lab's dad, then Tanya Svitova is the lab's mom, and she is indispensable. Somehow she knows how to do everything, where everything is, and she is willing to train the endless line of students who come through the lab. I have been fortunate to have great undergraduates. Although our research has not always rewarded their dedication with publications, I hope that they have taken something away from their experiences. David Chang conducted many of the spreading experiments in Chapter 4; Kevin Okimura helped keep the faith alive in dark times and calibrated the infrared thermocouple; Nghia Ho was the boss of the evaporation apparatus and essentially did all of the experiments in Chapter 4; and Yuzhang Li persevered through a lot of failures and built a goggle evaporimeter that will answer all the remaining questions in this dissertation.

I must recognize the cows whose deaths provided me with eyelids full of bovine meibum. They had no say in their lives, in their deaths, or in the use of their bodies. The scientific knowledge gained from studying their meibum certainly does not offset the pain of their deaths, but I hope it brings a trace of good from them. My experiences in the slaughterhouses of Rancho Veal and U.C. Davis have changed how I think about the meat as food.

Above all, there is Clay, who is undoubtedly the most genuine person I know. I could not have asked for a better adviser or mentor. As a scientist, Clay taught me to think physically, to think critically, and to do these two things consistently. My academic "father," Clay is true to the role of a parent. I have been supported, scolded, and everything in between. I believe that Clay cares more about the emotional wellbeing of his students than does any other adviser. I am honored to know Clay, and I will truly miss him after leaving.

for keeping me (in)sane,

I do not function well when cooped up. Unfortunately, studying chemical engineering has, so far, required working for extended periods trapped in computer rooms, labs, or libraries. My ability to perform indoors revolves around my ability to escape to be with friends and to enjoy the activities that rejuvenate me.

I thank all of my friends over the years that have enriched my life in and out of school to make life awesome even when school sucked. Surviving Cornell ChemE and most of graduate school would have been impossible without Debby Yanes. Thanks, Diego, Farzon, Edgar, and the rest of Pazzi for supporting me (or was it encouraging me?) when I was intoxicated and in various altercations with the law. I don't know how we are still alive, but I wouldn't be living if I couldn't say that.

The amazing friends, roommates, classmates, soccer teammates, snowboarding buddies, etc. that I have met at Berkeley are too numerous to list. Thank you for sharing unforgettable memories while drinking, camping, hiking, snowboarding, jamming, gnarbling, and talking. Without these experiences, I could not stick myself at a bench or desk in lab and work on a daily basis. Special thanks go to Akemi Kunibe, whose impact transcends the usual emotional and

biological support associated with a significant other. She has reminded me of everything important to me at what now seems like a crucial juncture in my life. Her genuine love of the simple beautiful things in life, like animals and flowers, inspires me.

I must also thank Bruce and Deborah Wagman. They started as good friends of my parents, morphed into my *de facto* godparents, and are now my Bay-Area parents. Thank you for supporting me with food, money, music, and love. Bruce and Deborah, if you read this, please do not read Chapters 3 and 4. I hope you understand.

and for being my family.

There are too many examples of how important my family is to me and how integral they are in my development into Colin the person, Colin the scientist, Colin the engineer, and, now, Colin the doctor, so I won't share them. I substitute all examples with one simple fact: I have the best family ever. That makes me lucky. My brothers, Luca and Eric, are my best friends. I would hang out with them every day if I could. My parents, Dan and Susan, are the best people I know. They are as perfect as parents can be, especially raising three boys. Their ability to do what they love inspires me to do the same. I thank my family for everything I achieve because, ultimately, it is my foundation. Thankfully, that foundation has thick footers and lots of rebar.

Dedicated to

Kevin Schwab

Chapter 1

Introduction

1.1 Motivation and goals

Dry eye is an increasingly common disease of the human tear film that coats the anterior surface of the eye. It infects up to 30 % of the global population, especially post-menopausal women, older adults in general, and contact-lens wearers [1]. A vicious cycle of tear-film instability, ocular-surface inflammation, pain, and epithelial-cell damage apparently originates from chronically salty tears [2-10]. Dry eye and elevated tear osmolarity are strongly linked with a deficient tear-film lipid layer (TFLL), which is a thin, oily film coating the aqueous tear film, as well as with increased tear-evaporation rates [8, 11-13]. The thickness of the TFLL is around 100 nm [14-18], many times thicker than a monolayer. As such, it is a duplex-oil film introduced by Langmuir and Harkins to be thick enough to contain two distinct interfaces (water/lipid and lipid/air) with bulk oil in between, but thin enough for the effects of gravity to be negligible [19, 20]. Researchers believe that the oily TFLL retards water evaporation from human aqueous tears by up to 90 % [21-23] preventing tear hyperosmolarity and dry-eye disease in healthy individuals. In the absence of an intact lipid layer, or in adverse environmental conditions, water evaporates from aqueous tears at an elevated rate, concentrating the salt in the remaining tears, and eventually leading to dry-eye symptoms. Despite substantial clinical evidence linking a defective TFLL to dry eye and to increased tear evaporation [7, 8, 11, 24], no direct evidence demonstrates water-evaporation reduction by the human tear lipid. Instead, thin layers of human tear lipid deposited on an *in-vitro* water surface exhibit only marginal water-evaporation reduction (<10 %) [25-27]. Clearly, a fundamental understanding of the role of the TFLL in dry eye is necessary. Such knowledge guides the development of care solutions and of strategies for dry-eye management.

This dissertation focuses on two central issues: (1) the role of evaporation in dry eye, and (2) the ability of the TFLL to reduce evaporation. To uncover the underlying physics, these two questions are addressed within a chemical-engineering framework. The first question asks what tear-dynamics parameters (e.g., hydraulic flow rate, tear-evaporation rate, degree of mixing, tear hydrodynamics, etc.) are the main drivers of tear osmolarity. The second question asks by what mechanism a duplex-oil film reduces the evaporation of an underlying water substrate. To appreciate fully these two questions, the following sections provide background information on the relevant physiological and physicochemical processes, as well as a brief overview of previous research.

1.2 Evaporation in dry eye

Understanding how tear evaporation leads to dry eye requires basic knowledge of dry-eye disease and tear physiology. This section reviews the basics of anterior-eye anatomy and of tear flow, and then addresses the changes to these in dry eye. Motivation for developing a predictive mathematical model for tear dynamics is introduced, and previous modeling works are covered. Finally, the need for an improved mathematical model for tear dynamics is highlighted, and is later presented in Chapter 2.

Figure 1.1 depicts a cross-sectional view of the anterior eye and tear film, with an inset showing a more detailed view of the preocular tear film. Aqueous tear, supplied by the lacrimal and accessory lacrimal glands, bathes the ocular surface in a nearly isotonic solution of salts, proteins, and soluble mucins. As shown in the inset of Figure 1.1, the exposed preocular tear film is approximately 5 μm thick [16]. Upon each blink, the tear film coats the surface of the eye and, among other things, helps maintain proper hydration of the ocular epithelial surface, presents a smooth refractive surface for vision, and provides nutrients and cleansing [17]. Meibomian glands located in the upper and lower eyelids excrete a complex mixture of lipids, called meibum, that makes up the tear-film lipid layer (TFLL). With each blink, the TFLL spreads over the exposed aqueous tear film as a duplex film about 100-nm thick. Water evaporates from the exposed tears while the eye is open, and the TFLL is thought to minimize evaporative water loss [28].

As shown in Figure 1.1, the tears are contained within various compartments across the ocular surface. Unexposed tear lies behind the upper and lower eyelids in the upper and lower conjunctival sacs. The upper and lower fornices lie at the extrema of the upper and lower conjunctival sacs. The main and accessory lacrimal glands produce tear that originates in the fornices and flows towards the tear menisci located along the eyelid margins. The upper and lower tear menisci run along the arc length of the lid margin and connect to the conjunctival sacs. Tear drains from the menisci to the nasal cavity via the puncta (not shown). The tear film and menisci make up the exposed tear, from which water evaporates while the eye is open. Fluid and solute flow between the tear film and the menisci is effectively cut off by a region of locally thinned tears called the black lines [29-31]. Tear supply from the lacrimal glands is augmented by osmotically driven water flow through the corneal and conjunctival epithelia that line the ocular surface [32-34].

In dry eye, tear physiology changes, as evidenced by irritation, ocular-surface inflammation, burning and stinging sensations, and, in some cases, epithelial-cell damage [2, 8, 35]. The International Dry Eye Workshop (DEWS), a group of leading dry-eye reasearchers, defines dry eye as [8]

> *… a multifactorial disease of the tears and ocular surface that results in symptoms of discomfort, visual disturbance, and tear film instability with potential damage to the ocular surface. It is accompanied by increased osmolarity of the tear film and inflammation of the ocular surface.*

The central role of tear hyperosmolarity in dry eye was first acertained by Gilbard [5, 35, 36], and continues to be suggested as the single most effective marker for dry-eye diagnosis [4, 6, 9, 10, 37, 38]. Tears are secreted as an isotonic solution [39], and they concentrate in the tear film by evaporation between blinks. Increased tear evaporation and decreased tear supply both

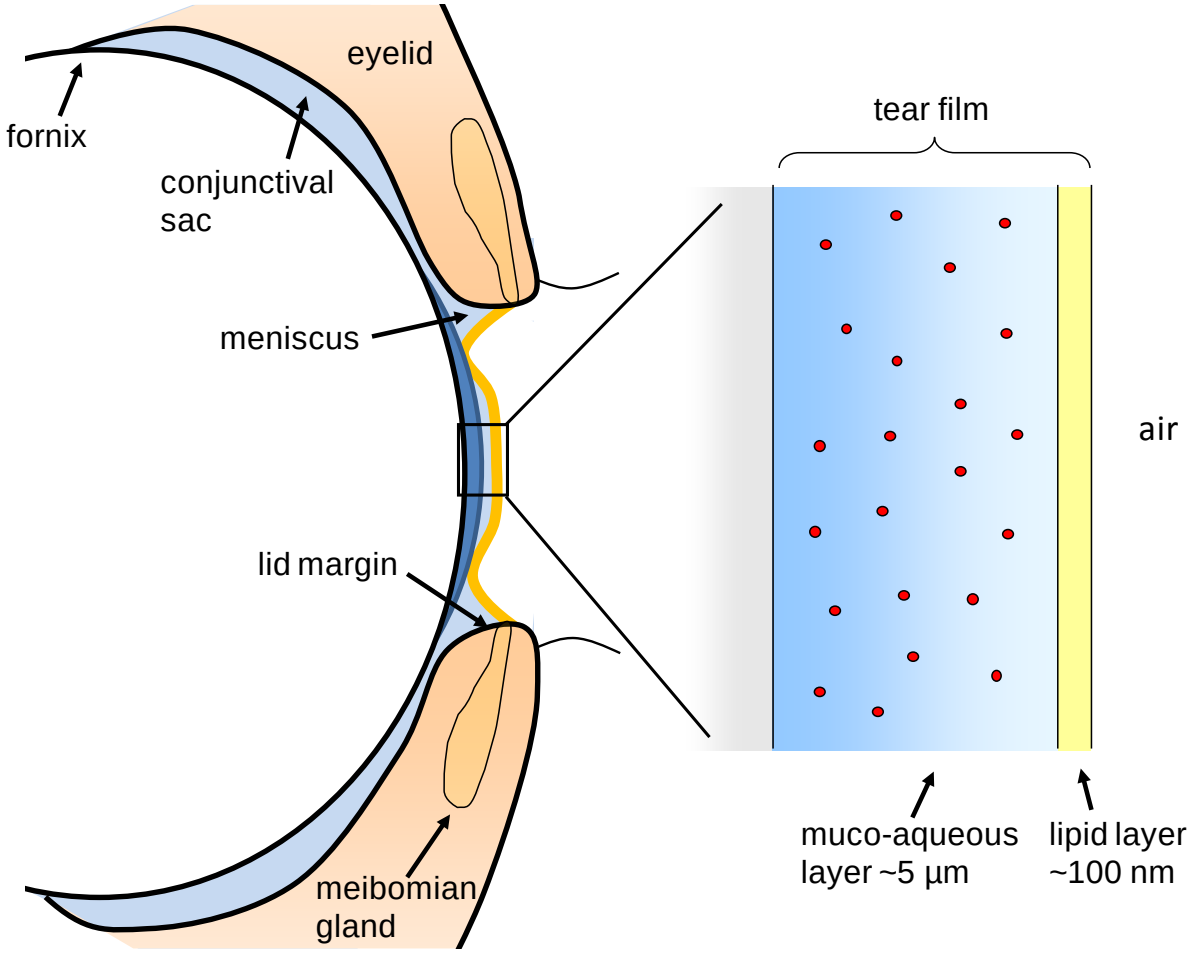

Figure 1.1: A cross-sectional side view of the anterior eye and tear film. Aqueous tear covers the exposed and unexposed ocular surface. The tear-film lipid layer (TFLL) coats the exposed tear film. The inset at the right shows a more detailed view of the preocular tear film. Drawing is not to scale.

amplify the concentrating effect; dry eye resulting primarily from these two stimuli is termed evaporative dry eye (EDE) or aqueous-deficient dry eye (ADDE), respectively. EDE typically results from lid-margin diseases such as blepharitis or meibomian gland disease (MGD) that affect the quality or quantity of lipid expressed from the meibomian glands or from adverse environmental conditions such as high wind speeds or low ambient humidity that presumably lead to increased evaporation [8, 40]. ADDE stems from decreased tear-supply rate due to aging, systemic drugs, lacrimal-gland obstruction, or inflammatory damage to the lacrimal gland [8, 40]. Any of these triggers may lead to hyperosmolarity significant enough to elicit an inflammatory response at the ocular surface that initiates a vicious cycle of inflammation and ocular-surface damage [2, 8, 40]. Clinical measurements confirm that dry-eye patients generally exhibit increased tear-evaporation rates, decreased tear-supply rates, and increased tear osmolarity [4, 5, 9, 10, 13, 23, 37, 38, 41].

The clinical description of dry eye makes it clear that tear production and evaporation are two major causative factors. A mechanistic understanding of how tear supply and tear-evaporation rate set the tear osmolarity, however, is more involved. One must relate the lacrimal tear supply, which originates in the fornices, to the exposed tear film subject to evaporation and to the tears located in the lower tear meniscus from which clinicians take tear-osmolarity measurements. *In-vivo* control and measurement of water and solute distribution within the human tear system under varying conditions is difficult at best. We develop a physiology-based mathematical model that tracks the distribution and flow of tear water and salt across the ocular surface, and calibrate against measureable tear behavior.

During the past decade, researchers developed various mathematical models with similar goals. In 2004, Levin and Verkman [33] predicted tear osmolarity in mice as a function of tear-supply and tear-evaporation rates. Their rudimentary model treated the entire volume of tear as a well-mixed compartment with inflows and outflows corresponding to tear evaporation, lacrimal supply, trans-epithelial osmotic flow, and punctal drainage. Their basic model predicts the role of evaporation and lacrimal supply in dry eye: as the tear-evaporation rate increases and the tear-supply rate decreases, the tear osmolarity increases.

More recently, Zhu and Chauhan published a series of papers modeling tear drainage [42], tear mixing [43], and tear osmolarity [34, 44]. Their 2007 model [34] is an extension of that of Levin and Verkman [33] still depicting the tears as one continuous, well-mixed compartment with inflows and outflows. To recognize tear-compartmentalization, however, Zhu and Chauhan calculate the volume distribution between the menisci and tear film. As a result, their effort predicts tear volume as well as osmolarity, and includes detailed descriptions of trans-conjunctival water flow via osmosis and electro-osmosis. Zhu and Chauhan predict increased tear osmolarity with enhanced tear evaporation, but do not probe throroughly dry-eye conditions.

Although the previous contributions confirm the importance of tear-supply and tear-evaporation rates on tear osmolarity in dry eye, important information on tear compartmentalization and mixing dynamics are not included. Additionally, the tear-flow parameters utilized do not always follow closely those reported clinically. The tear-dynamics model described in Chapter 2 of this dissertation includes tear compartmentalization and tear exchange between each compartment. Clinical measurements against which to benchmark the model are tear-evaporation and tear-supply rates, tear osmolarity, and tear volume. Gaffney *et al.* [45] independently published a similar model. The Gaffney model calculates transient tear dynamics for the compartmentalized tears, tracking water and solute distribution and exchange in

time over the ocular surface. As expected, the tear-film osmolarity is elevated over that of the menisci or the conjunctival sacs, and tear osmolarity increases when the tear-supply rate decreases (ADDE) or the tear-evaporation rate increases (EDE). Additionally, increased blink rate alleviates elevated tear-film osmolarity in EDE conditions. The Gaffney model represents a significant advance in understanding and predicting tear dynamics in normal and dry-eye conditions. Despite the improvements, however, the Gaffney model is constrained to the lowest tear-evaporation rates and the highest tear-supply rates to predict a normal tear osmolarity.

Chapter 2 follows a similar compartmental approach to that of Gaffney *et al.*; however, several key differences produce results that align better with clinical observations. Most importantly, the model includes the effects of osmotically driven water flow through the cornea and conjunctiva. Consequently, normal tear osmolarities are predicted for much higher tear-evaporation rates and much lower tear-supply rates. Additionally, the physics of tear drainage and tear-film deposition is integrated into the model and varies with tear-supply and tear-evaporation rates. Model predictions of tear osmolarity and tear volume agree closely with recent clinical measurements for healthy, ADDE, and EDE conditions. Tear-evaporation rate is established as the single largest driver of tear hyperosmolarity, attesting to its primary role in dry eye.

1.3 Evaporation reduction by the TFLL

The central role of tear evaporation in dry eye highlights the purported function of the TFLL in tear-evaporation reduction. Despite no *in-vitro* proof of its ability to suppress water evaporation, ongoing research focuses on development of dry-eye care solutions containing oils to reduce tear evaporation [46-48]. A basic understanding of the TFLL's role in evaporation reduction is lacking. Chapters 3 and 4, respectively, advance knowledge of the structure of the TFLL and of the role of thin lipid layers in reducing water evaporation. This introduction section first covers the basics of the TFLL and motivates the pursuit of more information about the structural and physical properties of the meibum that constitutes the TFLL, the topic of Chapter 3. Previous work in evaporation suppression by duplex-oil films is addressed, and the challenges inherent in evaporation-reduction measurement are outlined. The failure of *in-vitro* experiments with spread meibum to exhibit significant water-evaporation reduction appears to stem from inadequate experimental control. Thus, there is considerable need for improved experiments, which are the topic of Chapter 4.

The TFLL that coats anterior surface of the aqueous tear film is shown schematically in Figure 1.1. The duplex-lipid film is typically 50- to 100-nm thick [11, 14, 49], but may be 200 nm or thicker [15, 18] depending on the individual and on the measurement location on the exposed ocular surface. The TFLL is believed to play an important role in tear-film stability and in tear-evaporation reduction [28]. Upon the lid upstroke of each blink, meibum at the lower-lid margin spreads rapidly upwards over the aqueous tear film by surface tension to form the duplex-lipid tear film [28, 50-52].

Meibum is a holocrine secretion of the meibomian glands and is composed of a rich mixture of lipids and possibly cellular debris. Wax esters and cholesterol esters are the major lipid components, together making up roughly 60-70 % of the total meibum content, with lesser amounts of diesters, triacylglycerols, polar lipids, and fatty acids making up the balance [53-58]. Many of the individual lipid chains are greater than 20 carbons long. Lipids with one or more alkyl chains, such as wax esters, diesters and tracylglycerols, contain as many as 40-60 carbon atoms. The degree of saturation varies as well: saturated, monounsaturated, and polyunsaturated

lipids are all present in meibum [53, 54, 56, 59]. Meibomian-gland secretions have also been shown to contain proteins that could disrupt regions of ordered lipids [60, 61].

Despite substantial knowledge of meibum's chemical composition, relatively little is known of its physical properties relevant to TFLL dynamics. Meibum exhibits a wide melting range, becoming liquid-like near body temperature [26, 28]. Because water diffusivity through the lipid layer depends on lipid viscosity, meibum viscosity plays an important role in evaporation reduction. Crude viscosity measurements by Tiffany and Dart [62] report that meibum is extremely viscous, but temperature or shear dependence were not pursued. Despite references to its viscoelasticity [52], no data prove bulk meibum to be viscoelastic. Detailed rheological data including oscillatory rheology, temperature dependence, and shear-rate dependence presented in Chapter 3 shed light on the behavior and structure of the TFLL. No data are available on the surface and interfacial tensions of meibum, which provide information about the spreading and stability of the duplex-lipid film.

Until very recently, surprisingly few details of the structure of the TFLL were available. Although the TFLL is well over 10 to 20 molecules thick, most interfacial studies "mimicking" the TFLL are conducted with monolayers [63-68]. This confusion permeates the current literature, as most diagrams of the TFLL interfacial structure depict a few layers of stacked molecules at the water/air interface [53, 66, 69-71]. This picture amounts to a TFLL only 10 nm thick. In contrast, the duplex-lipid film must have two distinct interfaces separated by bulk meibum, as referenced by Holly [51, 72].

Recent studies by Leiske *et al.* [73, 74] using small-angle x-ray scattering (SAXS) and grazing-incidence x-ray diffraction (GIXD) show that both bulk meibum and meibum multilayers on water contain crystalline lipid structures that melt around 34-40 °C. The presence of crystalline structures in both bulk meibum and meibum multilayers suggest that the TFLL has a complex structure unrecognized by monolayer studies. Understanding the structure and its effect on the physical and rheological properties of bulk meibum provides information on the behavior of the TFLL and water transport through it.

A major barrier to measurement of structural and physical properties of human meibum is the limited amount of material that can be expressed from the human meibomian glands. One human subject yields around 1 mg of meibum per expression [53]. Bovines, however, produce as much as 5-10 times more meibum per animal, and the chemical composition is similar to that of humans [57]. Readily available from the abattoir, bovine eyelids provide a source for collecting enough meibum to make rheological and other measurements. In Chapter 3, we present the results of collaboration with Stanford researchers to explore the structural and rheological properties of bovine and human meibomian lipids. X-ray scattering, bulk and interfacial rheology, differential scanning calorimetry (DSC), and polarized-light microscopy are employed to probe bovine and human meibum. Meibum is found to contain multiple crystalline lipid structures that melt near eye temperature. Meibum is a shear-thinning, viscoelastic fluid whose rheology is dictated by the presence of crystalline lipids. As discussed in Chapter 3, these properties help understand the role of the TFLL in tear-film stability and in evaporation reduction.

Chapter 4 deals with the tear-evaporation reduction by meibum. Research into evaporation suppression by lipids is longstanding. Physical chemists began fundamental research on water-evaporation reduction by interfacial molecular films in the 1920s via deposition of insoluble lipid monolayers at the air/water interface [75-77]. Growing interest in preventing reservoir-water loss soon led to studies on water-evaporation reduction by duplex-oil

films 100 nm – 100 μm thick [78-83]. Although nearly all lipids and oils spread as a monolayer at the water/air surface, duplex-film formation is more difficult. Initial duplex-film formation requires low-surface-tension oil capable of spreading on water [19, 20]. Aliphatic hydrocarbons with molecular weight larger than that of octane do not spread on water [84]. Many duplex-oil films are formed from oxidized mineral oil that has been heated in the presence of oxygen to form surfactant molecules [51, 81-83, 85] that renders it spreadable. Likewise, surfactants may be independently added to an otherwise non-spreading oil to render it spreadable [19, 79, 80, 86-88].

Early evaporation-reduction studies with duplex-oil films utilized oxidized mineral oil [81-83]. Unfortunately, duplex-oil films are unstable and eventually dewet into nonuniform regions of oil lenses surrounded by monolayer coverage [19, 89]. Clearly, effective evaporation reduction necessitates a uniform duplex-oil film. To overcome this issue, Heymann and coworkers [79, 80] employed films of mineral oil with small amounts of high-molecular-weight polymerized surfactant molecules. These surfactants imparted interfacial structure to the films, which resisted dewetting and reduced evaporation for a period of several months [80].

Early evaporation-reduction studies by duplex-oil films revealed several important conclusions. Firstly, evaporation reduction increases with increasing duplex-film thickness [79, 81, 82]. Langmuir and Schaefer [81] were the first to suggest that duplex-oil films impede water evaporation by a diffusive mechanism. The resistance of a duplex-oil film to water transport is defined as $R_F = L/Dk$, where L is the film thickness and Dk is the permeability of the oil film to water, i.e., the product of the diffusion coefficient of water in oil, D, and the equilibrium partition coefficient of water in oil, k. Thus, if water has no solubility in the spread oil film, evaporation halts. Additionally, evaporation reduction depends on the environmental conditions in the surrounding air such as airflow, humidity, and absolute pressure. Evaporation reduction depends on water-transport through the duplex-oil film and through the gas-phase, as well as on the water-vapor concentration driving force. Thus, evaporation reduction cannot be compared practically among experimenters. The water permeability in the film, Dk, however, is a material property of the spread oil and may be compared between experiments provided it is known. By characterizing the gas-phase mass transport and the concentration driving force, Langmuir and Schaefer [81] were the first to report the measured water permeability in duplex-oil films. With the exception of Powell [82], other researchers reported only the evaporation reduction, making comparison difficult.

Water evaporation through the TFLL, a duplex-lipid film, must follow the same physical mechanism as that for the duplex films already studied. Therefore, it is critical that *in-vitro* evaporation-reduction experiments using meibum heed the lessons learned by early research. Previous *in-vitro* experiments on meibum, however, have ignored the roles of gas-phase transport and of duplex-film uniformity. The early experiments of Brown and Dervichian [26] were conducted with no airflow control and no confirmation of duplex-lipid film coverage over the water surface. No water-evaporation reduction was measured. Borchman *et al.* [25] reported only minimal evaporation reduction with an 85-μm thick model lipid film, which they attributed to a lack of film uniformity. Herok *et al.* [27] measured water-evaporation reduction by deposited layers of human and bovine meibum. With enough meibum deposited to form a 4-μm thick film, water-evaporation rate was reduced by only 7 %. However, a low airflow velocity and no confirmation of duplex-film uniformity obscure meibum's role in evaporation reduction. None of the available *in-vitro* experiments on meibum or meibum mimics achieved the 90 % evaporation reduction attributed to the *in-vivo* TFLL [21-23]. However, current *in-vitro*

experiments lack proper control and measurement of relevant quantities. *In-vitro* evaporation-reduction experiments are sorely needed that adequately address the physics of evaporation.

Chapter 4 first reviews the relevant water-evaporation experiments conducted with duplex-oil films. Next, background theory underlying duplex-film spreading and stability is presented. A physically based theoretical model is then outlined to describe water evaporation both from clean surfaces and through duplex-oil films. Importantly, the transport model addresses the roles of the vapor-phase composition, mass transfer, heat transfer, and film thickness and composition on evaporation rate. Following the theoretical section, an improved method for measuring evaporation reduction is then presented that enables assessment of water-surface temperature, continuous visualization of film coverage, and controlled vapor-phase mass-transfer resistance. New *in-vitro* evaporation results with model films of oxidized mineral oil and of bovine-meibomian lipid demonstrate significant reduction in evaporation by a dissolution-diffusion mechanism for thicknesses ranging between 100 nm and 100 μm. For the first time, the water permeability of bovine-meibum is reported. Finally, the significance of these new results to human-tear evaporation and dry eye is discussed.

Chapter 5 of the dissertation concludes with a summary of the new findings on the role of the TFLL in tear dynamics and in dry eye. Broader impacts are discussed and future work is suggested.

1.4 References

[1] (No authors listed). The epidemiology of dry eye disease: report of the Epidemiology Subcommittee of the International Dry Eye WorkShop (2007). *Ocul Surf*. 2007;5:93-107.

[2] Baudouin C. The Pathology of Dry Eye. *Surv Ophthalmol*. 2001;45:S211-S20.

[3] Chen W, Zhang X, Zhang J, Chen J, Wang S, Wang Q, et al. A Murine Model of Dry Eye Induced by an Intelligently Controlled Environmental System. *Invest Ophthalmol Vis Sci*. 2008;49:1386-91.

[4] Farris RL. Tear Osmolarity - A New Gold Standard? *Adv Exp Med Biol*. 1994;350:495-503.

[5] Gilbard JP, Farris RL, Santamaria J. Osmolarity of Tear Microvolumes in Keratoconjunctivitis Sicca. *Arch Ophthalmol*. 1978;96:677-81.

[6] Lemp MA, Bron AJ, Baudouin C, Benitez Del Castillo JM, Geffen D, Tauber J, et al. Tear Osmolarity in the Diagnosis and Management of Dry Eye Disease. *Am J Ophthalmol*. 2011;151:792-8.

[7] Lemp MA, Crews LA, Bron AJ, Foulks GN, Sullivan BD. Distribution of Aqueous-Deficient and Evaporative Dry Eye in a Clinic-Based Patient Cohort: A Retrospective Study. *Cornea*. 2012;31:472-8.

[8] (No authors listed). The definition and classification of dry eye disease: report of the Definition and Classification Subcommittee of the International Dry Eye Workshop (2007). *Ocul Surf*. 2007;5:75-92.

[9] Sullivan BD, Whitmer D, Nichols KK, Tomlinson A, Foulks GN, Geerling G, et al. An Objective Approach to Dry Eye Severity. *Invest Ophthalmol Vis Sci*. 2010;51:6125-30.

[10] Suzuki M, Massingale ML, Ye F, Godbold J, Elfassy T, Vallabhajosyula M, et al. Tear Osmolarity as a Biomarker for Dry Eye Disease Severity. *Invest Ophthalmol Vis Sci*. 2010;51:4557-61.

[11] Craig JP, Tomlinson A. Importance of the lipid layer in human tear film stability and evaporation. *Optom Vis Sci*. 1997;74:8-13.

[12] Isreb MA, Greiner JV, Korb DR, Glonek T, Mody SS, Finnemore VM, et al. Correlation of lipid layer thickness measurements with fluorescein tear film break-up time and Schirmer's test. *Eye*. 2003;17:79-83.

[13] Tomlinson A, Doane MG, McFayden A. Inputs and Outputs of the Lacrimal System: Review of Production and Evaporative Loss. *Ocul Surf*. 2009;7:186-98.

[14] Goto E, Dogru M, Kojima T, Tsubota K. Computer-synthesis of an interference color chart of human tear lipid layer, by a colorimetric approach. *Invest Ophthalmol Vis Sci*. 2003;44:4693-7.

[15] Guillon J-P. Tear film photography and contact lens wear. *Cont Lens Anterior Eye*. 1982;5:84-7.

[16] King-Smith PE, Fink B, Hill R, Koelling K, Tiffany JM. The Thickness of the Tear Film. *Curr Eye Res*. 2004;29:357-68.

[17] Korb DR, Craig JP, Doughty M, Guillon J-P, Smith G, Tomlinson A. *The Tear Film: structure, function, and clinical examination*. Oxford: Butterworth-Heinemann; 2002.

[18] McDonald JE. Surface Phenomena of Tear Films. *Trans Am Ophthalmol Soc*. 1968;66:905-39.

[19] Harkins WD. A general thermodynamic theory of the spreading of liquids to form duplex films and of liquids or solids to form monolayers. *J Chem Phys*. 1941;9:552-68.

[20] Langmuir I. Oil lenses on water and the nature of monomolecular expanded films. *J Chem Phys*. 1933;1:756-76.

[21] Iwata S, Lemp MA, Holly FJ, Dohlman CH. Evapoartion Rate of Water from the Precorneal Tear Film and Cornea in the Rabbit. *Invest Ophthalmol*. 1969;8:613-9.

[22] Mishima S, Maurice DM. The oily layer of the tear film and evaporation from the corneal surface. *Exp Eye Res*. 1961;1:39-45.

[23] Tomlinson A, Khanal S. Assessment of Tear Film Dynamics: Quantification Approach. *Ocul Surf*. 2005;3:81-95.

[24] Goto E, Endo K, Suzuki A, Fujikura Y, Matsumoto Y, Tsubota K. Tear evaporation dynamics in normal subjects and subjects with obstructive meibomian gland dysfunction. *Invest Ophthalmol Vis Sci*. 2003;44:533-9.

[25] Borchman D, Foulks GN, Yappert MC, Mathews J, Leake K, Bell J. Factors affecting evaporation rates of tear film components measured in vitro. *Eye Contact Lens*. 2009;35:32-7.

[26] Brown SI, Dervichian DG. The oils of the meibomian glands: physical and surface characteristics. *Arch Ophthalmol*. 1969;82:537-40.

[27] Herok GH, Mudgil P, Millar TJ. The effect of meibomian lipids and tear proteins on evaporation rate under controlled in vitro conditions. *Curr Eye Res*. 2009;34:589-97.

[28] Bron AJ, Tiffany JM, Gouveia SM, Yokoi N, Voon LW. Functional aspects of the tear film lipid layer. *Exp Eye Res*. 2004;78:347-60.

[29] McDonald JE, Brubaker S. Meniscus-induced thinning of tear films. *Am J Ophthalmol*. 1971;72:139.

[30] Miller KL, Polse KA, Radke CJ. Black-line formation and the "perched" human tear film. *Curr Eye Res*. 2002;25:155-62.

[31] Wong H, Fatt I, Radke CJ. Deposition and Thinning of the Human Tear Film. *J Colloid Interface Sci*. 1996;184:44-51.

[32] Leung BK, Bonanno JA, Radke CJ. A Model for Corneal Metabolism. *Prog Retin Eye Res*. 2011;30:471-92.

[33] Levin MH, Verkman AS. Aquaporin-Dependent Water Permeation at the Mouse Ocular Surface: In Vivo Microfluorimetric Measurements in Cornea and Conjunctiva. *Invest Ophthalmol Vis Sci*. 2004;45:4423-32.

[34] Zhu H, Chauhan A. Tear Dynamics Model. *Curr Eye Res*. 2007;32:177-97.

[35] Gilbard JP, Carter JB, Sang DN, Refojo MF, Hanninen LA, Kenyon KR. Morphological Effect of Hyperosmolarity on Rabbit Corneal Epithelium. *Ophthalmol*. 1984;91:1205-12.

[36] Gilbard JP, Farris RL. Tear Osmolarity and Ocular Surface Disease in Keratoconjunctivitis Sicca. *Arch Ophthalmol*. 1979;97:1642-6.

[37] Khanal S, Tomlinson A, McFayden A, Diaper CJM, Ramaesh K. Dry Eye Diagnosis. *Invest Ophthalmol Vis Sci*. 2008;49:1407-14.

[38] Tomlinson A, Khanal S, Ramaesh K, Diaper CJM, McFayden A. Tear Film Osmolarity: Determination of a Referent for Dry Eye Diagnosis. *Invest Ophthalmol Vis Sci*. 2006;47:4309-15.

[39] Murube J. Tear Osmolarity. *Ocul Surf*. 2006;4:62-73.

[40] Bron AJ, Yokoi Y, Gaffney EA, Tiffany JM. Predicted Phenotypes of Dry Eye: Proposed Consequences of Its Natural History. *Ocul Surf*. 2009;7:78-92.

[41] Khanal S, Tomlinson A, Diaper CJM. Tear Physiology of Aqueous Deficiency and Evaporative Dry Eye. *Optom Vis Sci*. 2009;86:1235-40.

[42] Zhu H, Chauhan A. A Mathematical Model for Tear Drainage through the Canaliculi. *Curr Eye Res*. 2005;30:621-30.

[43] Zhu H, Chauhan A. A Mathematical Model of Tear Mixing Under the Lower Lid. *Curr Eye Res*. 2007;32:1023-35.

[44] Zhu H, Chauhan A. A Mathematical Model for Ocular Tear and Solute Balance. *Curr Eye Res*. 2005;30:841-54.

[45] Gaffney EA, Tiffany JM, Yokoi N, Bron AJ. A Mass and Solute Balance Model for Tear Volume and Osmolarity in the Normal and Dry Eye. *Prog Retin Eye Res*. 2010;29:59-78.

[46] Goto E, Shimazaki J, Monden Yu, Takano Y, Yagi Y, Shimmura S, et al. Low-concentration homogenized castor oil eye drops for noninflamed obstructive meibomian gland dysfunction. *Ophthalmol*. 2002;109:2030-5.

[47] Khanal S, Tomlinson A, Pearce EI, Simmons PA. Effect of an Oil-in-Water Emulsion on the Tear Physiology of Patients With Mild to Moderate Dry Eye. *Cornea*. 2007;26:175-81.

[48] Korb DR, Scaffidi RC, Greiner JV, Kenyon KR, Herman JP, Blackie CA, et al. The Effect of Two Novel Lubricant Eye Drops on Tear Film Lipid Layer Thickness in Subjects With Dry Eye Symptoms. *Optom Vis Sci*. 2005;82:594-601.

[49] King-Smith PE, Hinel EA, Nichols JJ. Application of a novel interferometric method to investigate the relation between lipid layer thickness and tear film thinning. *Invest Ophthalmol Vis Sci*. 2010;51:2418-23.

[50] Brown SI, Dervichian D. Hydrodynamics of Blinking - In Vitro Study of the Interaction of the Superficial Oily Layer and the Tears. *Arch Ophthalmol*. 1969;82:541-7.

[51] Holly FJ. Surface chemistry of tear film component analogs. *J Colloid Interface Sci*. 1974;49:221-31.

[52] Yokoi N, Yamada H, Mizukusa Y, Bron AJ, Tiffany JM, Kato T, et al. Rheology of Tear Film Lipid Layer Spread in Normal and Aqueous Tear-Deficient Dry Eyes. *Invest Ophthalmol Vis Sci*. 2008;49:5319-24.

[53] Butovich IA, Millar TJ, Ham BM. Understanding and analyzing meibomian lipids - A review. *Curr Eye Res*. 2008;33:405-20.

[54] Butovich IA, Uchiyama E, McCulley JP. Lipids of human meibum: mass-spectrometric analysis and structural elucidation. *J Lipid Res*. 2007;48:2220-35.

[55] Butovich IA, Wojtowicz JC, Molai M. Human tear film and meibum. Very long chain wax esters and (O-acyl)-omega-hydroxy fatty acids of meibum. *J Lipid Res*. 2009;50:2471-85.

[56] Chen JZ, Green-Church KB, Nichols KK. Shotgun Lipidomic Analysis of Human Meibomian Gland Secretions with Electrospray Ionization Tandem Mass Spectrometry. *Invest Ophthalmol Vis Sci*. 2010;51:6220-31.

[57] Nicolaides N, Kaitaranta JK, Rawdah TN, Macy JI, Boswell FM, Smith RE. Meibomian Gland Studies - Comparison of Steer and Human Lipids. *Invest Ophthalmol Vis Sci*. 1981;20:522-36.

[58] Nicolaides N, Ruth EC. Unusual Fatty-Acids in the Lipids of Steer and Human Meibomian Gland Excreta. *Curr Eye Res*. 1982;2:93-8.

[59] Butovich IA. Cholesteryl esters as a depot for very long chain fatty acids in human meibum. *J Lipid Res*. 2009;50:501-13.

[60] Borchman D, Yappert MC, Foulks GN. Changes in human meibum lipid with meibomian gland dysfunction using principal component analysis. *Exp Eye Res*. 2010;91:246-56.

[61] Tsai PS, Evans JE, Green KM, Sullivan RM, Schaumberg DA, Richards SM, et al. Proteomic analysis of human meibomian gland secretions. *Br J Ophthalmol*. 2006;90:372-7.

[62] Tiffany JM, Dart J. Normal and Abnormal Functions of the Meibomian Secretion. *R Soc Med Int Congr Symp Ser*. 1981;40:1061-4.

[63] Arciniega JC, Nadji EJ, Butovich IA. Effects of free fatty acids on meibomian lipid films. *Exp Eye Res*. 2011;93:452-9.

[64] Butovich IA, Arciniega JC, Wojtowicz JC. Meibomian Lipid Films and the Impact of Temperature. *Invest Ophthalmol Vis Sci*. 2010;51:5508-18.

[65] Millar TJ, Mudgil P. Penetration of tear proteins into a meibomian lipid layer. *Invest Ophthalmol Vis Sci*. 2005;46:4418.

[66] Millar TJ, Tragoulias ST, Anderton PJ, Ball MS, Miano F, Dennis GR, et al. The surface activity of purified ocular mucin at the air-liquid interface and interactions with meibomian lipids. *Cornea*. 2006;25:91-100.

[67] Mudgil P, Torres M, Millar TJ. Adsorption of lysozyme to phospholipid and meibomian lipid monolayer films. *Colloids Surf B Biointerfaces*. 2006;48:128-37.

[68] Rantamaki AH, Javanainen M, Vattulainen I, Holopainen JM. Do Lipids Retard the Evaporation of the Tear Fluid? *Invest Ophthalmol Vis Sci*. 2012;53:6442-7.

[69] Green-Church KB, Butovich I, Willcox M, Borchman D, Paulsen F, Barabino S, et al. The International Workshop on Meibomian Gland Dysfunction: Report of the Subcommittee on Tear Film Lipids and Lipid-Protein Interactions in Health and Disease. *Invest Ophthalmol Vis Sci*. 2011;52:1979-93.

[70] McCulley JP, Shine W. A compositional based model for the tear film lipid layer. *Trans Am Ophthalmol Soc*. 1997;95:79-93.

[71] McCulley JP, Shine WE. The lipid layer: The outer surface of the ocular surface tear film. *Biosci Rep*. 2001;21:407-18.

[72] Holly FJ. Formation and Rupture of the Tear Film. *Exp Eye Res*. 1973;15:515-25.

[73] Leiske D, Leiske C, Leiske D, Toney M, Senchyna M, Ketelson H, et al. Temperature-induced transitions in the structure and interfacial rheology of human meibum. *Biophys J*. 2012;102:719-.

[74] Leiske DL, Miller CE, Rosenfeld L, Cerretani C, Ayzner A, Lin B, et al. Molecular Structure of Interfacial Human Meibum Films. *Langmuir*. 2012;28:11858-65.

[75] Hedestrand G. On the influence of thin surface films on the evaporation of water. *J Phys Chem*. 1924;28:1245-52.

[76] Langmuir I, Langmuir DB. The effect of monomolecular films on the evaporation of ether solutions. *J Phys Chem*. 1927;31:1719-31.

[77] Rideal EK. On the influence of thin surface films on the evaporation of water. *J Phys Chem*. 1925;29:1585-8.

[78] Docking AR, Heymann E, Kerley LF, Mortensen KN. Evaporation of water through multimolecular films. *Nature*. 1940;146:265.

[79] Gilby AR, Heymann E. The rate of evaporation of water through duplex films. *Aust J Sci Res A*. 1948;1:197-212.

[80] Heymann E, Yoffe A. The stability of multimolecular films of hydrocarbon oils, containing spreaders, on water surfaces. *Trans Faraday Soc*. 1942;38:408-17.

[81] Langmuir I, Schaefer VJ. Rates of evaporation of water through compressed monolayers on water. *J Franklin Inst*. 1943;235:119-62.

[82] Powell RW. The influence of surface films of oil on the evaporation of water. *Trans Faraday Soc*. 1943;39:311-8.

[83] Sebba F, Briscoe HVA. The evaporation of water through unimolecular films. *J Chem Soc*. 1940;39:106-14.

[84] Pomerantz P, Clinton WC, Zisman WA. Spreading Pressures and Coefficients, Interfacial Tensions, and Adhesion Energies of the Lower Alkanes, Alkenese, and Alkyl Benzenes on Water. *J Colloid Interface Sci*. 1967;24:16-28.

[85] Blodgett KB. Interference Colors in Oil Films on Water. *J Opt Soc Am*. 1934;24:313-5.

[86] Zisman WA. The spreading of oils on water part I. Ionized molecules having only one polar group. *J Chem Phys*. 1941;9:534-51.

[87] Zisman WA. The spreading of oils on water Part II. Non-ionized molecules having only one polar group. *J Chem Phys*. 1941;9:729-41.

[88] Zisman WA. The spreading of oils on water. III. Spreading-pressures and the Gibbs adsorption relation. *J Chem Phys*. 1941;9:789-793793.

[89] Mansfield WW. Effect of Surface Films on the Evaporation of Water. *Nature*. 1953;172:1101.

Chapter 2

Tear Dynamics in Healthy and Dry Eyes

2.1 Abstract

Dry-eye disease, an increasingly prevalent ocular-surface disorder, significantly alters tear physiology. Understanding the basic physics of tear dynamics in healthy and dry eyes benefits both diagnosis and treatment of dry eye. We present a physiological-based model to describe tear dynamics during blinking.

Tears are compartmentalized over the ocular surface; the blink cycle is divided into three repeating phases. Conservation laws quantify the tear volume and tear osmolarity of each compartment during each blink phase. Lacrimal-supply and tear-evaporation rates are varied to reveal the dependence of tear dynamics on dry-eye conditions, specifically tear osmolarity, tear volume, tear-turnover rate (TTR), and osmotic water flow.

Predicted periodic-steady tear-meniscus osmolarity is 309 and 321 mOsM in normal and dry eyes, respectively. Tear osmolarity, volume, and TTR all match available clinical measurements. Osmotic water flow through the cornea and conjunctiva contribute 20 and 50 % to the total tear supply in healthy and dry-eye conditions, respectively. TTR in aqueous-deficient dry eye (ADDE) is only half that in evaporative dry eye (EDE).

The compartmental periodic-steady tear-dynamics model accurately predicts tear behavior in normal and dry eyes. Inclusion of osmotic water flow is crucial to match measured tear osmolarity. Tear-dynamics predictions corroborate the use of TTR as a clinical discriminator between ADDE and EDE. The proposed model is readily extended to predict the dynamics of aqueous solutes such as fluorescent tags or drugs.

2.2 Introduction

Dry eye, one of the most common ocular-surface disorders, may affect as much as 30 % of the worldwide population [1]. The International Dry Eye Workshop [2] (DEWS) defines dry eye as *"a multifactorial disease of the tears and ocular surface that results in symptoms of discomfort, visual disturbance, and tear film instability. It is accompanied by increased osmolarity of the tear film and inflammation of the ocular surface."* The role of increased tear osmolarity (salinity) in dry eye was suspected by early investigators [3-5], but not proven convincingly until 1978 by Gilbard [6, 7]. More than 30 y later, enhanced osmolarity remains central to the definition of dry eye [2]. Because tear hyperosmolarity repeatedly correlates with both the presence and severity of dry eye [8, 9], it has been suggested to be the single most effective marker of dry eye [10-12].

Tear bathing the ocular surface contains dissolved salts, proteins, and mucins, and is produced as an isotonic fluid by the main and accessory lacrimal glands of the eye [13]. Water evaporates from the exposed 3-5 μm thick tear film between blinks, thereby concentrating the salt. Whereas the measured tear osmolarity for healthy individuals is near 300 milli-Osmoles per liter (mOsM), it can reach up to 400 mOsM for dry-eye sufferers [6, 7, 9, 11, 12]. Increased tear evaporation and decreased tear supply both amplify this effect; dry eye resulting from these two stimuli is termed, respectively, evaporative dry eye (EDE) and aqueous-deficient dry eye (ADDE).

Increased evaporation typically originates from lid diseases, such as meibomian gland dysfunction (MGD), that lead to a compromised tear-film lipid layer (TFLL) or from arid or windy environments [14-19]. Deficient lacrimal-tear production is commonly a result of aging or of Sjögrens syndrome [2]. Resulting tear hyperosmolarity decreases mucin expression and triggers a proinflammatory signaling cascade that leads to tear instability, inflammation, and epithelial cell death [20]. It is currently understood that these stressors exacerbate each other, perpetuating a vicious cycle of inflammation and ocular-surface damage that is dry eye [20, 21].

Increased tear-evaporation rate and decreased tear-supply rate both correlate experimentally with increased tear osmolarity and dry-eye disease. Thus, tear-flow dynamics is fundamental to dry eye. Development of a mechanistic quantitative relationship between tear dynamics and tear osmolarity, however, is difficult to accomplish experimentally. Simultaneous tracking of salt and water flows over the ocular surface while also measuring tear flow and evaporation rates is impractical. Continuum modeling of tear dynamics relates tear flows to tear osmolarity, and enables interrogation of tear behavior over a wide range of tear-evaporation and tear-supply rates not easily assessed in the clinic.

Based on their study of corneal and conjunctival water permeability, Levin and Verkman [22] were the first to develop a simple mathematical model to predict tear osmolarity in mice eyes. They assumed that the tears occupy a single, well-mixed compartment and they accounted for tear evaporation, lacrimal secretion, and osmotically driven water flow through the ocular surface. For normal tear-evaporation and lacrimal-supply rates, analytical solution predicted a normal tear osmolarity approximately 7 mOsM above isotonic. In agreement with clinical observations, they found that increased evaporation, decreased lacrimal secretion, and decreased osmotic flow resulted in elevated tear osmolarity.

Zhu and Chauhan published several papers modeling tear drainage [23], mixing [24], osmolarity, and volume [25, 26]. Their improved calculations incorporated not only the physics of tear deposition and drainage, but also detailed biological models of salt and water transport through the conjunctival epithelia, allowing them to predict total tear volume and osmolarity. They calculated a normal tear osmolarity of 298 mOsM, significantly less than their assumed 362 mOsM for the lacrimal-supply osmolarity. Active and passive water and solute transport through the conjunctiva played an important role in the predicted tear osmolarity and tear flow. Simplification of the tear compartmentalization over the ocular surface and absence of inter-compartmental blink dynamics prevented analysis of solute distribution across the eye.

Tears are not continuous over the ocular surface, but are distributed into different regions including the lid margins, the preocular tear film, and the conjunctival sacs. Different regions exhibit distinct tear volumes [27, 28] and are not continuous with each other. That is, it takes time for fluid and solute to mix between regions [29, 30]. Therefore, the salt concentration varies between regions depending on local dynamics. Because osmolarity initiates both ocular-

surface damage and transmembrane water transport through the epithelia, details of salt and water exchange in each compartment must be addressed.

The recent work of Gaffney *et al.* [31] accounted for tear compartmentalization, and represents a significant improvement as it describes the osmolarity difference between the meniscus and the tear film. The perched tear film experiences tear evaporation that significantly concentrates the remaining fluid because it is hydraulically isolated from the menisci by the black lines [32, 33]. This result is of particular importance because clinically reported tear osmolarities are almost always obtained by sampling from the lower meniscus, whereas the osmolarity experienced by the epithelial cells in most of the palpebral aperture is considerably higher [31, 34]. For a normal individual, a tear osmolarity of 313 mOsM was predicted by Gaffney *et al.*, 11 mOsM higher than the lacrimal secretion osmolarity. Gaffney *et al.* investigated tear behavior (i.e., transient compartment volumes and osmolarities) over a range of tear-evaporation rates, lacrimal-supply rates, blink frequencies, and inter-compartmental mixing schemes. They describe tear dynamics for EDE and ADDE, and discuss the effectiveness of blink-rate increases in combating dry-eye induced tear hyperosmolarity. Many tear fluxes and geometries, however, are estimated for the normal case only, decoupling the interblink dynamics from deposition and drainage physics. Additionally, Gaffney *et al.* do not include water flow through the ocular epithelial surfaces. Consequently, their results are limited to low tear-evaporation rates and to high lacrimal-supply rates in order to obtain normal tear osmolarity.

We couple the physics of tear-film deposition, tear drainage, water and solute distribution, and osmotic-driven water flow through the cornea and conjunctiva. Although our effort shares similar assumptions to those of Gaffney *et al.* [31], we consider only the periodic steady-state behavior of the tears. In addition, inclusion of osmotic water flow through the conjunctival and corneal epithelia enables matching to a wider range of clinically reported tear measurements, and highlights the role of conjunctival and corneal water secretion in maintaining tear osmolarity. In dry-eye conditions, we find that osmotic water-flow rate through the cornea and conjunctiva can be as much as half of the lacrimal-supply rate.

Predicted results are compared to important clinical tear measurements including tear production, tear turnover rate (*TTR*), tear volume, tear-film thickness, and tear osmolarity. By treating the lacrimal-supply and tear-evaporation rates as parameters, we predict tear dynamics for a wide range of conditions, primarily those of dry eye. Comparison to clinical measurements generates insight into the differences in tear dynamics between normal, ADDE, and EDE subjects and corroborates the use of *TTR* as a useful clinical discriminator between ADDE and EDE. We also examine the ramifications of the highest measured tear-film thinning rates [35, 36] on tear osmolarity. These high evaporation rates lead to tear osmolarities well above those measured in dry-eye conditions.

2.3 Model Description

Tear dynamics describes the distribution and flow of water through and over the ocular surface. Based on tear physiology, we divide tears into five distinct compartments and perform water and salt balances on each compartment to yield tear volumes and salt concentrations for each. Periodic-steady transient changes in salt concentration and tear volume are predicted within individual compartments over repeating blink cycles. Figure 2.1 shows sagittal cross-sections of the anterior eye during the three phases of the blink cycle: tear deposition that starts as the upper lid rises; interblink, during which the eye remains open; and closure, that occurs as the upper lid falls. Volumetric tear-flow rates during interblink are indicated by the symbol q

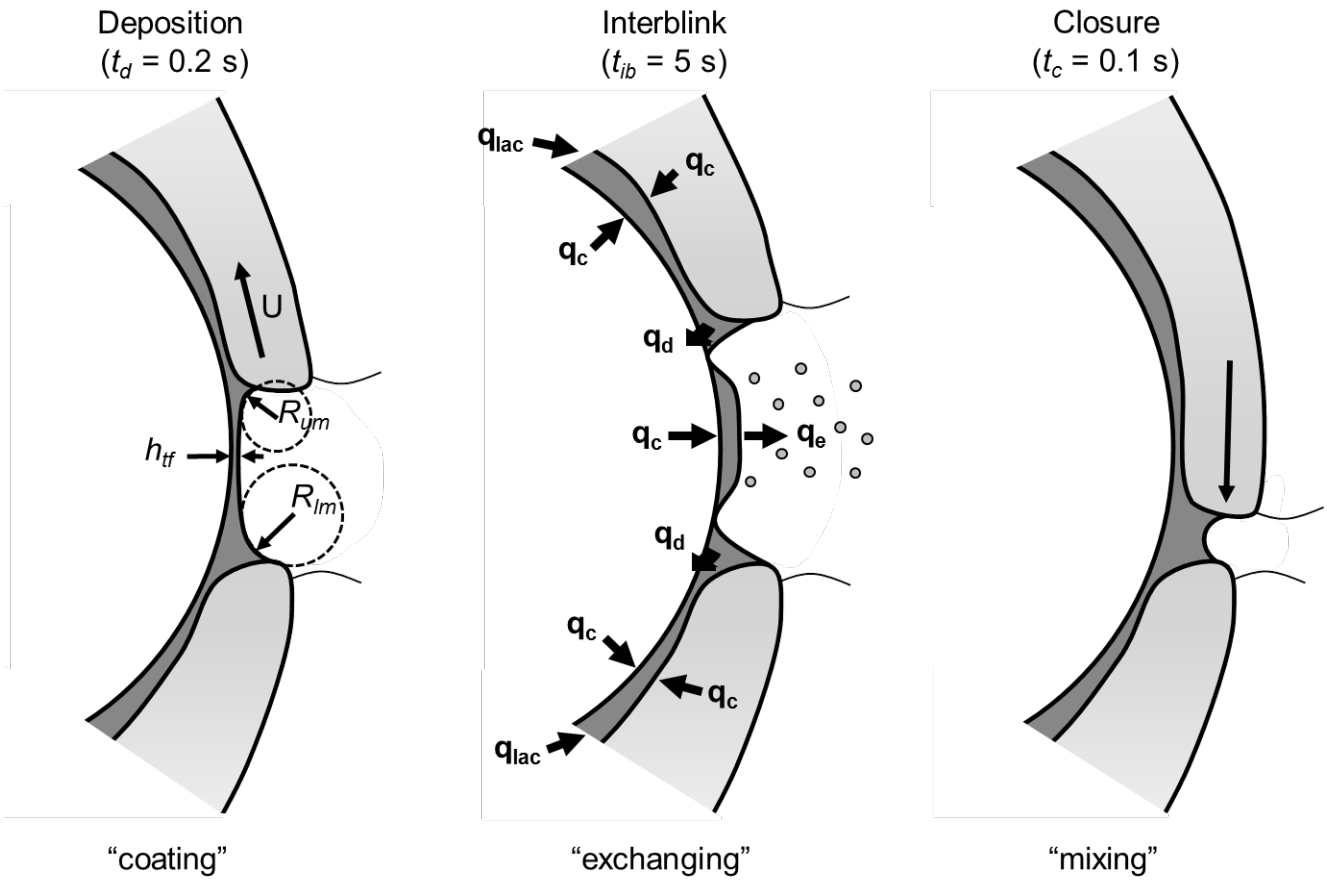

Figure 2.1: Schematic sagittal view of the anterior eye and lids including tear film thickness h_{tf}. The blink cycle is divided into three phases that repeat continuously: deposition, interblink, and closure. Water-flow streams are indicated by arrows labeled with pertinent volumetric flow rates q.

[m^3/s]. After closure, the cycle begins anew, repeating identically: a periodic steady state results. We describe below the tear compartmentalization and geometries, the water and salt balances for each compartment during each blink phase, parameter estimation, and finally the numerical method to solve the resulting coupled nonlinear ordinary differential equations. Chosen values for compartment geometries (Appendix 2A), tear physical properties, and other required parameters are listed in Table 2.1.

Table 2.1: Parameters used in model for "normal" individual

Parameter	**Symbol**	**Value** (common)	(SI units)	**Source(s)**
Eye-globe radius	R	1.2 mm	0.012 m	[37, 38]
Palpebral-aperture height	h_{pa}	9.0 mm	0.009 m	[27, 39, 40]
Palpebral-aperture area	A_{pa}	2.1 cm^2	0.0021 m^2	[27, 40, 41]
Lid-margin perimeter	S_{lid}	30 mm	0.03 m	[27]
Upper-fornical area	A_{uf}	3.8 cm^2	0.0038 m^2	Geometry, [42]
Lower-fornical area	A_{lf}	2.7 cm^2	0.0017 m^2	Geometry, [42]
Total conjunctival area	A_{conj}	14.1 cm^2	0.0141 m^2	Calculation
Center lid-opening velocity	U	5 cm/s	0.05 m/s	Calculation, [43]
Deposition time	t_d	0.18 s	0.18 s	Calculation, [43]
Interblink time	t_{ib}	5.0 s	5.0 s	[37]
Secreted-tear osmolarity	c_{lac}	300 mOsM	150 mol/m^3	[44]
Tear viscosity	μ	1.5 cP	0.0015 Pa·s	[45]
Tear surface tension	σ	45 mN/m	0.045 N/m	[46]
Tear mass density	ρ	1 g/cm^3	10^3 kg/m^3	
Lid-ocular surface gap thickness	h_0	2 µm	2.0×10^{-6} m	Calculated
Conjunctival-sac thickness	h_c	7.0 µm	7.0×10^{-6} m	[27, 47]
Conjunctival water permeability	P_{ci}	0.00125 cm/s	1.25×10^{-5} m/s	
Corneal water permeability	P_{cn}	0.00125 cm/s	1.25×10^{-5} m/s	
Maximum drainage rate	q_m	1.0 µL/min	2.8×10^{-11} m^3/s	Based on [23]
Minimum drainage radius	R_0	120 µm	1.2×10^{-4} m	Based on [23]
Mixing fraction in conjunctival sac	β_i	1.0	1.0	
Fraction of q_{lac}	λ_u	0.80	0.80	[48]
Healthy lacrimal tear-secretion rate	q_{lac}	1.10 µL/min	2.1×10^{-11} m^3/s	[49]
Healthy tear-evaporation rate	q_e	0.15 µL/min	1.2×10^{-12} m^3/s	[49]

2.3.1 Tear flow and compartments

The leftmost panel in Figure 2.1 shows the tear-deposition phase as the upper lid rises at velocity U to leave behind the aqueous tear film over the exposed ocular surface. The upper and lower menisci radii are labeled R_{um} and R_{lm}, respectively. The lower meniscus remains static while the upper-meniscus volume shrinks due to loss of fluid to the deposited tear film. The tear-film thickness, h_{tf}, is proportional to R_{um}. More tear in the upper meniscus increases h_{tf} [50]. As the upper lid rises, some tear is uncovered behind the meniscus, partially replenishing the upper-meniscus volume. At the end of the 0.2-s deposition phase, the upper-meniscus radius is smaller than that of the lower meniscus due to fluid loss to the tear film.

Within 0.03 s of lid closure, capillary forces locally thin the tear film to form the black lines originally observed by McDonald and Brubaker [32, 33, 50]. These deep channels pinch off the tear film, isolating it from the bordering menisci. Consequently, the central panel in Figure 2.1 partitions the exposed tears during an interblink into three compartments: the upper and lower menisci that lie along the lid margins and the perched preocular tear film that coats the exposed cornea and conjunctiva [27, 47]. No water or solute exchange occurs between the menisci and the perched tear film [32, 33]. Conjunctival sacs behind the upper and lower lids also serve as reservoirs for tear fluid. These five regions define the five tear compartments of the modeling effort.

The majority of tear flow occurs during interblink. Aqueous tear originates as a nearly isotonic mixture of water, salt, and proteins [44]. Tear produced in the main and accessory lacrimal glands enters the base of the upper and lower conjunctival sacs at a combined volumetric flow rate q_{lac}. Later λ_u and λ_l quantify the fractions of the total lacrimal supply that enter the upper and lower conjunctival sacs, respectively. Osmotically driven water flow through the palpebral and bulbar conjunctivae, labeled q_c, enhances tear flow in the conjunctival sacs where osmolarity is elevated above isotonic. Experiments utilizing radioactive tracer (scintigraphy) [29] and fluorescein dye [30] demonstrate that solutes instilled in the conjunctival sacs eventually reach the precorneal tear film by mixing and flow. Thus, lacrimal-secreted tear reaches the lid margin and enters the menisci.

In the exposed tear, small particles placed in the menisci flow laterally along the lid margin towards the puncta before draining into the canaliculi, but do not flow into the isolated tear film during interblink [47]. Thus, tear from the conjunctival sacs enters the superior and inferior menisci from which it is lost via punctal drainage or evaporation. Evaporative loss from the menisci is minimal. However, the large surface area of the perched tear film results in significant water loss. Similar to the conjunctival sacs, water enters or exits the tear film through the cornea and conjunctiva. Gradients in hydraulic pressure, osmotic pressure, and electrical potential drive water flow between the tears and blood serum through the conjunctiva or between the tears and aqueous humor through the cornea. As with many biological membranes, water transport through these tissues occurs through a complex combination of passive and active transport [51]. Detailed descriptions of coupled ion and water transport have been worked out for both the cornea and conjunctiva [26, 52]. We approximate water flow through the palpebral and bulbar conjunctivae as osmotic-driven flow characterized solely by the water permeability of the membrane P_{cj} [m/s] and the osmotic concentration difference between the tears and serum, similar to Levin and Verkman [22]. To describe trans-corneal water flow, we utilize the results of Leung *et al*. [52] for water flow through the cornea, q_{cn}, versus tear osmolarity as described previously by Cerretani *et al*. [53].

After interblink, the upper lid descends toward the lower lid, initiating the closure phase, which lasts about 0.1 s. During closure, shown in the rightmost panel of Figure 2.1, tear originating from the various compartments mixes. Tear in the exposed compartments mixes completely. The extent of fluid mixing in the tear of the conjunctival sacs during a normal blink, however, is unclear. Under controlled gaze in a scintigraphy study [29], tracer inserted in the menisci rarely traveled back under the lids. Nevertheless, most current fluorescence studies rely on the observation that fluorescent dye placed in upper and lower conjunctival sacs dilutes over the total tear volume after forceful blinking [27, 49, 54, 55]. The difference in mixing behavior is likely due to differences in blinking strength and eye movement. We hypothesize that

complete mixing of the exposed tear with unexposed tear may not occur with every blink, but over a long time period, tear is effectively mixed.

At the end of closure, the upper lid rises, commencing the deposition phase. A new blink cycle begins. Within one transient blink cycle, compartment volumes and salt concentrations vary, but they repeat identically after each blink cycle. Thus, tear dynamics follows a periodic-steady state.

2.3.2 Water and salt balances

To predict compartment volumes and osmolarities in a periodic-steady state, we conserve the mass of water and salt that enters or exits each compartment during each phase of the blink cycle. Upon neglecting water-density variation due to dilute salts present in the tears, water volumes must balance in each of the 5 compartments

$$\frac{dV_\alpha}{dt} = \sum_j^J (q_j)_{in} - \sum_k^K (q_k)_{out} \tag{1}$$

where V_α is the water volume of compartment α [m^3], q_j and q_k are the volumetric flow rates [m^3/s] of the j-th and k-th streams of fluid entering or exiting the compartment, respectively. There are J total streams entering compartment α and K total streams exiting it. The left side of Equation 1 represents the instantaneous rate of change of compartment volume. Flow rates on the right side of Equation 1 are functions of time, geometry, salinity, and a number of physical properties governing water transport via evaporation and osmotic flow.

Mass conservation for salt within each compartment is

$$\frac{d(c_\alpha V_\alpha)}{dt} = \sum_j^J (c_j q_j)_{in} - \sum_k^K (c_k q_k)_{out} \tag{2}$$

where c_α, c_j, and c_k are the concentrations [mol/m^3] of salt in compartment α, in the j-th inlet stream, and in the k-th outlet stream, respectively. We consider tear salts as a single 1:1 electrolyte species (i.e., NaCl), but the model is readily extended to include other solutes, such as instilled drugs. Therefore, concentrations reported below in osmolarity units refer to twice the molar concentration, $2c$.

Solution of coupled Equations 1 and 2 for compartment α subject to the appropriate initial conditions gives the transient compartment volume and salinity, $V_\alpha(t)$ and $c_\alpha(t)$, during each of the blink stages. We now outline the relevant physical processes for each compartment during each blink phase. Detailed equations are relegated to Appendix 2B.

2.3.2a Deposition phase

During the deposition stage of a blink, the upper lid rises to its open position [43]. As Wong *et al*. [50] describe, the upper meniscus deposits tear fluid onto the cornea and conjunctiva as the lid passes over the palpebral aperture. Outflow of fluid from the upper meniscus becomes the tear film. Thus, the upper meniscus coats the anterior corneal and conjunctival surfaces with a film of tear. The volume initially held in the upper meniscus alone is insufficient to provide fluid for a 3 to 5-μm tear film and to retain a typical meniscus volume [56-58]. To account for this discrepancy, we postulate that a thin layer of tear from the conjunctival sac is uncovered from behind the upper-lid margin during lid upward motion. A hydrodynamic-lubrication analysis for the liquid between the corneal and lid-margin surfaces predicts the thin layer of tear between the two to be on the order of microns thick [59]. We select a 2-μm gap between the lid and cornea. Fluid inflow into the upper meniscus prevents significant volume reduction as it

leaves behind the tear film. Likewise, hydrodynamic coating theory describes the dependence of deposited tear-film thickness on upper meniscus radius R_{um}, upper-lid velocity U, tear viscosity μ, and tear surface tension σ (Equation B.4) [50]. Equation B.5 describes water conservation in the upper meniscus during deposition and, thus, deposited tear-film thickness. For the typical parameters listed in Table 2.1, a normal upper-meniscus radius of 300 μm results in a 4-μm thick deposited tear film in good agreement with current interferometric measurement [56].

2.3.2b Interblink phase

Interblink is the 5-s phase between the end of deposition and the beginning of lid closure [43, 60]. Fluid transfer via lacrimal secretion, corneal and cojunctival osmosis, punctal drainage, and tear evaporation occurs primarily during this longest period of the blink cycle.

Conjunctival Sacs

Both the upper and lower conjunctival sacs are approximated as rectangular channels of height h_c and lengths L_{uc} and L_{lc}, respectively, that span the width of the lids. Channel length is the average distance from the meniscus to the termination of the fornix. Freshly secreted tear flowing into the conjunctival sacs from the lacrimal glands with salt concentration c_{lac} is supplemented by osmotically driven water flow through the bulbar and palpebral conjunctivae wherever the salt concentration in the fornix is greater than c_{lac}. Conjunctival sacs serve as fixed-height conduits for tear fluid. Transient flow and solute concentration in the fornices are described by Equations B.9 and B.10, respectively.

Menisci

During interblink, tear fluid exiting the conjunctival sacs carries water and salt into each meniscus at the lid margins. Simultaneously, tears drain from the meniscus via suction through the puncta, and water evaporates from the exposed surface. Equations B.11 and B.13 describe water and salt mass conservation, respectively, in each meniscus. Drainage rate through the puncta is based on capillary suction, as previously enunciated by Zhu and Chauhan [23]. Thus, the drainage rate from the meniscus, q_{di}, is proportional to the difference in curvatures between that of the meniscus, and that characteristic of the corresponding punctum, as quantified in Equation B.12. That is, the larger is the meniscus radius of curvature, R_{im}, the smaller is the opposing suction pressure in the meniscus and, therefore, the larger is the drainage rate. As the meniscus drains during an interblink, the meniscus radius of curvature decreases and the drainage rate subsides [47, 60]. We account for evaporative loss of water from the menisci, but this loss is small compared to those in other flows because of minimal exposed surface area.

Tear film

At the beginning of interblink, suction from the upper and lower menisci rapidly pinches off the tear film to produce superior and inferior black lines [32, 50, 61, 62]. The now-perched tear film is isolated from the menisci; flow between the menisci and the tear film is negligible [33]. During interblink, the tear film loses water to the environment by evaporation and gains water from osmotic imbibition through the cornea and conjunctiva, as described by Equation B.14. We assume that the tear film resists dewetting for the entire interblink and ignore the presence of possible growing dimples and salinity hot spots [63-65]. Negligible salt transport occurs through the anterior epithelium [52]. Therefore, salt initially present in the tear film concentrates according to Equation B.15 as water evaporates into the environment. Evaporative tear loss is the physical origin of hyperosmolarity: evaporation concentrates salt in the tear film, which then distributes into the remaining tears during blinking. There can be no dry eye without tear evaporation.

2.3.2c Closure phase

At the end of interblink, the upper lid closes to meet the stationary lower lid. Lid meeting signifies the beginning of closure. During closure, the motion of the lids and eyeball mixes the tear in the menisci and that in the tear film and, to a certain extent, with that in the upper and lower conjunctival sacs. We include a parameter, β_i, described in Appendix 2B, to characterize the extent of mixing in the upper and lower conjunctival sacs during closure, β_u and β_l. β_i ranges between 0 and 1, indicating no mixing and complete mixing. We find a minor effect of β on tear osmolarity. Nevertheless, we set $\beta = 1$, as stated earlier, because tear is assumed well mixed over many blinks. Consequently, upon completion of closure, the tear fluid exhibits a homogeneous bulk salt concentration, c_b, in the menisci, tear film, and conjunctival sacs. The bulk salt concentration c_b, calculated in Equation B.16, is a volume-average salt concentration depending on the volumes and osmolarities in each compartment at the end of interblink. $2c_b$ corresponds to measured tear osmolarity. After closure, deposition begins again starting with uniform salt concentration, c_b. During the course of deposition and interblink, compartment volumes redistribute and the osmolarities in each compartment change until they reset during the closure phase.

2.3.3 Solution methodology

Tear on the ocular surface is in a periodic-steady state. Otherwise, the tear thickness, menisci volumes, and salt concentrations drift in time to a new periodically repeated value. Therefore, the volumes and concentrations in each compartment must be the same at the beginning or end of each blink cycle. To conserve water in the periodic-steady state, the total amount of water flowing in and out of all five tear compartments over the three blink phases must be equal. As described in Appendix 2C, the total flow rate from the lacrimal and accessory lacrimal glands, q_{lac}, plus the total average flow rate of water through the cornea and conjunctiva, q_c, must equal the average flow rate of tears into both puncta, q_d, plus the flow rate of water by evaporation from the tear film, q_e.

Conservation of salt in the periodic-steady state demands that the amount of salt supplied by the lacrimal and accessory lacrimal glands must equal that exiting in the tear draining through the puncta (Equation C.2). Upon imposition of periodicity, we utilize an iterative method to solve for the compartment volumes and c_b. After choosing an initial guess for the bulk salt concentration, c_b, and for the upper- and lower-meniscus radii of curvature at the beginning of deposition, R_b, we numerically integrate the ordinary differential equations corresponding to the deposition, interblink, and closure balances by a Runge-Kutta algorithm, as outlined in Appendix 2C. An extended *Regula-Falsi* method [66] is adopted to iterate choices of c_b and R_b until both the water and salt balances close over a complete blink cycle. Compared to a full transient solution [31], computations are efficient because only the periodic steady state need be ascertained.

2.3.4 Parameters

2.3.4a Lacrimal supply

Direct measurements of the lacrimal-supply rate, q_{lac}, in humans are not available. Instead, measurement of the tear turnover rate, *TTR* [%/min], permits calculation of q_{lac} using a model for tear flow over the ocular surface. There is a wealth of clinically measured *TTR*s in the literature, most of which are summarized in two recent reviews by Tomlinson *et al*. [49, 54]. *TTR* is determined quantitatively using fluorophotometry to gauge *in-situ* decay of a fluorescent

dye instilled in the tears neglecting any penetration into the cornea or conjunctiva. Typically, fluorescence in the tear film decays exponentially in time. The slope of the long-time portion of the log of fluorescent intensity versus time yields the *TTR* [49, 54, 55]. Next, initial dye dilution allows calculation of the total tear volume, V_t. Calculation of q_{lac} from *TTR* and V_t is described in the literature [27, 49, 54, 55] and in Appendix 2D. Current literature, however, ignores the contributions of osmotic water flow and evaporation to tear flow. Although this is an accurate approximation for most healthy subjects, both of these flows are elevated for dry-eye patients.

To account for all flows in healthy and dry-eye patients (Equations D.2 and D.3), we require additional clinical measurement of q_e and c_b. To our knowledge, two studies by Khanal *et al.* [12, 67] provide the only data encompassing all necessary tear parameters to complete a rigorous analysis. Since lacrimal-supply rates of Khanal *et al.* are higher than average, we base our normal tear-supply value, 1.10 µL/min, on the average tear flow established in the meta-analysis of Tomlinson *et al.* [11, 54]. We then use the data from Khanal *et al.* [12, 67] to choose the ratios between lacrimal-supply and tear-evaporation rates in the normal and dry-eye cases. Tear supply is varied over a wide range to examine its effect on tear dynamics, especially on meniscus osmolarity. Representative healthy, dry-eye, ADDE, and EDE tear-supply rates are listed in Table 2.2.

Table 2.2: Tear-evaporation and lacrimal-supply rates for normal and dry-eye cases.

Case	Tear-evaporation rate, q_e [µL/min]	Lacrimal-supply rate, q_{lac} [µL/min]
Normal	0.15	1.10
Dry eye	0.30	0.55
Aqueous-deficient dry eye (ADDE)	0.25	0.40
Evaporative dry eye (EDE)	0.35	0.80

2.3.4b Evaporation

Similar to the tear-flow data, *in-vivo* tear-evaporation rates have been reported for many decades and are summarized by Tomlinson *et al.* [49, 54]. Tear-evaporation measurements on the human eye generally come in two forms. The most common measurement type involves placing specially designed goggles over the eye to measure water loss from the ocular surface [40, 41, 49, 54, 68-70]. The second method employs optical interferometry to measure the tear-film thinning rate at a specific spot in the tear film [36]. Evaporation rates measured with interferometry are significantly higher than those obtained with goggle wear. For a review discussion, refer to Tomlinson *et al.* [49]. We chose the average reported evaporation rate from the meta-analysis of Tomlinson *et al.* [49], 0.75 µm/min, for normals. In choosing the tear-evaporation rates for various dry-eye scenarios, we again use the ratios of evaporation rates provided by Khanal *et al.* [12, 67].

Separately, we study high evaporation rates measured interferometrically by Nichols *et al.* [36] and fluorescently by King-Smith *et al.* [35]. Nichols *et al.* [36] measured an average thinning rate of 3.79 µm/min in a 33 x 35 µm patch of the precorneal tear film. Using fluorescence imaging, King-Smith *et al.* [35] estimated evaporation rates in precorneal and preconjunctival tear films to be 2.4 and 1.4 µm/min, respectively. We approximate the overall evaporation rate to be the average of the two rates, or 1.9 µm/min. By considering these

evaporation rates, we investigate how high the tear-supply rate or osmotic water permeability of the cornea and conjunctiva must be to enable normal bulk tear osmolarity.

2.3.4c Tissue water permeability

In contrast to the above parameters, all estimated from measurements on humans, whole-tissue water permeability has been directly measured only on animals [22]. Mouse eyes yielded corneal and conjunctival-tissue water permeabilities of 1.1 and 1.7×10^{-5} m/s, respectively. Recently reported measurements of evaporation and fluorescence decay in human eyes [35] indirectly estimate these permeabilities to be about 1.2 and 5.5×10^{-5} m/s, respectively. Mathematical modeling of corneal metabolism and water transport [52] also gives a corneal water permeability of 2.1×10^{-5} m/s, with a basal transcorneal secretion rate of 0.013 µL/min [53]. The value 1.25×10^{-5} m/s was chosen for both corneal and conjunctival water permeability. We also adopt the basal water-secretion rate from Leung *et al.* [52], which is not a function of osmolarity. These values agree with the small body of available literature [22, 35, 52], and result in tear osmolarities that match reported values for normal and dry eyes [11]. It is important to note, however, that, since changing tissue water permeabilities results in significant changes in predicted tear dynamics, we also investigate the effect of varying them as parameters.

2.4 Results

2.4.1 Normal and dry-eye conditions

Given the parameters in Table 2.1 for normal individuals, the coupled water and salt balances predict the periodic-steady-state tear dynamics. Additionally, we predict behavior for tear-evaporation and lacrimal-supply rates representative of all dry eye (DE), aqueous-deficient dry eye (ADDE), and evaporative dry eye (EDE), as listed in Table 2.2. Figures 2.2 and 2.3 show the periodic-steady osmolarities and volumes of various compartments over five blink cycles for normal and dry-eye conditions. Right brackets in each figure differentiate between normal and dry-eye subjects. Solid, dotted, and dashed lines in Figure 2.2 correspond to the tear-film, menisci, and conjunctival-sac osmolarities, respectively. Osmolarity differences between the upper and lower menisci and conjunctival sacs are negligible. Solid, dotted, and dashed lines in Figure 2.3 correspond to the tear-film, upper-meniscus, and lower-meniscus tear volumes, respectively. The total volume of the conjunctival sacs is constant at 4.5 µL for all cases, or 2.25 µL each. Just after tear deposition to the left of a cycle, each compartment begins with an initial volume and osmolarity. During 5-s interblink, fluid and solute obey the conservation balances, causing gradual changes in compartment osmolarity and volume. At the end of interblink to the right of a blink cycle, closure occurs, mixing the compartments and resetting their volumes and salinities back to their initial states before deposition. Clearly, the tear-film osmolarity increases during the interblink because the water-evaporation rate exceeds that due to osmotic inflow. Osmotic inflow causes the small decline in the fornix osmolarity during interblink. Figure 2.2 shows minimal changes in meniscus osmolarity during the blink cycle. Therefore, the bulk-tear osmolarity, c_b, is representative of that in the lower meniscus, from which clinical samples are obtained [6, 8, 9, 11]. Water evaporation from the tear film demands that the bulk-tear osmolarity always be greater than that of the isotonic secreted lacrimal tears.

For normal conditions, the upper meniscus begins interblink with 40 % less volume than that in the lower meniscus. This is because the upper meniscus supplies the tear-film volume.

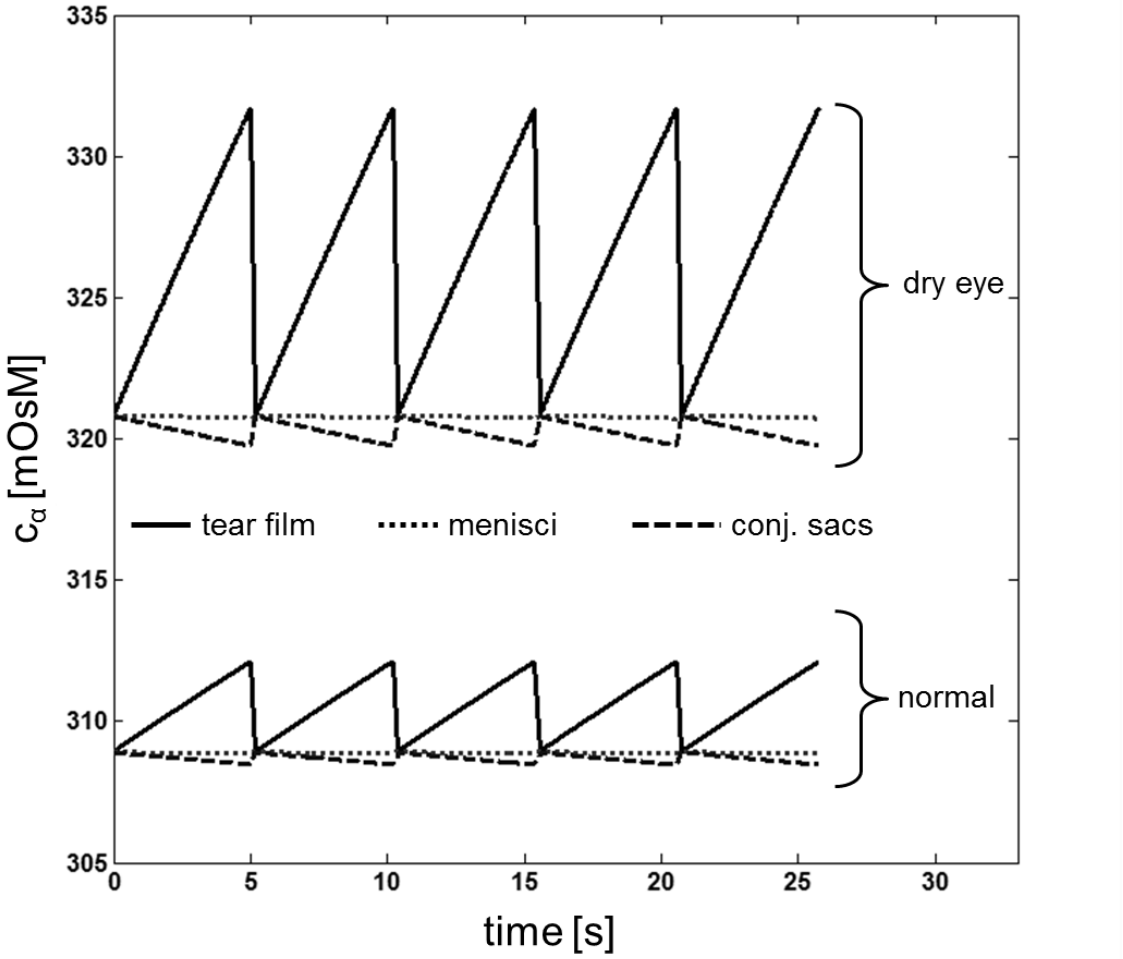

Figure 2.2: Periodic steady-state osmolarities of upper and lower meniscus, conjunctival sacs, and tear film over 5 blink cycles for normal and dry-eye conditions. Solid, dotted, and dashed lines correspond to the tear film, the menisci, and the conjunctival sacs, respectively. The osmolarity difference between the upper and lower conjunctival sacs and menisci is negligible. Brackets indicate normal (q_e = 0.15 µL/min; q_{lac} = 1.10 µL/min) and dry-eye conditions (q_e = 0.30 µL/min; q_{lac} = 0.55 µL/min).

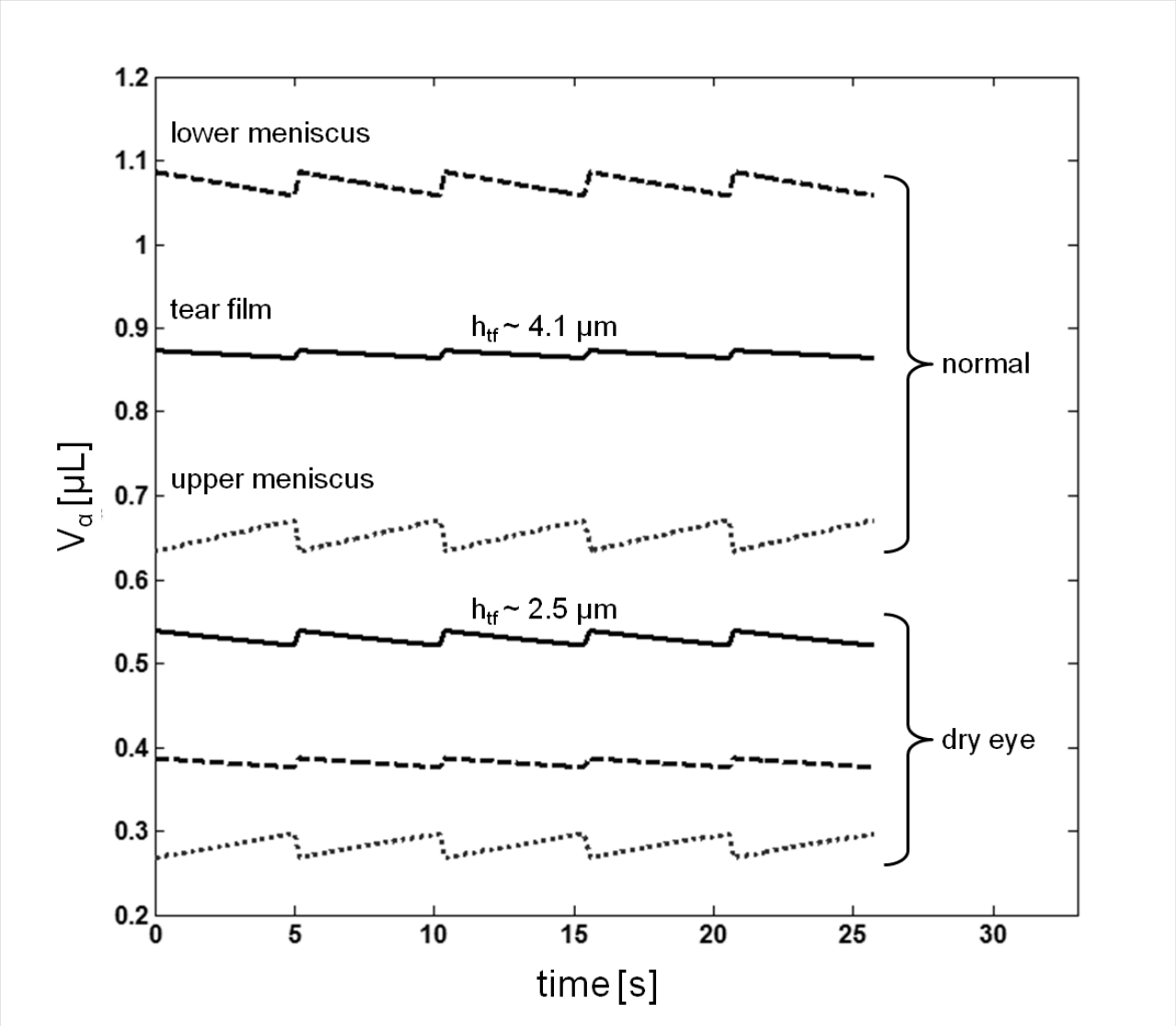

Figure 2.3: Periodic steady-state volumes of upper and lower meniscus and tear film over 5 blink cycles for normal and dry-eye conditions. Solid, dotted, and dashed lines correspond to the tear film, the upper meniscus, and the lower meniscus, respectively. The total volume of the conjunctival sacs is constant at 4.5 µL for all cases. Right brackets indicate normal (q_e = 0.15 µL/min; q_{lac} = 1.10 µL/min) and dry-eye conditions (q_e = 0.30 µL/min; q_{lac} = 0.30 µL/min). The average tear-film thickness is labeled as 4.1 and 2.5 µm for normal and dry-eye subjects, respectively.

Since the majority of the lacrimal tear supply arrives from the upper fornix, the upper meniscus grows by 6 % in volume during interblink whereas the lower meniscus drains more than it gains, shrinking by 3 % in volume. The tear film loses about 1 % of its volume and thickness to evaporation during interblink. The upper and lower conjunctival sacs receive fresh tear from the lacrimal glands and water through the conjunctiva, slightly diluting their osmolarities. The tear film, which is initially at 309 mOsM, experiences a 3-mOsM spike in osmolarity from evaporation. Menisci receive fresh tears from the conjunctival sacs, which outweighs the minor concentrating effect of evaporation.

Overall, the situation is similar for dry-eye conditions, as illustrated in Figures 2.2 and 2.3. Changes in lacrimal supply and evaporation rates, however, cause quantitative differences. As shown in Table 2.2, we use 0.55 and 0.30 μL/min for lacrimal-secretion and tear-evaporation rate in dry eye, respectively. A decreased lacrimal supply shrinks the dry-eye upper and lower menisci volumes to less than one-half (43 and 36 %) of their normal values, while the tear-film volume and thickness decreases to 62 % of their normal values. Increased tear-evaporation and decreased lacrimal-supply rates elevate c_b to 321 mOsM, 12 mOsM greater than that predicted under normal conditions. Increased evaporation causes the tear-film osmolarity to spike strongly during interblink to 11 mOsM above the bulk osmolarity. Most importantly, the epithelial cells of the cornea and exposed conjunctiva experience the spikes in osmolarity whereas the measured osmolarity of the menisci, c_b, remains lower and essentially constant.

2.4.2 Tear-evaporation and lacrimal secretion

By varying tear-evaporation and lacrimal-supply rates while holding all other parameters constant, we explore a wide range of possible tear-dynamics scenarios. Figures 2.4 and 2.5 show contour plots of bulk tear osmolarity, c_b, and of total transcorneal and transconjunctival water flow, q_c, as a function of evaporation rate q_e and lacrimal-supply rate q_{lac}. Contour lines for c_b in Figure 2.4 appear every 5 mOsM between 305 and 335 mOsM, and those for q_c in Figure 2.5 appear every 0.05 μL/min between 0.05 and 0.45 μL/min. For reference, open markers are placed on the graphs at the locations representing normal (○), dry-eye (□), ADDE (▽), and EDE (△) conditions. Reported osmolarities correspond to those in the lower meniscus not those actually experienced by the corneal epithelium.

As expected, tear osmolarity increases as evaporation rate increases and lacrimal supply decreases. Osmolarities predicted by our model for normal, dry-eye, ADDE, and EDE conditions are 309, 321, 317, and 323 mOsM, respectively. Data in Figure 2.5 demonstrate that increasing tear evaporation and decreasing lacrimal supply increases the osmotic water inflow q_c because higher salinity increases osmotic water withdrawal through the cornea and conjunctiva. Osmotic water flows predicted by our model for normal, dry-eye, ADDE, and EDE conditions are 0.12, 0.26, 0.23, and 0.29 μL/min, respectively.

Appendix 2E contains predictions for additional clinically relevant tear-dynamics as functions of tear-evaporation and lacrimal-supply rates. Figures 2E.1-2E.5 show predictions of tear-turnover rate (*TTR*), deposited tear-film thickness, maximum tear-film osmolarity, initial meniscus radius during deposition, and total tear volume, respectively, for the same range of q_e and q_{lac} as those in Figures 2.4 and 2.5. *TTR* are predicted at 14.7, 8.6, 6.5, and 11.7 %/min for normal, dry-eye, ADDE, and EDE conditions (Figure 2E.1). Correponding clinically measured values are 15.2, 7.8, 5.7, and 12.6 %/min for the same cases [12, 67]. Although there is only a 2 % difference in c_b between ADDE and EDE, the *TTR* in EDE is 80 % higher than that in ADDE.

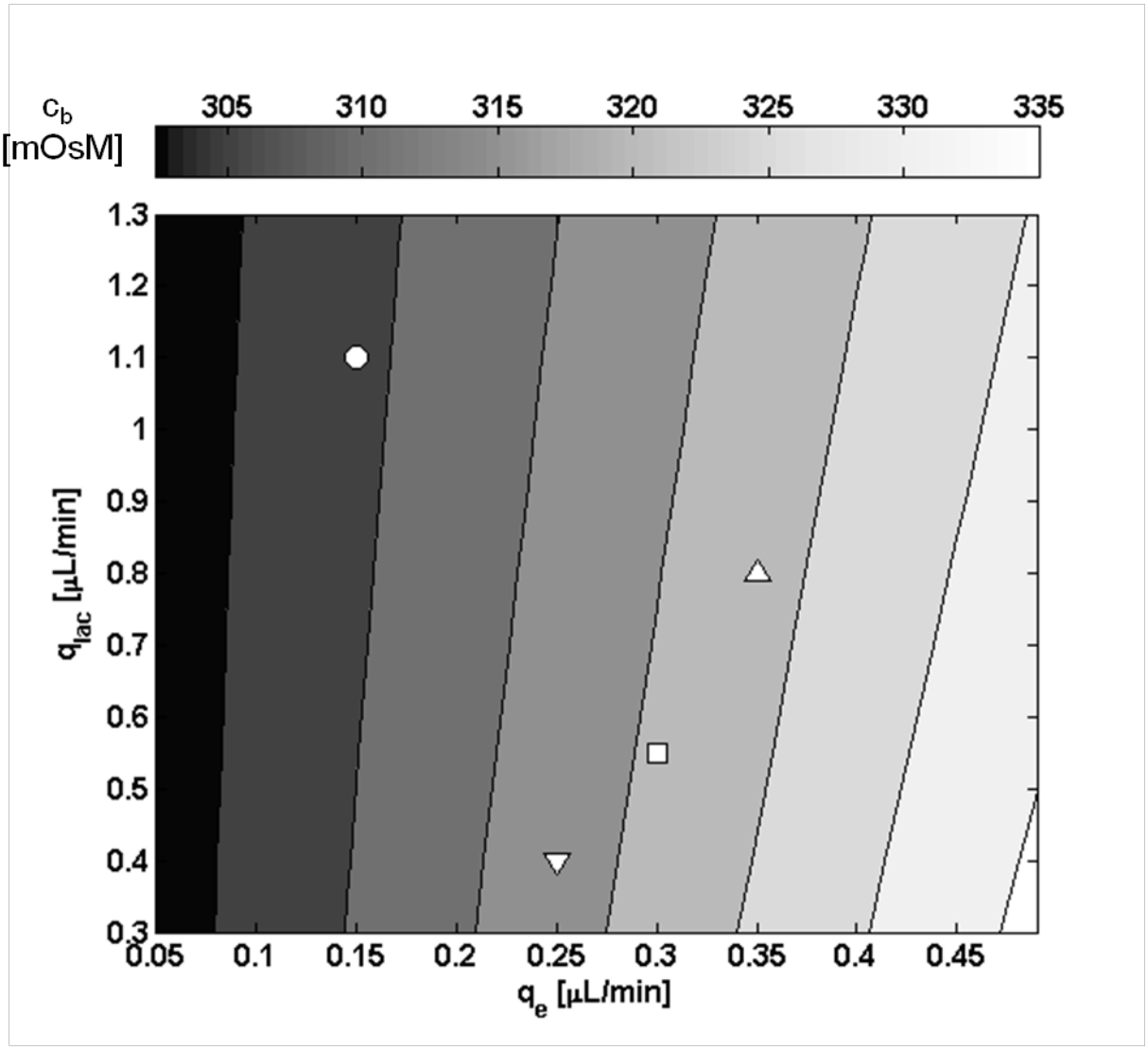

Figure 2.4: Contours of bulk tear osmolarity, c_b, as a function of tear-evaporation rate, q_e, and lacrimal-supply rate, q_{lac}. Contour lines for c_b appear every 5 mOsM between 305 and 335 mOsM. Open markers signify normal (○), dry -eye (□), ADDE (▽), and EDE (△) conditions as described in Table 2.2. Predicted osmolarities for normal, dry-eye, ADDE, and EDE conditions are 309, 321, 317, and 323 mOsM, respectively.

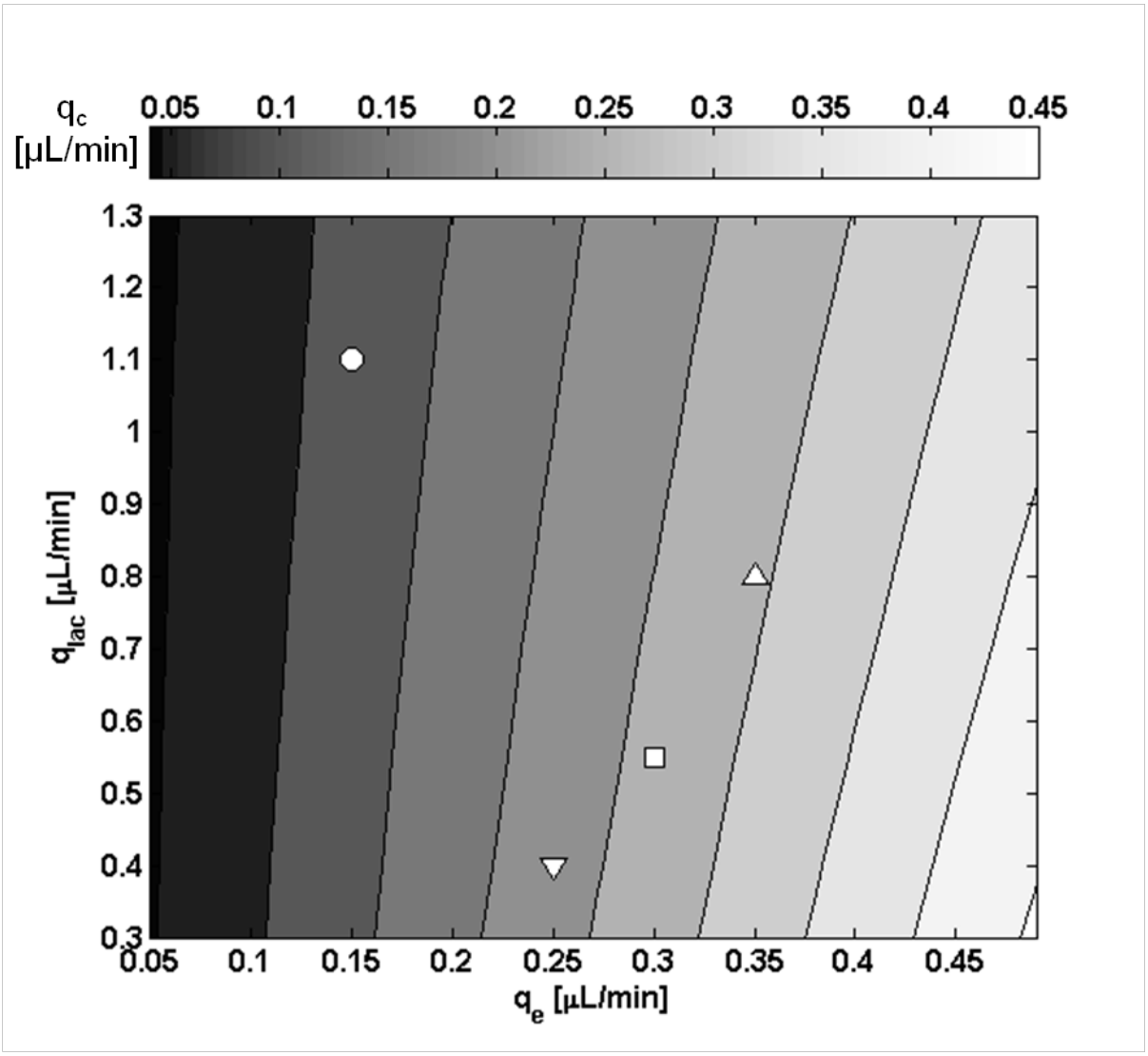

Figure 2.5: Contours of total transcorneal and transconjunctival water flow, q_c, as a function of tear-evaporation rate, q_e, and lacrimal-supply rate, q_{lac}. Contour lines for q_c appear every 0.05 µL/min between 0.05 and 0.45 µL/min. Open markers signify normal (○), dry -eye (□), ADDE (▽), and EDE (△) conditions as described in Table 2.2. Predicted total transmembrane water flows for normal, dry-eye, ADDE, and EDE conditions are 0.12, 0.26, 0.23, and 0.29 µL/min, respectively.

With the highest evaporation rates measured by King-Smith *et al.* [35] and Nichols *et al.* [36], of 0.40 and 0.76 μL/min, and normal lacrimal-supply rate, corneal and conjunctival water permeability values, the blink model predicts c_b of 335 mOsM and 370 mOsM, respectively. We investigate how much q_{lac} or P_{cj} and P_{cn} must increase to predict a normal c_b of 309 mOsM. For simplicity, we set $P_{cj} = P_{cn}$. For evaporation rates of 0.40 and 0.76 μL/min and a fixed $P_{cn} = P_{cj}$ of 1.25×10^{-5} m/s, q_{lac} must increase from 1.10 to 11 and 22 μL/min, respectively, or more than tenfold. Lacrimal-supply rates this far outside the normal range necessitate increasing the maximum drainage rate to enable sufficient drainage to prevent tear overflow. For q_{lac} fixed at 1.10 μL/min with the same evaporation rates, then P_{cn} and P_{cj} must increase to 11.5×10^{-5} and 6.3×10^{-5} m/s, respectively. To mimic dry eye under these conditions, we doubled q_e and halved q_{lac}. With fixed P_{cn} and P_{cj} and increased q_{lac}, predicted c_b increases to ~330 mOsM at both evaporation rates. With fixed q_{lac} and increased P_{cn} and P_{cj}, c_b increases from 309 to ~315 mOsM at both evaporation rates.

2.4.3 Conjunctival and corneal water permeability

The water permeability of the cornea and the conjunctiva to osmotic flow are varied independently from 5×10^{-7} to 4×10^{-5} m/s while fixing the evaporation and lacrimal supply rates constant. Changes in water permeability affect the dynamics of all tear compartments, but the most important metric is tear osmolarity. Figure 2.6 shows the contours of bulk tear concentration, c_b, in osmolarity units over the range of P_{cn} and P_{cj} for normal lacrimal-supply and tear-evaporation rates. Contour lines in Figure 2.6 appear every 3 mOsM between 306 and 330 mOsM. Osmolarity decreases as both permeabilities increase. Due to the conjunctiva's large surface area, the conjunctival permeability plays a stronger role in determining meniscus osmolarity than does the corneal permeability. As both P_{cn} and P_{cj} approach zero, tear osmolarity under normal lacrimal-supply and evaporation conditions increases rapidly towards that observed in dry eye. In the limit of zero transcorneal or transconjunctival osmotic flow, c_b equals 344 mOsM.

2.5 Discussion

The proposed periodic-steady tear-dynamics model includes realistic description of drainage, tear-film deposition, and under-lid flow to capture actual tear-system physics. Periodic-steady state is reasonable because blinking occurs frequently compared to the changes in environmental conditions that set tear-evaporation and lacrimal-supply rates. Notable exceptions follow application of topical eye-care solutions, in which case time is required for the tear volume and osmolarity to reset to their normal, periodic-steady values.

The tear-dynamics model demonstrates the importance of osmotic-driven water flow through the cornea and conjunctiva. Under normal conditions, we predict a meniscus osmolarity of 309 mOsM, slightly higher than the average of all reported tear osmolarities, 302 mOsM [11, 12, 71], but close to the 308 mOsM value reported by Khanal *et al.* [12, 67]. Because water flow through the ocular surface counteracts the concentrating effect of evaporation, our tear dynamics matches the observed osmolarity without being limited to low evaporation rates and high lacrimal supply rates [31]. Without inclusion of osmotically driven water flow, tear osmolarity under normal conditions reaches 344 mOsM, well above that measured in healthy individuals [6, 8, 9, 11, 12, 67, 71]. In our model, osmotic-driven water flow accounts for 10 % of the total water supply under normal conditions. This amount is less than the 25 % predicted by Zhu and Chauhan [26], who use an evaporation rate that is over 5 times higher than the average reported

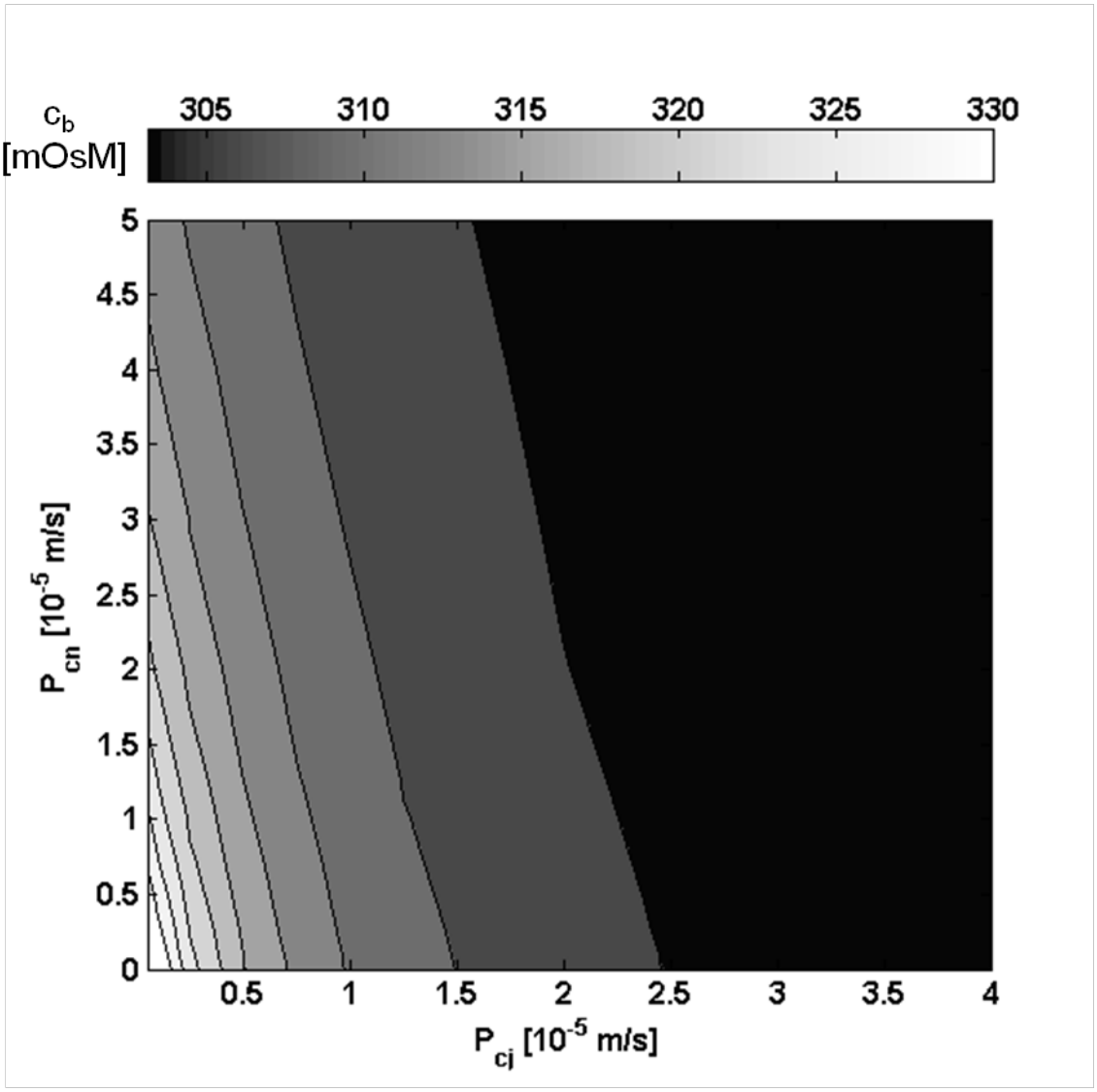

Figure 2.6: Contours of bulk tear concentration, c_b, reported as osmolarity, as a function of conjunctival, P_{cj}, and corneal permeability, P_{cn} for normal conditions (q_{lac} = 1.10 µL/min; q_e = 0.15 µL/min). Contour lines appear every 3 mOsM between 306 and 330 mOsM. Normal permeability in this model is $P_{cj} = P_{cn} = 1.25 \times 10^{-5}$ m/s corresponding to c_b = 309 mOsM. At $P_{cj} = P_{cn} = 0$, c_b = 344 mOsM.

tear-evaporation rate and an extremely high secreted-tear osmolarity (necessitating greater water secretion to prevent hyperosmolarity). In dry eye, increased tear osmolarity drives the osmotic water flow up to 0.26 µL/min, or almost 50 % of the lacrimal-supply rate, making it a significant contributor to tear flow. Thus, analysis of fluorescent-dyed tear-flow experiments must account for this diluting effect. The magnitudes of predicted osmotic water flow into the upper conjunctival sac, lower conjunctival sac, and tear film are approximately equal under healthy conditions. In dry eye, however, evaporation-driven hyperosmolarity in the tear film intensifies, causing the relative contribution of osmotically driven flow into the tear film to increase.

By varying the lacrimal-supply and tear-evaporation rates, in Figures 2.4 and 2.5 and Figures 2E.1-2E.5, we investigate the effect of dry-eye conditions on tear dynamics. Increasing evaporation and decreasing lacrimal supply generally decreases *TTR*, total tear volume, meniscus radii, and tear-film thickness while increasing osmolarity and trans-corneal/conjunctival water flow. Figure 2E.1 indicates that *TTR* is an exception when q_{lac} is above 1.2-1.3 µL/min. These trends are in agreement with clinical data [11, 67, 72, 73] and with previous modeling efforts [26, 31]. Although, in general, tear osmolarity increases for dry eye, EDE exhibits the highest osmolarity and ADDE the lowest. The difference, though, is only 5 mOsM, or less than 2 %, which makes it a poor clinical discriminator between the two dry-eye subcases. Higher osmolarity with EDE suggests that it causes the most hyperosmotic damage and is a more severe form of dry eye. Total tear volume, meniscus radii, and tear-film thickness all increase with increasing lacrimal supply rate. There are modest differences in these variables between ADDE and EDE, but *TTR* is the single best differentiator. The *TTR* in EDE is 12 %/min, which is double the value for ADDE, 6 %/min. This result compares closely with those of Khanal *et al.* [12, 67], who report *TTR*s of 13 and 6 %/min for ADDE and EDE, respectively. We corroborate the conclusion of Khanal *et al.* [67] that tear osmolarity is a useful clinical indicator of dry eye in general, and that *TTR* can be used to discriminate between the ADDE and EDE subtypes.

We predict tear osmolarities of 335 and 370 mOsM for the higher evaporation rates reported by King-Smith *et al.* [35] and Nichols *et al.* [36], respectively, with otherwise normal physical parameters. These osmolarities are clearly too high to be observed in a healthy subject. To predict normal osmolarities at these evaporation rates, q_{lac} or P_{cn} and P_{cj} must increase significantly. All else held constant, q_{lac} must be 10-20 times the average reported value of 1.10 µL/min. Even the highest clinical measurements are not close to this value [27, 74]. Alternatively, water flow through the cornea and conjunctiva could provide the extra water to offset hyperosmolarity induced by the increased evaporation. For evaporation rates of 0.40 and 0.76 µL/min, increasing P_{cn} and P_{cj} to 6.25 or 11.5×10^{-5} m/s, respectively, enables enough water flow through the ocular surface to permit a normal tear osmolarity. Although these values are about 5-10 times higher than the values adopted for a healthy eye, lack of human data makes it difficult to tell if these values are unrealistic. Such high tissue-water permeabilities, however, result in inconsistencies between the model and observations. When already high evaporation rates are doubled and the tear supply is halved to simulate dry-eye conditions, the bulk-average tear osmolarity rises to about 315 mOsM, which is only 6 mOsM higher than the healthy case. Thus, with high water permeabilities, increased evaporation and decreased lacrimal supply do not lead to significant hyperosmolarity as observed clinically.

These results suggest that the average tear-evaporation rate over the entire exposed tear surface must be lower than the localized measurements of 1.9-3.79 µm/min by King-Smith *et al.* [35] and Nichols *et al.* [36]. As King-Smith *et al.* report [35], the tear-evaporation rate varies across the eye, probably due to local differences in lipid-layer thickness and airflow. We expect

that the lipid layer is thickest near its origin at the meibomian glands and the airflow is also the lowest in these regions compared to those in the middle of the palpebral aperture. Thus, the evaporation rate should be highest in the middle, where both Nichols *et al.* [36] and King-Smith *et al.* [35] measure thinning rates. In contrast, goggle experiments, which measure the total water loss from the ocular surface, establish an average evaporation rate over the entire exposed tear film. More experiments are necessary to reconcile the goggle and open-environment evaporation measurements.

Results in Figure 2.6 not only show the significant effect of corneal/conjunctival water permeability, but also give upper and lower limits to these values. Although larger permeabilities yield lower tear osmolarities, permeabilities that are too high effectively render the ocular surface so water permeable that hyperosmolarity cannot occur even under dry-eye conditions. At the other extreme, lower permeabilities produce very high osmolarities for dry-eye and normal conditions alike. Given that most osmotically driven water transport is transcellular and that the corneal epithelium contains more tight junctions than the conjunctival epithelium, it seems reasonable to assume that the conjunctival water permeability should not be less than that of the cornea. Experimental data both support [35] and contest [22] this statement. Only a small range of tissue water permeabilities for our given set of evaporation and lacrimal supply rates generates osmolarities in agreement with clinically measured values. This range of permeabilities lies near 10^{-5} m/s, very close to all experimentally measured values and model predictions, and lends confidence to our tear-dynamics model. From the water-permeability results from Leung *et al.* [52], we find that the cornea plays a significant role in supplying water to the tear film. Previous models have neglected this important contribution [26].

There are several limitations to the proposed tear-dynamics model, due mainly to lack of quantitative parameters. An issue of particular concern is the choice of a "normal" evaporation rate. We chose average values from a meta-analysis by Tomlinson *et al.* [49] that covers 437 patients from 15 studies from about 10 different authors. Despite these extensive data, two main issues arise with tear-evaporation measurements. First, measured evaporation rates range over two orders of magnitude, from 0.02 to 6.3×10^{-6} g/cm^2/s. Evaporation rates from different ends of this spectrum yield extremely different tear osmolarities. More importantly, evaporation rate depends on airflow, environmental humidity, and temperature. There is no one tear-evaporation rate. Therefore, averaging over a large subject size is irrelevant if the airflow and ambient conditions are not controlled and representative.

Another limiting factor is the absence of experiments in which a sufficient number of tear variables is measured. Most experiments do not measure simultaneously *TTR*, tear volume, evaporation rate, and osmolarity. Unless all of these measurements are taken, lacrimal tear supply and osmotically driven water flow cannot be disentangled. More experiments similar to those of Khanal *et al.* [12, 67] are needed. To address this issue, we used average values from the larger body of literature, but applied the ratios of tear flow in ADDE or EDE conditions from those reported by Khanal *et al*. [12], [67]. Our model can be refined as more detailed tear-flow data become available.

Despite the limitations, our proposed periodic-steady-state tear-dynamics model captures the basic physics of water and salt dynamics in the eye self-consistently and agrees well with available clinical data. One important application is topical delivery of drugs or care solutions to the ocular surface. The normal tear turnover rate is so high that instilled fluids and solutes are rapidly removed from the eye, minimizing drug availability. Maximizing the residence time of these substances on the eye is an important question in topical delivery of drugs and eye-care

solutions. Although we focus on salt osmolarity here, the presented solute balances are general and readily extended to drugs, fluorescent tracers, or other solutes of interest. Studying the dynamics of instilled drugs can guide treatment regimens to maximize bioavailability of topically delivered drug molecules. Additionally, introduction of the viscosity dependence of the tear-drainage rate can predict the role of viscosity enhancers in lengthening residence time of either fluid or solute on the eye.

2.6 List of Symbols

Variable	SI, Common	Description
A_{cn}, A_{cj}, A_{pa}	m^2, cm^2	Exposed surface area of the cornea, conjunctiva, palpebral aperture
c	mol/m^3, mOsM	Salt concentration in...
c_α	″	...compartment α
c_j, c_k	″	...stream j or k entering or leaving compartment α
c_{lac}	″	...tear secreted from lacrimal gland
c_{im}	″	...meniscus $i = u$ or l for upper or lower
c_{si}	″	...meniscus $i = u$ or l for upper or lower
c_{tf}, $c_{tf,max}$	″	...the tear film, maximum salt concentration in tear film
$c(x,t)$	″	...conjunctival sac as a function of x and t
$c_{\alpha F}$	″	...compartment α at end of interblink
c_b	″	Bulk salt concentration after mixing
$c_{b,it}$	″	c_b of a given iteration during *Regula-Falsi* numerical solution
C_D, $C_D(0)$	mol/m^3	Concentration of dye in tear, initial C_D upon instillation
CS, CS_0, CS_{tf}		Control surface of upper meniscus during deposition. *0* and *tf* denote control surfaces over which tear fluid enters and exits
CV		Control volume of upper meniscus during deposition
h_0	m, μm	Distance between upper lid and ocular surface during
h_c	m, μm	Thickness of tear fluid in the conjunctival sacs
h_{tf}, $h_{tf,D}$	m, μm	Tear-film thickness, *D* denotes the deposited thickness
h_{pa}	m, μm	Palpebral-aperture height
I		Subscript index denoting upper (u) or lower (l)
J		Subscript index denoting j-th stream entering compartment α
J_e	m/s, μm/min	Volumetric evaporative water flux
J_w, $J_{w,n}$	m/s, μm/min	Volumetric osmotic water flux through cornea or conjunctiva ($n = cn$ or cj)
J, K		Total number of entering (J) or exiting streams (K) in compartment α
k		Subscript index denoting k-th stream exiting compartment α
L_{ic}	m, μm	Average depth of fornix i
$\underline{n}$		Outward-pointing unit normal for control surface CS
P_{cn}, P_{cj}	m/s	Corneal (cn) and conjunctival (cj) osmotic water permeability
q	m^3/s, μL/min	Volumetric water flow rate...
q_0	″	...into the upper meniscus from the conjunctival sac during deposition

q_c	″	...due to osmosis through the entire cornea and conjunctiva
q_{cn}	″	...due to osmotic flow through the cornea
q_d, q_{di}	″	...from drainage through both puncta, or from punctum *i*
q_e, q_{ei}	″	...from evaporation from all surfaces, or from meniscus *i*
q_j, q_k	″	...in stream *J* (*j*) or *K* (*k*) entering or exiting compartment α
q_{lac}	″	...from the lacrimal supply into the conjunctival sacs
q_m	″	...maximum drainage volumetric flow rate from each meniscus
q_{si}	″	...from conjunctival sac *i* into meniscus *i* during interblink
R	m, cm	Eye-globe radius
R_0	m, μm	Minimum meniscus radius for drainage
R_b	m, μm	Upper- and lower-meniscus radii at beginning of deposition
R_{im}	m, μm	Radius of meniscus *i*
S_{lid}	m, cm	Lid-margin perimeter for a single lid
t	s	Time
t_c	s	Duration of the closure phase
t_d	s	Duration of the deposition phase
t_{ib}	s	Duration of the interblink phase
t_{ci}	s	Characteristic time for clearance of conjunctival sac *i*
TTR	%/s, %/min	Tear-turnover rate
$\underline{u}$	m/s	Fluid velocity entering control surface *CS*
u_{lac}	m/s	Average fluid velocity entering conjunctival sac at $x = 0$
U	m/s, cm/s	Linear velocity of rising upper lid during deposition
v_w	m^3/mol,	Specific volume of water
V_α, $V_{\alpha F}$	m^3, μL	Volume of compartment α, at the end of interblink
V_{im}	″	Volume of meniscus *i*
V_t	″	Total tear volume as measured by fluorescent dilution
V_T, V_{TD}, V_{TF}	″	Total model tear volume, at beginning of deposition (*D*) or end of interblink (*F*)
V_{tf}	″	Tear-film volume
x	m, μm	Distance along conjunctival sac beginning from the apex of
α		Subscript index denoting compartment
β_i		Mixing parameter for conjunctival sac *i*
γ		Characteristic ratio from Equations B.9-10
θ_1, θ_2	rad	Beginning (θ_1) and end (θ_2) positions of palpebral aperture
θ_A	rad	Angular medial-lateral width of palpebral aperture
κ	s^{-1}, min^{-1}	Tear-turnover rate in min^{-1}
λ_i		Fraction of total lacrimal secretion directed to conjunctival sac
μ	Pa·s, cP	Tear viscosity
ρ	kg/m^3, g/cm^3	Tear density
σ	N/m, mN/m	Tear surface tension
φ_A	rad	Angular superior-inferior height of palpebral aperture
ω	rad/s	Lid-opening angular velocity during deposition

2.7 Acknowledgements

We thank A. Tomlinson and M.C. Lin for valuable clinical insights during the formulation of this model, A. Chauhan for helpful discussion, and J. Newman for proposing the two-parameter *Regula Falsi* solution method. CFC acknowledges Alcon Corporation for partial funding.

2.8 References

[1] (No authors listed). The epidemiology of dry eye disease: report of the Epidemiology Subcommittee of the International Dry Eye WorkShop (2007). *Ocul Surf*. 2007;5:93-107.

[2] (No authors listed). The definition and classification of dry eye disease: report of the Definition and Classification Subcommittee of the International Dry Eye Workshop (2007). *Ocul Surf*. 2007;5:75-92.

[3] Von Bahr G. Konte der Flussigkeitsabgang durch die Cornea von physiologischer Bedeutung Sein? *Acta Ophthalmol*. 1941;19:125-34.

[4] Balik J. The Lacrimal Fluid in Keratoconjunctivitis Sicca:A Quantitative and Qualitative Investigation. *Am J Ophthalmol*. 1952;35:773-82.

[5] Mastman GJ, Baldes EJ, Henderson JW. The Total Osmotic Pressure of Tears in Normal and Various Pathologic Conditions. *Arch Ophthalmol*. 1961;65:509-13.

[6] Gilbard JP, Farris RL, Santamaria J. Osmolarity of Tear Microvolumes in Keratoconjunctivitis Sicca. *Arch Ophthalmol*. 1978;96:677-81.

[7] Gilbard JP, Farris RL. Tear Osmolarity and Ocular Surface Disease in Keratoconjunctivitis Sicca. *Arch Ophthalmol*. 1979;97:1642-6.

[8] Suzuki M, Massingale ML, Ye F, Godbold J, Elfassy T, Vallabhajosyula M, et al. Tear Osmolarity as a Biomarker for Dry Eye Disease Severity. *Invest Ophthalmol Vis Sci*. 2010;51:4557-61.

[9] Sullivan BD, Whitmer D, Nichols KK, Tomlinson A, Foulks GN, Geerling G, et al. An Objective Approach to Dry Eye Severity. *Invest Ophthalmol Vis Sci*. 2010;51:6125-30.

[10] Farris RL. Tear Osmolarity - A New Gold Standard? *Adv Exp Med Biol*. 1994;350:495-503.

[11] Tomlinson A, Khanal S, Ramaesh K, Diaper CJM, McFayden A. Tear Film Osmolarity: Determination of a Referent for Dry Eye Diagnosis. *Invest Ophthalmol Vis Sci*. 2006;47:4309-15.

[12] Khanal S, Tomlinson A, McFayden A, Diaper CJM, Ramaesh K. Dry Eye Diagnosis. *Invest Ophthalmol Vis Sci*. 2008;49:1407-14.

[13] Korb DR, Craig JP, Doughty M, Guillon J-P, Smith G, Tomlinson A. *The Tear Film: structure, function, and clinical examination*. Oxford: Butterworth-Heinemann; 2002.

[14] Bron AJ, Tiffany JM. The Contribution of Meibomian Disease to Dry Eye. *Ocul Surf*. 2004;2:149-64.

[15] Bron AJ, Tiffany JM, Gouveia SM, Yokoi N, Voon LW. Functional aspects of the tear film lipid layer. *Exp Eye Res*. 2004;78:347-60.

[16] Foulks GN, Bron AJ. Meibomian Gland Dysfunction: A Clinical Scheme for Description, Diagnosis, Classification, and Grading. *Ocul Surf*. 2003;1:107-26.

[17] Chen W, Zhang X, Zhang J, Chen J, Wang S, Wang Q, et al. A Murine Model of Dry Eye Induced by an Intelligently Controlled Environmental System. *Invest Ophthalmol Vis Sci*. 2008;49:1386-91.

[18] McCulley JP, Aronowicz JD, Uchiyama E, Shine WE, Butovich IA. Correlations in a Change in Aqueous Tear Evaporation With a Change in Relative Humidity and the Impact. *Am J Ophthalmol*. 2006;141:758-60.

[19] Niederkorn JY, Stern ME, Pflugfelder SC, De Paiva CS, Corrales RM, Gao J, et al. Desiccating Stress Induces T Cell-Mediated Sjögren's Syndrome-Like Lacrimal Keratoconjunctivitis. *The Journal of Immunology*. 2006;176:3950-7.

[20] Bron AJ, Yokoi Y, Gaffney EA, Tiffany JM. Predicted Phenotypes of Dry Eye: Proposed Consequences of Its Natural History. *Ocul Surf*. 2009;7:78-92.

[21] Baudouin C. The Pathology of Dry Eye. *Surv Ophthalmol*. 2001;45:S211-S20.

[22] Levin MH, Verkman AS. Aquaporin-Dependent Water Permeation at the Mouse Ocular Surface: In Vivo Microfluorimetric Measurements in Cornea and Conjunctiva. *Invest Ophthalmol Vis Sci*. 2004;45:4423-32.

[23] Zhu H, Chauhan A. A Mathematical Model for Tear Drainage through the Canaliculi. *Curr Eye Res*. 2005;30:621-30.

[24] Zhu H, Chauhan A. A Mathematical Model of Tear Mixing Under the Lower Lid. *Curr Eye Res*. 2007;32:1023-35.

[25] Zhu H, Chauhan A. A Mathematical Model for Ocular Tear and Solute Balance. *Curr Eye Res*. 2005;30:841-54.

[26] Zhu H, Chauhan A. Tear Dynamics Model. *Curr Eye Res*. 2007;32:177-97.

[27] Mishima S, Gasset A, Klyce SD, Baum JL. Determination of Tear Volume and Tear Flow. *Invest Ophthalmol*. 1966;5:264-76.

[28] Port MJA, Asaria TS. The Assessment of Human Tear Volume. *Cont Lens Anterior Eye*. 1990;13:76-82.

[29] Fraunfelder FT. Extraocular Fluid Dynamics: How Best to Apply Topical Ocular Medication. *Trans Am Ophthalmol Soc*. 1976;74:457-87.

[30] Macdonald EA, Maurice DM. The Kinetics of Tear Fluid Under the Lower Lid. *Exp Eye Res*. 1991;53:421-5.

[31] Gaffney EA, Tiffany JM, Yokoi N, Bron AJ. A Mass and Solute Balance Model for Tear Volume and Osmolarity in the Normal and Dry Eye. *Prog Retin Eye Res*. 2010;29:59-78.

[32] McDonald JE, Brubaker S. Meniscus-induced thinning of tear films. *Am J Ophthalmol*. 1971;72:139.

[33] Miller KL, Polse KA, Radke CJ. Black-line formation and the "perched" human tear film. *Curr Eye Res*. 2002;25:155-62.

[34] Bron AJ, Tiffany JM, Yokoi N, Gouveia SM. Using osmolarity to diagnose dry eye: A compartmental hypothesis and review of our assumptions. In: Sullivan DA, Stern ME, Tsubota K, Dartt DA, Sullivan RM, Bromberg BB, (editors). *Lacrimal Gland, Tear Film, and Dry Eye Syndromes 3: Basic Science and Clinical Relevance*, 2002;506:1087-95.

[35] King-Smith PE, Ramamoorthy P, Nichols KK, Braun RJ, Nichols JJ. If tear evaporation is so high, why is osmolarity so low? *The 6th International Conference on the Tear Film & Ocular Surface*. Florence, ITA2010.

[36] Nichols JJ, Mitchell GJ, King-Smith PE. Thinning Rate of the Precorneal and Prelens Tear Films. *Invest Ophthalmol Vis Sci*. 2005;46:2353-61.

[37] Fatt I, Weissman BA. *Physiology of the Eye: An Introduction to the Vegetative Functions*. 2nd ed. Stoneham, MA: Butterworth-Heinemann; 1992.

[38] Forrester JV, Dick AD, McMenamin PG, Lee WR. *The Eye: Basic Scienes in Practice*. 2nd ed. Philadelphia: Saunders (Elsevier); 2002.

[39] Goto E, Dogru M, Kojima T, Tsubota K. Computer-synthesis of an interference color chart of human tear lipid layer, by a colorimetric approach. *Invest Ophthalmol Vis Sci*. 2003;44:4693-7.

[40] Rolando M, Refojo MF. Tear evaporimeter for measuring water evaporation rate from the tear film under controlled conditions in humans. *Exp Eye Res*. 1983;36:25-33.

[41] Goto E, Endo K, Suzuki A, Fujikura Y, Matsumoto Y, Tsubota K. Tear evaporation dynamics in normal subjects and subjects with obstructive meibomian gland dysfunction. *Invest Ophthalmol Vis Sci*. 2003;44:533-9.

[42] Kawakita T, Kawashima M, Murat D, Tsubota K, Shimazaki J. Measurement of fornix depth and area: a novel method of determining the severity of fornix shortening. *Eye*. 2009;23:1115-9.

[43] Doane MG. Interactions of eyelids and tears in corneal wetting and the dynamics of the normal human eyeblink. *Am J Ophthalmol*. 1980;89:507-16.

[44] Murube J. Tear Osmolarity. *Ocul Surf*. 2006;4:62-73.

[45] Ehlers N. The precorneal film: Biomicroscopical, histological and chemical investigations. *Acta Ophthalmol*. 1965:1-136.

[46] Tiffany JM, Winter N, Bliss G. Tear Film Stability and Tear Surface Tension. *Curr Eye Res*. 1989;8:507-15.

[47] Maurice DM. The Dynamics and Drainage of Tears. *Int Ophthalmol Clin*. 1973;13:103-16.

[48] Hodges R, Dartt DA. Keratoconjunctivitis sicca: physiology and biochemistry of the tear film. In: Foster C, Azar D, Dohlman CH, (editors). *Smolin and Thoft's The Cornea: Scientific Foundations and Clinical Practice*. 4 ed. Philadelphia, PA: Lippincott Williams & Wilkins; 2005. p. 591.

[49] Tomlinson A, Doane MG, McFayden A. Inputs and Outputs of the Lacrimal System: Review of Production and Evaporative Loss. *Ocul Surf*. 2009;7:186-98.

[50] Wong H, Fatt I, Radke CJ. Deposition and Thinning of the Human Tear Film. *J Colloid Interface Sci*. 1996;184:44-51.

[51] Candia OA. Electrolyte and fluid transport across corneal, conjunctival and lens epithelia. *Exp Eye Res*. 2004;78:527-35.

[52] Leung BK, Bonanno JA, Radke CJ. A Model for Corneal Metabolism. *Prog Retin Eye Res*. 2011;30:471-92.

[53] Cerretani C, Peng C-C, Chauhan A, Radke CJ. Aqueous salt transport through soft contact lenses: An osmotic-withdrawal mechanism for prevention of adherence. *Contact Lens & Anterior Eye*. 2012;35:260-5.

[54] Tomlinson A, Khanal S. Assessment of Tear Film Dynamics: Quantification Approach. *Ocul Surf*. 2005;3:81-95.

[55] Van Best JA, Benitez del Castillo JM, Coulangeon L-M. Measurement of Basal Tear Turnover Using a Standardized Protocol. *Graefes Arch Clin Exp Ophthalmol*. 1995;233:1-7.

[56] King-Smith PE, Fink B, Hill R, Koelling K, Tiffany JM. The Thickness of the Tear Film. *Curr Eye Res*. 2004;29:357-68.

[57] Jones MB, Please CP, McElwain DLS, Fulford GR, Roberts AP, Collins MJ. Dynamics of Tear-Film Deposition and Draining. *Math Med Biol*. 2005;22:265-88.

[58] Braun RJ, King-Smith PE. Model Problems for the Tear Film in a Blink Cycle: Single-Equation Models. *J Fluid Mech*. 2007;586:465-90.

[59] Jones MB, Fulford GR, Please CP, McElwain DLS, Collins MJ. Elastohydrodynamics of the eyelid wiper. *Bull Math Biol*. 2008;70:323-43.

[60] Doane MG. Blinking and the Mechanics of the Lacrimal Drainage System. *Ophthalmol*. 1981;88:844-50.

[61] Fatt I. Observations of tear-film break up on model eyes. *Contact Lens Association of Ophthalmologists Journal*. 1991;17:267-81.

[62] Sharma A, Tiwari S, Khanna R, Tiffany JM. Hydrodynamics of meniscus-induced thinning of the tear film. *Adv Exp Med Biol*. 1998;438:425-31.

[63] Braun RJ, Begley C, Winkeler A, Nam J, Siddique J. Mathematical Modeling of Tear Break-up Based on Experimental Imaging. *Invest Ophthalmol Vis Sci*. 2011;53:554.

[64] Liu HX, Begley C, Chen MH, Bradley A, Bonanno J, McNamara NA, et al. A Link between Tear Instability and Hyperosmolarity in Dry Eye. *Invest Ophthalmol Vis Sci*. 2009;50:3671-9.

[65] Peng C-C, Cerretani C, Braun RJ, Radke CJ. Evaporation-Driven Instability of the Precorneal Tear Film. *Adv Colloid Interface Sci*.

[66] Carnahan B, Luther H, Wilkes J. *Applied Numerical Methods*. New York: John Wiley & Sons; 1969.

[67] Khanal S, Tomlinson A, Diaper CJM. Tear Physiology of Aqueous Deficiency and Evaporative Dry Eye. *Optom Vis Sci*. 2009;86:1235-40.

[68] Mathers WD, Binarao G, Petroll M. Ocular Water Evaporation and the Dry Eye - A New Measuring Device. *Cornea*. 1993;12:335-40.

[69] Trees GR, Tomlinson A. Effect of Artificial Tear Solutions and Saline on Tear Film Evaporation. *Optom Vis Sci*. 1990;67:886-90.

[70] Tsubota K, Yamada M. Tear Evaporation from the Ocular Surface. *Invest Ophthalmol Vis Sci*. 1992;33:2942-50.

[71] Lemp MA, Crews LA, Bron AJ, Foulks GN, Sullivan BD. Distribution of Aqueous-Deficient and Evaporative Dry Eye in a Clinic-Based Patient Cohort: A Retrospective Study. *Cornea*. 2012;31:472-8.

[72] Mainstone JC, Bruce AS, Golding TR. Tear meniscus measurement in the diagnosis of dry eye. *Curr Eye Res*. 1996;15:653-61.

[73] Creech JL, Do LT, Fatt I, Radke CJ. In vivo tear-film thickness determination and implications for tear-film stability. *Curr Eye Res*. 1998;17:1058-66.

[74] Eter N, Gobbels M. A new technique for tear film fluorophotometry. *Br J Ophthalmol*. 2002;86:616-9.

[75] Ehlers N. On the size of the conjunctival sac. *Acta Ophthalmol*. 1965;43:205-10.

[76] Watsky MA, Jablonski MM, Edelhauser HF. Comparison of conjunctival and corneal surface areas in rabbit and human. *Curr Eye Res*. 1988;7:483-6.

[77] Rhee H-K, Aris R, Amundson N. *First-Order Partial Differential Equations, Volume 1 Theory and Application of Single Equations*. Englewood Cliffs, NJ: Prentice-Hall; 1986.

[78] Fell CJD, Hutchison H. Diffusion Coefficients for Sodium and Potassium Chlorides in Water at Elevated Temperatures. *J Chem Eng Data*. 1971;16:427-9.

[79] Cerretani C, Ho N, Radke CJ. Water-Evaporation Reduction by Duplex Films: Application to the Human Tear Film. *Adv Colloid Interface Sci*. 2013.

[80] Van Best JA, Oosterhuis JA. Computer Fluorophotometry. *Doc Ophthalmol*. 1983;56:89-97.

[81] Shen MX, Li JH, Wang JH, Ma HX, Cai CY, Tao AZ, et al. Upper and Lower Tear Menisci in the Diagnosis of Dry Eye. *Invest Ophthalmol Vis Sci*. 2009;50:2722-6.

[82] Wang JH, Aquavella J, Palakuru J, Chung S, Feng CY. Relationships between central tear film thickness and tear menisci of the upper and lower eyelids. *Invest Ophthalmol Vis Sci*. 2006;47:4349-55.

Appendix 2A: Geometries

Since the human eye is an oblate spheroid, we adopt spherical coordinates to describe its geometry, as diagrammed in Figure 2A.1. With an average human-eye radius of 1.2 cm, we calculate the aperture geometries that serve as the boundaries of the exposed ocular surface. We assume typical values for eyeball radius R (1.2 cm) [37, 38], lid length S_{lid} (3.0 cm) [27], and palpebral-aperture height h_{pa} (0.9 cm) [40, 41], and then calculate the remaining dimensions.

For a circular arc, as in the side view in Figure 2A.1, $\varphi_a = 2 \sin^{-1}(h_{pa}/2R)$, which gives $\varphi_A = 0.769$ (44 °). Given S_{lid} and R, the aperture angle $\theta_A = S_{lid}/R$, giving $\theta_A = 2.50$ (143 °) and $\theta_1 =$

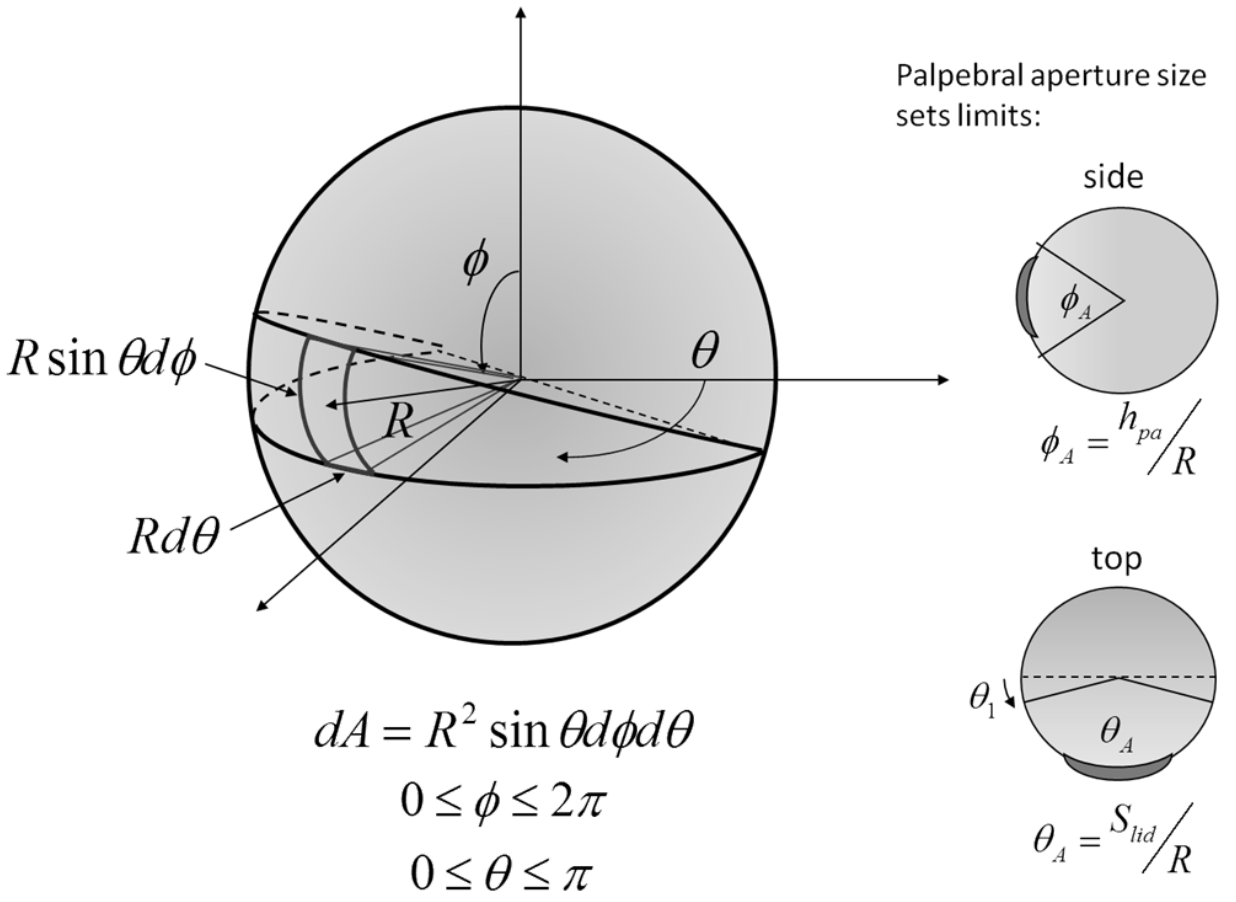

Figure 2.A1: Spherical coordinates adopted for the human eye. θ and φ are coordinates on a spherical surface of radius R as shown. Side and top views show the palpebral-aperture limits.

0.321 (18 °). With these values, the palpebral aperture area, A_{pa}, is established via integration in spherical coordinates

$$A_{pa} = R^2 \int_0^{\varphi_A} d\varphi \int_{\theta 1}^{\theta 2} \sin\theta d\theta = 2R^2 \varphi_A \cos\theta_A \tag{A.1}$$

where $\theta_2 = \theta_A + \theta_1$, as shown in Figure 2A.1. Substitution of the numerical values yields A_{pa} = 2.10 cm^2, which is very close to clinically observed values [27, 40, 41].

Similarly, we calculate the surface area of the bulbar conjunctiva in the upper and lower fornices. By assuming that the fornices extend to the poles of the eye, the total surface area of the palpebral aperture plus the conjunctival sacs is $2\pi R^2 \cos\theta_1$, or 8.59 cm^2. The ratio of lengths of the superior to inferior fornices is 1.4:1 [42]. Consequently, of the remaining globe area, 3.77 cm^2 is attributed to the superior conjunctival sac and 2.71 cm^2 is attributed to the inferior conjunctival sac. The radius of the cornea is approximately 1.12 cm [38], giving an area of 0.985 cm^2. Thus, the total area of the palpebral and bulbar conjunctivae is 7.61 and 6.48 cm^2, respectively. The total conjunctival area is 14.1 cm^2, similar to values measured in the literature [75, 76]. The geometric framework in Figure 2A.1 specifies the compartments for which we impose mass balances.

Appendix 2B: Water and salt balances

2B.1 Deposition

Upon lid upstroke of a blink, the upper lid rises to its open position held during interblink [43]. Fluid from the upper meniscus is deposited onto the cornea and conjunctiva as the upper lid passes over the palpebral aperture [50]. This fluid becomes the tear film. The volume held in the upper meniscus alone is insufficient to provide fluid for a 3- to 5-μm thick tear film and to retain a typical meniscus volume [56-58]. To overcome this insufficiency, we recognize that a small amount of fluid from the conjunctival sac is uncovered from behind the lid margin as the lid rises (see Figure 2B.1). The gap between the lid and ocular surface, h_0, is set at 2 μm. As shown in Figure 2B.1, the meniscus shape is that of a fluted prism. Conservation of water in the upper meniscus yields

$$\frac{d}{dt}\iiint_{CV} \rho dV = -\iint_{CS} \rho\left(\underline{u}\cdot\underline{n}\right)dA \tag{B.1}$$

where $\underline{u}$ and $\underline{n}$ are the surface velocity and unit outward normal to the fluted meniscus, respectively, *CV* stands for the upper-meniscus control volume, *CS* stands for the upper-meniscus surface area, and *dV* and *dA* are the differential volumes and areas. With constant fluid density ρ and a meniscus volume of $V_{um} = 2\left(1-\pi/4\right)R_{um}^2 S_{lid}$, Equation B.1 simplifies to

$$\frac{d}{dt}V_{um} = -\left[\iint_{CS_0} -U dA + \iint_{CS_{tf}} U dA\right] \tag{B.2}$$

where *U* is the lid-opening linear velocity taken here as independent of time, and the first and second integrals are over the control surfaces through which the meniscus uncovers fluid (CS_0) and deposits fluid (CS_{tf}), respectively. Since the palpebral-aperture height varies with θ, the upper-lid linear velocity, and, therefore, the deposited tear-film thickness also varies with θ. If the upper lid opens at a constant angular velocity ω, then the linear velocity is $U = \omega R\sin\theta$. Thus, we rewrite the water balance as:

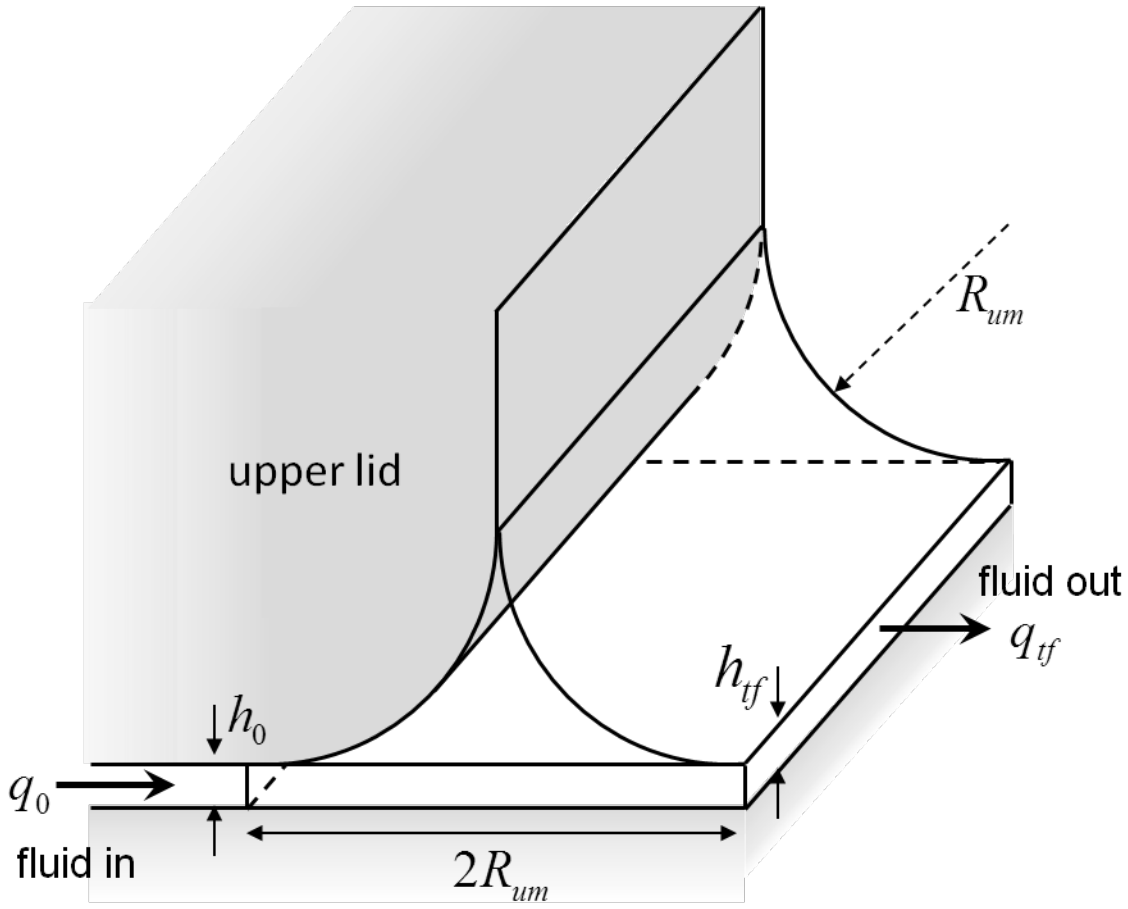

Figure 2B.1: Schematic of the upper-meniscus control volume during deposition. In a coordinate system fixed to the upper meniscus, fluid enters on the left under the upper lid as the lid uncovers conjunctival-sac tear. Fluid leaves the meniscus as the tear film deposits.

$$\frac{dV_{um}}{dt} = \int_{\theta 1}^{\theta 2} \omega R \sin\theta h_0 R d\theta - \int_{\theta 1}^{\theta 2} \omega R \sin\theta h_{tf} R d\theta \qquad \text{(B.3)}$$

where h_0 (2 μm) is the average film thickness uncovered in the superior conjunctival sac, shown in Figure 2B.1. The first term on the right of Equation B.3 is the volumetric flow rate of water into the meniscus, q_0 labeled in Figure 2B.1, and the second term is the volumetric flow rate of water out of the meniscus, q_{tf}, also labeled in Figure 2B.1. The tear-film thickness is given by coating theory [50, 56]:

$$h_{tf} = 1.338 R_{um} \left(\mu U/\sigma\right)^{2/3} = 1.338 R_{um} \left(\mu \omega R \sin\theta/\sigma\right)^{2/3} \qquad \text{(B.4)}$$

where μ and σ are the viscosity and surface tension of aqueous tears. With this result, Equation B.3 becomes

$$4\left(1-\pi/4\right) R_{um} S_{lid} \frac{dR_{um}}{dt} = 2h_0 \omega R^2 \int_{\theta 1}^{\pi/2} \sin\theta d\theta - 1.338 R_{um} 2\omega R^2 \left(\frac{\mu\omega R}{\sigma}\right)^{2/3} \int_{\theta 1}^{\pi/2} \sin^{5/3}\theta \, d\theta \qquad \text{(B.5)}$$

Equation B.5 is solved numerically using ode45 in Matlab to find the upper-meniscus radius as a function of time, $R_{um}(t)$, and, therefore, the transient upper-meniscus volume, $V_{um}(t)$, during deposition. Solution of Equation B.5 also permits calculation of the tear-film thickness from Equation B.4 and, hence, the tear-film volume. The lower meniscus remains static during tear-film deposition. In this manner, the volumes of the upper and lower menisci and of the tear film at the end of deposition (and beginning of interblink) are established.

2B.2 Interblink

Interblink corresponds to the phase between the end of deposition and the beginning of closure. Because it is the longest of the phases at around 5 s [43, 60], fluid transfer via secretion, osmosis, drainage, and evaporation is considered during this period.

2B.2a Conjunctival Sac

Figure 2B.2 is a schematic of one of the conjunctival sacs. These are modeled as 1-D rectangular channels of height h_c and lengths L_{uc} and L_{lc}, respectively, that span the arc length of the lids. The channel length is taken to be the average distance from the meniscus to the apex of the fornix. The effective length over which the fluid in the conjunctival sacs mixes with the preocular tears during closure, however, is $\beta_i L_{ic}$, where β_i is the fraction of the fornix over which complete mixing occurs. The subscript i represents l or u denoting the lower or upper conjunctival sac, respectively. Over long periods of time relevant to the periodic-steady state, we assume the tears are well mixed, so $\beta_i = \beta = 1$. Freshly secreted tear from the lacrimal glands of salt concentration c_{lac} is supplemented by osmotically driven water flow through the bulbar and palpebral conjunctiva wherever the salt concentration is greater than c_{lac}. In our model, we assume that the conjunctival sacs serve as fixed conduits for tear fluid. Upon neglect of axial diffusion, the mass balance on salt in each conjunctival sac reads

$$\frac{\partial c}{\partial t} + \frac{\partial}{\partial x}\left(uc\right) = 0\,, \qquad \text{(B.6)}$$

and that for water is:

$$\frac{\partial u}{\partial x} = \frac{2J_w}{h_c} \qquad \text{(B.7)}$$

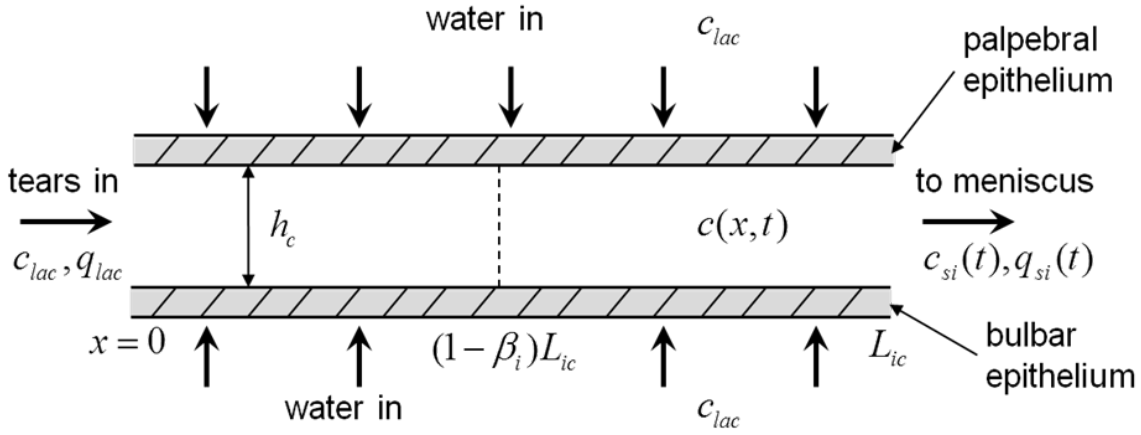

Figure 2B.2: Schematic of conjunctival sac. Tear flow in the fornix is simplified to 1-D plug flow originating at the base of the fornix ($x = 0$) and ending at the lid margin ($x = L_{ic}$) where $i = u$ or l. Water enters the channel through the palpebral and bulbar conjunctivae due to osmotic suction where that $c(x,t) > c_{lac}$.

where $c(x,t)$ and $u(x,t)$ are the height-averaged salt concentration and fluid velocity, respectively, that vary with channel position and time, and J_w is the osmotically driven water flux through the palpebral or conjunctival epithelium

$$J_w = P_{cj} v_w \left(c(x,t) - c_{lac}\right) \tag{B.8}$$

where P_{cj} denotes the water transmissibility in units of m/s, v_w is the molar volume of water, and $c(x,t)$ is the local salt concentration. Solution of coupled differential equations B.6 and B.7 by the method of characteristics [77] (see Appendix 2F) yields the needed fluid velocity, u_{si}, and salt concentration, c_{si}, at the lid margin (i.e., at $x = L_{ic}$ in Figure 2B.2):

$$u_{si} = u(t, L_{ic}) = \begin{cases} u_{lac,i} + \dfrac{\gamma c_{lac}[c_b - c_{lac}]}{c_b[exp(\gamma c_{lac} t) - 1] + c_{lac}} (\beta_i L_{ic} - u_{lac,i} t), & t \le t_{ci} \\ u_{lac,i}, & t > t_{ci} \end{cases} \tag{B.9}$$

$$c_{si} = c(t, L_{ic}) = \begin{cases} \dfrac{c_{lac} c_b exp(\gamma c_{lac} t)}{c_b[exp(\gamma c_{lac} t) - 1] + c_{lac}}, & t \le t_{ci} \\ c_{lac}, & t > t_{ci} \end{cases} \tag{B.10}$$

where $i = u$ or l, $t_{ci} = \beta_i L_{ic}/u_{lac,i}$ is the characteristic time for lacrimal gland to fill the mixed portion of conjunctival sac; $u_{lac,i} = q_{lac,i}/h_c S_{lid}$ is the average fluid velocity at the base of the fornix ($x = 0$); $q_{lac,i} = \lambda_i q_{lac}$ and λ_i are the portion and fraction of the total lacrimal supply directed to conjunctival sac i, respectively; c_b is the bulk-average tear concentration at the end of closure; and $\gamma = 2P_{cj} v_w/h_c$. These equations describe the fluid and salt flows that leave the conjunctival sacs and enters the menisci over the period of interblink, t_{ib}. Due to the greater number of accessory lacrimal glands in the upper fornix, we assume $\lambda_u = 0.8$ [48]. Variation of this factor does not noticeably affect tear osmolarity, but does change the drainage dynamics of the upper and lower menisci during interblink.

Calculation of the Peclet number for the upper and lower conjunctival sacs verifies the neglect of axial diffusion during the interblink. The Peclet number is $Pe = \langle u_{si} \rangle L_{ic}/D_s$, where $\langle u_{si} \rangle$ is the time-average tear velocity at the outlet and D_s is the diffusion coefficient for salt in water, about 10^{-5} cm^2/s [78]. *Pe* is a dimensionless ratio of the solute transport rate by convection to that by diffusion. For normal lacrimal-supply and tear-evaporation rates, *Pe* is ~900 and 200 for the upper and lower conjunctival sacs, respectively. Because $Pe >> 1$, salt transport by axial diffusion is negligible during interblink.

2B.2b Menisci

During interblink, tear fluid from the conjunctival sacs flows into each meniscus while tears drain from the meniscus via suction through the puncta [47, 60]. Thus, water conservation in an individual meniscus is written as

$$\frac{dV_{im}}{dt} = q_{si}(t) - q_{di} - q_{ei} \tag{B.11}$$

where $i = u$ or l, $q_{si}(t) = u(t,L_{ic}) h_c S_{lid}$ is the water flow entering from the conjunctival sac, $V_{im} = 2(1 - \pi/4) R_{im}^2 S_{lid}$ is the meniscus volume, and S_{lid} is the lid perimeter. The evaporation flow rate q_{ei} is the volumetric evaporative flux, J_e, times the meniscus area, $A_{im} = \pi R_{im} S_{lid}/2$.

The drainage rate q_{di}, as a function of R_{im}, is based on that of Zhu and Chauhan [23]

$$q_{di} = q_m \left(1 - R_0 / R_{im}\right) \tag{B.12}$$

where q_m is the maximum drainage rate and R_0 is the meniscus radius below which drainage ceases. The values of q_m and R_0 listed in Table 2.1 are chosen to give similar results to those of Zhu and Chauhan [23].

Since salt enters and leaves in the streams to the puncta and from the conjunctival sac, salt conservation reads

$$\frac{dc_{im}V_{im}}{dt} = c_{si}(t)q_{si}(t) - c_{im}q_{di} \tag{B.13}$$

where $i = u$ or l, c_{im} is the salt concentration in the meniscus. The final, coupled ordinary differential equations for water and salt are functions of time only and are integrated numerically by a Runge-Kutta algorithm (ode45 in MATLAB) to yield the meniscus radius and concentration over interblink.

2B.2c Tear film

The perched tear film loses water via evaporation during the interblink and gains water from osmotic-driven flow through the cornea and conjunctiva. Water conservation for the tear film is

$$\frac{dV_{tf}}{dt} = J_{w,cj}A_{cj} + J_{w,cn}A_{cn} - J_eA_{pa} \tag{B.14}$$

where $J_{w,n}$ is the osmotic water flux given in Equation B.8 and n represents either *cj* (conjunctiva) or *cn* (cornea); A_n is the exposed area and *pa* denotes palpebral-aperture area; and J_e is the volumetric evaporative flux in $m^3/m^2/s$. Strictly, the evaporative flux J_e depends on airflow, geometry, and the difference in water-vapor pressure between the tear and the environment. These details are not required here because evaporation rate is varied as a parameter. Cerretani *et al.* [79] describe evaporation-rate physics relevant to the human eye.

Upon assuming that no salt is lost or gained through the ocular surface, salt conservation in the isolated tear film is

$$\frac{d}{dt}\left(c_{tf}V_{tf}\right) = 0 \tag{B.15}$$

The coupled salt and water balances are solved numerically again by a Runge-Kutta algorithm to give the salt concentration and the volume of the tear film during interblink.

2B.3 Closure

At the end of interblink, the upper lid closes to meet the lower lid. Lid meeting signifies the beginning the closure period. We assume that during closure, motion of the lids and eyeball causes the tear in the menisci and in the tear film to mix with a fraction, β_u and β_l, of the upper and lower conjunctival sacs, respectively. Varying β corresponds to varying the extent of mixing. We assume $\beta = 1$ since variation of β shows only minor differences in tear dynamics, and the tears are expected to be mixed over many blinks. Mixing results in the tear fluid with a homogeneous bulk salt concentration, c_b, in the menisci, tear film, and in an appropriate fraction of the conjunctival sacs. To calculate c_b, we perform a salt balance on the compartments involved in mixing:

$$c_bV_T = \sum_{\alpha=1}^{5} c_{\alpha F}V_{\alpha F} \tag{B.16}$$

where $V_T = \sum_{\alpha=1}^{5} V_{\alpha F}$ is the total volume mixed over, $c_{\alpha F}$ and $V_{\alpha F}$ denote the salt concentration and volume in the α-th compartment (of 5 total) at the end of interblink. Using the values from the end of interblink, we calculate c_b.

The calculations described in Appendices 2A and 2B are executed by a set of m-files coded in MATLAB and included in the supplementary files. The file *mfileTree.m* describes the m-file hierarchy and a brief description each file's function.

Appendix 2C: Solution methodology

Tear dynamics on the ocular surface follows a periodic-steady state. Therefore, no initial conditions are imposed for the governing ordinary differential equations. Rather, the volumes and salt concentrations in each compartment must be the same at the beginning and end of each blink cycle. The water balance in the periodic-steady state is

$$0 = \int_{V_{TD}}^{V_{TF}} dV_T = \int_0^{t_{ib}} \left[q_{lac} + q_c - q_{du} - q_{dl} - q_e \right] dt \tag{C.1}$$

where V_{TD} and V_{TF} are the total tear volumes before deposition and after closure, q_{lac} is the total tear secretion rate from the lacrimal and accessory lacrimal glands, q_c is the total amount of water supplied by osmosis through the conjunctiva and cornea, q_{du} and q_{dl} are the drainage rates through the upper and lower puncta, and q_e is the evaporation flow rate. With the imposition of periodicity, we utilize an iterative method to solve for c_b, and R_b, where R_b is the radius of the upper and lower menisci at the start of deposition. After choosing initial guesses for c_b and R_b, we perform all the deposition, interblink, and closure balances numerically. Then, we update the overall water balance in Equation C.1 and the calculated value of c_b in Equation B.16 until the guessed and final calculated values are equivalent

$$c_{b,it} - \frac{1}{V_T} \sum_{\alpha=1}^{5} c_{\alpha F} V_{\alpha F} = 0 \tag{C.2}$$

where $c_{b,it}$ is the iterated guess for c_b. Specifically, we use a two-variable *Regula-Falsi* algorithm [66] described in Appendix 2G to iterate on choices of c_b and R_b until Equations C.1 and C.2 are satisfied.

Appendix 2D: Estimation of tear flow and lacrimal supply

Considerable clinical tear-flow data are available [49, 54]. Tear flow is determined quantitatively using *in-situ* fluorophotometry to measure the decay of a fluorescent dye instilled in the tear. Determining tear flow from fluorescence decay requires a model for tear flow over the ocular surface. Typically, tear is assumed well mixed in a single compartment of volume V_t with inflows q_{lac} and q_c and outflows q_d and q_e. Fluorescence in the tear film is measured over time, and the slope of the long-time portion of the decay yields the turnover rate. Initial dye dilution allows calculation of V_t. Upon assuming that the tear volume remains constant over time, the resulting dye and water balances yield:

$$C_D = C_D(0) \exp(-\kappa t) \tag{D.1}$$

and

$$\kappa = \frac{q_d}{V_t} = \frac{q_{lac} + q_c - q_e}{V_t} \tag{D.2}$$

where C_D is the concentration of fluorescent dye in the tear at time t; $C_D(0)$ is the initial dye concentration; $\kappa = TTR/100$ is the tear turnover rate in min^{-1}; and q_d, q_{lac}, q_c, and q_e are the drainage, lacrimal secretion, osmotic, and evaporation water-flow rates, respectively. In the literature, "tear flow" is calculated assuming that evaporation and osmotic water flow are negligible and that no dye is lost to the cornea or conjunctiva. Thus, q_{lac} can be calculated by measuring κ and V_t alone [27, 49, 54, 55, 80].

For most normal individuals with healthy lipid layers and near-isotonic tears, negligible evaporation and osmotic flow is probably a reasonable assumption. However, many studies report tear flow in dry-eye sufferers, for whom it is likely that evaporation or osmotic-driven flow play more significant roles. In this case, more information is necessary to isolate the contribution of the lacrimal gland, q_{lac}, to the total tear flow. If the meniscus tear osmolarity, c_b, is measured, then a salt balance on the single tear compartment yields

$$q_{lac} = q_d \frac{c_b}{c_{lac}} = \kappa V_t \frac{c_b}{c_{lac}} \tag{D.3}$$

With this information, the lacrimal secretion flow rate is calculated assuming that the lacrimal gland secretes isotonic fluid. Additionally, if q_e is also measured, q_c follows from Equation D.2, provided all other tear-flow parameters are known.

For most of the tear-flow data available, however, salt concentrations and evaporation rate are not measured simultaneously. Thus, it is impossible to identify specific contributions to q_d. To our knowledge, the two studies by Khanal *et al.* [12, 67] provide the only complete data sets with all tear parameters ascertained to make the necessary analysis.

Application of Equations D.2 and D.3 to the data of Khanal *et al.* [12], [67] for normal subjects yields a q_{lac} only 4 % higher than that calculated if $q_e = q_c = 0$. In dry-eye conditions, the same percentage difference increases to 10 %. Since tear flows reported by Khanal *et al.* are higher than average, we base our normal tear supply values on the average tear flow as compiled by the meta-analysis performed by Tomlinson *et al.* [11, 54]. However, because we can use the complete analysis mentioned above to treat the data of Khanal *et al*. [12, 67], these data guide the choice of ratios between tear flows in the normal and different dry-eye cases. In our analysis, we vary tear supply over a wide range to establish its effect on tear parameters, especially osmolarity.

Appendix 2E: Additional tear-dynamics predictions

Figures 2E.1-2E.5 display additional tear-dynamics predictions for tear-turnover rate, *TTR*; deposited tear-film thickness h_{tfD}; maximum tear-film osmolarity, $c_{tf,max}$; initial menisci radius during deposition, R_b; and total tear volume, V_T, respectively. Contours of each variable appear as functions of tear-evaporation rate, q_e, and lacrimal-supply rate, q_{lac}, over the same range as that in Figures 2.4 and 2.5. Open markers in each figure signify normal (○), dry-eye (□), ADDE (▽), and EDE (△) conditions as described in Table 2.2.

Figure 2E.1 contains contours of tear-turnover rate, *TTR*, as a function of tear-evaporation rate, q_e, and lacrimal-supply rate, q_{lac}. Contour lines for *TTR* appear every 1 %/min between 5 and 15 %/min. Open markers signify normal (○), dry -eye (□), ADDE (▽), and EDE (△) conditions as described in Table 2.2. Predicted *TTR* for normal, dry-eye, ADDE, and EDE conditions is 14.7, 8.6, 6.5, and 11.7 %/min, respectively. Correponding clinically measured values are 15.2, 7.8, 5.7, and 12.6 %/min for the same cases [12, 67], *TTR* in EDE is 80 % greater than that in ADDE. Figure 2E.2 shows contours of deposited tear-film thickness, h_{tfD}, as

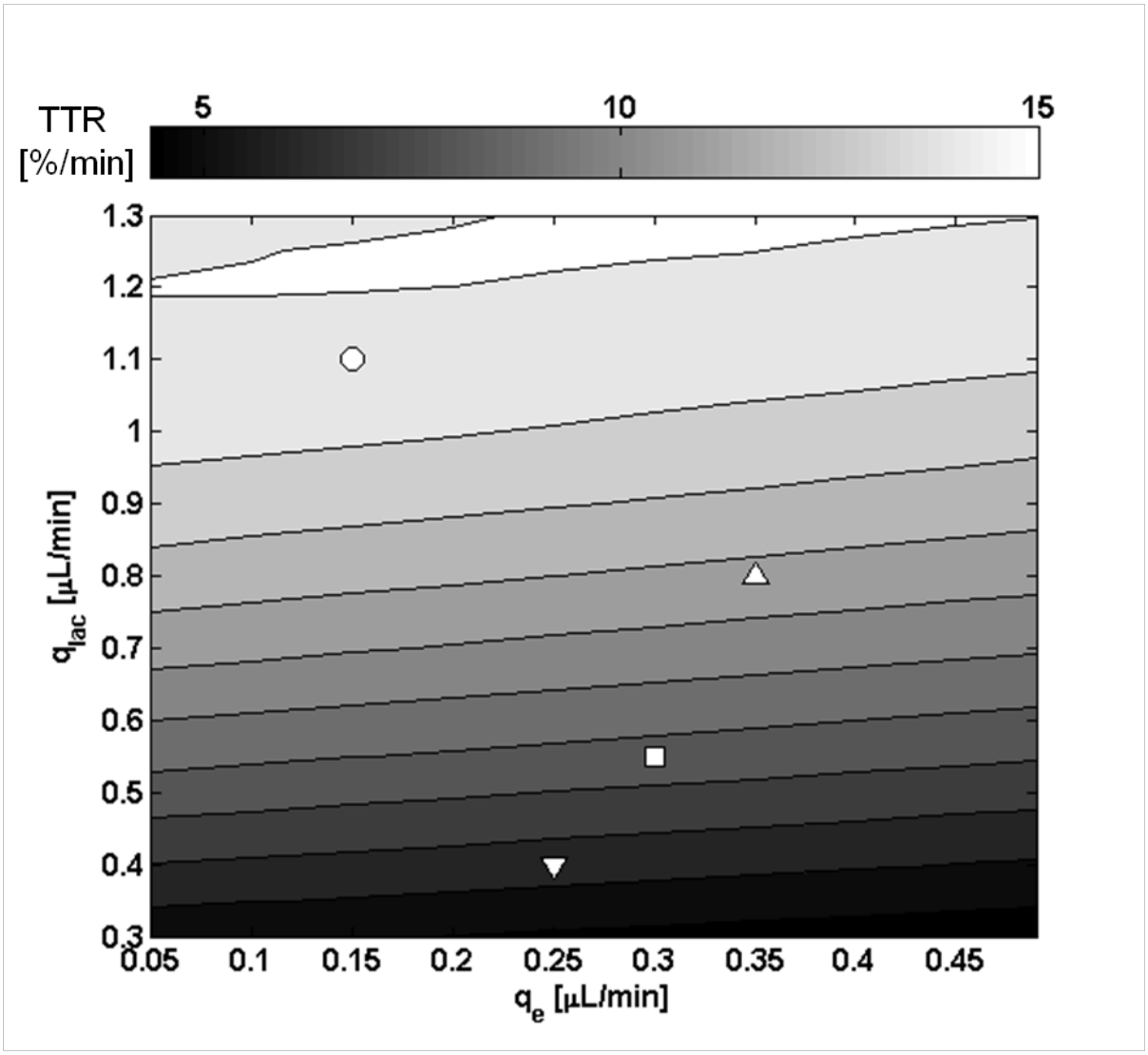

Figure 2E.1: Contours of tear-turnover rate, *TTR*, as a function of tear-evaporation rate, q_e, and lacrimal-supply rate, q_{lac}. Contour lines for *TTR* appear every 1 %/min between 5 and 15 %/min. Open markers signify normal (○), dry-eye (□), ADDE (▽), and EDE (△) conditions as described in Table 2.2. Predicted *TTR* for normal, dry-eye, ADDE, and EDE conditions is 14.7, 8.6, 6.5, and 11.7 %/min, respectively.

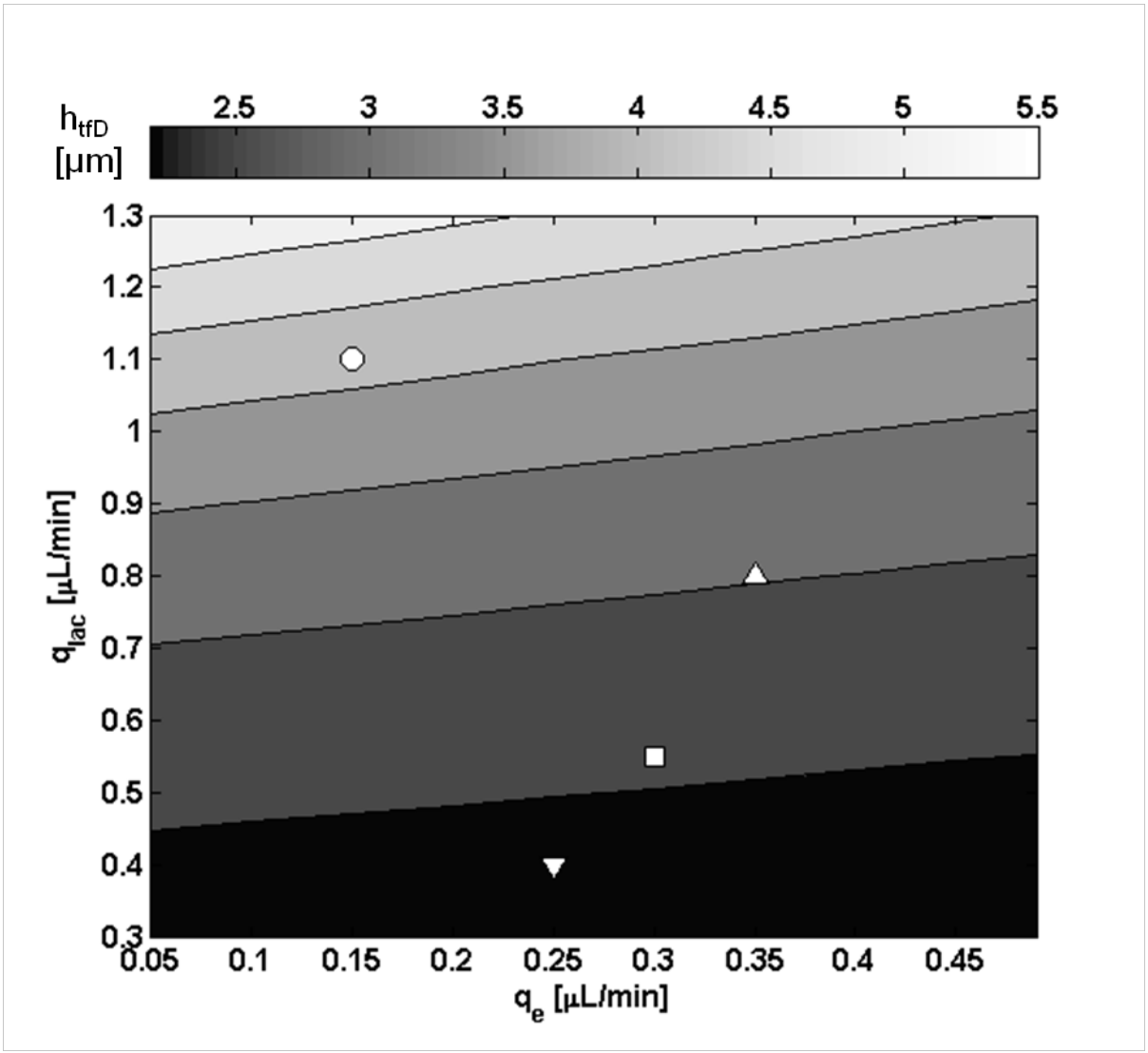

Figure 2E.2: Contours of deposited tear-film thickness, h_{tfD}, as a function of tear-evaporation rate, q_e, and lacrimal-supply rate, q_{lac}. Contour lines for h_{tfD} appear every 0.5 μm between 2.5 and 5.0 μm. Open markers signify normal (○), dry-eye (□), ADDE (▽), and EDE (△) conditions as described in Table 2.2. Predicted h_{tfD} for normal, dry-eye, ADDE, and EDE conditions is 4.2, 2.6, 2.4, and 3.0 μm, respectively.

a function of tear-evaporation rate, q_e, and lacrimal-supply rate, q_{lac}. Contour lines for h_{tfD} appear every 0.5 μm between 2.5 and 5.0 μm. Predicted h_{tfD} for normal, dry-eye, ADDE, and EDE conditions is 4.2, 2.6, 2.4, and 3.0 μm, respectively. Measured tear-film thicknesses for healthy subjects typically fall between 3-5 μm [56]. To our knowledge, there are no measurements of tear-film thickness in dry-eye conditions.

Figure 2E.3 displays contours of the maximum tear-film osmolarity, $c_{tf,max}$, as a function of tear-evaporation rate, q_e, and lacrimal-supply rate, q_{lac}. The $c_{tf,max}$ corresponds to the maximum of the osmolarity spikes for the tear film illustrated in Figure 2.2. Contour lines for $c_{tf,max}$ appear every 10 mOsM between 310 and 350 mOsM. Predicted $c_{tf,max}$ for normal, dry-eye, ADDE, and EDE conditions is 312, 332, 327, and 334 mOsM, respectively. Subtracting c_b in Figure 2.4 from $c_{tf,max}$ in Figure 2E.3 gives elevation of the transient tear-film osmolarity spikes. The tear-film-osmolarity elevation for normal, dry-eye, ADDE, and EDE conditions is 3, 9, 10, and 11 mOsM, respectively. Not surprisingly, the difference between the tear-film and meniscus osmolarities is largest for EDE conditions.

Figure 2E.4 presents contours of the upper- and lower-meniscus radii at the commencement of tear-film deposition, R_b, as a function of tear-evaporation rate, q_e, and lacrimal-supply rate, q_{lac}. R_b also represents the lower-meniscus radius at the onset of interblink. Contour lines for R_b appear every 50 μm between 150 and 350 μm. Predicted R_b for normal, dry-eye, ADDE, and EDE conditions is 291, 173, 156, and 209 μm, respectively. The upper-meniscus radius typically shrinks by about 20-40 % during tear-film deposition while the lower meniscus remains constant. During interblink, the upper-meniscus radius increases by 2-5 %, and the lower-meniscus radius decreases by about 1 %. Consequently, R_b is representative of the lower meniscus over the entire blink cycle. Clinical measurements of the lower-meniscus radius in healthy subjects with optical coherence tomography (OCT) give radii near 240-250 μm [81, 82], close to that predicted here for normal conditions. Additionally, Lu *et al.* [81] measure smaller meniscus radii in ADDE conditions, as predicted here.

Figure 2E.5 contains contours of the total tear volume, V_T, as a function of tear-evaporation rate, q_e, and lacrimal-supply rate, q_{lac}. Contour lines for V_T appear every 0.5 μL between 5.5 and 8.5 μL. Predicted V_T for normal, dry-eye, ADDE, and EDE conditions is 7.1, 5.7, 5.6, and 6.1 μL, respectively. Predicted volumes are near the healthy tear volume of 7 μL [27, 49, 54]. Khanal *et al.* [12, 67] report smaller tear volumes in dry-eye, ADDE, and EDE conditions compared to those in normal conditions.

Appendix 2F: Method-of-characteristics solution

The coupled partial differential equations described in Equations B.6-B.8 are solved with the method of characteristics. Equations B.7 and B.8 are subject to boundary conditions

$$c(0,t) = c_{lac} \tag{F.1}$$

$$u(0,t) = u_{lac}\,, \tag{F.2}$$

and initial condition

$$c(x,0) = \begin{Bmatrix} c_{lac} & 0 < x < (1-\beta)L \\ c_b & (1-\beta)L < x < L \end{Bmatrix} \tag{F.3}$$

where the subscripts *i* and *c* have been omitted from u_{lac}, L, and β. No variables in Appendix 2F contain subscripts, but it is implicit that the equations describe the tear flow and salt

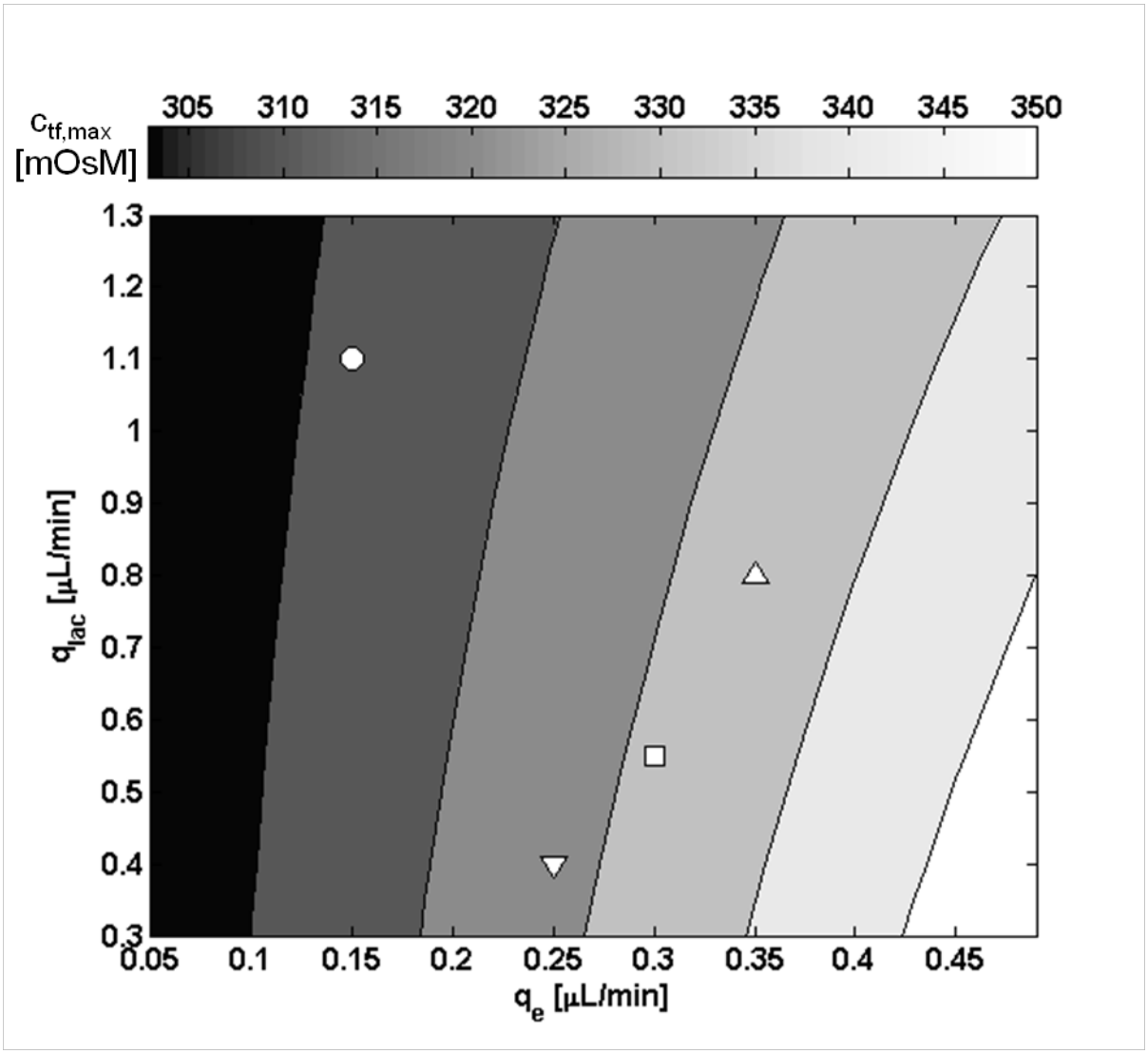

Figure 2E.3: Contours of the maximum tear-film concentration, $c_{tf,max}$, expressed as osmolarity units, as a function of tear-evaporation rate, q_e, and lacrimal-supply rate, q_{lac}. The $c_{tf,max}$ corresponds to the maximum of the osmolarity spikes for the tear film illustrated in Figure 2.2. Contour lines for $c_{tf,max}$ appear every 10 mOsM between 310 and 350 mOsM. Open markers signify normal (○), dry-eye (□), ADDE (▽), and EDE (△) conditions as described in Table 2.2. Predicted $c_{tf,max}$ for normal, dry-eye, ADDE, and EDE conditions is 312, 332, 327, and 334 mOsM, respectively.

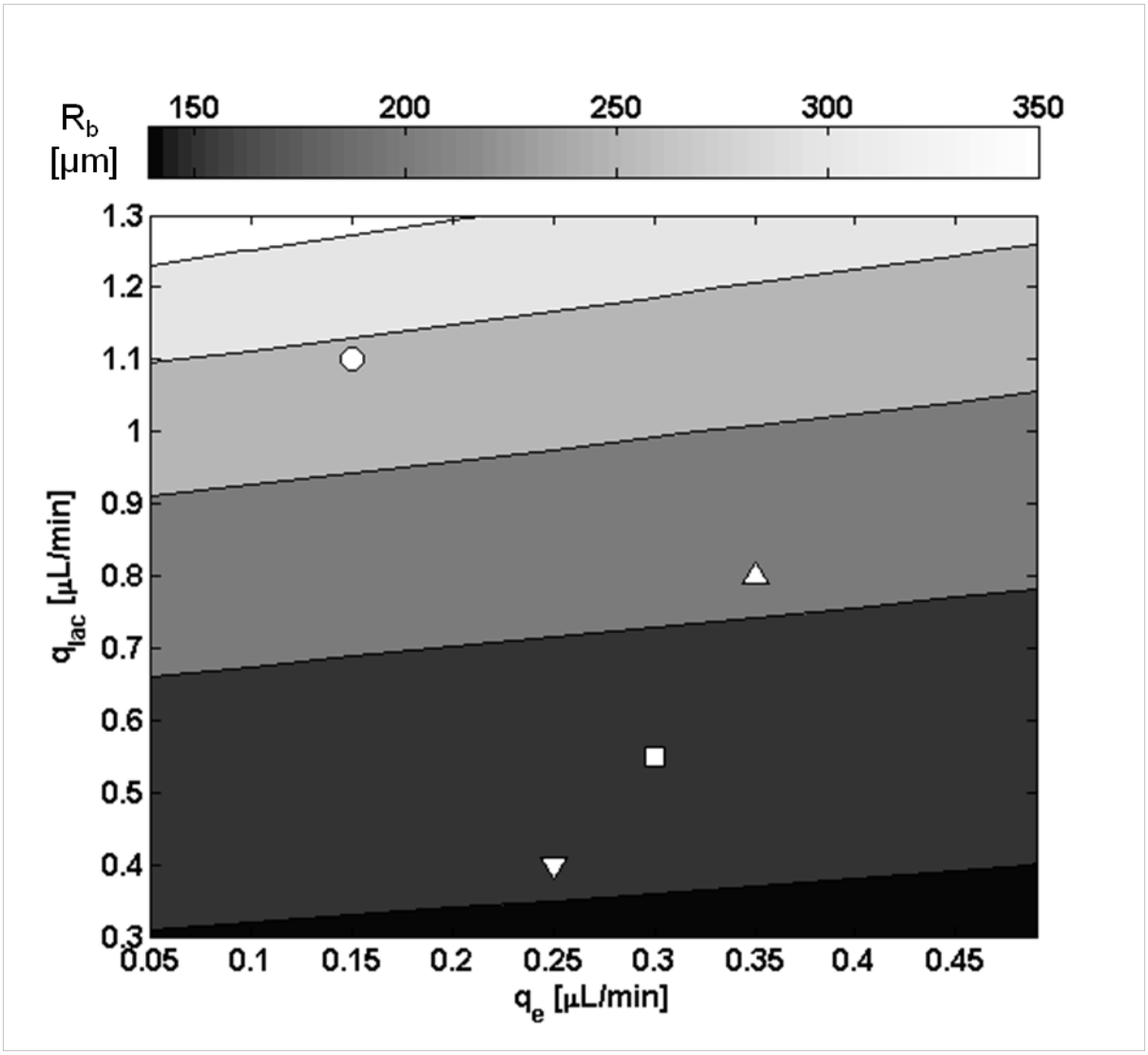

Figure 2E.4: Contours of the upper- and lower-meniscus radius prior to tear-film deposition, R_b, as a function of tear-evaporation rate, q_e, and lacrimal-supply rate, q_{lac}. Contour lines for R_b appear every 50 μm between 150 and 350 μm. Open markers signify normal (○), dry-eye (□), ADDE (▽), and EDE (△) conditions as described in Table 2.2. Predicted R_b for normal, dry-eye, ADDE, and EDE conditions is 291, 173, 156, and 209 μm, respectively.

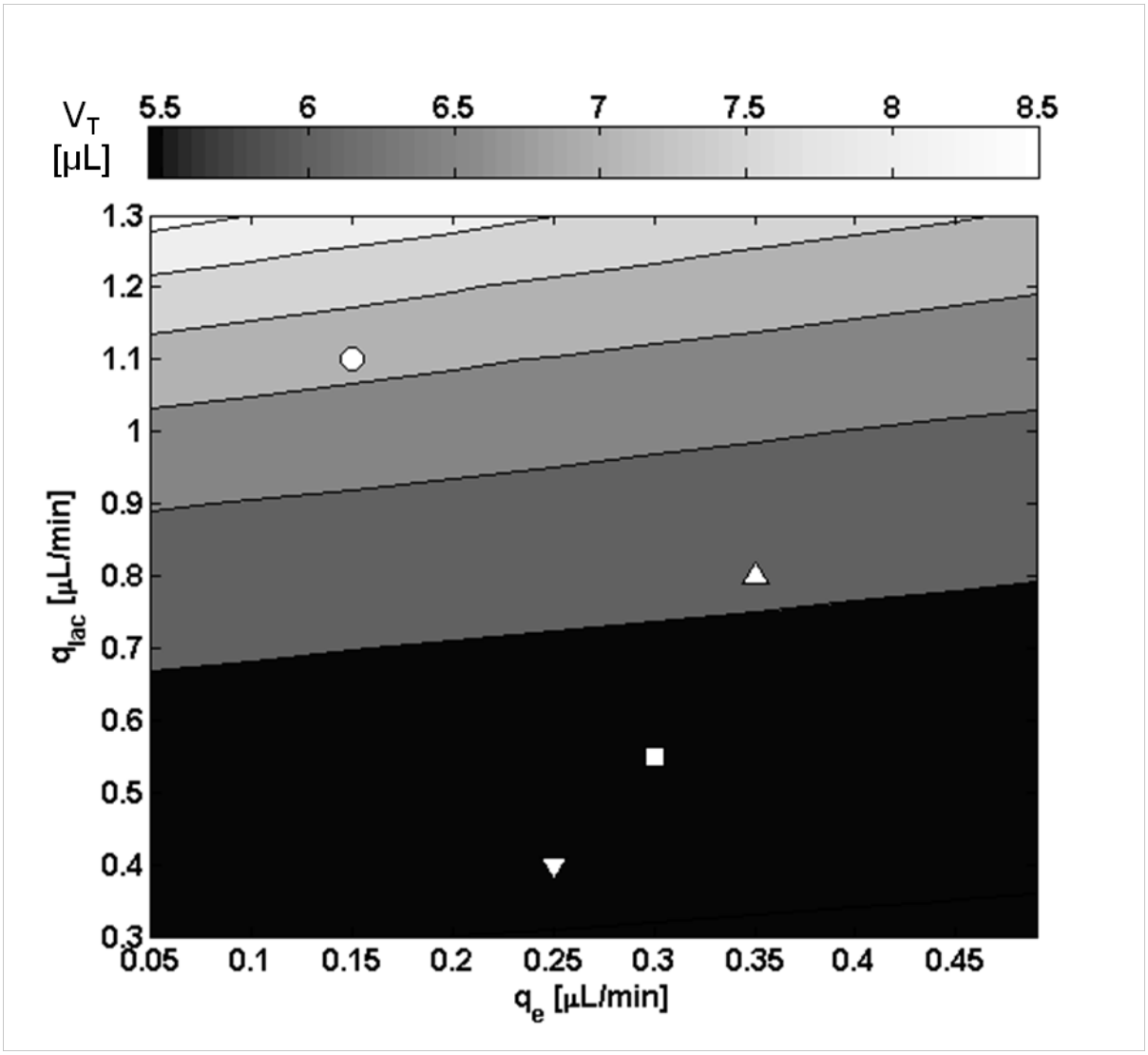

Figure 2E.5: Contours of the total tear volume, V_T, as a function of tear-evaporation rate, q_e, and lacrimal-supply rate, q_{lac}. Contour lines for V_T appear every 0.5 μL between 5.5 and 8.5 μL. Open markers signify normal (○), dry-eye (□), ADDE (▽), and EDE (△) conditions as described in Table 2.2. Predicted V_T for normal, dry-eye, ADDE, and EDE conditions is 7.1, 5.7, 5.6, and 6.1 μL, respectively.

concentration in each conjunctival sac. There are two regions within the conjunctival sac corresponding to the extent of mixing β. The initial tear concentration in Region I, for x between 0 and $(1-\beta)L$, is that of the secreted tear, c_{lac}. Since tear in the rest of the conjunctival sac, Region II, is subject to mixing with the other compartments during closure, it begins interblink at the concentration of the bulk tear, c_b. As mentioned, $\beta = 1$ for all reported calculations. Substitution of Equation B.8 into Equation B.7 gives a differential equation for $u(x,t)$

$$\frac{\partial u}{\partial x} = \frac{2P_{cj}v_w}{h_c}\left(c(x,t) - c_{lac}\right) \tag{F.4}$$

Integration of Equation F.4 over the region 0 to x yields an expression for the flow velocity as a function of tear concentration

$$u(x,t) = u_{lac} + \gamma\int_0^x (c - c_{lac})dx' \tag{F.5}$$

where $\gamma \equiv 2P_{cj}v_w/h_c$. Combination of Equations F.4 and F.5 with Equation B.6 yields a partial differential equation for $c(x,t)$

$$\frac{\partial c}{\partial t} + \left[u_{lac} + \gamma\int_0^x (c - c_{lac})dx'\right]\frac{\partial c}{\partial x} = -\gamma(c - c_{lac})c \tag{F.6}$$

This first-order, inhomogeneous partial differential equation is amenable to solution by the method of characteristics. Upon approximating $u(x,t) \sim u_{lac}$, Equation F.6 simplifies to

$$\frac{\partial c}{\partial t} + u_{lac}\frac{\partial c}{\partial x} = -\gamma(c - c_{lac})c \tag{F.7}$$

The characteristic ODEs for Equation F.7 are

$$\frac{dx}{ds}(r,s) = u_{lac}, \tag{F.8}$$

$$\frac{dt}{ds}(r,s) = 1, \tag{F.9}$$

and

$$\frac{dz}{ds}(r,s) = -\gamma(c - c_{lac})c \tag{F.10}$$

where s and r parametrize the solution curve. The corresponding transformed initial conditions for this system of ODEs are

$$x(r,0) = r, \tag{F.11}$$

$$t(r,0) = 0, \tag{F.12}$$

and

$$z(r,0) = \begin{Bmatrix} c_{lac}, 0 < r < (1-\beta)L \\ c_b,\ (1-\beta)L < r < L \end{Bmatrix} \tag{F.13}$$

Solution of Equations F.8 and F.9 subject to Equations F.11 and F.12 defines the characteristic lines

$$r = x - u_{lac}t \tag{F.14}$$

The remaining ODE for z in Equation F.10 is separable:

$$\int_{z(r,0)}^{z} \frac{dz'}{z(z - c_{lac})} = -\gamma\int_0^s ds' \tag{F.15}$$

The definite integral of Equation F.15 is

$$\frac{1}{c_{lac}}\ln\left[\frac{z(r,s) - c_{lac}}{z(r,s)}\right] - \frac{1}{c_{lac}}\ln\left[\frac{z(r,0) - c_{lac}}{z(r,0)}\right] = -\gamma s \tag{F.16}$$

Rearrangement of Equation F.16 produces

$$z(r,s) = \frac{z(r,0)c_{lac}exp(\gamma c_{lac}s)}{c_{lac} + z(r,0)\left[exp(\gamma c_{lac}s) - 1\right]} \tag{F.17}$$

Transformation of the final solution into x and t space subject to boundary condition F.13 gives the transient concentration profile in the conjunctival sac

$$c(x,t) = \begin{cases} c_{lac}, & 0 < x - u_{lac}t < (1-\beta)L \\ \dfrac{c_{lac}c_b exp(\gamma c_{lac}t)}{c_{lac} + c_b\left[exp(\gamma c_{lac}t) - 1\right]}, & (1-\beta)L < x - u_{lac}t < L \end{cases} \tag{F.18}$$

The region of tear at concentration c_{lac} initially spans $x = 0$ to $x = (1\text{-}\beta)L$, but as time passes, fresh tear flows towards the meniscus, enlarging Region I and diminishing Region II.

Fluid velocity $u(x,t)$ follows from $c(x,t)$. In Region I, where $c = c_{lac}$, Equation F.4 dictates that $\partial u/\partial x = 0$. Thus, $u(x,t) = u_{lac}$ in Region I due to the absence of osmotic water influx through the conjunctiva. In Region II, Equation F.4 becomes

$$\frac{\partial u}{\partial x} = \left\{ \frac{\gamma c_{lac}c_b exp(\gamma c_{lac}t)}{c_{lac} + c_b\left[exp(\gamma c_{lac}t) - 1\right]} - c_{lac} \right\} \tag{F.19}$$

Integration of Equation F.19 subject to Equation F.4 yields $u(x,t)$ in Region II:

$$u(x,t) = \begin{cases} u_{lac}, & 0 < x - u_{lac}t < (1-\beta)L \\ u_{lac} + \dfrac{\gamma c_{lac}(c_b - c_{lac})}{c_{lac} + c_b\left[exp(\gamma c_{lac}t) - 1\right]}\left[x - (1-\beta)L - u_{lac}t\right], & (1-\beta)L < x - u_{lac}t < L \end{cases} \tag{F.20}$$

The tear-flow behavior mirrors that of the tear-salt concentration. To the left of the moving front (Region I), the tear-flow velocity in the conjunctival sac is constant at u_{lac}. The tear-flow velocity in diminishing Region II is transient and decreasing in time.

Water and salt conservation equations for the meniscus, Equations B.11 and B.13, respectively, require the tear-flow velocity and salt concentration entering the meniscus from the conjunctival sac, $u(L,t)$ and $c(L,t)$. Equations F.18 and F.20 evaluated at x = L are

$$c(L,t) = \begin{cases} \dfrac{c_{lac}c_b exp(\gamma c_{lac}t)}{c_{lac} + c_b\left[exp(\gamma c_{lac}t) - 1\right]}, & t < \beta L / u_{lac} \\ c_{lac}, & t > \beta L/u_{lac} \end{cases} \tag{F.21}$$

and

$$u(L,t) = \begin{cases} u_{lac} + \dfrac{\gamma c_{lac}(c_b - c_{lac})}{c_{lac} + c_b\left[exp(\gamma c_{lac}t) - 1\right]}\left[\beta L - u_{lac}t\right], & t < \beta L / u_{lac} \\ u_{lac}, & t > \beta L / u_{lac} \end{cases} \tag{F.22}$$

Equations F.21 and F.22 describe the tear-osmolarity and the tear-flow velocity entering a meniscus during interblink. Water and salt dynamics change at time $t_c \equiv \beta L/u_{lac}$. For $t < t_c$, the tear-flow velocity and salt concentration decrease transiently. For $t > t_c$, the conjunctival sac is flushed of hypersomolar tear, and the tear flow and salt osmolarity are those secreted by the lacrimal glands. The 5-s interblink time t_{ib} is much smaller than the 3- and 9-min t_c for both the upper and the lower conjunctival sacs. Therefore, the transient solution in Equations F.21 and F.22 describes tear flow and osmolarity entering the menisci during interblink.

A posteriori assessment of the simplifying assumption that $u(x,t) \sim u_{lac}$ reveals that the time-average of $u(L,t)$ over interblink is less than 15 % higher than u_{lac} in both menisci.

Consequently, the model underestimates slightly the water flow rate through the conjunctival sacs and, correspondingly, overestimates tear osmolarity. The error increases in dry-eye conditions.

Appendix 2G: Two-parameter *Regula-Falsi* algorithm

Appendix 2C outlines the solution methodology for the coupled water- and solute-conservation equations. We employ an iterative scheme to locate simultaneously the roots of the two functions defined by Equations C.1 and C.2, which result from the set of coupled differential algebraic equations (DAEs) for water and salt conservation described in Appendix 2B. Equations C.1 and C.2, respectively, are of the form

$$\Delta V_T = f(c_b, R_b, \underline{\Pi}) = 0 \tag{G.1}$$

and

$$\Delta(c_b) = g(c_b, R_b, \underline{\Pi}) = 0 \tag{G.2}$$

where Δ indicates the difference between values at the beginning and end of a blink cycle, V_T is the total tear volume, c_b is the average salt concentration in the tear, R_b is the upper and lower meniscus radius before deposition and after closure, $\underline{\Pi}$ is the vector of remaining parameters (i.e., geometries, physical properties, flow rates, etc.), and f and g are the expressions for water and salt conservation over the entire blink period. We locate the roots of f and g using a *Regula-Falsi* algorithm to iterate on c_b and V_b. Carnahan *et al.* describe application of the *Regula-Falsi* algorithm to locate the root of a function $y = f(x)$ dependent upon a single independent variable x [66].

Our tear-dynamics model, however, requires simultaneous calculation of the roots of f and g, which are both functions of independent variables c_b and R_b. We developed an extended two-parameter *Regula-Falsi* algorithm to address this situation. The two-parameter *Regula-Falsi* algorithm requires an initial guess for osmolarity, c_{b0}, and a range of c_b and R_b to bracket the root. The range for R_b and c_b must contain the solution, otherwise the method fails to locate the root. First, the *Regula-Falsi* method outlined by Carnahan *et al.* [66] iterates on R_b with fixed c_{b0} to find the root (R_{b1}, c_{b0}) of f in Equation G.1. If the resulting root (R_{b1}, c_{b0}) also satisfies $g = 0$ from Equation G.2, then the solution has been located. If not, then the *Regula-Falsi* method iterates on c_b with fixed R_{b1} to find the root (R_{b1}, c_{b1}) of g in Equation G.2. If the resulting root (R_{b1}, c_{b1}) satisfies $f = 0$ in Equation G.1, then the solution has been located. If not, the *Regula-Falsi* method continues to iterate alternatively on R_b and c_b for N times until the root (R_{bN}, c_{bN}) satisfies both Equations G.1 and G.2 to within the desired tolerance. The algorithm executed requires that $| f | \leq 1.0x10^{-6}$ µL and $| g | \leq 1.0x10^{-4}$ mOsM.

The m-files titled *f2DRegFalsi.m*, *fCRegFalsi.m*, *fWRegFalsi.m*, and *fBALws.m* contained in the supplementary material to the dissertation execute this two-parameter *Regula-Falsi* algorithm. *f2DRegFalsi.m* defines the range for c_b and R_b and alternates between executing the *Regula-Falsi* iteration on f (via *fWRegFalsi.m*) and g (via *fCRegFalsi.m*) until the roots satisfy both equations. Given a set of parameters and R_b and c_b, *fBALws.m* calculates the values of f and g using the set of DAEs outlined in Appendix 2B. Since the two-parameter *Regula-Falsi* method typically converges within 2 to 3 iterations the tear-dynamics model, we never pursued implementation of another self-consistent algorithm such as two-variable Newton-Raphson.

Chapter 3

Structural and Rheological Properties of Meibomian Lipids

3.1 Abstract

We explore the unique rheological and structural properties of human and bovine meibomian lipids to provide insight into the physical behavior of the human tear-film lipid layer (TFLL).

Bulk rheological properties of pooled meibomian lipids were measured by a commercial stress-controlled rheometer; a home-built interfacial stress rheometer (ISR) probed the interfacial viscoelasticity of spread layers of meibomian lipids. Small- and wide-angle X-ray scattering detected the presence and melting of dispersed crystal structures. Microscope examination under cross polarizers provided confirmation of ordered crystals. A differential scanning calorimeter (DSC) analyzed phase transitions in bulk samples of bovine meibum.

Bulk and interfacial rheology measurements show that meibum is extremely viscous and highly elastic. It is also a non-Newtonian, shear-thinning fluid. Small- and wide-angle x-ray diffraction (SAXS and WAXS), as well as differential scanning calorimetry (DSC) and polarizing microscopy, confirm the presence of suspended lamellar-crystal structures at physiologic temperature.

We studied meibum architecture and its relation to bulk and interfacial rheology. Bovine and human meibomian lipids exhibit similar physical properties. From all structural probes utilized, we find a melt transition near eye temperature at which lamellar crystals liquefy. Our proposed structure for the tear-film lipid layer at physiologic temperature is a highly viscoelastic, shear-thinning liquid suspension consisting of lipid lamellar-crystallite particulates immersed in a continuous liquid phase with no long range order. When spread over on-eye tear, the TFLL is a duplex film that exhibits bulk liquid properties and two separate interfaces, air/lipid and water/lipid, with aqueous protein and surfactant-like lipids adsorbed at the water/lipid surface.

3.2 Introduction

Meibomian lipids are the major component of the tear-film lipid layer (TFLL), the outermost portion of the tear film. Between the lipid layer and the corneal surface exists a 3-10 μm aqueous layer [1] containing salts, mucins, and proteins. The primary role of the aqueous tear film is to hydrate and protect the corneal surface. The lipid layer, estimated to be ~100-nm thick [1, 2] is a duplex film that spreads over the aqueous tear film after each blink. It is thought to

reduce evaporation from the aqueous phase and to play an important role in maintaining tear-film stability [2, 3]. Tear-film instability and increased tear evaporation are major signs of dry-eye disease, an ocular surface disease that leads to discomfort and possible damage to the corneal and conjunctival epithelia [4]. Since the physical and mechanical properties of the TFLL depend on the structure of meibum, knowledge of meibum's structure is indispensible to understand the function of the TFLL in tear-film behavior.

Produced in the meibomian glands, meibum is a holocrine secretion composed of a rich mixture of lipids and possibly cellular debris. Wax esters and cholesterol esters are the major lipid components, together making up roughly 60-70% of the total meibum content, with lesser amounts of diesters, triacylglycerols, polar lipids, and fatty acids making up the balance. Many of the individual chains are greater than 20 carbons long, leaving lipids with one or more alkyl chains, such as wax esters, diesters and tracylglycerols, to contain as many as 40-60 carbon atoms. The degree of saturation varies as well: saturated, monounsaturated, and polyunsaturated lipids are all present in meibum [5-8]. Meibomian-gland secretions have also been shown to contain proteins, which could disrupt regions of ordered lipids [9, 10].

To date, most efforts at characterizing meibum have focused on chemical analysis of the secretion. Less is known about the structure and physical properties of meibum. Various authors found that meibum exhibits a broad melting range, becoming liquid near body temperature [11]. Viscosity measurements by Tiffany and Dart [12] demonstrated meibum to be viscous, although the effects of shear rate or temperature were not pursued. Borchman *et al*. [13] utilized infrared spectroscopy to characterize the molecular conformation of hydrocarbon chains in human meibum, finding that as meibum melts, hydrocarbon chains of the lipids transition from the *trans* to *gauche* rotomers. The increased disorder reduces the packing efficiency of the lipids. By using small-angle x-ray scattering (SAXS), Leiske *et al*. [14] observed crystalline structures in bulk human meibum. Two crystal populations were present, one melting at 34 °C and another persisting up to 40 °C. They also measured rheology of interfacial meibum films spread on water and found that the film undergoes a sharp phase transition from solid-like to liquid-like behavior below physiological temperature.

A major reason for the scarcity of information about meibum is the difficulty in obtaining large enough human samples for making measurements. Consequently, researchers often use other mammals as a source of meibum [15-17]. Nicolaides *et al.* [16, 17] studied the lipid composition of both steer and human meibum and found them to be similar.

In this work, we explore the bulk and interfacial properties of human and bovine meibum in an effort to understand how its structure relates to its physical properties. We explore temperature-induced transitions in the structure and mechanical properties of these meibomian lipids. Using SAXS, we detect the presence of crystal structures and observe their melt behavior. In addition, differential scanning calorimetry provides temperatures at which phase changes occur and their corresponding latent heats. We perform interfacial and bulk rheology measurements to probe how thin films and bulk samples of meibum respond to deformation over a range of shear rates and temperatures. By comparing the behavior of dispersed crystal structures to the measured mechanical properties over a range of temperatures, we gain understanding of how meibum's molecular organization contributes to its physical behavior.

3.3 Methods

3.3.1 Meibomian lipid collection

Animal and human ethics were approved for the collection of meibomian lipids; the study was carried out in accordance with the tenets of the Declaration of Helsinki. Bovine eyelids of over 200 animals were dissected post-mortem at a slaughterhouse. The eyelids were warmed to 37 °C, and the meibomian lipids were extruded by hard expression of the superior and inferior eyelid margins [16, 17] with pliers, yielding an average of 3 mg per eye. The excreta were scraped from the lid margin with a metal spatula and deposited onto a small glass cover slip that was then placed in an amber jar for storage at -20 °C until use. The excreted fluid was a clear liquid at 37 °C, and became opaque and yellowish upon solidification at room temperature. The bulk rheological experiments required pooling of bovine meibum from multiple animals to generate samples large enough for analysis. Otherwise, samples from individual animals were stored and tested separately.

Twelve human-meibum samples, each less than 1 mg, were collected from healthy, non-dry-eye, non-lens-wearing volunteers. A meibum sample was collected if, upon examination, the volunteer met the following criteria: lack of dry eye symptoms (<5) as determined by the Schein Questionnaire [18]; minimal to absence of sodium fluorescein staining in the cornea; tear-film break-up time >7 s; and absence of meibomian gland dysfunction (MGD) as determined by normal meibum appearance.

Meibum was expressed from the lower lids by applying pressure with a sterile cotton swab against a Mastrota paddle. Gentle scraping of the eyelid margin with a small, degreased metal ocular spud collected secreted meibum. Samples collected from the right and left eyes of a single volunteer were pooled and transferred onto a small glass cover slip that was then placed in an amber jar for storage at -20 °C until use. Here too, the bulk rheological experiments required pooling samples from 4 individuals.

3.3.2 Interfacial Shear Rheometry

An interfacial stress rheometer (ISR) probed the interfacial viscoelasticity of the meibomian lipids. Validation and merits of this technique are available elsewhere [19, 20]. Briefly, the ISR is a two-dimensional analogue to a classic, three-dimensional sliding-plate rheometer. It ascertains the viscoelastic properties of monolayers. Our ISR utilizes a KSV mini-trough coupled with a Wilhelmy balance and moveable barriers to monitor and control surface pressure. Two Helmholtz coils apply an oscillating magnetic field used to move the magnetic, Teflon-coated rod along its major axis at sinusoidal strains. The rod floats at the interface in a rectangular, quartz channel. The long axis of the channel is perpendicular to the trough barriers so that compression of the monolayer throughout the trough (inside and outside the channel) is uniform. The channel maintains the lateral position of the rod during the experiments and defines the velocity profile created by the rod motion. The resulting stress was calculated from a calibration constant that converted the strength of the magnetic field to the force (the rheometer was calibrated prior to deposition of every monolayer). Rod position was monitored with a CCD camera (Basler Electric Company, Highland, IL), and strain was ascertained from the images. The trough surface was heated to 35 °C to facilitate sample spreading. Solid meibum touched to the trough surface with a metal spatula spread spontaneously. To ensure reproducible measurements, each sample was first spread to a constant surface pressure of 2 mN/m. After spreading, the trough was cooled to 20 °C over a period of one hour before the film was compressed to the desired surface pressure. Trough surface area was held constant as the

interface was slowly heated to 35 °C at 0.3 °C/min. During the heating cycle, interfacial rheology was monitored at a frequency of 1 Hz and a strain of 1.74 %, which is within the linear viscoelastic region of meibum. Temperature changes in time were monitored by placing a temperature probe 1-2 mm below the surface behind the trough barriers.

Recent BAM (Brewster angle microscopy) measurements [15] showed that upon deposition, meibomian lipids spread from solvent are inhomogeneous. At 15 mN/m and above, the surface pressure at which the elasticity of the film increased, the film was homogeneous on length scales as small as the limit of BAM.

3.3.3. Bulk Shear Rheometry

Shear rheology of pooled bovine meibomian lipids was measured using a stress-controlled rheometer (TA Instruments, Model AR G2, New Castle, DE) with an 8-mm parallel plate and a gap size of 250 μm. Due to the small volume of an individual human-meibum sample (of the order of 0.3 μL), shear rheology of pooled human meibomian lipids was measured with a 3-mm parallel plate and a gap size of 100 μm. Samples were loaded at 23 °C. Both steady shear rheology and oscillatory shear rheology were performed on every sample. For oscillatory rheological measurements, a stress sweep was first performed to obtain the linear viscoelastic region. Then the sample was heated at a constant rate of 1 °C/min while oscillating the upper plate at 1 Hz and 0.1% strain, which is within the linear viscoelastic region for the sample.

3.3.4 Small-Angle X-ray Scattering (SAXS)

SAXS experiments were performed at the Stanford Synchrotron Radiation Lightsource (SSRL) on beamline 1-4. Bovine-meibum samples were sandwiched between two Kapton windows in a sample holder. A 2-D detector collected scattering intensity *I(q)* over 2-min intervals for the combined sample and holder. Scattering of the empty sample holder with Kapton windows was also recorded. Transmission of the holder and sample were measured to normalize intensity and remove scattering volume dependence; an empty cell was subtracted as the parasitic scattering. Background (diffuse) scattering was removed, and a function was fit to the baseline and subtracted from the data, ensuring that the background was independent of the scattering vector, q [$Å^{-1}$], which for ordered structures is related to length scales in real space, d [Å], by the expression: $q = 2\pi/d$. Scattering peaks were fit with Gaussian functions to determine peak centers and widths. Scattering spectra of the samples were measured at temperature increments of 3-4 °C between 26-45 °C. Samples were heated until the peaks disappeared; therefore, not all samples were heated to 45 °C.

3.3.5 Wide-Angle X-ray Scattering (WAXS)

WAXS experiments were also performed at SSRL beamline 1-4. The technique was the same as that for SAXS. However, the distance between the sample and the detector was shorter, and, thus, diffraction maxima at larger angles were observed.

3.3.6 Polarized-Light Microscopy

Micrographs of bovine meibum were obtained with a polarized-light microscope (Olympus BX51, Tokyo, Japan) attached to a color digital camera (Olympus C-5060, Tokyo, Japan). A sample from a single animal was sandwiched between a glass slide and a cover slip, placed on a temperature-controlled stage, and subjected to temperature cycling between 15 and 150 °C at a rate of 2 °C/min with still images (1024x768 pixels) captured every 30 s. Two

polarizing filters were oriented 90° to each other: one between the light source and the sample, and one between the sample and the camera. Birefringence due to anisotropic crystal structures was evident in the visible bright areas of the images.

To quantify birefringence intensity, images were converted to grayscale, and the average intensity, I, of all image pixels (~$8x10^5$ pixels) was calculated. We define a relative intensity, I/I_{max} where I_{max} corresponds to the average pixel intensity of the brightest image. To ascertain melting or crystallization transitions, we tracked I/I_{max} versus temperature.

3.3.7 Differential Scanning Calorimetry

A TA Instruments (Model DSC Q20, New Castle, DE) differential scanning calorimeter (DSC) was used to analyze phase transitions in bulk samples of bovine meibum. At temperatures where phase transitions occur, latent heat is absorbed or released, resulting in a peak in heat inflow or outflow at that temperature. Peak location and width reveal the temperature ranges for a particular phase transition; integration of the peak gives the total latent heat released or absorbed for a given phase transition. 5- to 10-mg individual and pooled samples of bovine meibum taken from storage at -20 °C were hermetically sealed into aluminum TA-Tzero sample pans (TA Instruments, New Castle, DE). Carefully sealed samples were then placed in the DSC holder, and temperature was cycled between -30 and 200 °C at a rate of 2 °C/min for at least two complete cycles. Peak areas were quantified with the TA Analysis software.

3.4 Results

3.4.1 Interfacial Shear Rheology

The change in bovine-meibum interfacial viscoelastic properties as the film was (a) heated or (b) cooled is presented in Figure 3.1. *G'* stands for the elastic modulus while *G''* stands for the viscous modulus. At 23 °C and a surface pressure of 24 mN/m, the film was quite elastic (*G' > G''*) with high values, near 10 mN/m. As the film was heated, the interfacial moduli decreased by almost three orders of magnitude. Between 29 and 31 °C, the interfacial elastic modulus dropped most rapidly; the film became primarily viscous (*G'' > G'*) around 30 °C. At 35 °C, the interfacial viscous modulus was at the sensitivity limit for the ISR (0.02 mN/m). After reaching 35 °C, the film was cooled back to 23 °C (Figure 3.1(b)). Over the temperature range, 35-31 °C, the film was viscous with no measureable elastic component. An interfacial elastic modulus was discernible at 31 °C and rose very quickly between 31-29 °C. The film became primarily elastic at 29 °C. Comparison between the two curves reveals a sharper transition when the film is cooled; the film becomes rigid over a very narrow temperature range. Moreover, the values of both the interfacial elastic and viscous moduli are higher at the base temperature (23 °C) after heating and then cooling.

3.4.2 Bulk Shear Rheology

The bulk viscoelastic properties obtained from oscillatory shear rheology of pooled samples are presented in Figure 3.2 for bovine meibum and in Figure 3.3 for human meibum. The elastic (*G'*) and viscous (*G"*) moduli are shown as functions of temperature. Temperature sweeps from 25-40 °C and 40-25 °C were performed as presented in Figures 3.2(a) and 3.2(b) for bovine meibum and in Figures 3.3(a) and 3.3(b) for human meibum. For the bovine meibum, the major melt transition occurred between 29 and 35 °C. In that 6 °C temperature range, the viscous and elastic moduli both decreased by three orders of magnitude during heating. Despite the dramatic decrease in viscoelasticity, the fluid remains predominantly elastic (*G'>G''*).

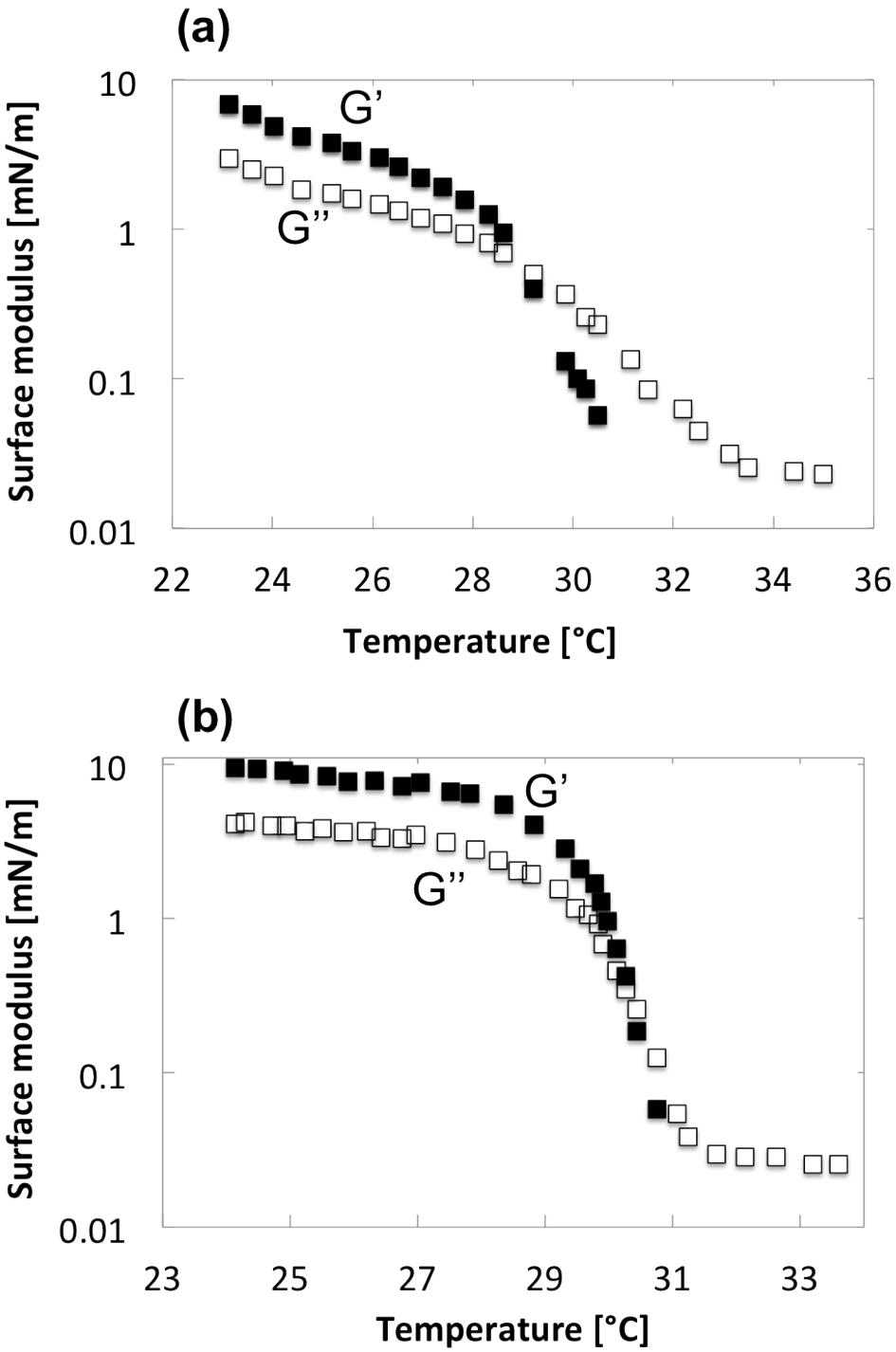

Figure 3.1: Interfacial moduli as a function of temperature for a representative bovine-meibomian lipid film at a frequency of 1 Hz and a strain of 1.74 %. The film was initially compressed to 24 mN/m at 23 °C, then the surface area was held constant as the film was heated to 35 °C (a) and then cooled back to 23 °C (b). Filled symbols represent the elastic modulus, *G'*, and open symbols represent the viscous modulus, *G''*.

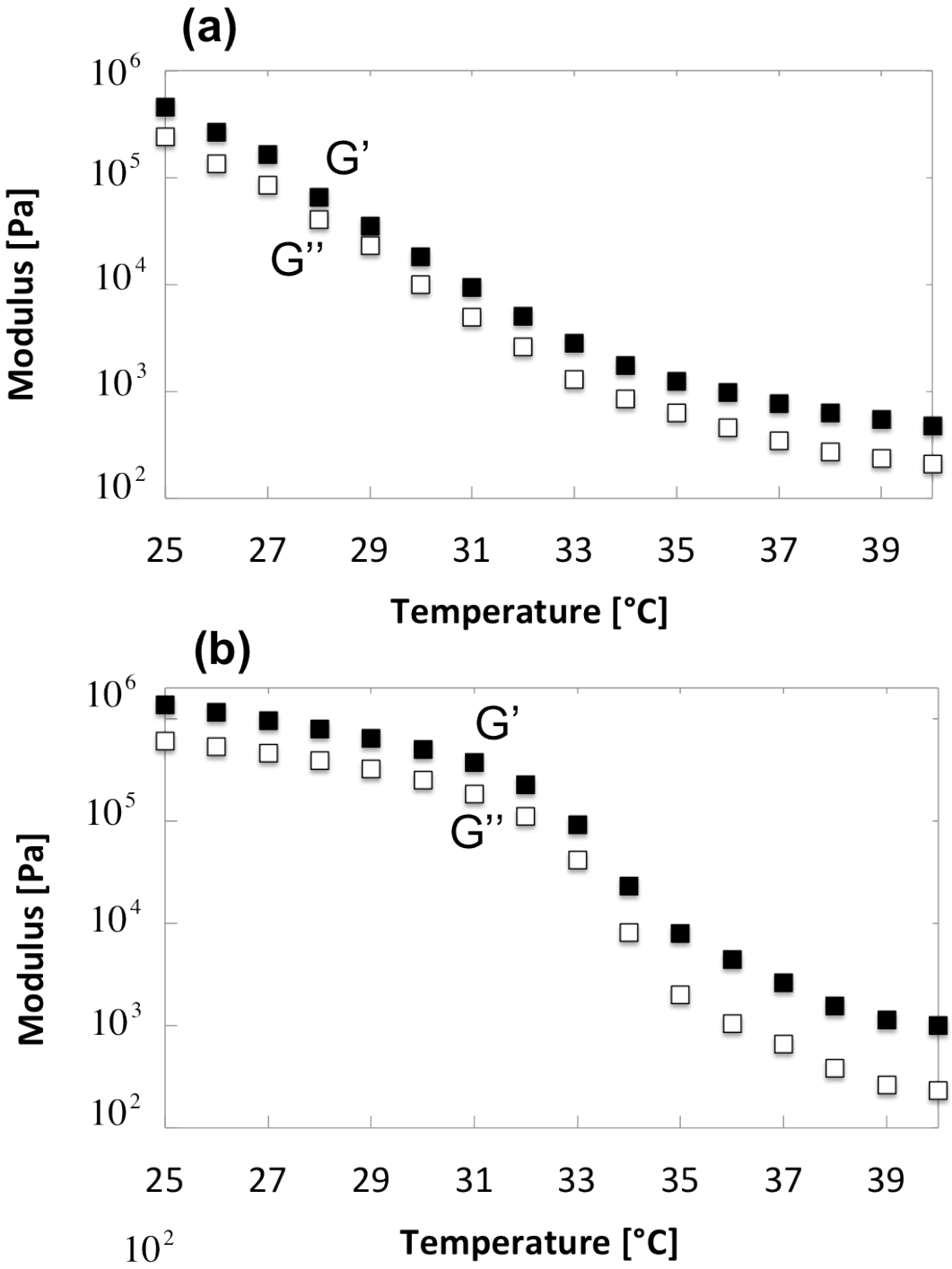

Figure 3.2: Bulk moduli as a function of temperature for pooled bovine-meibomian lipid. The sample was loaded at 25 °C and heated to 40 °C (a) and cooled back to 25 °C (b). Filled symbols represent the elastic modulus, *G'*, and open symbols represent the viscous modulus, *G''*.

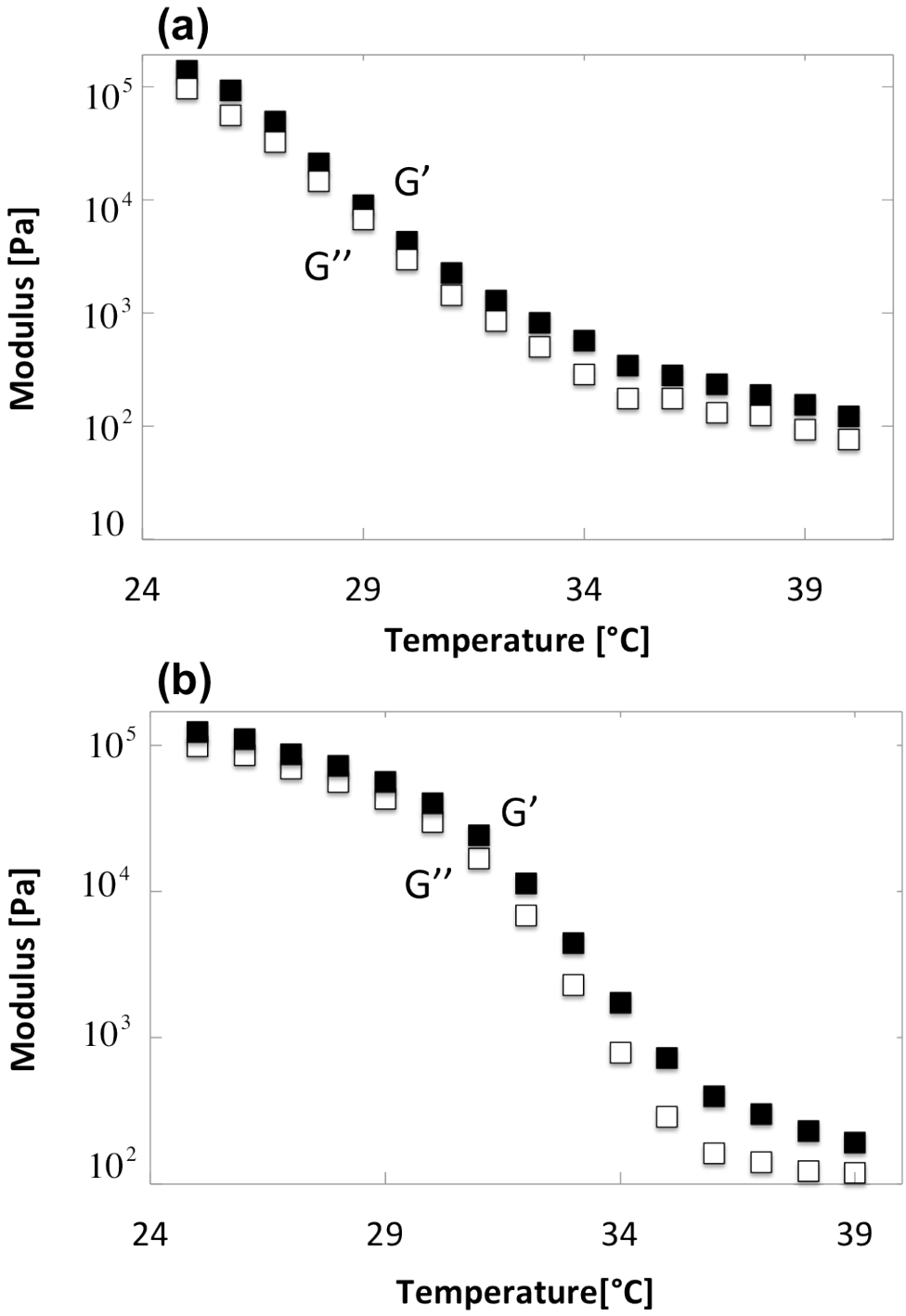

Figure 3.3: Bulk moduli as a function of temperature for pooled human-meibomian lipid. The sample was loaded at 25 °C and heated to 40 °C (a) and cooled back to 25 °C (b). Filled symbols represents the elastic modulus, *G'*, and open symbols represent the viscous modulus, *G''*.

Comparison of the two curves reveals that the transition during cooling is sharper than that during heating. Moreover, the temperature range in which the transition occurs, 32-36 °C, is higher in the cooling process than in the heating process, 27-35 °C.

The human-meibum shear rheology in Figure 3.3 displays the same general behavior as that for the bovine meibum. Here too, a phase transition is observed between 29 and 35 °C where the viscous and elastic moduli both decrease by three orders of magnitude. The maximum magnitude of the viscous and elastic moduli is lower than that of bovine meibum but within the same order of magnitude.

Additional temperature sweeps for bovine meibum were performed from 25 to 150 °C and back to 25 °C to reveal the temperature at which the fluid becomes purely viscous (the point at which the elastic modulus cannot be detected). Results are presented in Figure 3.4. They show that the fluid is mostly elastic even at very high temperatures. Only above 140 °C does the fluid become more viscous than elastic. In human meibum, measurements were not performed at temperatures higher than 40 °C due to the small sample size and the difficulty in obtaining signal at high temperature.

The bulk viscosity of meibum as a function of shear rate at various temperatures is presented on log-log scales in Figure 3.5 for bovine meibum and in Figure 3.6 for human meibum. Measured bovine-meibum viscosity is very large, about 10^5 times more viscous than water at 35 °C. It decreases with shear rate even up to 150 °C where the elastic modulus is undetectable. Human-meibum shear viscosity likewise decreases with increasing shear rate. Hence, human and bovine meibum are non-Newtonian even when the viscous modulus dominates the elastic modulus.

3.4.3 Small-Angle X-ray Scattering (SAXS)

Small-angle x-ray-scattering spectra of bovine meibum were recorded for 10 individual-animal samples at 5 temperatures between 27 and 40 °C. A representative diffraction pattern is shown in Figure 3.7. Several peaks are detected at different scattering vectors, q. All samples contained at least three lipid phases. Peak A, which has 1st and 2nd order peaks at q of 0.122±0.002 and 0.244±0.003 Å^{-1} (average ± standard deviation of 10 samples), corresponds to a lamellar packing of 51.24±0.54 Å. Peak B, which has 1st and 2nd order peaks at q of 0.062±0.02 and 0.124±0.01 Å^{-1}, corresponds to a lamellar packing of 101.6±0.78 Å. The fact that we observe two peaks with peak q ratios of 2:1 shows that the scattering originates from lamellar-ordered phases. Peak C at q of 0.164±0.025 Å^{-1} corresponds to a packing of 40.27±0.51 Å, and peak D at q of 0.272±0.015 Å^{-1} corresponds to a packing of 23.1±0.46 Å. Peaks A, B, and C were detected in all 10 samples. Peak D was detected in 5 out of 10 samples. Phase A, corresponding to peak A, is referred to as the majority crystallite phase, since its measured intensity is the largest. The temperature dependence of each peak's maximum intensity was extrapolated linearly to zero intensity to reveal the melt temperature. The average melt temperature of the majority crystalline phase (phase A) is 37.4 °C (Figure 3.8(a)). Phase B, with longer lamellar spacing, melted at a lower temperature, 34.3 °C, than that of phase A (Figure 3.8(b)). The two other lamellar phases, C and D, melted at 36.1 and 36.3 °C, respectively. Since peaks C and D melt at the same temperature, we believe that they are from the same lamellar phase. In fact, the 5 samples in which peak D did not appear had lower intensities than the other 5 samples. Since the intensity of peak D is weaker than that of peak C, it is not detected when the total intensity from the sample is weak.

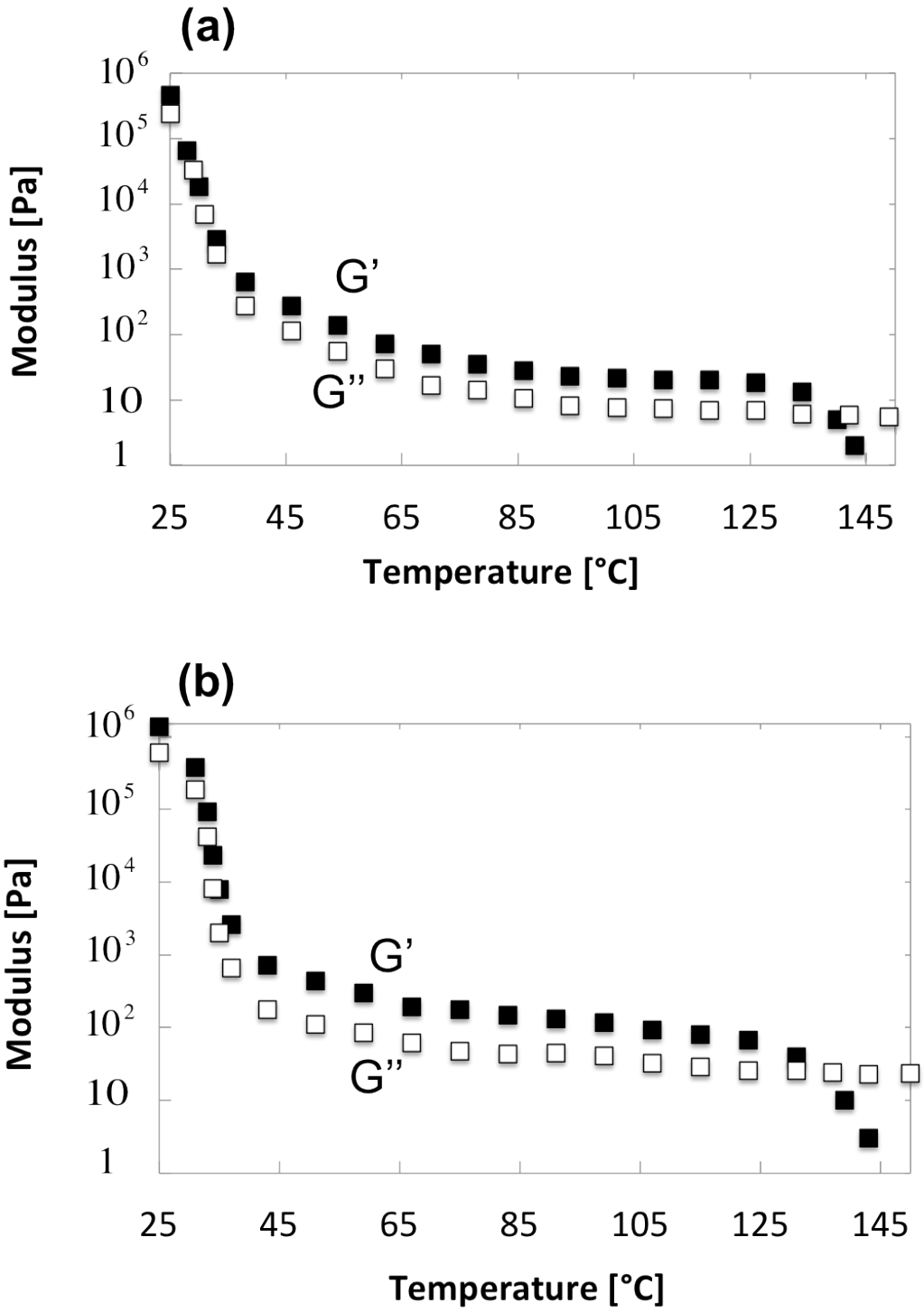

Figure 3.4: Bulk moduli as a function of temperature for pooled bovine-meibomian lipid. The sample was loaded at 25 °C and heated to 150 °C (a) and cooled back to 25 °C (b). Filled symbols represents the elastic modulus, G', and open symbols represent the viscous modulus, G''.

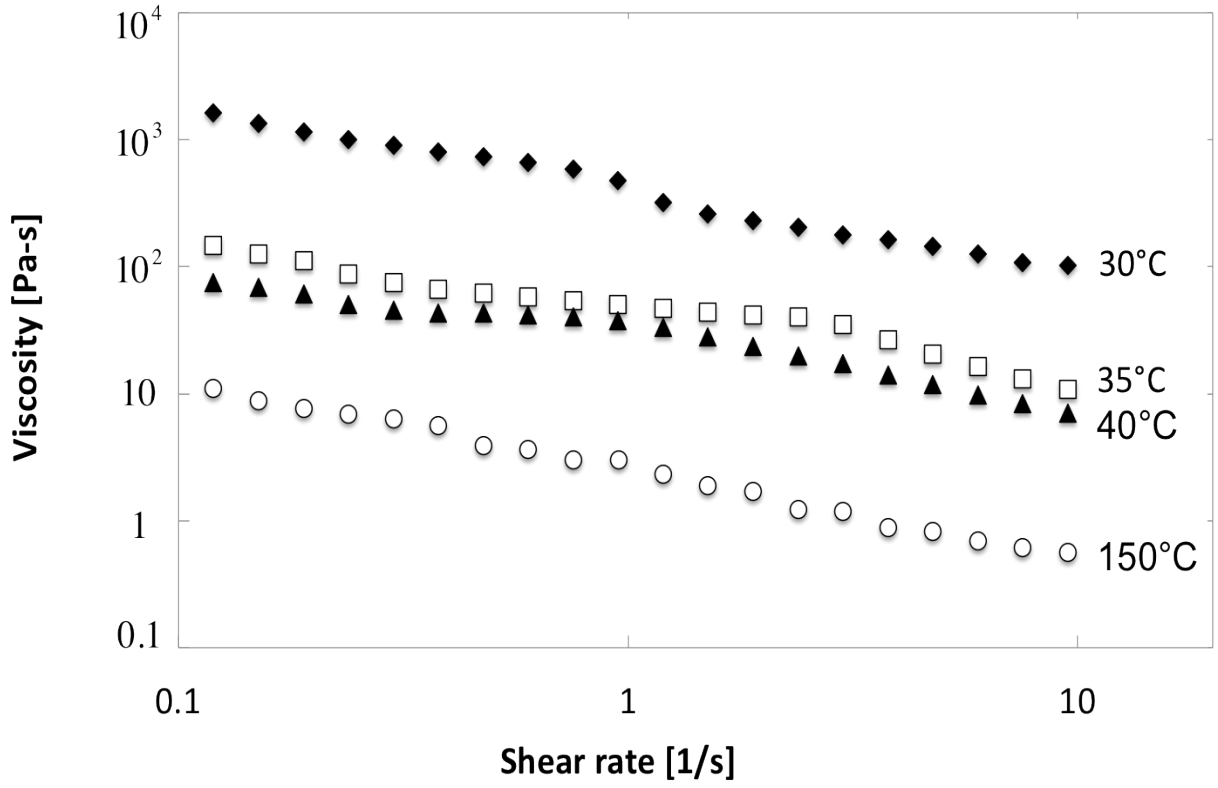

Figure 3.5: Bovine-meibum bulk viscosity as a function of shear rate for various temperatures.

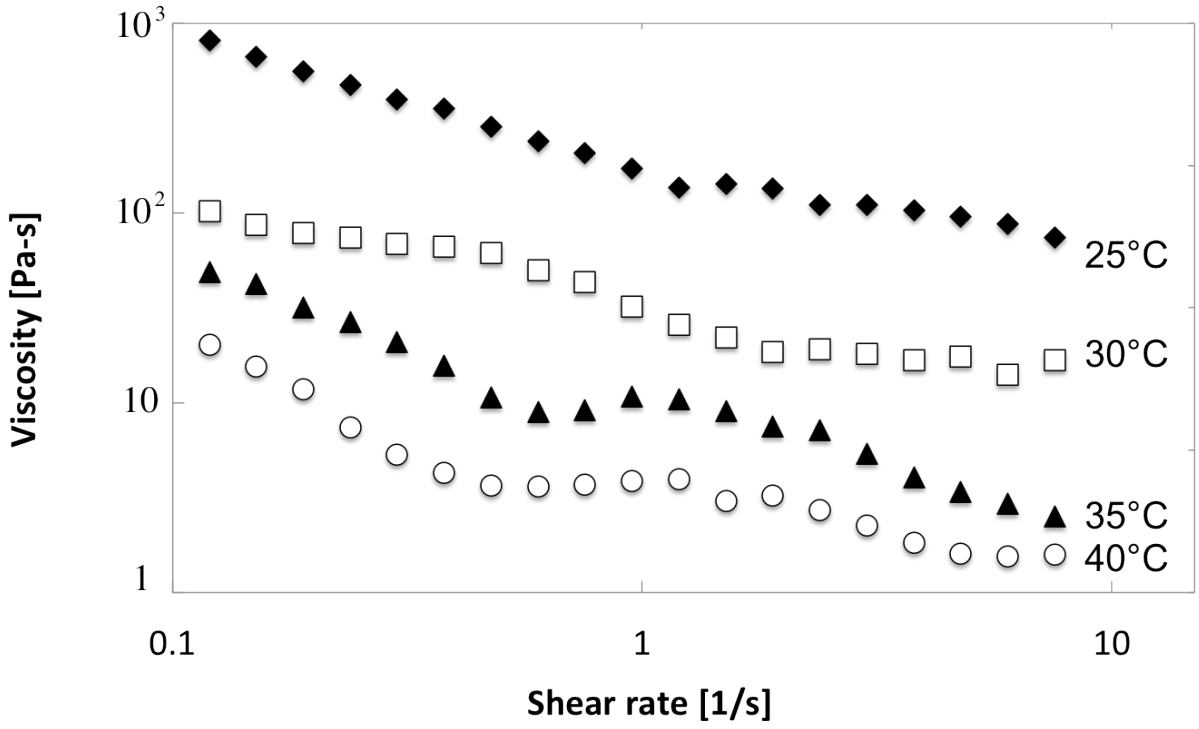

Figure 3.6: Human-meibum bulk viscosity as a function of shear rate for various temperatures.

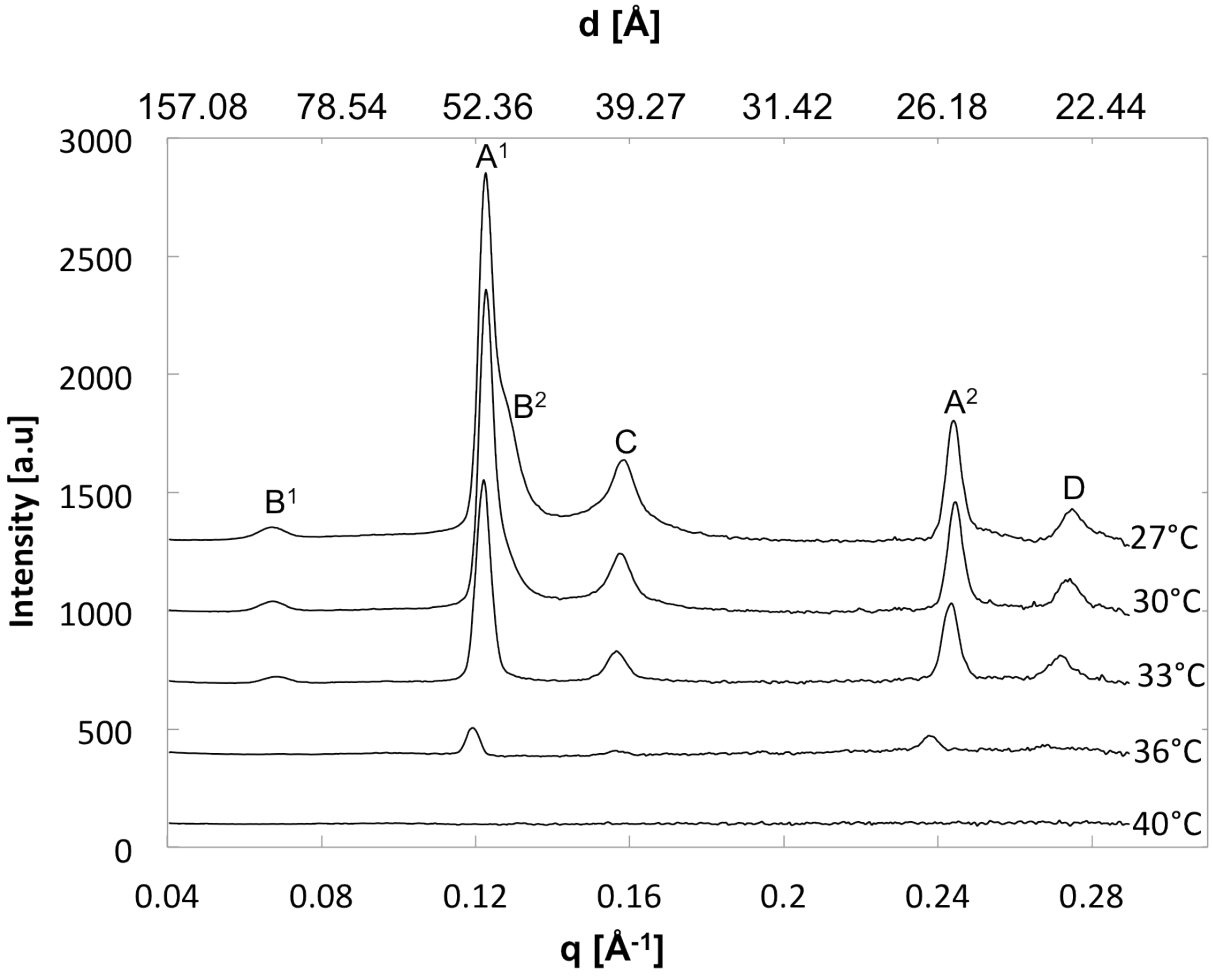

Figure 3.7: SAXS diffraction spectra of bovine meibum containing crystalline structures. Scattering at multiple temperatures between 27 and 40 °C is shown. Peaks representing unique phases are lettered A, B, C, and D while the superscripts above the peak labels denote the order of the peak (1^{st} or 2^{nd}).

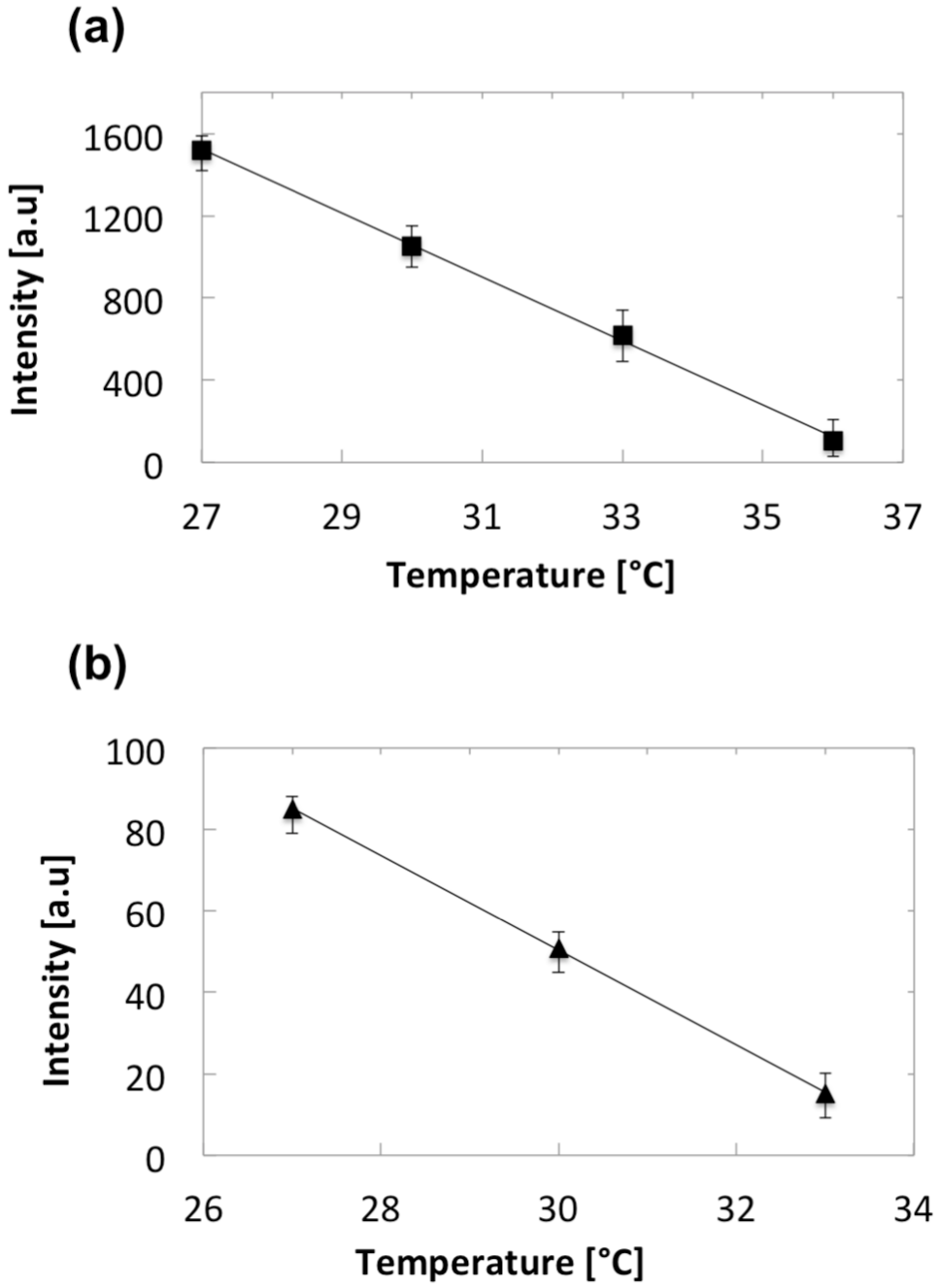

Figure 3.8: (a) Maximum intensity of peak A in Figure 3.7 as a function of temperature with standard deviation of 10 samples. The melt temperature for this peak is 37.4 °C. (b) Maximum intensity of peak B in Figure 3.7 as a function of temperature with standard deviation of 10 samples. The melt temperature for this peak is 34.32 °C. The intensity of both peaks decreases linearly with temperature as the crystallites melt.

3.4.4 Wide-Angle X-ray Scattering (WAXS)

Wide-angle x-ray-scattering spectra were recorded for 5 individual-animal samples at 11 temperatures between 27 and 145 °C. As illustrated in Figure 3.9, two broad peaks were detected in all samples. Peak E at q of 1.52±0.002 $Å^{-1}$ corresponds to a lamellar packing of 4.13±0.03 Å, and peak F at q of 1.35±0.001 $Å^{-1}$ corresponds to a lamellar packing of 4.64±0.02 Å. With increasing temperature, the phase represented by peak E melts into phase F, raising the intensity of peak F until peak E completely disappears at 34.34±0.3 °C. Because the melt temperatures for WAXS peak E and SAXS peak B in Figure 3.7 are the same, these peaks likely reflect the same material. SAXS peak B corresponds to the lamellar spacing in phase B, whereas WAXS peak E corresponds to the lateral spacing of the polar head groups in this crystalline phase. Due to crystallite melting, Peak F slowly disappears between 36 and 145 °C. Even at 145 °C, however, traces of peak F were detected. The width of peak F was much greater than that of peak E, indicating that peak F represents a maximum intensity of the combined E and F peaks. The temperature dependence of peak E and that of E and F combined is shown in Figure 3.10.

3.4.5 Polarized-Light Microscopy

Micrographs of bovine meibum viewed through cross-polarized light are comprised of dark areas indicating isotropic fluid and bright areas corresponding to optically anisotropic crystal structures. Figure 3.11 gives an I/I_{max} melting curve for a sample of bovine meibum, where I_{max} corresponds to the average brightness of the image at 30 °C. As the temperature increases at 2 °C/min from 30 °C, I/I_{max} decreases because anisotropic crystallites melt. By about 36 or 37 °C, almost all birefringent crystalline material has melted; I/I_{max} asymptotes with further increases in temperature. Samples imaged at temperatures above 37 °C are essentially black with almost no visible features. Upon further heating to 150 °C, no changes are seen in the cross-polarized images.

3.4.6 Differential Scanning Calorimetry

We subjected bovine meibum to differential scanning calorimetry. Two of the meibum samples were from individual animals, and the rest consisted of pooled meibum from multiple animals. There was no qualitative difference between the two sets of samples. Figure 3.12 is a typical heating/cooling scanning curve. Starting at -30 °C, the sample is slowly heated, and an endothermic peak occurs at about 0 °C. A second broader peak appears between 20 and 35 °C corresponding to melting of crystalline meibum, as seen in the SAXS spectra of Figure 3.7. Near 100 °C, several close endothermic peaks appear, followed by larger ones at 125 °C. Upon cooling from 200 °C, no corresponding high-temperature exothermic peaks appear, but a freezing transition is detected between 35 and 20 °C. Reheating of the sample from -30 to 200 °C results only in the broad melting peak near 30 °C. The 0, 100, and 125 °C peaks all disappear after the first heating cycle.

Some meibum samples were first dried in a desiccator for two days at ambient temperature and then scanned as above. Results were similar to those in Figure 3.12 with the notable absence of both the 0 °C and high-temperature peaks. Subsequently, meibum samples were hydrated in the desiccating chamber at approximately 90 % relative humidity for four days. DSC scans demonstrate the reappearance of the peaks at 0 and 100°C, but not that at 125 °C. If we divide the area under the 0 and 100 °C peaks by the enthalpy of water freezing and vaporization, respectively, the corresponding amount of water in the meibum samples is about 1 to 4 wt%.

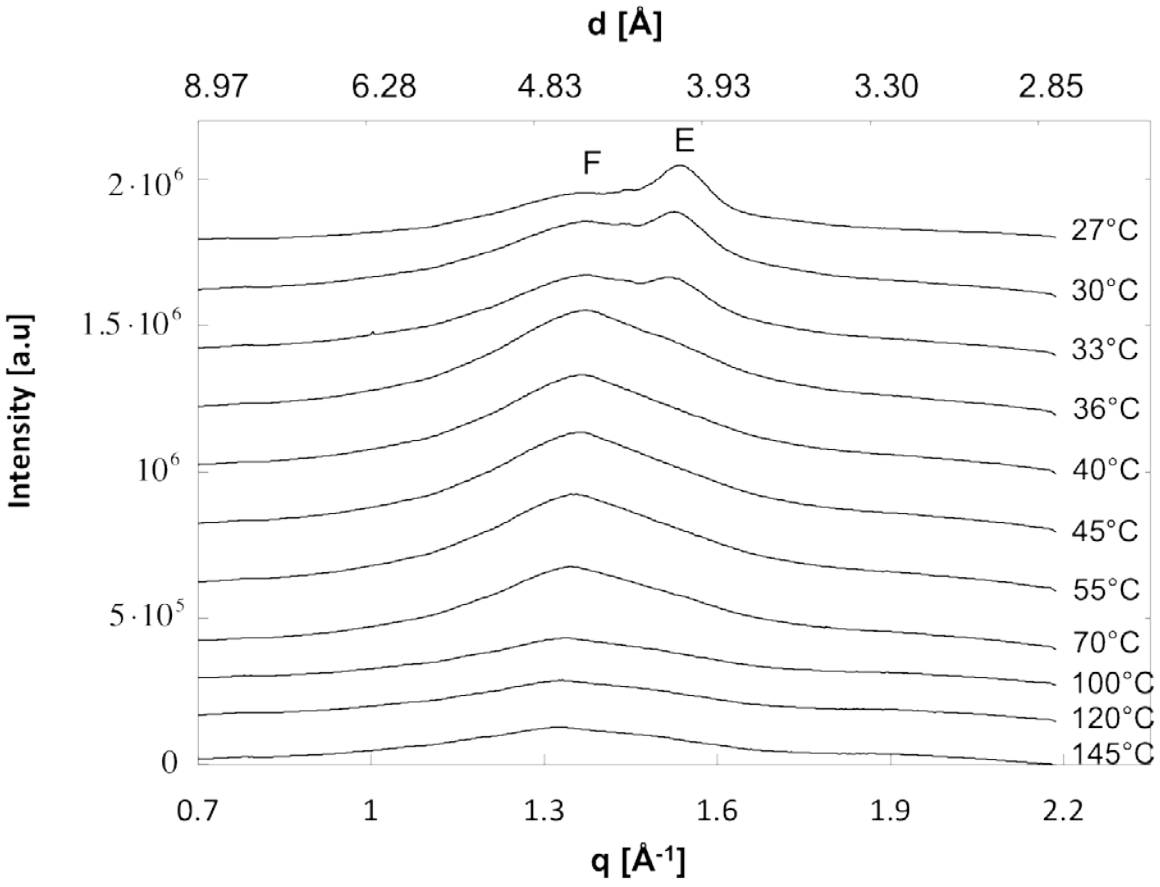

Figure 3.9: WAXS diffraction patterns of a representative bovine-meibomian lipid containing crystalline structures. Scattering at multiple temperatures between 27 and 145°C is shown.

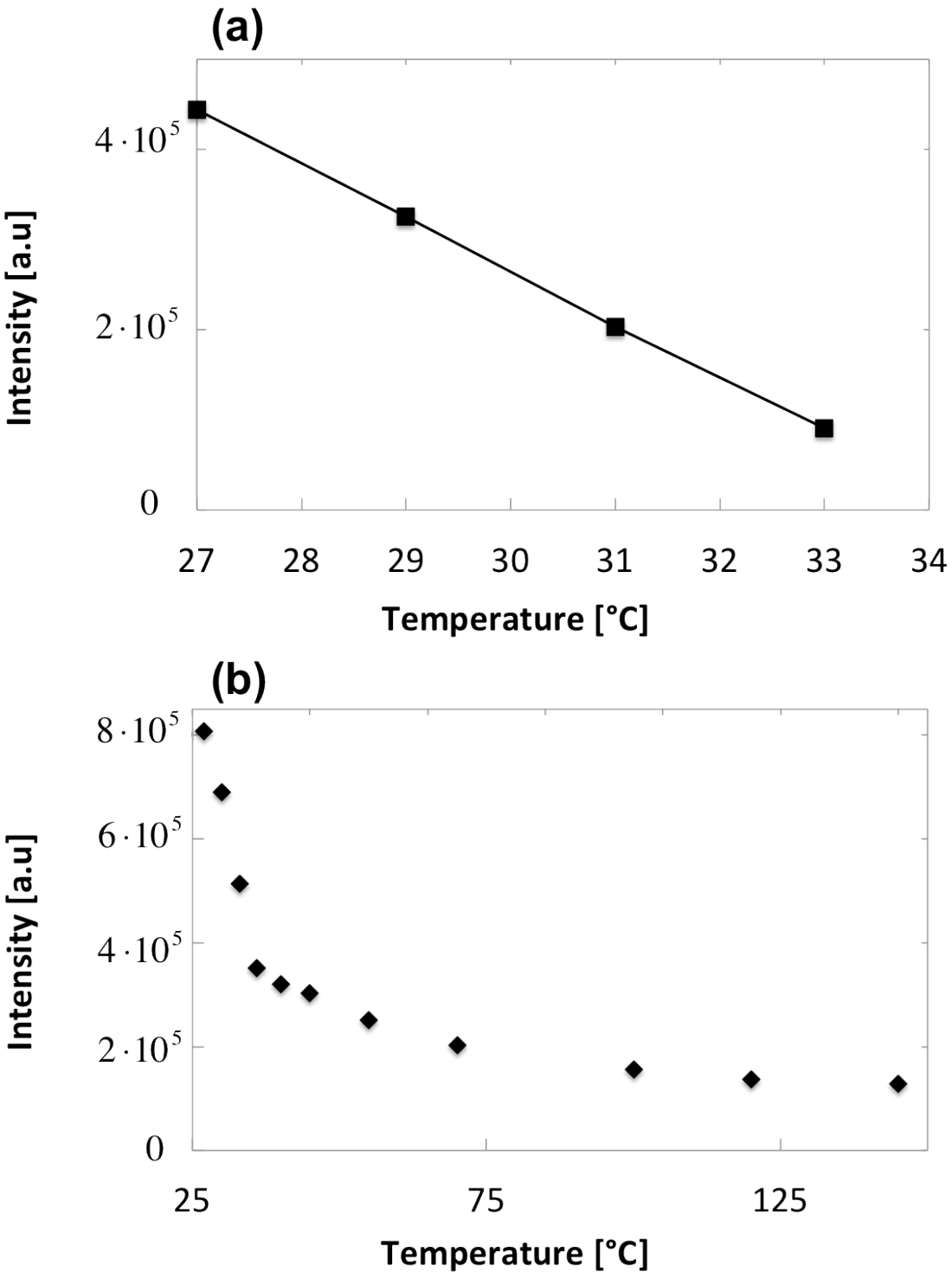

Figure 3.10: (a) Maximum intensity of peak E in Figure 3.9 as a function of temperature. The melt temperature for this peak is 34.34 °C. The intensity of this peak decreases linearly with temperature. (b) Maximum intensity of peaks E+F in Figure 3.9 as a function of temperature.

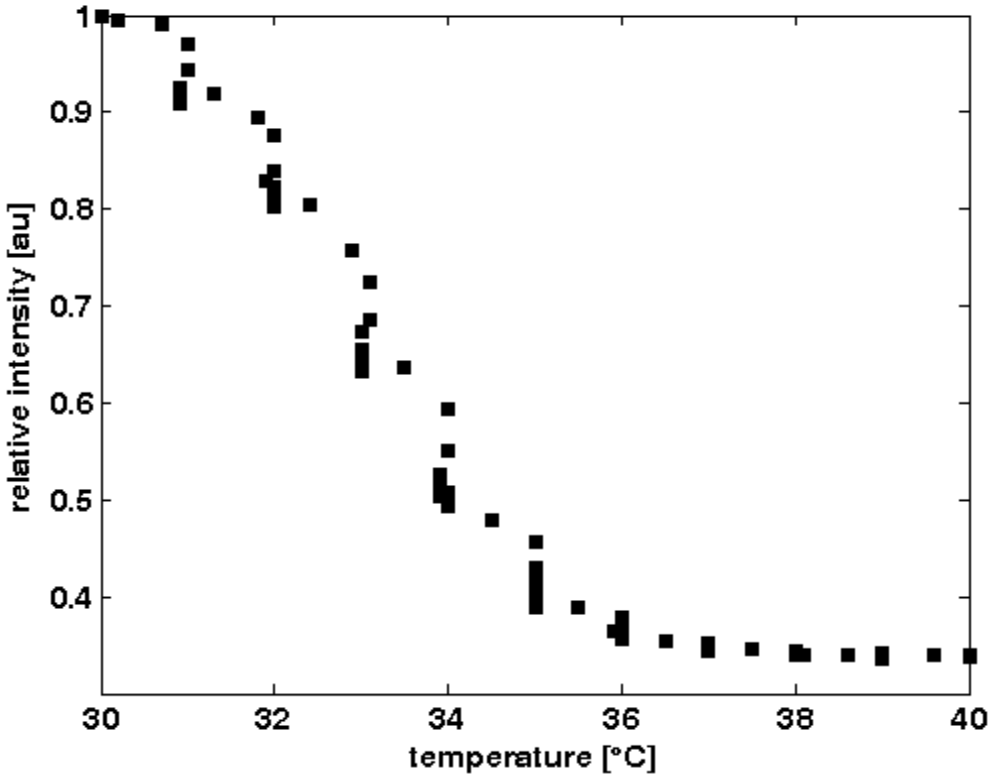

Figure 3.11: Birefrigence melt curve for bovine meibum showing I/I_{max} of micrographs versus temperature.

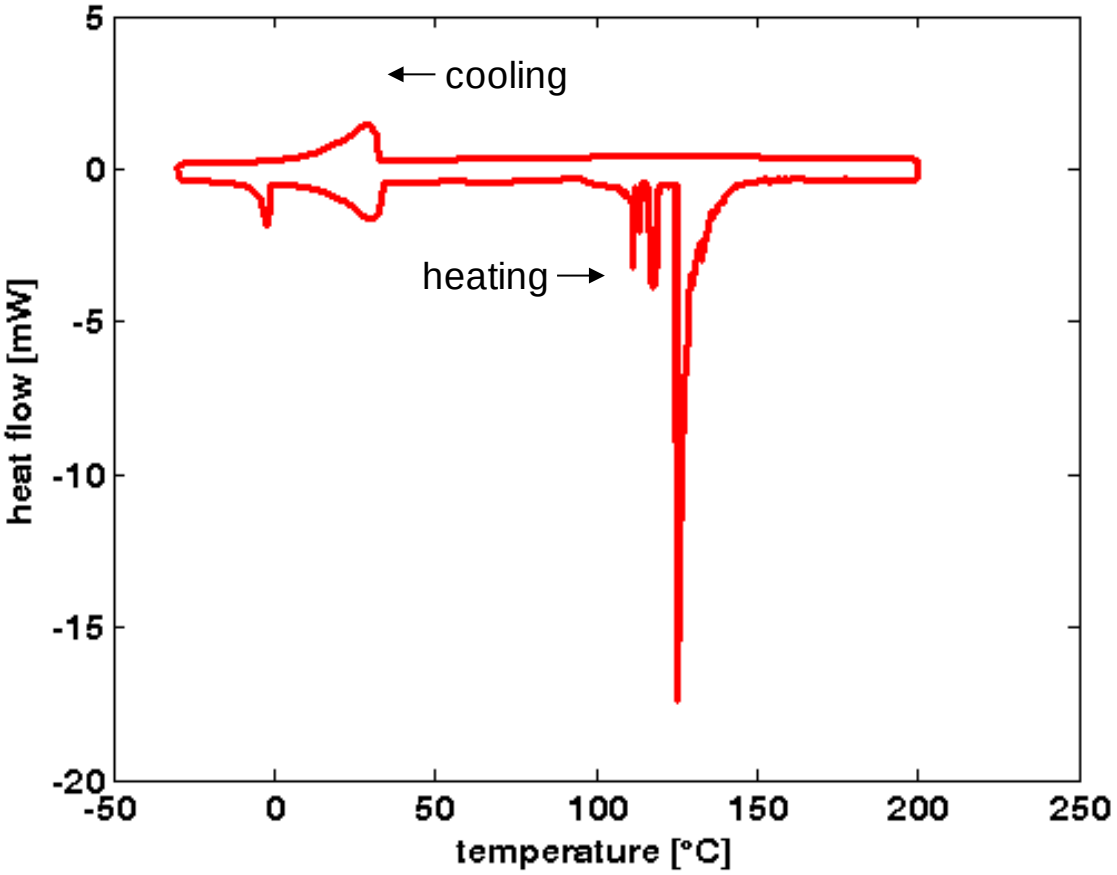

Figure 3.12: DSC heat flow versus temperature for bovine meibum collected from an individual animal. Downward peaks represent heat absorption by the sample (endothermic phase transitions) and upward peaks represent heat released from the sample (exothermic phase transitions). Sample mass is 9.5 mg. As indicated by the horizontal arrows, the lower portion of the curve corresponds to heating the sample from -30 to 200 °C, and the upper portion to cooling from 200 to -30 °C.

3.5 Discussion

Much is known about the chemical composition of human meibum [2, 5-8, 10, 11, 16, 17, 21-24] By comparison, surprisingly little is known about the physical structure of the TFLL and how that structure influences on-eye behavior. Most proposed structures are similar to the sketch of McCulley and Shine [23, 25] shown in Figure 3.13. Here the more polar lipids orient perpendicular to the water/lipid interface akin to surfactants at an oil/water interface. Less-polar lipids organize into several lamellar layers with the least-polar hydrocarbons perpendicularly oriented at the air/lipid interface. If we assume a typical length of 2.5 nm for a lipid molecule and accept Figure 3.13 literally, the thickness of the lipid layer is less than about 10 nm. In contrast to the accumulation of detailed information on the chemical composition of human meibum, the basic lamellar structure suggested by Figure 3.13 remains [8, 26] (see, for example, Figure 1 of the MGD report [8]). The one change in structure now made explicit is that proteins adsorb at the lipid/water interface and possibly intercalate into the remaining lipid layers [2, 8, 27, 28]. A recently proposed TFLL architecture better illustrates the duplex-film thickness of the film, but does not address the physical structure of the lipids within that film [29]. Our proposed picture of the human TFLL contrasts strongly [29] and also with that of McCulley and Shine [23, 25] (Figure 3.13).

Early evidence of the lipid-layer thickness cited interference color patterns observed under white light [30-36], which demands thicknesses near 100 nm. The more in-depth studies of King-Smith *et al.* using *in-situ* interferometry suggest lipid-layer thicknesses between 20 and 160 nm [37]. Even at the smallest cited thickness of 20 nm, the lipid layer is not well represented by a monolayer, but rather by 6 to 10 multilayers. At this thickness, the TFLL is best viewed as a duplex film i.e., an oily layer that is thick enough to exhibit bulk properties with two distinct interfaces [38, 39]. In this scenario, also suggested by Holly [40, 41], the tear-film lipid layer consists of two separate interfaces: air/lipid and water/lipid separated by bulk liquid. A stack of perpendicularly oriented lamellae extending across the entire film is an unlikely bulk structure as it demands an almost a rigid solid [42]. Also, a lamellar-stack structure disagrees with the discrete melting behavior found in our rheologic, scattering, and DSC experiments. As with most duplex films spread at the air/water interface, breakup into nonuniform regions is likely for the thinner lipid layers as has been observed both *in vitro* and *in vivo* for tear-film lipid layers [43, 44]. Lipid-layer breakup, however, is not anticipated in the thicker regions of the rising lipid curtain during initial spreading.

To provide a more complete description of the TFLL, we explored interfacial and bulk rheological and scattering properties of meibum. Because of sample availability, we focused primarily, although not exclusively, on bovine meibum. In addition to compositional similarity with human meibum [16], our experiments show that bovine meibum is both rheologically and structurally similar to human meibum [14]. To within minimal differences, bovine meibum is a useful physical model for human meibum.

Surprisingly few studies are available on the bulk rheology of human meibum. The previous effort of Tiffany and Dart [12] was semi-quantitative and did not examine the roles of shear rate or temperature. More recently, Yokoi *et al.* [45] analyzed the rise kinetics of the human lipid layer after a blink. Based on a simplified analysis, they concluded that the TFLL is elastic and that it drags the underlying viscous tear film upwards as it spreads. Thus, the entire tear film (i.e., tear film plus lipid layer) behaves as if viscoelastic. In our study, the bulk and interfacial rheology are examined over a range of temperatures, oscillatory frequencies, and shear rates. We find that bulk meibum is both viscous and elastic. At 35 °C, the shear viscosity

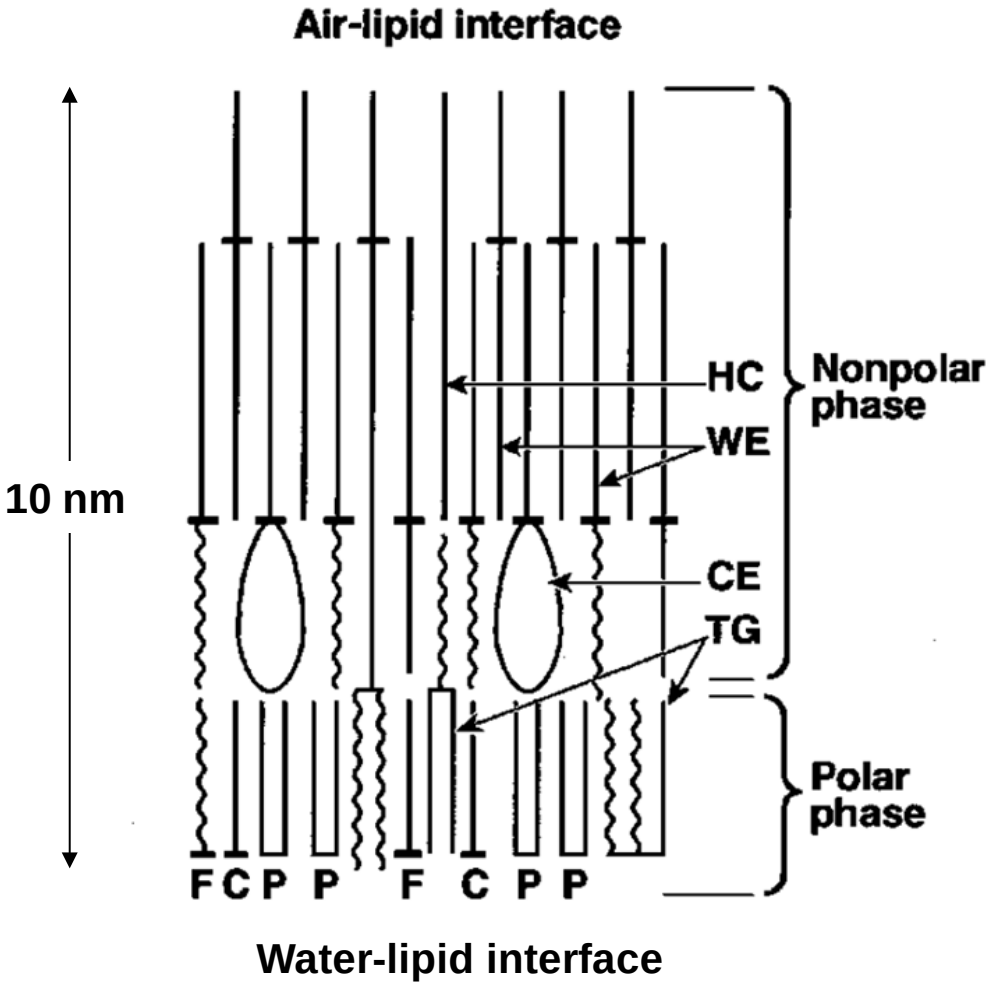

Figure 3.13: Lamellar structure of tear-film lipid layer modified from McCulley and Shine [23] with permission. Symbol key: P = phospholipids, TG = triglycerides, WE = waxy esters, C = cerebrosides, HC = hydrocarbons, F = fatty acids (free), CE = cholesteryl esters.

of bovine and human meibum is about 10^5 larger than that of water and 10 times that of honey [46]. Likewise, bulk meibum is strongly shear thinning even at temperatures up to 150 °C. The large viscosity and dramatic shear thinning indicate that bulk meibum is structured and inhomogeneous.

Bovine and human meibum are also highly elastic with elastic moduli even larger than their viscous moduli. The viscous and elastic moduli of bovine and human meibum are around 10^2 to 10^3 Pa at 35 °C at 1 Hz, which is in between that of ketchup (~50 Pa) [47] and soft-contact-lens materials (10^6 Pa) [48]. Oscillatory rheology shows that meibum remains primarily elastic until 140 °C. This observation is further confirmation of fluid structure even at high temperature. Both steady and oscillatory shear rheology demonstrate a dramatic decline in both meibum viscosity and storage and loss moduli between 30 and 36 °C, suggesting the presence and subsequent melting of crystalline material over that temperature range.

Interfacial rheological properties of the bovine- and human-meibomian lipids also show that meibum is viscoelastic at room temperature. Similar to bulk meibum, the interfacial elastic modulus below 30 °C is larger than the interfacial viscous modulus. The observed enhancement of the elastic and viscous moduli at 23 °C after heating and cooling corresponds with the observation by Mudgil and Millar [49], who reported that cooling enhances the surfactant properties of meibomian lipids. Again similar to bulk meibum, there is a melting transition near 30 °C at which both interfacial moduli diminish dramatically. Thus, bulk and interfacial rheology indicate that meibum is viscoelastic and that at ambient temperature crystalline material is present that partially melts near eye temperature. Surprisingly, the fully melted material above 40 °C remains viscoelastic even to high temperature.

X-ray scattering from human and bovine meibum is consonant with the rheological characterization. SAXS spectra demonstrate the presence of lamellar crystalline structures in bulk meibum. One crystal population melts by 34 °C, two more by 36 °C, and the majority crystalline phase by 37 °C. At bovine ocular-surface temperature [50] around 34 to 38 °C, as many as three crystal populations are present. SAXS diffraction of bovine meibum differs only slightly from that of humans [14]. Grazing-incidence x-ray diffraction (GIXD) measurements of human meibum by Leiske *et al.* [51] show the presence of crystalline lamellar regions of lipid even in films only several molecular layers thick spread over water. Based on the similarity between the bulk structure of bovine and human meibum as demonstrated by SAXS and WAXS, we expect multimolecular films of bovine meibum to be structured as well. It is apparent that meibum is structured from a thick bulk-oil film down to films of several molecular layers in thickness.

In addition to the lamellar crystals identified in SAXS as melting by 37 °C, scattering at wide angles (WAXS) demonstrates a broad peak that persists up to 145 °C. The broad nature of this peak indicates that although lipid molecules are ordered, the spacing of that ordering is not conserved and there is a distribution of spacings. Such a distribution suggests that the lipids are in a bulk disordered phase.

The birefringence shown in micrographs with polarized light indicates that the crystalline material in bovine meibum is anisotropic. The birefringence disappears when samples are heated past 37 °C, the same temperature at which the SAXS shows disappearance of the last crystalline material. Thus, all structural evidence obtained in this work agrees that the crystalline material is lamellar in structure. The absence of birefringence above 37°C is consistent with the WAXS spectra indicating a disordered fluid phase.

Thermal analysis of bovine meibum with DSC corroborates the results of SAXS, WAXS, rheology, and light microscopy confirming phase transitions and their reversibility over the temperature range of 20 to 35 °C. The transition region corresponds to the melting/crystallization of the three ordered lamellar phases identified by x-ray scattering. The two thermal peaks detected at 0 and 100 °C, their disappearance upon heating to 200 °C or upon desiccation, and their reappearance upon water-vapor saturation strongly links them to absorbed water that melts and then evaporates during heating. The significant amount of water detected rejects possible sample contamination or adsorbed surface water. Because unstirred meibum reversibly absorbs and desorbs water when in contact with humidified air, dispersed droplets are unlikely. More likely, molecular domains of water may be present in the TFLL, but further research is needed to determine the state of water within the TFLL. The complete loss of meibum elasticity observed at 140 °C (see Figure 3.4a) is not detected in the DSC experiments, suggesting that it is not due to a first-order phase transition. The thermal peak at 125 °C, which does not reappear after heating or upon water-vapor saturation, apparently belongs to an unidentified, relatively low-molecular-weight organic compound.

In Figure 3.14, we propose an alternative schematic of the TFLL based on the experimental structural information gained here. The picture emerging from our study, and illustrated in Figure 3.14, is that of a viscoelastic, shear-thinning duplex fluid film covering the aqueous tear film that is thick enough to consist of two distinct interfaces: lipid/water and lipid/air separated by intervening bulk liquid. In addition to a plethora of lipid chemical molecules present, the TFLL also apparently contains protein [9, 10] and water (not shown in Figure 3.14). At physiologic temperature, 34-35 °C, the bulk liquid is a suspension of lamellar crystallites (gray shading in Figure 3.14) in a continuous fluid (orange shading in Figure 3.14) and is highly viscoelastic and shear-thinning. The presence of lamellar crystals in both bulk samples and thin films of meibum [14, 51] confirm that they are also present in the *in-vivo* tear film. Asymmetric lamellar crystals added to oil mixtures in cosmetics and food emulsions are well known to impart structure reflected in material texture [52-54]. In fact, many of the lipids chemically identified in meibum, including polar lipids, wax esters, triglycerides, and fatty acids are known oil structurants [54]. The lamellar solids in meibum are minority components, yet they impart strong viscoelasticity. This result suggests that they are randomly oriented and highly asymmetric (e.g., needle-like). We have no evidence to support the picture in Figure 3.13 of the lipid layer as an ordered, stacked array of lamellar layers.

The solid lamellar particles (shown gray in Figure 3.14) are dispersed in a continuous liquid phase (seen as orange in Figure 3.14) that exhibits short-range order at physiologic temperature, but is overall disordered. We do not have definite evidence for the detailed molecular structure of the suspending, continuous liquid phase. However, above 37 °C where all crystallites melt, this fluid is viscoelastic and non-Newtonian, although less so than with the crystalline particulates present. The different lamellar crystallites presented in Figure 3.14 refer to the lamellar phases found in bovine meibum. However, due to the similarity between the bulk structure of bovine and human meibum, the proposed model can describe the human TFLL with slight changes in the spacing of the lamellae.

Since hydrocarbons are not surface active at an oil/air interface, no significant segregation in either composition or molecular orientation is expected at the lipid/air interface of the tear-film lipid layer. Conversely, amphiphilic surfactant-like molecules, such as phospholipids, fatty acids, or omega-hydroxy acyl fatty acids, are expected to concentrate and orient at the water/lipid interface of the TFLL. Within a few layers, the molecular-orienting

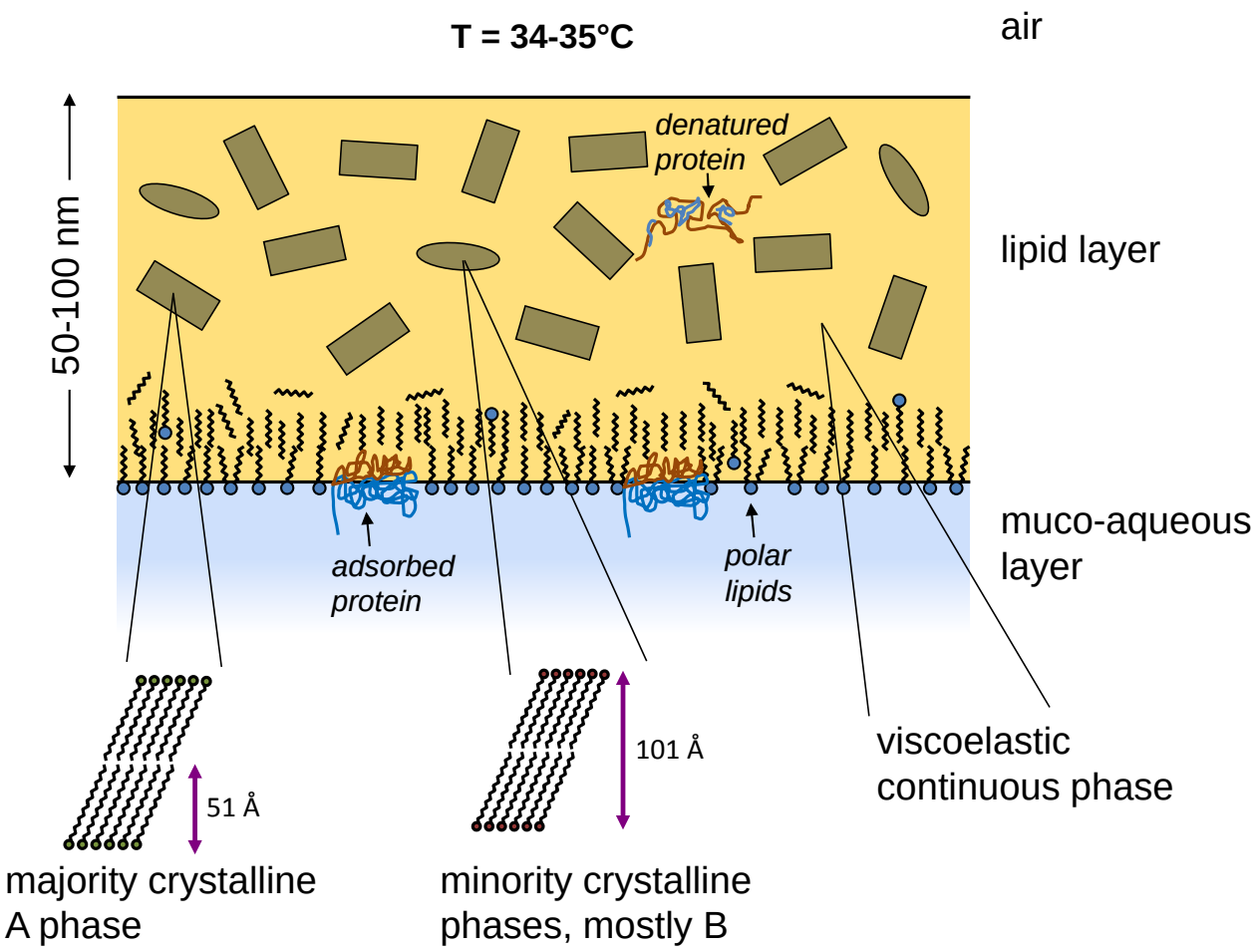

Figure 3.14: Proposed schematic of the tear-film lipid layer. At eye temperature, about 34-35 °C, crystalline phases A-D are dispersed within an isotropic, viscoelastic continuous liquid (orange shading). Solid phase A (gray rectangles) is the majority crystalline phase. Crystallites are presumed highly asymmetric in shape. Polar lipids orient at the aqueous/lipid interface, but orientation does not persist deep into the bulk lipid layer. Proteins may also competitively adsorb at the aqueous/lipid and possibly intercalate. No specific orientation of lipid molecules is expected at the lipid/air interface. Water in the lipid layer is not shown. Drawing is not to scale.

effect of the lipid/water interface is lost. As indicated in Figure 3.14, aqueous protein can also competitively adsorb at this interface and slowly unravel and irreversibly attach [55-58]. Penetration of aqueous protein into the bulk of the tear lipid layer [2, 26, 27, 59, 60] (see for instance Figure 6 of [2]) appears unlikely as no favorable driving force is evident. Protein observed in the chemical makeup of human meibum [9, 10] might arise as detritus from the holocrine cells that produce meibum. However, protein within expelled meibum is likely to be partially denatured and not enzymatically active [8].

The unique temperature dependence of the interfacial and bulk rheological properties of meibum is important to on-eye behavior. In a healthy eye, a smaller viscosity at body temperature facilitates expression from the glands and spreading of fresh lipid onto the tear-film surface. The TFLL is likely comprised of both thick regions (~100-nm) and thinner regions away from the spreading front, possibly down to several monolayers. Thus, both bulk and interfacial rheology are pertinent. During spreading over the aqueous tear film, lipids cool, and their bulk and interfacial elasticity increase. Increased elasticity may enhance the stability of the tear film, protecting against rupture (i.e., formation of black spots). In the thinner regions of the lipid layer, dewetting of the lipid film may occur resulting in lipid lenses interspersed in a monolayer or several-layer-thick oily film at the air/tear interface [43, 44]. Lipid-layer breakup is detrimental because tear evaporation through the resulting thin monolayer regions is likely enhanced compared to that through the thicker regions of the lipid film. Cooling of the spreading lipid layer greatly increases its viscoelasticity, protecting against lipid-layer dewetting.

There is, thus, a delicate balance between lipid fluidity and structure necessary to enable uniform spreading over the tear film and also to resist dewetting of both the tear film and lipid layer itself. Accordingly, small changes in meibum melt temperature could detrimentally influence both lipid secretion and lipid-layer performance, raising important questions about the connection between meibum chemical composition and lipid-layer mechanical behavior on eye, especially for dry-eye and meibomian-gland-disease (MGD) subjects. Our proposed lipid-layer structure in Figure 3.14 provides a new paradigm for understanding the human TFLL, but one that requires additional experimental verification and amplification.

3.6 Acknowledgements

The authors thank Alcon Research Ltd. for partial funding, Dr. Michelle Senchyna for collection of human-meibum samples, Prof. R. Segalman at U.C. Berkeley for use of the DSC and microscope, and John Pople at SLAC for help conducting SAXS and WAXS experiments. Portions of this research were carried out at the Stanford Synchrotron Radiation Lightsource, a Directorate of SLAC National Accelerator Laboratory and an Office of Science User Facility operated for the U.S. Department of Energy Office of Science by Stanford University.

3.7 References

[1] King-Smith PE, Fink B, Hill R, Koelling K, Tiffany JM. The thickness of the tear film. *Curr Eye Res.* 2004;29:357-368.

[2] Butovich IA, Millar TJ, Ham BM. Understanding and analyzing meibomian lipids - a review. *Curr Eye Res.* 2008;33:405-420.

[3] Nagyova B, Tiffany JM. Components responsible for the surface tension of human tears. *Curr Eye Res.* 1999;19:4-11.

[4] The definition and classification of dry eye disease: Report of the definition and classification subcommittee of the international dry eye workshop. *Ocul Surf.* 2007;5:75-92.

[5] Butovich IA. Cholesteryl esters as a depot for very long chain fatty acids in human meibum. *J Lipid Res.* 2009;50:501-513.

[6] Butovich IA, Uchiyama E, McCulley JP. Lipids of human meibum: mass-spectrometric analysis and structural elucidation. *J Lipid Res.* 2007;48:2220-2235.

[7] Chen JZ, Green-Church KB, Nichols KK. Shotgun lipidomic analysis of human meibomian gland secretions with electrospray ionization tandem mass spectrometry. *Invest Ophthalmol Vis Sci.* 2010;51:6220-6231.

[8] Green-Church KB, Butovich I, Willcox M, et al. The international workshop on meibomian gland dysfunction: Report of the subcommittee on tear film lipids and lipid-protein interactions in health and disease. *Invest Ophthalmol Vis Sci.* 2011;52:1979-1993.

[9] Borchman D, Yappert MC, Foulks GN. Changes in human meibum lipid with meibomian gland dysfunction using principal component analysis. *Exp Eye Res.* 2010;91:246-256.

[10] Tsai PS, Evans JE, Green KM, et al. Proteomic analysis of human meibomian gland secretions. *Br J Ophthalmol.* 2006;90:372-377.

[11] Bron AJ, Tiffany JM, Gouveia SM, Yokoi N, Voon LW. Functional aspects of the tear film lipid layer. *Exp Eye Res.* 2004;78:347-360.

[12] Tiffany JM, Dart J. Normal and abnormal functions of the meibomian secretion. *Royal Society Medical International Congress and Symposium Series.* 1981;40:1061-1064.

[13] Borchman D, Foulks GN, Yappert MC, Ho DV. Temperature-induced conformational changes in human tear lipids hydrocarbon chains. *Biopolymers.* 2007;87:124-133.

[14] Leiske DL, Leiske C, Leiske D, et al. Temperature-induced transitions in the structure and interfacial rheology of human meibum. *Biophys J.* 2012;102:369-376.

[15] Leiske DL, Raju SR, Ketelson HA, Millar TJ, Fuller GG. The interfacial viscoelastic properties and structures of human and animal meibomian lipids. *Exp Eye Res.* 2010;90:598-604.

[16] Nicolaides N, Kaitaranta JK, Rawdah TN, Macy JI, Boswell FM, Smith RE. Meibomian gland studies - comparison of steer and human lipids. *Invest Ophthalmol Vis Sci.* 1981;20:522-536.

[17] Nicolaides N, Ruth EC. Unusual fatty-acids in the lipids of steer and human meibomian gland excreta. *Curr Eye Res.* 1982;2:93-98.

[18] Schein OD, Tielsch JM, Munoz B, Bandeen-Roche K, West S. Relation between signs and symptoms of dry eye in the elderly. A population based perspective. *Ophthalmology* 1997; 104:1395-1401.

[19] Brooks CF, Fuller GG, Frank CW, Robertson CR. An interfacial stress rheometer to study rheological transitions in monolayers at the air-water interface. *Langmuir* 1999;15:2450-2459.

[20] Reynaert S, Brooks CF, Moldenaers P, Vermant J, Fuller GG. Analysis of the magnetic rod interfacial stress rheometer. *J Rheol* 2008;52:261-285.

[21] Butovich IA. Lipidomics of human meibomian gland secretions: Chemistry, biophysics, and physiological role of meibomian lipids. *Prog Lipid Res.* 2011;50:278-301.

[22] Butovich IA, Wojtowicz JC, Molai M. Human tear film and meibum. Very long chain wax esters and (o-acyl)-omega-hydroxy fatty acids of meibum. *J Lipid Res.* 2009;50:2471-2485.

[23] McCulley JP, Shine W. A compositional based model for the tear film lipid layer. *Trans Am Ophthalmol Soc.* 1997;95:79-93.

[24] Tiffany JM. Individual variations in human meibomian lipid-composition. *Exp Eye Res. 1*978;27:289-300.

[25] McCulley JP, Shine WE. The lipid layer: The outer surface of the ocular surface tear film. *Biosci Rep.* 2001;21:407-418.

[26] Millar TJ, Tragoulias ST, Anderton PJ, et al. The surface activity of purified ocular mucin at the air-liquid interface and interactions with meibomian lipids. *Cornea.* 2006;25:91-100.

[27] Millar TJ, Mudgil P. Penetration of tear proteins into a meibomian lipid layer. *Invest Ophthalmol Vis Sci.* 2005;46.

[28] Tragoulias ST, Anderton PJ, Dennis GR, Miano F, Millar TJ. Surface pressure measurements of human tears and individual tear film components indicate that proteins are major contributors to the surface pressure. *Cornea.* 2005;24:189-200.

[29] Butovich IA. The meibomian puzzle: Combining pieces together. *Prog Ret Eye Res.* 2009;28:483-498.

[30] Doane MG. An instrument for in vivo tear film interferometry. *Optom Vis Sci.* 1989;66:383-388.

[31] Ehlers N. The precorneal film: Biomicroscopical, histological and chemical investigations. *Acta Ophthalmol.* 1965;1-136.

[32] Fatt I, Weissman BA. *Physiology of the eye: An introduction to the vegetative functions*. 2nd ed. Stoneham, MA: Butterworth-Heinemann; 1992.

[33] Goto E, Dogru M, Kojima T, Tsubota K. Computer-synthesis of an interference color chart of human tear lipid layer, by a colorimetric approach. *Invest Ophthalmol Vis Sci.* 2003;44:4693-4697.

[34] Guillon J-P. Tear film photography and contact lens wear. *Journal of the British Contact Lens Association.* 1982;5:84-87.

[35] Korb DR, Greiner JV, Glonek T, et al. Human and rabbit lipid layer and interference pattern observations. *Lacrimal gland, tear film, and dry eye syndromes 2: Basic science and clinical relevance.* New York: Plenum Press Div Plenum Publishing Corp; 1998:305-308.

[36] McDonald JE. Surface phenomena of tear film. *Am J Ophthalmol.* 1969;67:56-&.

[37] King-Smith PE, Hinel EA, Nichols JJ. Application of a novel interferometric method to investigate the relation between lipid layer thickness and tear film thinning. *Invest Ophthalmol Vis Sci.* 2010;51:2418-2423.

[38] Harkins WD. A general thermodynamic theory of the spreading of liquids to form duplex films and of liquids or solids to form monolayers. *J Chem Phys.* 1941;9:552-568.

[39] Heymann E, Yoffe A. The stability of multimolecular films of hydrocarbon oils, containing spreaders, on water surfaces. *Transactions of the Faraday Society.* 1942;38:408-417.

[40] Holly FJ. Formation and rupture of the tear film. *Exp Eye Res.* 1973;15:515-525.

[41] Holly FJ. Surface chemistry of tear film component analogs. *J. Colloid Interface Sci.* 1974;49:221-231.

[42] Bron AJ, Yokoi N, Georgiev GA, Tifffany JM. The lipid layer forms a semi-rigid carapace over the tear film, following spreading in the interblink. *Invest Ophthalmol Vis Sci.* 2011;52:2096-.

[43] King-Smith PE, Nichols JJ, Braun RJ, Nichols KK. High resolution microscopy of the lipid layer of the tear film. *Ocul Surf.* 2011;9:197-211.

[44] Millar TJ, King-Smith PE. Analysis of comparison of human meibomian lipid films and mixtures with cholesteryl esters in vitro films using high resolution color microscopy. *Invest Ophthalmol Vis Sci.* 2012;53:4710-4719.

[45] Yokoi N, Yamada H, Mizukusa Y, et al. Rheology of tear film lipid layer spread in normal and aqueous tear-deficient dry eyes. *Invest Ophthalmol Vis Sci.* 2008;49:5319-5324.

[46] Rao MA. Rheology of liquid foods – a review. *J Texture Stud.* 1977;8:135-168.

[47] Yilmaz MT, Karaman S, Cankurt H, Kayacier A, Sagdic O. Steady and dynamic oscillatory shear rheological properties of ketchup-processed cheese mixtures: effect of temperature and concentration. *J Food Eng.* 2011;103:197-210.

[48] Kim J, Conway A, Chauhan A. Extended delivery of ophthalmic drugs by silicone hydrogel contact lenses. *Biomaterials.* 2008;29:2259-2269.

[49] Mudgil P, Millar TJ. Surfactant properties of human meibomian lipids. *Invest Ophthalmol Vis Sci.* 2011: 52: 1661-1670.

[50] Stewart M, Stafford KJ, Dowling SK, Schaefer AL, Webster JR. Eye temperature and heart rate variability of calves disbudded with or without local anaesthetic. *Physiol Behav.* 2008;93:789-797.

[51] Leiske DL, Miller CE, Rosenfeld L, et al. Molecular structure of interfacial human meibum films. *Langmuir.* 2012;28:11867-11874.

[52] Floter E, Bot A. Developing products with modified fats. In: Williams C, Buttriss J (eds), *Improving fat content of foods.* Cambridge: Woodhead Publishing; 2006:411-427.

[53] Floter E, van Dujin G. Tran-free fat for use in foods. In: Gunstone F (ed), *Modifying lipids for food use.* Cambridge: Woodhead Publishing; 2006:429-443.

[54] Pernetti M, van Malssen KF, Floter E, Bot A. Structuring of edible oils by alternatives to crystalline fat. *Curr Opin Colloid Interface Sci.* 2007;12:221-231.

[55] Beverung CJ, Radke CJ, Blanch HW. Protein adsorption at the oil/water interface: Characterization of adsorption kinetics by dynamic interfacial tension measurements. *Biophys Chem.* 1999;81:59-80.

[56] Cascao Pereira LG, Hickel A, Radke CJ, Blanch HW. A kinetic model for enzyme interfacial activity and stability: Pa-hydroxynitrile lyase at the diisopropyl ether/water interface. *Biotechnol Bioeng.* 2002;78:595-605.

[57] Hickel A, Radke CJ, Blanch HW. Hydroxynitrile lyase adsorption at liquid/liquid interfaces. *J Mol Catal B-Enzym.* 1998;5:349-354.

[58] Tupy MJ, Blanch HW, Radke CJ. Total internal reflection fluorescence spectrometer to study dynamic adsorption phenomena at liquid/liquid interfaces. *Ind Eng Chem Res.* 1998;37:3159-3168.

[59] Miano F, Calcara M, Millar TJ, Enea V. Insertion of tear proteins into a meibomian lipids film. *Colloid Surf B-Biointerfaces.* 2005;44:49-55.

[60] Mudgil P, Torres M, Millar TJ. Adsorption of lysozyme to phospholipid and meibomian lipid monolayer films. *Colloid Surf B-Biointerfaces.* 2006;48:128-137.

Chapter 4

Evaporation Reduction by Duplex Films: Application to the Human Tear Film

4.1 Abstract

Water-evaporation reduction by duplex-oil films is especially important to understanding the physiology of the human tear film. Secreted lipids, called meibum, form a duplex film that coats the aqueous tear film and purportedly reduces tear evaporation. Lipid-layer deficiency is correlated with the occurrence of dry-eye disease; however, *in-vitro* experiments fail to show water-evaporation reduction by tear-lipid duplex films. We review the available literature on water-evaporation reduction by duplex-oil films and outline the theoretical underpinnings of spreading and evaporation kinetics that govern behavior of these systems. A dissolution-diffusion model unifies the data reported in the literature and identifies dewetting of duplex films into lenses as a key challenge to obtaining significant evaporation reduction.

We develop an improved apparatus for measuring evaporation reduction by duplex-oil films including simultaneous assessment of film coverage, stability, and temperature, all under controlled external mass transfer. New data reported in this study fit into the larger body of work conducted on water-evaporation reduction by duplex-oil films. Duplex-oil films of oxidized mineral oil/mucin (MOx/BSM), human meibum (HM), and bovine meibum (BM) reduce water evaporation by a dissolution-diffusion mechanism, as confirmed by agreement between measurement and theory. The water permeability of oxidized-mineral-oil duplex films agrees with those reported in the literature, after correction for the presence of mucin.

We find that duplex-oil films of bovine and human meibum at physiologic temperature reduce water evaporation only 6-8 % for a 100-nm film thickness pertinent to the human tear film. Comparison to *in-vivo* human tear-evaporation measurements is inconclusive because evaporation from a clean-water surface is not measured and because the mass-transfer resistance is not characterized.

4.2 Introduction

Water evaporation is relevant to countless chemical and biochemical processes. It is a nonequilibrium process whose driving force is the chemical-potential difference between liquid water and water in a sub-saturated vapor environment. Evaporation rate depends on the magnitudes of both the chemical-potential (i.e., concentration) driving force and transport resistances between the water surface and the surrounding gas. Resistances arise from various

mechanisms including: kinetic escape of water molecules to and from the interface, transport through possible layers of immiscible molecules covering the water surface, and convective-diffusion of water vapor through the surrounding gas. There is a rich history on evaporative mass-transfer resistance afforded by insoluble monolayers spread at the air/water surface [1-3]. A lesser studied, but equally important, resistance is the that of liquid duplex-oil films *O*(100 nm – 100 μm in thickness) spread over a water surface. Duplex films are defined as thick enough to display bulk properties with two separate interfaces, but thin enough that the effects of gravity are negligible [4-6].

There are two major applications of evaporation reduction by immiscible-liquid duplex films and, correspondingly, two schools of research. Initial work explored alternatives for surfactant monolayers in slowing evaporation from water reservoirs [5,7,8]. The goal was to reduce water loss over that achieved with surfactant monolayers. Thicker oil films were hypothesized to provide more resistance against evaporation and better structural integrity than those of monolayers [5, 9]. Indeed, duplex-oil films with thicknesses on the order of tens of micrometers reduced water evaporation more effectively than insoluble monolayers, but, in practice, the effectiveness of the films was questionable. Heymann and Yoffe [5] successfully established oil films that remained stable for months under laboratory conditions. With environmental conditions, however, evaporation reduction was compromised by film breakup (into lenses), fracture by wind and dust, and increased water temperature under a film-blanketed surface [10, 11].

More recently, the increasing prevalence of human dry-eye disease [12] spurred study of duplex-oil films in controlling the evaporation rate of water from the lipid-covered human tear film [13, 14]. Water evaporation from the tear film plays a central role in dry eye, which affects up to 30 % of the global population [15]. The human tear film is approximately 5 μm thick [16]. Upon each blink, it coats the surface of the eye and, among other things, helps maintain proper hydration of the ocular epithelial surface, presents a smooth refractive surface for vision, and provides nutrients and cleansing [17]. The majority of the tear film is an aqueous solution containing salts, proteins, and soluble mucins. At the outermost layer of the tear film resides a lipid layer about 100-nm thick, composed of a complex mixture of lipids produced by the meibomian glands embedded in the eyelids. In healthy individuals, blink-secreted lipid, i.e., meibum, spreads upward as a thin-film curtain over the aqueous layer [18, 19]. The lipid layer is thought to function as a barrier against water evaporation from the underlying aqueous portion of the tear film [20-22].

The current paradigm for dry eye holds that increased water evaporation from the tear film through a defective lipid layer increases salinity of the remaining tear film [23-25]. Chronic salty tear triggers an immune response that initiates a vicious cycle of ocular discomfort, inflammation, and damage [12, 25-27]. Clinical observations indicate that dry-eye patients exhibit less uniform tear-film lipid layers (TFLL), lower tear production, increased tear-evaporation rates, and increased tear salinity compared to healthy individuals [12, 23, 24, 28-31]. Although clinical data suggest that the meibum film reduces tear evaporation considerably [20, 21, 32], *in-vitro* experiments with duplex films of tear lipid or similar lipids have so far failed to confirm significant evaporation reduction [13, 14, 33]. Thus, elucidation of the role of the tear-film duplex-lipid layer in water-evaporation reduction can provide both better understanding of dry eye and aid development of care solutions for individuals with compromised lipid layers [34-36].

We first provide a detailed summary of the previous literature on water-evaporation reduction by duplex-oil films. Next, background theory underlying duplex-film spreading and stability is presented. A physically based theoretical model is then outlined to describe water evaporation both from clean surfaces and through duplex-oil films. Importantly, the model addresses the roles of the vapor-phase composition, mass transfer, heat transfer, and film thickness and composition on evaporation rate. Following the theoretical section, an improved method for measuring evaporation reduction is then presented that enables assessment of water-surface temperature, continuous visualization of film coverage, and controlled vapor-phase mass-transfer resistance. New *in-vitro* evaporation results with model films of oxidized mineral oil and of bovine-meibomian lipid demonstrate significant reduction in evaporation by a dissolution-diffusion mechanism for thicknesses ranging between 100 nm and 100 μm. Finally, the significance of these new results to human-tear evaporation and dry eye is discussed.

4.3 Background

Research in water-evaporation reduction by duplex-oil films arises primarily in two different disciplines: physical chemists seeking mechanistic understanding for application to water conservation and vision scientists researching the tear-film lipid layer (TFLL). Motivation, methodology, and analyses are significantly different between the two approaches. Our review is divided into these two categories.

4.3.1 Oil duplex films

In their study of water evaporation through surfactant monolayers, Sebba and Briscoe [7] mention briefly evaporation reduction by duplex films of indicator oil. Indicator oil, first described by Blodgett [37] and later used extensively [7, 8, 38-40], is a mineral oil heated to its smoke point in the presence of oxygen. Oxidation products [41-43], such as fatty acids, alcohols, ketones, and others, render the mineral oil spreadable on water [37]. Without oxidation, mineral-oil films immediately form lenses at the air/water interface. Sebba and Briscoe [7] found that although tightly packed monolayers of long-chain alcohols, such as docosanol (C_{22}), reduce water evaporation by up to 99 %, duplex films of indicator oil evidence a noticeably smaller effect. For duplex-oil films that exhibit colored interference patterns, likely 100 to 200-nm thick, evaporation was reduced by only 3 %. Even films thick enough to be devoid of interference patterns, presumably on the order of microns, showed only a modest reduction of 73 % despite being over 100 molecules thick. These early results, however, are far from conclusive. Film thickness and surface temperature are unknown, spread-film areal coverage and stability are not examined, and measurements report only evaporation reduction. As described in §3.2.1, evaporation reduction depends on the experimental apparatus and on environmental conditions; thus, quantitative comparison among experimenters is not possible. Nevertheless, it is clear that the resistance to water evaporation mustered by a duplex-oil film is not as significant as that expected based on the results of monomolecular films. Still, the experiments of Sebba and Briscoe [7] marked the beginning of a decade of physical-chemistry research into water-evaporation reduction by duplex films.

Also in 1940, Docking *et al.* [9] suggested that duplex-oil films can indeed reduce evaporation by as much as compressed monolayers when they are carefully engineered to spread and remain stable against lens formation. Films consisting of high-molecular-weight polymerized oils dissolved in mineral oil and 1-2 μm in thickness reduced water evaporation by 50-60 % [9]. Additionally, 0.5-1 μm films composed of oil originating from fractions of

vertical-retort tar reduced evaporation by 99 %. Although few experimental details are given, Docking *et al.* [9] noted the importance and difficulty of obtaining uniform, stable films to avoid holes that compromise water-evaporation reduction.

Two years later, Heymann and Yoffe [5] studied the stability of duplex paraffin-oil films containing dissolved "polymerized spreaders." Their films consisted of non-spreading paraffin oil mixed with various amphipathic molecules including carboxylic acids; stand oil; polymerized oleic, ricinoleic, and linoleic acids; and distillation residue from eucalyptus oils. In addition to a comprehensive explanation of oil-film spreading and stability on the water surface, these authors report evaporation reduction by 5 and 10-µm films of a stand oil/mineral oil mixture. For a 5-µm film, evaporation reduction decreased from 80 to 60 % over the course of the experiment, whereas that for a 10-µm film remained relatively constant at 80 %. Measurements of the equilibrium oil/water, water/air, and oil/air interfacial and surface tensions indicated that the studied films have positive initial and negative equilibrium spreading coefficients. Thus, the films were susceptible to dewetting (see §3.1.2), but the "rigidity" [5] of the additive-stabilized films rendered them impervious to lens formation for as long as 18 months. As a result, the films effectively reduced water evaporation over this time period. A physical explanation of "rigidity" does not appear in the article. Apparently, exposure to oxygen causes the added spreaders to polymerize over time [44].

Langmuir and Schaefer in 1943 [8] carefully investigated the role of surfactant monolayers and duplex-oil films in evaporation reduction of water. Duplex-oil films of oxidized turbine oil and Aroclor (a mixture of polychlorinated biphenyls) were spread over water at thicknesses varying from 120 nm to 1 µm in what is now called a "Langmuir trough" with moveable barriers. A desiccant-containing receiving chamber placed 2 mm above the air/water surface absorbed the evaporated water vapor, and was weighed periodically to ascertain the evaporation rate. Careful calibration of the instrument allowed estimation of the gas-phase mass-transfer resistance, as well as the vapor concentration at the air/water and air/desiccant interfaces. No mention was made of any difficulties in obtaining uniform stable films.

Langmuir and Schaefer were apparently the first to suggest that duplex-oil films impede water evaporation by a diffusive mechanism. The resistance of a duplex-oil film to water transport is $R_F = L/Dk$, where L is the film thickness and Dk is the permeability of the oil film to water, i.e., the product of the diffusion coefficient of water in oil, D, and the equilibrium partition coefficient of water in oil, k. Thus, if water has no solubility in the spread oil film, evaporation halts. The experiments of Langmuir and Schaefer [8] exhibited a linear dependence of measured mass-transfer resistance on film thickness, supporting the proposed diffusive mechanism. Film resistance approached zero as the film thickness approached zero, indicating no interfacial resistance at either the water/oil or oil/air interfaces. By fitting their experimental data to theory, Langmuir and Schaefer found permeabilities, Dk, of water in oxidized turbine oil and Aroclor of 2.1×10^{-5} and 3.9×10^{-5} cm^2/s, respectively. It is important to report film water permeability rather than percentage evaporation reduction because Dk is a material property of the film. Conversely, evaporation reduction depends on the specific measurement apparatus and on environmental conditions (see §3.2.1) in addition to film thickness. Similar to Sebba and Briscoe [7], Langmuir and Schaefer discovered that monolayers of tricosanoic acid (C_{23}) at a surface pressure of 55 mN/m exhibit a resistance of 62 s/cm, significantly higher than that of a duplex-oil film 1-µm thick, with a resistance of 5 s/cm. No explanation was offered for this seemingly counterintuitive finding.

In the same year, Powell [45] studied water evaporation through films of mineral oil, vacuum oil, and a mineral oil oxidized during use in steel quenching (referred to as "AO"). Glass dishes containing evaporating water were placed in a wind tunnel at different air speeds directed parallel to the evaporating surface. From the evaporation rate of pure water, the mass-transfer boundary-layer thickness in the air was determined as a function of air speed. Most of Powell's work focused on relatively thick films between 2 and 25-mm thick that strictly lie outside the realm of duplex films. A few thinner films, however, were studied between 280 nm and 70 µm. For films of AO and oxidized vacuum oil, Powell determined the water permeability of both oils at 22 °C as $3x10^{-5}$ cm^2/s, similar to Langmuir's results. At an air speed of 150 cm/s, a 510-nm thick oil film reduced the water-evaporation rate by almost 90 %. Powell mentions that thinner films are difficult to study because they break up into lenses or are blown to one side of the dish. In agreement with the earlier studies of Rideal [2] and Langmuir and Langmuir [46], increasing the air speed reduced the gas-phase mass-transport resistance resulting in greater evaporation reduction. Thus, both oil-film and gas-phase resistances contribute to the overall water-evaporation rate.

In 1948, Gilby and Heymann published a comprehensive study of evaporation reduction by duplex-oil films including the effects of spreader molecules, film thickness, and gas-phase resistance [47]. A battery of evaporation experiments was conducted with films of 2 wt% polymerized spreader mixed with paraffin oil and deposited over a range of thicknesses from 1 to 100 µm. Spreaders were similar to those of Heymann and Yoffe [5]: stand oil, eucalyptus residue, polymerized oleic acid, and linseed oil. To explore the effects of the air environment on evaporation reduction, the authors varied air speed, relative humidity, and ambient pressure. Air flow was directed parallel to the evaporating surface in a laminar wind tunnel over the range 1.6 to 12.9 km/h. To investigate the role of humidity, water was also evaporated from dishes placed in a sealed desiccator containing 96 % sulfuric acid. Additionally, the same desiccator with sulfuric acid was evacuated to 15 mm Hg to eliminate most of the air. Apparently, Gilby and Heymann [47] were the first to observe the films visually during evaporation. They reported nonuniform films at thicknesses less than 10 µm, exhibiting changing interference patterns. Evaporation rates were reported as "relative evaporation resistance," or J_0/J_F, where J_0 is the molar evaporation flux of water from a clean surface and J_F is the corresponding molar evaporation flux of water through an oil film under the same nominal conditions. The authors present a resistance-in-series theory for predicting evaporation rate including an interfacial resistance to evaporation by a structured layer of spreader molecules at the water/oil interface. As with previous theories, no evaporative cooling of the air/water surface was accounted for, which greatly simplifies the expression for J_0/J_F. Unfortunately, the assumption of isothermal evaporation is not accurate.

Gilby and Heymann [47] demonstrated significant evaporation resistance for duplex-oil films containing several different polymerized spreaders under various gas-phase conditions. Reduction of the gas-phase mass-transfer resistance by increasing wind velocity or by applying vacuum increased evaporation reduction. A 5-µm film of eucalyptus oil in paraffin oil reduced water evaporation by 79 % in still air, but by 97 % under a 12.9-km/h wind. For all film thicknesses, flow conditions, and air environments, the magnitude of evaporation reduction depended on the spreader molecule chosen. For films containing 2 wt% spreader, the spreaders listed in the order from most-to-least effective at reducing evaporation were: eucalyptus oil > stand oil > polymerized oleic acid > linseed oil. That evaporation reduction depends on the chemical nature of the spreader supports the authors' claim that the studied spreader molecules

form resistive interfacial films at the water/oil interface. As further proof of this assertion, Gilby and Heymann [47] cite earlier experiments [5] in which after the duplex-oil films retracted into lenses, a visible semi-solid "skin" remained between the lenses that still reduced evaporation substantially. Unfortunately, Gilby and Heymann report only relative humidity and ambient temperature for two experiments, and apparently never measure the water-surface temperature. Because they report only J_0/J_F, calculation of the film and air resistances is not possible, and quantitative comparison to their data is compromised.

Interest in duplex-oil films as evaporation-reducing agents subsided significantly after the 1940s. To our knowledge, only one more paper appeared in the literature. In 1965, Fox [48] reported improved evaporation reduction over the traditional oil-surfactant duplex films by adding wax particles to the oil film. Details of the type of oils, surfactants, and waxes were not included other than that the oil and wax were petroleum based. Temperature or air flow was not listed. According to Fox, films of the oil/wax/surfactant system spread at approximately 1- and 10-µm thickness reduced water evaporation by 46 and 98 %, respectively, for as long as 20 days. A comparable oil-surfactant system without wax particles reduced evaporation by 25 and 82 % at approximately 1- and 10-µm thickness, respectively.

Understanding of water-evaporation reduction by duplex-oil films remains opaque. Only two studies report the relative humidity and ambient temperature. No study measures the water/air surface temperature, which controls the interface vapor pressure and, hence, the evaporation rate. Calculation of the oil-film and air resistances, therefore, is not possible. Except for Langmuir and Schaefer [8] and Powell [45], all investigations give values only for the evaporation ratio J_F/J_0. Accordingly, quantitative comparison among the various studies is also not possible. We re-emphasize the importance of reporting material properties of the coating oil film (i.e., *Dk*) in addition to evaporation reduction. To achieve this task, temperatures of the water/oil and oil/air interfaces must be known.

4.3.2 Lipid duplex films

In the 1960s, vision-science researchers initiated studies of the 100-nm lipid layer, i.e., meibum, spread over the human tear film upon each blink. The goal was to understand the physiologic role that meibum plays in the anterior eye [19, 21, 33, 40, 49]. The lipid layer, a complex viscous mixture of long-chain wax and cholesteryl esters, diesters, triglycerides, and polar lipids with currently over 100 different identified species [50-58], was assumed to reduce tear evaporation significantly [21, 22, 32]. As research began to link increased tear evaporation with dry-eye symptoms [28, 59-67], studies sought to understand how the lipid layer reduces tear evaporation. Lowering tear-evaporation rate, thereby maintaining a thicker tear film, might mitigate dry eye.

Mishima and Maurice [21] and later Iwata *et al.* [32] performed *in-vivo* studies on rabbit eyes verifying that the lipid layer reduces tear-evaporation rate. Mishima and Maurice indirectly measured evaporation by filling the anterior chamber of the rabbit eye with paraffin oil and measuring corneal thinning using pachymetry. By assuming that water lost from the cornea was due only to evaporation, they measured the thinning rates before after the meibomian glands had been cauterized and the ocular surface washed. After this treatment, the corneal thinning rate was about 15 times greater. Following corneal wash, the authors smeared previously collected rabbit meibomian secretion over the cornea and closed the eye. Upon opening the eye, the lipid layer re-formed and corneal thinning subsided. Thinning rates were not reported, but apparently the lipid layer reduced evaporation by a factor of 10 to 20. It remains unclear whether the lipid

layer reformed over an intact tear film or directly over the corneal surface. The study leaves many questions unanswered, but qualitatively validates evaporation reduction by the lipid layer.

Later, Iwata *et al.* [32] affixed a plastic chamber to the cornea of an anesthetized rabbit before and after the lipid layer was removed. In an effort to be quantitative, evaporation rates from the tear film into dry air flowing through the chamber were measured by weighing the amount of moisture extracted from the effluent air by anhydrous $CaCl_2$. Citing Langmuir and Schaefer's work [8], Iwata *et al.* [32] reported mass-transfer resistance in addition to evaporation reduction. By comparing evaporation rates measured with and without the lipid layer present, Iwata *et al.* attributed a mass-transfer resistance of 13 s/cm to the rabbit lipid layer, corresponding to 75 % evaporation reduction in their apparatus. If we assume a lipid-film thickness of 100 nm, this translates into a water permeability in rabbit lipid of 10^{-6} cm^2/s, which is an order of magnitude smaller than that observed for the most impermeable mineral-oil films reported by Langmuir and Schaefer [8]. However, *in-vivo* experimental conditions are difficult to control precisely. To remove the lipid layer, the entire tear film was rinsed with physiologic saline solution, and the cornea was wiped clean with tissue. The rabbit was prevented from blinking, so the thickness and constitution of the lipid-less tear film are likely not those of the native tear film. Additionally, the air-flow rate through the chamber during lipid-less tear evaporation was significantly less than that with the lipid-layer present. Consequently, quantitative reliability of the reported evaporation rates is suspect.

Brown and Dervichian [33] were apparently the first to measure evaporation reduction by human-meibum films *in vitro*. Their experiments were mostly qualitative with few experimental parameters controlled. Human meibum was spread over aqueous saline warmed to 35-40 °C in glass beakers; water mass loss was followed over time. No difference was detected in the evaporation rates among saline-filled beakers with and without spread meibum films, even compared to water in beakers placed in a desiccator. Since the authors placed meibum on the water/air surface until lenses appeared, the film thickness was unknown and nonuniform. Additionally, gas-phase resistance was not ascertained. As a result, the experiments of Brown and Dervichian [33] are inconclusive.

Despite a growing understanding of the role of TFLL in dry-eye disease, subsequent decades focused only on *in-vivo* evaporation rates [20, 28, 59-73]. Tomlinson *et al.* [70] recently reviewed essentially all published studies reporting evaporation rates from human healthy and dry eyes. *In-vivo* tear evaporation is typically measured by one of three methods. Commonly, a sealed goggle is placed over the eye, and the humidity increase of stagnant air in the goggle is measured [63, 72]. A second goggle method measures the humidity gradient between two points near the ocular surface in uncontrolled flow conditions [71]. A few goggle experiments operate under forced-flow conditions [60, 73]. Regardless of the method employed, it is impossible to remove and reconstitute the lipid layer; thus, only comparative evaporation rates are available. Although qualitatively useful for developing correlations between lipid-layer appearance and evaporation rate [20], available *in-vivo* studies are not quantitative. Tear-surface temperature, lipid-layer thickness and coverage, and vapor-phase mass-transfer dynamics are all unknown and can vary significantly among people and between studies.

No fundamental *in-vitro* evaporation-reduction studies appeared until 2009, driven primarily by the desire to produce a palliative for dry-eye sufferers. In early 2009, Borchman *et al.* [13] investigated the possible role of tear-film components on water evaporation determined by mass lost over time. Water evaporated at 25 °C and 40 % relative humidity for most experiments. The surface temperature of the water, which is assuredly cooler than 25 °C, was

not reported. Although numerous proteins, salts, and mucins were mixed with the water to form artificial tear, only those solutions covered by a mimic lipid film showed any effect on evaporation. A 1:1 mixture of palmityl oleate and *n*-tetradecane served as the artificial lipid layer. Evaporation reduction was minimal: an 85-μm lipid film reduced evaporation by only 27 %. Duplex-oil films of palmityl oleate and tetradecane (1:1 vol:vol) have not been previously probed, but available data suggest duplex films this thick should reduce evaporation more drastically [5, 8, 45, 47]. In our experience, stearyl-oleate films mixed with mineral oil initially spread, but rapidly break up into lenses. Unfortunately, no visual examination was performed on the duplex films of Borchman *et al.* during evaporative loss. As Borchman *et al.* note, their films were not uniform during evaporation, resulting in unreliable data.

Later that same year, Herok *et al*. [14] investigated the role of human meibum and meibum mimics in water-evaporation reduction. Meibum was collected from humans, rabbits, and bovines. Mixtures of dipalmitoyl phosphatidylcholine (DPPC) and cholesterol in varying ratios served as meibum mimics. Evaporation was measured gravimetrically by TGA in a ceramic crucible containing water covered by lipid spread from hexane. Air temperature was controlled, and air flow was directed upward around the crucible. Relative humidity was not measured. For human meibum, evaporation reduction increased monotonically from 0 to 7 % as the film thickness increased from 26 nm to 4 μm. Results for rabbit- and bovine-meibum films were nearly identical to those of human-meibum films over the same range of film thickness. Similar to Brown and Dervichian [33], meibum layers did not reduce evaporation significantly, even for thick duplex films. As with Brown and Dervichian [33] and Borchman *et al.* [13], however, no visual examination of the lipid layer during water evaporation was pursued, and no information on water-surface temperature was given.

With the small crucible utilized by Herok *et al.*, water temperature should be close to ambient. From the evaporation rate reported for a clean water surface and an estimated 30 % relative humidity, we calculate a gas-phase mass-transfer coefficient, k_m, of 0.04 cm/s. As discussed later (§4), this means that the gas-phase resistance is much larger than the resistance of the lipid film and likely sets the evaporation rate independent of lipid-film presence. Thus, in addition to likely film dewetting into lenses, the reported evaporation rates are controlled by gas-phase resistances and appear of limited applicability.

Vision scientists have also investigated *in-vitro* evaporation through monolayers of lipid molecules [74, 75] even though the human lipid layer is a duplex film near 100-nm thick, well above the thickness of a monolayer [16, 19, 49, 76-81]. Miano *et al*. [74] found that monolayers of bovine meibum, dipalmitoyl phosphatidylcholine (DPPC), and cholesteryl palmitate spread at surface pressures of ~30 mN/m reduced water evaporation from a pendant drop by 30, 10, and 2 %, respectively. Recently, Rantamäki *et al*. [75] measured evaporation reduction by monolayers of phosphatidylcholine (PC), behenyl alcohol, and behenyl oleate. Although PC had no effect on water evaporation, behenyl alcohol and behenyl oleate monolayers reduced evaporation by 45 and 23 %, respectively. Applicability of these results to the human tear film is limited to possible monolayers present in dewetted areas of the tear-film lipid layer. Whether or not the tear-film lipid layer dewets in healthy subjects is unknown [82].

Lack of *in-vitro* corroboration for water-evaporation reduction by duplex meibum films is surprising. Although meibum is more polar than surfactant-mineral oil systems, meibum is 3-4 orders of magnitude more viscous [83, 84]. Thus, we expect reduced diffusivity of water dissolved in meibum, and hence, reduced evaporation rates, especially for thick meibum films. A rigorous set of *in-vitro* experiments similar to those conducted on petroleum-based duplex

films is requisite. To design a reliable, quantitative experiment requires, first, that the duplex lipid films spread and remain stable over the air/water interface during the period of evaporation.

4.4 Duplex films

A primary challenge for reducing water evaporation with duplex-oil films is achieving a uniform-thickness film that remains stable long enough to affect evaporation rates. The oil layer must initially spread over the aqueous surface into a uniform-thickness duplex film and must resist dewetting over a timescale relevant to evaporation measurement. For large water reservoirs, this timescale may be weeks to months. On the eye, it is seconds since the tear film reforms after each blink. In most laboratory experiments, the oil film must last minutes to hours. Unfortunately, duplex-oil films are unstable and dewet, often rapidly. Therefore, understanding oil-film spreading and dewetting is necessary to engineer duplex films for possible evaporation reduction.

4.4.1 Spreading

Detailed discussions of the thermodynamic theory of spreading (i.e., spontaneous formation of a thin, immiscible, and uniform layer) date back to the early 1900s [4, 5, 85]. We briefly summarize those findings. Consider a macroscopic oil lens initially at the water/air interface as shown in Figure 4.1A. The Helmholtz free energy change, ΔF, for a completely immiscible lens to relax at fixed temperature and lens volume into a slightly more elongated shape illustrated in Figure 4.1B is

$$\Delta F = \gamma_w \Delta A_{wa} + \gamma_o \Delta A_{oa} + \gamma_{ow} \Delta A_{ow} \tag{1}$$

where γ_w, γ_o, and γ_{ow} are the water/air, oil/air, and oil/water surface and interfacial tensions, respectively, and ΔA_{wa}, ΔA_{oa}, and ΔA_{ow} are the respective changes in the water/air, oil/air, and oil/water interfacial areas. For a thin lens with a small lens angle, we approximate that the area changes as $\Delta A_{wa} = \Delta A_{oa} = \Delta A_{ow} = \Delta A$. Consequently, in the limit as $\Delta A \rightarrow 0$, the differential free-energy change is

$$-dF / dA = \gamma_w - \gamma_o - \gamma_{ow} \equiv S \tag{2}$$

where S is defined as the spreading coefficient. If the free energy decreases as the lens elongates, then $S > 0$, and the lens spreads. Conversely, if the free energy increases as the lens expands, $S < 0$, and the oil remains as a lens. Importantly, the interfacial tensions change with time when the oil and water phases are not pre-equilibrated. To reflect this change, initial and final (equilibrium) spreading coefficients, S_0 and S_∞, are distinguished. Whereas the initial spreading coefficient, S_0, may be negative or positive, a large body of experiment and theory shows that the equilibrium spreading coefficient must be less than or equal to zero for any immiscible liquid droplet deposited on water [4, 86, 87]. Fortunately, a positive initial spreading coefficient is often enough to form initially a duplex-oil film.

For pure aliphatic hydrocarbons of molecular weight larger than that of octane, the initial spreading coefficient is negative [88]. Consequently, mineral oils and long-chain hydrocarbons that are typically used as duplex-oil films in evaporation studies do not spread on water, even initially. To obtain a duplex film from these oils, S_0 must be rendered positive. One way to increase S_0 is to dissolve the oil into a volatile solvent with a positive initial spreading coefficient. A thin oil layer is left behind after spreading and solvent evaporation. Unfortunately, the final deposited layer is rarely uniform, unless the oil itself has a positive initial spreading coefficient.

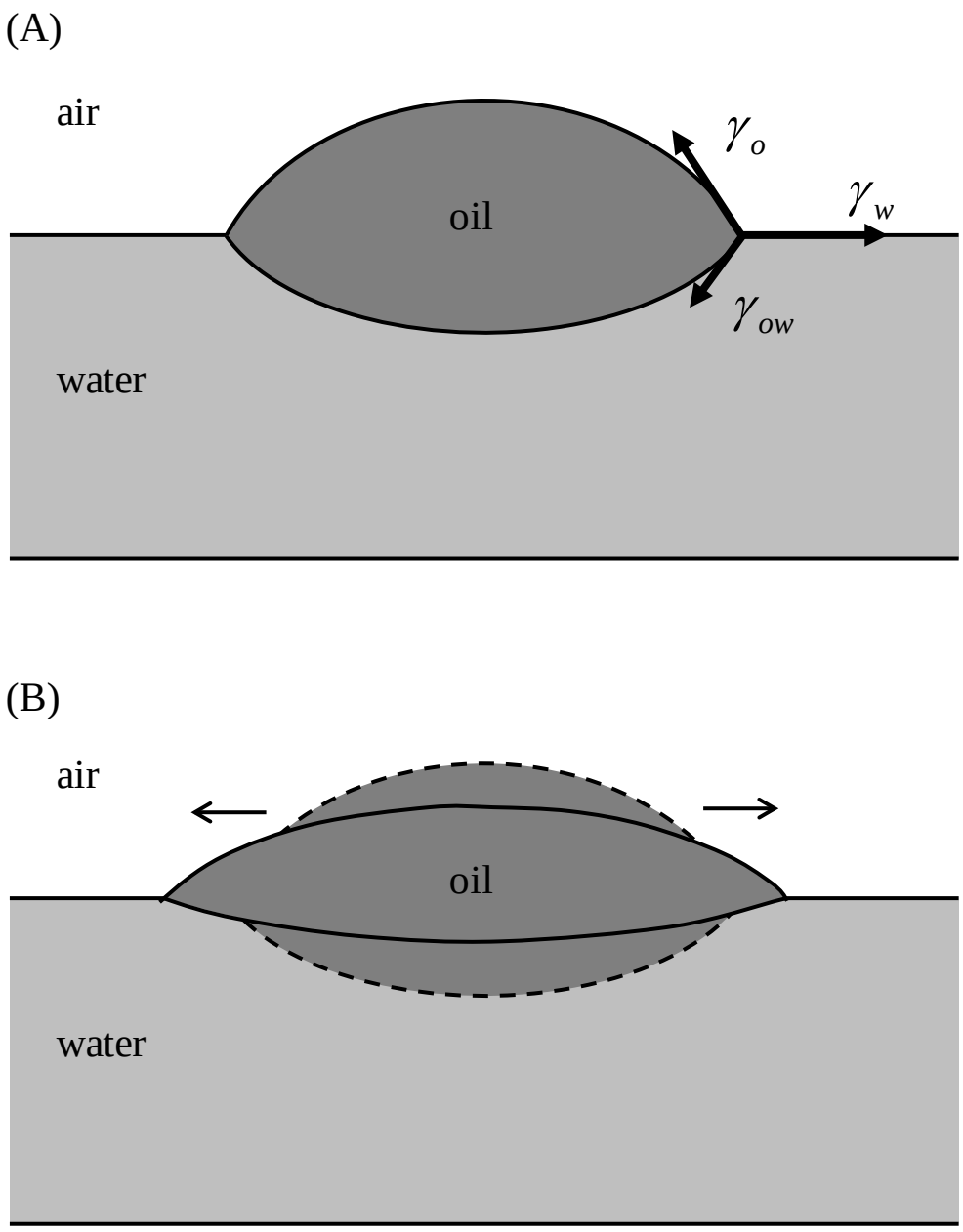

Figure 4.1: Schematic of an oil lens spreading at the water/air interface. The directions of the oil (γ_o) and water (γ_w) surface tensions and the oil/water interfacial tension (γ_{ow}) are shown in (A). Between (A) and (B), the lens elongates during outward relaxation, as indicated by the horizontal arrows.

To induce spreading, small amounts of oil-soluble surfactants, such as fatty acids or fatty alcohols, are dissolved into the oil. Heymann and Yoffe [5] refer to these additives as "spreaders." Water-soluble surfactants are ineffective in this role because they partition predominately into the water phase and lower γ_w, which makes S more negative. Oil-soluble spreaders, however, lower the water/oil tension and the oil/air tension, thereby raising the spreading coefficient. With the appropriate amount of oil-soluble spreader, the initial spreading coefficient is positive, and the oil initially spreads as a duplex film. Unfortunately, spreader molecules soon escape from the spreading oil to adsorb at the water/air interface of the expanding triple line [4, 5]; the water/air surface tension falls. A building water/air surface pressure slows, and eventually stops, the spreading oil film. At equilibrium, spreader molecules partition between the bulk oil and the oil/water, oil/air, and water/air interfaces such that the tension at all interfaces declines. As mentioned previously, for all pure and spreader-containing liquids measured, the equilibrium spreading coefficient is negative. Accordingly, the initially spread oil film subsequently dewets.

4.4.2 Dewetting

Dewetting at the fluid/fluid interface is a kinetic process by which an initially spread, immiscible liquid film rearranges into lenses. An equilibrated duplex-oil film must dewet (i.e., $S_\infty < 0$). The first kinetic step in dewetting is the formation of holes in the film [89, 90]. Once a hole forms, it expands, and others form to collapse the film into rivulets that eventually gather into lenses [89]. We follow Sharma and Ruckenstein [91] to predict the stability of duplex-oil films against hole formation.

Consider a duplex-oil film of initial uniform thickness L_0 on water as shown in Figure 4.2A. If a hole of radius r_0 forms and ruptures the film, then the oil film takes the shape illustrated in Figure 4.2B with thickness L. For holes of radius much smaller than the overall dimension of the film, the change in film thickness is negligible and $L \sim L_0$. The change in free energy corresponding to formation of a hole is then [91, 92]

$$\Delta F = F_{hole} - F_{film} = \left(\frac{1}{2}\tilde{\rho} g L_0^2 + S\right)A_H + \gamma_o\left(A_H + A_1 - A_{H1}\right) + \gamma_{ow}\left(A_H + A_2 - A_{H2}\right) \qquad (3)$$

where $\tilde{\rho} = \rho_o\left(1 - \rho_o/\rho_w\right)$, ρ_o and ρ_w are oil and water densities [kg/m^3], g is the gravitational acceleration constant [m/s^2], $A_H = \pi r_0^2$ is the area of the hole at the air/water interface, A_1 and A_2 are the areas of the oil/air and oil/water surfaces from $r = r_0$ to $r = r_1$ and $r = r_2$, respectively, $A_{H1} = \pi r_1^2$, and $A_{H2} = \pi r_2^2$. Hole radii r_1 and r_2 at the oil/air and oil/water interfaces are labeled in Figure 4.2B. Evaluation of ΔF requires the interface profile, $r(z)$, as described by Equation A.7 in Appendix 4A. Equation 3 accounts for changes in gravitational-potential energy and surface energy, i.e., S. Strictly, duplex-oil films are thin enough for gravity to be negligible. Gravity is included here for completeness. ΔF decreases when S is negative because hole formation becomes favorable by exposing a low-energy water/air interface. Favorable hole formation is counteracted by an increase in free energy due to creation of high-energy oil/air and oil/water interfaces around the hole rim, as well as due to increasing the overall height of the duplex-oil film. Above a critical film thickness, L_c, $\Delta F \geq 0$, and hole formation is unfavorable. With $r(z)$ specified by Equation A.7, evaluation of Equation 3 at $\Delta F = 0$ gives the critical thickness L_c as

$$L_c = r_0 f(\gamma_w, \gamma_o, \gamma_{ow}, g) \qquad (4)$$

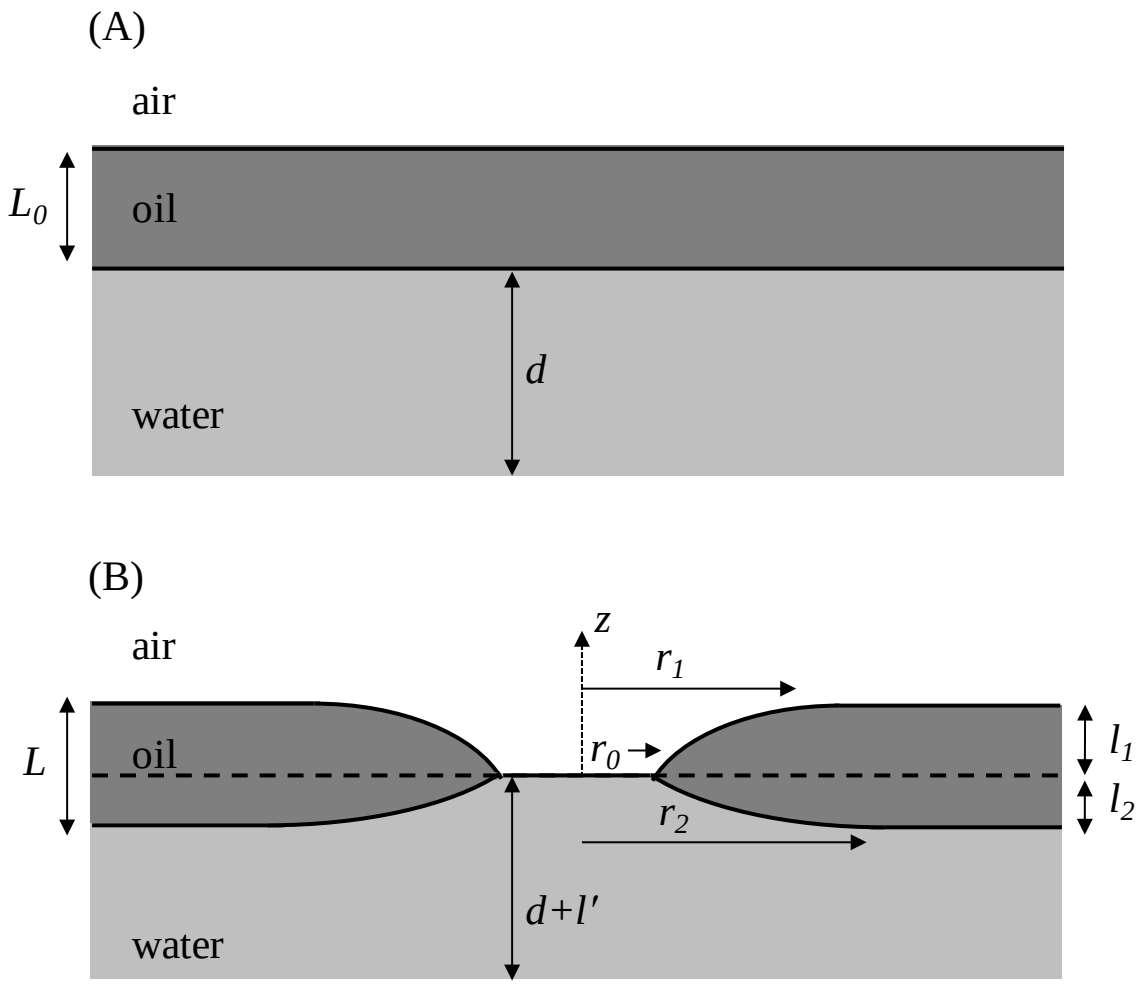

Figure 4.2: Schematic of a duplex-oil film (gravity free) of initial thickness L_0 with $S < 0$ resting on a water substrate of depth d before and $d+l'$ after hole formation. Hole formation exposes water/air surface of area A_H at the expense of oil/air and oil/water surface area, A_1 and A_2. Drawing is not to scale.

where the function f is calculated in Appendix 4A, and takes on values between 0.1-1 for the range of typical surface energies. The critical film thickness, L_c, is directly proportional to the hole radius, r_0; therefore, a film of initial thickness L_0 is unstable to holes of radius r_0 larger than L_0/f and stable to smaller holes. For a duplex-oil film initially covering a water/air area of radius r_A, the largest possible hole radius $r_0 = r_A$. Thus, any film of initial thickness $L_0 < r_A f$ is unstable to hole formation and rupture. Conversely, no holes may form in duplex-oil films of thickness $L_0 > r_A f$, guaranteeing the stability of thick films. For example, the exposed area of the eye has a radius, $r_A \sim 5$ mm; hence, any oily duplex film covering this area and thinner than about 2.5 mm is unstable to rupture into lenses. Since the tear-film lipid layer on the eye is ~100-nm thick, it is unstable to holes of $r_0 > 200$ nm. Hole formation is documented both in the *in-vivo* tear-film lipid layer (TFLL) [82] and in model films of oxidized mineral oil [89]. Measured holes in a TFLL about 50-nm thick were ~1-2 μm in radius [82]; those in a 100-nm thick mineral-oil film were ~100 μm in radius [89]. Such hole radii are consistent with Equation 3 since film thicknesses are well below the critical thickness.

For large holes of radii near 1 cm, the critical film thickness is large enough for the gravitational energy and the spreading coefficient to dominate Equation 3. In this limit, we recover the expression for critical thickness given by Brochard-Wyart *et al*. [90], $L_c = \left(-2S/\tilde{\rho}g\right)^{1/2}$ that ignores the contribution of curvature near the three-phase contact line towards creating high-energy surface area.

Since duplex-film dewetting of a nonvolatile oil appears inevitable, the best scenario is to slow the process. An understanding of the physics underlying dewetting dynamics is, therefore, necessary. Considerable information is available on dewetting of thin liquid films on solid substrates [93]. Unfortunately, the dynamics of dewetting on liquid substrates has attracted far less attention [90, 92, 94]. The physics is similar, except that substrate hydrodynamics can be important. Liquid/liquid dewetting has four stages: initial rupture, hole growth, hole coalescence, and retraction into lenses. The ability of a duplex-oil film to reduce water evaporation is already compromised during the first stages of dewetting when holes begin to form and expand. Attractive Hamaker forces between the oil/air and oil/water interfaces destabilize the thinnest duplex films nearing 100 nm in thickness [90], whereas thicker duplex-oil films apparently destabilize due to contamination by foreign particles such as dust [5]. Once holes form, they expand at a rate that depends on the interfacial tensions and the substrate and film viscosities [90]. The more negative is the spreading coefficient and the less viscous are the fluids, the faster the film dewets. To slow dewetting, spreadable and viscous films must be engineered. Accordingly, Heymann and Yoffe [5] used polymerized spreaders that lowered the final spreading coefficient and increased the film viscosity. In fact, the chosen spreaders apparently solidified over time, allowing films to resist dewetting for months [5]. We consider next water evaporation through duplex-oil films.

4.5 Water evaporation

Evaporation of water is not a simple process. In addition to molecular properties, it depends on water-concentration profiles both in the liquid and in the surrounding vapor. Therefore, evaporation rate depends on system geometry and convective heat and mass transfer in the liquid and vapor phases. Evaporation through a duplex-oil or lipid film is more involved. We consider steady-state water evaporation from a quiescent, locally flat substrate into humid air with known airflow, first for a clean-water surface, and then for a water surface covered with an

oily film of uniform thickness. The resulting analysis predicts the evaporation rate through duplex-oil films. If appropriate temperatures and humidities are measured in addition to the evaporation rate, the model equations provide the desired water permeability of the oily film, *Dk*.

4.5.1 Pure water

Escape of water molecules from a clean surface into pure water vapor occurs via molecular kinetics. Gas-kinetic theory of Hertz and Knudsen (HK) [95, 96] describes the evaporative flux as

$$J_k = \alpha\left(\frac{1}{2\pi M R_g}\right)^{1/2}\left[\frac{P_w^{sat}(T_S)}{T_S^{1/2}} - \frac{P_w}{T_\infty^{1/2}}\right] \tag{5}$$

where J_k is the molecular-kinetic evaporative flux [mol/m^2/s], M is the molar mass of water [g/mol], R_g is the universal gas constant, T_S and T_∞ are the temperatures [K] of the liquid surface and gas far away from the surface, respectively, $P_w^{sat}(T_S)$ is the vapor pressure of water in equilibrium with the water surface at T_S, and P_w is the partial pressure of water vapor in the bulk gas phase. The first term in the brackets on the right of Equation 5 corresponds to evaporation and the second term to condensation. α is an evaporation (or condensation) coefficient indicating that only a fraction of the molecules colliding with the interface evaporate (or condense) and is usually adjusted to give agreement between experiment and theory [97]. Extensions of HK theory account for differences between evaporation and condensation coefficients and for non-equilibrium velocity distributions [98, 99]. When experiments are carefully controlled under vacuum conditions, the evaporation coefficient approaches unity [3, 98, 100, 101].

Upon expressing the vapor partial pressure as concentration by the ideal gas law, HK theory simplifies to

$$J_k = \alpha\left(\frac{R_g}{2\pi M}\right)^{1/2}\left[C_w^{sat}(T_S)T_S^{1/2} - C_{w\infty}^{G}T_\infty^{1/2}\right] \tag{6}$$

where C_w^{sat} is the molar water-vapor concentration in equilibrium with the liquid phase at T_S and $C_{w\infty}^{G}$ is the molar concentration of water in the vapor phase far from the interface at temperature T_∞. If liquid water is in contact with only its own vapor, then the evaporative flux is well-described by Equation 6 [3, 98, 100, 101].

In practice, however, evaporation rates are almost always measured at atmospheric conditions instead of under vacuum. When an evaporating water surface is exposed to air, water molecules must not only escape the surface but also must transport through the air molecules by convective-diffusion as illustrated by the concentration profile in Figure 4.3. Convective-diffusion in the air substantially hinders the evaporation rate. Over the distance λ, where λ is about the mean-free path of molecules escaping from the water/air surface shown in Figure 4.3, water molecules vacate the surface at the rate J_k from Equation 6. The surface temperature, T_S corresponds to an average over this distance. Beyond the interfacial zone ($z > \lambda$), collisions with air molecules demand that water vapor travels by convection or diffusion through the air. Without special precautions to eliminate environmental air currents and temperature gradients, it is difficult to evaporate by molecular diffusion alone. Hence, convective-diffusion must be accounted for.

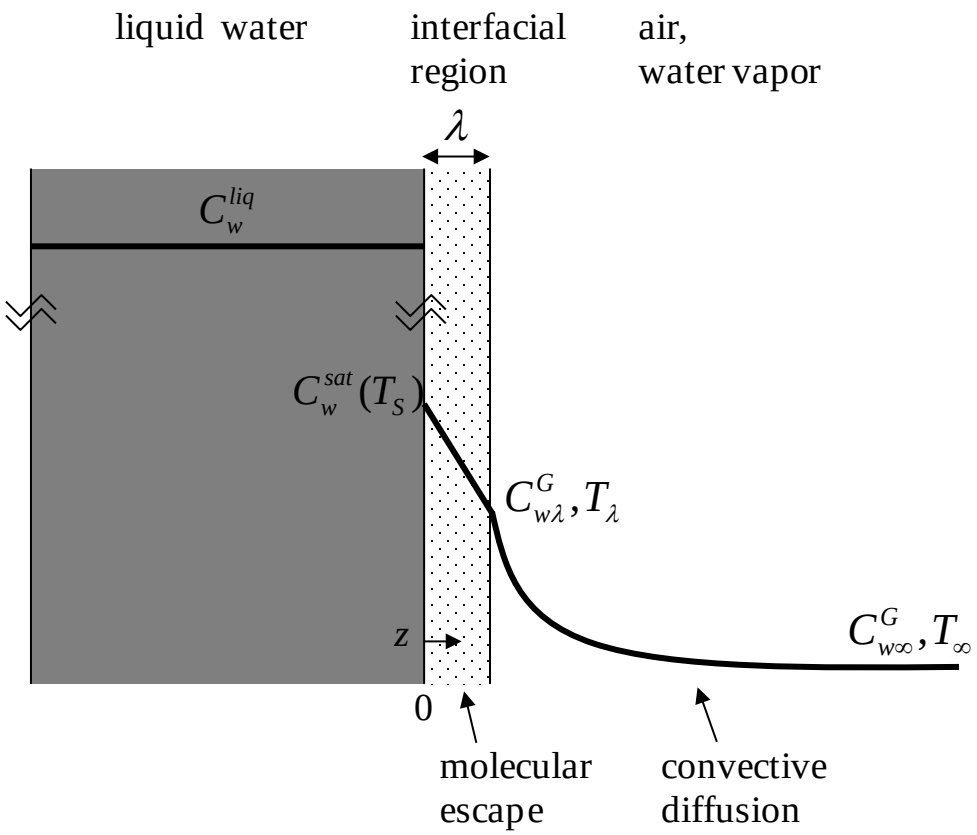

Figure 4.3: Schematic water-concentration profile across a liquid/gas interface during evaporation. There is a discontinuity in concentration at $z = 0$ corresponding to the change in density from liquid to vapor. Within the interfacial region of thickness λ, molecules escape at the kinetic rate. However, to evaporate into the environment, they must convect and diffuse through the air subject to the air flow ($z > \lambda$).

Convective-diffusion mass-transfer flux follows a form analogous to Newton's law of cooling [102, 103]: $J_c = k_m \Delta C$ where k_m is the mass-transfer coefficient of water in the gas phase [m/s] and ΔC is concentration difference driving the evaporative flux

$$J_c = k_m \left(C_{w\lambda}^G - C_{w\infty}^G \right) \tag{7}$$

where $C_{w\lambda}^G$ and $C_{w\infty}^G$ are the water-vapor concentrations [mol/m^3] at $z = \lambda$ and in the environment far from the surface, respectively. When there is gas-phase resistance to water transport, HK theory becomes

$$J_k = \alpha \left(\frac{R_g T_S}{2\pi M} \right)^{1/2} \left[C_w^{sat}(T_S) - C_{w\lambda}^G \right] \tag{8}$$

where T_S is the water temperature at the water/air interface. Equation 8 specifies the rate at which water molecules in the interfacial region escape the surface. Molecules in the surface region are presumed to remain in thermal equilibrium. At steady state, no mass accumulates at the $z = \lambda$ plane. Accordingly, the two fluxes in series J_k and J_c, are equal, giving the overall evaporative flux of water, J as

$$J = J_k = J_c = \frac{\left[C_w^{sat}(T_S) - C_{w\infty}^G(T_\infty) \right]}{R_k + R_m} \tag{9}$$

Thus, J is proportional to the overall concentration driving force between the vapor at the water surface and that in the bulk air, and inversely proportional to the series resistances of molecular-kinetic escape, R_k and convective-diffusion, R_m, defined from Equations 7 and 8, respectively, as

$$R_k = \frac{1}{\alpha} \left(\frac{2\pi M}{R_g T_S} \right)^{1/2} \tag{10}$$

and

$$R_m = 1/k_m \tag{11}$$

The molecular-kinetic resistance for water evaporation is calculated to be ~10^{-4} s/cm from 20-37 °C. The convective mass-transfer resistance depends on the type and magnitude of airflow at the water surface. Expressions for mass-transfer coefficients are well documented for a variety of geometries and gas flows both parallel and perpendicular to the surface [102-105]. The water-vapor mass-transfer coefficient, k_m, typically ranges from roughly 0.5-10 cm/s for air flow both parallel and perpendicular to a flat plate over flow velocities from 0.1 to 10 m/s (Re ~ 300 to 3000). Thus, the practical range of the mass-transfer resistance is approximately R_m ~ 0.1-2 s/cm. Even at the highest value of the mass-transfer coefficient, the ratio of R_k/R_m ~10^{-3}. In completely diffusion-controlled evaporation (i.e., zero air flow), the mass-transfer resistance is even higher than that for convective-controlled mass transfer. Therefore, for most all foreseeable experimental conditions in air, water evaporation is gas-phase mass-transfer controlled. The resistance to kinetic escape from the surface is minimal. Only in a vacuum that eliminates air does the mass-transfer resistance disappear allowing water to evaporate at rates predicted by molecular kinetics [1, 2, 100]. One important exception is evaporation from micrometer-sized or smaller droplets. When the drop radius approaches the mean-free path of molecules in the gas, the kinetic resistance dominates because there is effectively a vacuous shell encompassing the sphere [106, 107]. Consequently, we neglect the molecular-kinetic resistance of the water surface in subsequent discussion.

4.5.2 Duplex-film covered water

4.5.2a Mass conservation

When the water surface is covered by an immiscible duplex-oil film, additional series resistances appear; Equation 9 requires modification. We adopt a one-dimensional mass- and heat-transfer model. Corresponding schematics of water-concentration and temperature profiles are shown in Figure 4.4. The duplex-oil film, of thickness L, is bounded by two interfaces: water/oil and oil/air, with bulk oil in between. Following Langmuir and Schaefer [8], we assume a dissolution-diffusion mechanism to describe water transport through the duplex-oil film. That is, water first dissolves into the oil and then diffuses through the duplex film. Upon neglect of interfacial resistances, Fick's law describes the steady mass flux of water through the oil film:

$$J_F = \frac{D}{L}\left[C_{w0}^F(T_{wo}) - C_{wL}^F(T_{oa})\right] \tag{12}$$

where J_F is the molar water flux [mol/m^2/s], D is the diffusion coefficient of water in the oil [m^2/s], L is the thickness of the oil film [m], and C_{w0}^F and C_{wL}^F are water concentrations [mol/m^3] in the oil film at the water/oil and oil/air interfaces at temperatures T_{wo} and T_{oa}, respectively. In most cases, gas-phase convection is present. The molar flux of water vapor through the air then follows as

$$J_c = k_m\left[C_{wL}^G(T_{oa}) - C_{w\infty}^G(T_\infty)\right] \tag{13}$$

where J_c is the molar flux [mol/m^2/s] of water vapor through the air, k_m is the mass-transfer coefficient of water vapor in air [m/s], and C_{wL}^G and $C_{w\infty}^G$ are the water-vapor concentrations at the oil/air interface and in the environment far from the interface, respectively.

At steady state, the water flux through the bulk oil film and that that through the air are equal. Further, we invoke local phase equilibrium of water at the water/oil and oil/air interfaces. Since water is sparingly soluble in oil, the water partition coefficient between liquid water and oil in Figure 4.4 is conveniently specified as that between pure water vapor equilibrated with pure liquid water and the immiscible oil film or $k_{wo} = C_{w0}^F \big/ C_w^{sat}(T_{wo})$. Likewise, the partition coefficient for water between the oil film and air is written as $k_{oa} = C_{wL}^F \big/ C_{wL}^G$. Since the temperature variation across the duplex-oil film is small, $k_{wo} = k_{oa} = k$. After some algebra, we recover the evaporative flux through a water surface covered with a uniform duplex-oil film and exposed to a water-subsaturated air phase

$$J_F = \frac{C_w^{sat}(T_{wo}) - R_H C_w^{sat}(T_\infty)}{R} \tag{14}$$

where we re-express the concentration of water in the air environment, $C_{w\infty}^G$, in terms of the ambient relative humidity, R_H, and the saturation water-vapor concentration at ambient temperature, $C_w^{sat}(T_\infty)$. As in Equation 9, the overall resistance to evaporation, R, in Equation 14 is the series sum of that due to water diffusion through the duplex-oil film, $R_F = L/Dk$ and that due mass-transfer through the air phase, $R_m = 1/k_m$:

$$R = R_F + R_m = L/Dk + 1/k_m \tag{15}$$

where the product Dk is the permeability of water dissolved in the duplex-oil film. Clearly, thick oil films with low water solubility and small water diffusion coefficients in the oil more effectively reduce the evaporation rate. If there are additional interfacial resistances due, for

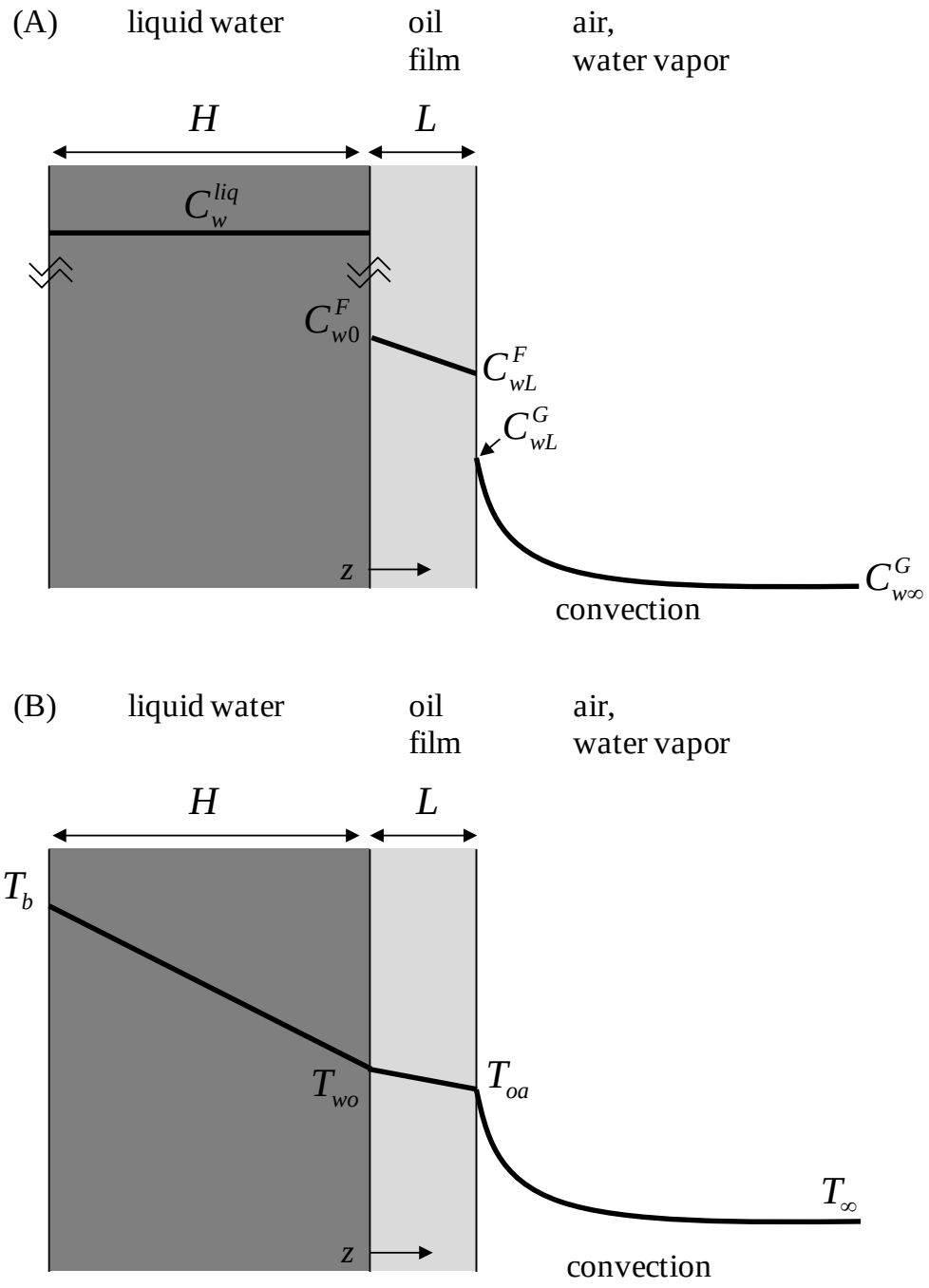

Figure 4.4: Schematic of (A) the concentration and (B) temperature profiles through the water, oil-film, and air phases during steady-state evaporation of water with depth H through a film of thickness L for the water substrate heated from the left at temperature T_b. There are discontinuities in concentration at $z = 0$ and $z = L$ corresponding to the solubility of water in oil.

example, to coherent molecular films at the water/oil or oil/water interfaces, it is customary to add an interfacial resistance [47]

$$R = R_I + R_F + R_m = R_I + L/Dk + 1/k_m \tag{16}$$

where R_I is the mass-transfer resistance of any interfacial molecular film.

Once k_m, humidity, and temperatures are known, Equation 16 provides the basis for assessing the water permeability of the duplex-oil film, Dk, by measuring R as a function of duplex-oil thickness, L [8]. To obtain the air-phase mass-transfer coefficient, k_m, the evaporation rate from a clean-water surface is ascertained. In this case, $R_I = R_F = 0$, and the evaporation rate, J_0, is

$$J_0 = k_m\left[C_w^{sat}(T_{S0}) - R_H C_w^{sat}(T_\infty)\right] \tag{17}$$

where T_{S0} is the steady-state temperature of the water/air interface, commonly referred to as the wet-bulb temperature [102, 103]. Equation 17 is identical to Equation 9 since molecular-kinetic escape from the water surface presents negligible resistance. k_m is established from Equation 17 given measurement of J_0 provided all other quantities are known including the water surface temperature, T_{S0}.

Next, the evaporation rate in the presence of a duplex-oil film, J_F, is measured. Typically, the evaporation ratio is reported i.e., the ratio of water evaporation through a duplex-oil film to that from a clean surface [7, 45]:

$$\frac{J_F}{J_0} = \frac{R_m}{R_I + R_F + R_m}\frac{\left[C_w^{sat}(T_{wo}) - R_H C_w^{sat}(T_\infty)\right]}{\left[C_w^{sat}(T_{S0}) - R_H C_w^{sat}(T_\infty)\right]} \equiv \frac{R_m}{R}\phi \tag{18}$$

Gilby and Heymann [47], however, report the inverse. Evaporation reduction is simply $1 - J_F/J_0$. The first ratio on the right of Equation 18 is the fraction of overall mass-transfer resistance due to gas-phase transport. This fraction depends on physical properties of the duplex-oil film as well as on the apparatus geometry and airflow. The second factor, ϕ, is the ratio of concentration driving forces, $\phi = \Delta C_F / \Delta C_0$, where$\Delta$ C_F is the overall concentration driving force for an oil-coated surface and ΔC_0 is the overall concentration driving force for a clean-water surface. These two driving forces differ because the temperature at the water/oil interface of the duplex-oil film, T_{wo}, is not the same as the wet-bulb temperature of the free water surface, T_{S0}. Thus, ϕ depends on heat and mass-transfer rates and ambient relative humidity and temperature, in addition to film properties. The thicker is the duplex-oil film, the more it reduces evaporation, and the warmer is the water surface. A warmer water/oil interface leads to a larger ΔC_F and, therefore, to a larger ϕ.

Although the evaporation ratio is often reported [5, 7, 9, 32, 45, 47, 48], direct comparison of values derived from Equation 18 between different experimental apparatus and conditions must be done with caution since heat and mass transfer rates vary. For this reason, Langmuir [8] reported the water permeability of the duplex-oil film, Dk, which is a material property of the film oil alone and enables meaningful comparison. Calculation of the oil-film water permeability from Equations 14-18 requires knowledge of the evaporative flux and the concentration driving force. Accordingly, the evaporation rate, water surface temperature, ambient temperature, and relative humidity must all be measured. Thus, to establish Dk, it is also critical to establish T_{wo} and T_{S0}.

4.5.2b Energy conservation

As shown in the schematic temperature profile of Figure 4.4B, the concentration of water vapor in equilibrium with the water/oil interface of the duplex-oil film, $C_w^{sat}(T_{wo})$, appearing in Equation 18, depends on the temperature T_{wo} or, in the case of a clean-water surface, on the temperature T_{S0}. Consider a stagnant water substrate heated from below at temperature T_b at (z = -H) as in Figure 4.4B. Special precautions are necessary to avoid buoyancy-driven convection in the aqueous substrate, as discussed later. With convection eliminated, steady conduction imposes a linear temperature profile through the water substrate with a conductive heat flux, q_s[W/m^2], given by Fourier's law:

$$q_s = \frac{k_s}{H}\left(T_b - T_{wo}\right) \tag{19}$$

where k_s is the thermal conductivity [W/m/K] of the substrate water and H is the substrate thickness [m].

The duplex-oil film is too thin to support natural convection. Thus, conductive heat flux through the film, q_F, is written as

$$q_F = \frac{k_{oil}}{L}\left(T_{wo} - T_{oa}\right) \tag{20}$$

where k_{oil} is the thermal conductivity [W/m/K] of the oil, L is the oil-film thickness [m], and T_{oa} is the temperature at the oil/air interface.

Gas-phase hydrodynamics controls the heat-transfer rate from the oil/air interface:

$$q_c = h\left(T_{oa} - T_\infty\right) \tag{21}$$

where q_c is the heat flux [W/m^2] into the air via convection, h is the convective heat-transfer coefficient [W/m^2/K], and T_∞ is the ambient temperature. The convective heat-transfer coefficient, h, depends on geometry, fluid properties, and air flow rate and direction [102-105].

At the water/oil interface, we demand conservation of energy

$$0 = q_s - q_F - J_F \tilde{H}_S \tag{22}$$

where $\Delta\tilde{H}_S$ is the molar enthalpy of solution [J/mol] for water dissolving into oil at the temperature of the water/oil interface, T_{wo}. Likewise, at the oil/air interface, we write

$$0 = q_F - q_c - J_F \tilde{H}_E \tag{23}$$

where $\Delta\tilde{H}_E$ is the molar enthalpy change [J/mol] between water dissolved in oil and water vapor at the temperature of the oil/air interface, T_{oa}. For thin duplex films with a small temperature difference across the film, sensible heats can be ignored and $\Delta\tilde{H}_S + \Delta\tilde{H}_E = \Delta\tilde{H}_V(T_{wo})$, where $\Delta\tilde{H}_V$ is the latent enthalpy of vaporization of pure water [J/mol] at T_{wo}.

Combination of the heat-flux expressions from Equations 19-21 with the energy balances in Equations 22 and 23 establishes the water/oil interface temperature as

$$T_{wo} = \frac{1}{U_W + U_F}\left(U_W T_b + U_F T_\infty - J_F \Delta\tilde{H}_V(T_{wo})\right) \tag{24}$$

where we define the following heat-transfer coefficients:

$$U_W = \frac{k_w}{H} \tag{25}$$

and

$$U_F = \left(\frac{1}{h} + \frac{L}{k_{oil}} \right)^{-1} \tag{26}$$

As the duplex-oil film thickness increases, the evaporation rate decreases; from Equation 24, and the temperature rises. In practice, the thinness of duplex-oil films guarantees that $T_{wo} \sim T_{oa}$ to within standard measurement precision. Therefore, we refer to T_{wo} as T_{SF} for simplicity. For a clean-water surface, Equation 24 simplifies to

$$T_{S0} = \frac{1}{U_W + h} \left(U_W T_b + h T_\infty - J_0 \Delta \tilde{H}_V (T_{S0}) \right) \tag{27}$$

This temperature corresponds to the highest evaporation rate and, thus, to the lowest surface temperature (i.e., the wet-bulb temperature). Equations 14 and 24 and Equations 17 and 27 are coupled and must be solved simultaneously to predict both the evaporation rate and the surface temperature of film-covered and clean surfaces, respectively.

Importantly, T_{SF} and T_{S0} are not equal unless $J_F \sim J_0$, and evaporation reduction is minimal. Failure to account for evaporative cooling of the water surface leads to inaccurate prediction of evaporation reduction. Most previous studies neglect the effect of surface cooling [7, 13, 14, 33, 47]. In our experiments described later, careful attention is paid to determining T_{SF} and T_{S0}.

The two sets of coupled equations, 14 and 24 and 17 and 27, describe completely the evaporation rates and surface temperatures from clean and duplex-oil-film-covered surfaces once all the parameters are specified. In practice, however, the goal is to obtain the water permeability of the oil film, *Dk*, which is an unknown material property of the covering oil. In a well-defined evaporation experiment, all other parameters in the coupled equations are measured or found in the literature leaving *Dk* as the sole fitting parameter. Measurement of the evaporation rate, surface temperature, and humidity from a clean-water surface supplies the mass-transfer coefficient, k_m, by Equation 17. For impinging-jet flow, the heat transfer coefficient, h, is related to the mass-transfer coefficient by Equation B.7. Water-evaporation measurements through duplex-oil films yield R by Equation 14 when the relative humidity and ambient and surface temperatures are known. Measurement of the evaporation rate through duplex-oil films of various thicknesses enables fitting a straight line to R versus L that provides *Dk* and R_I from Equation 16. Equations 24 and 27 are ancillary to the calculation of *Dk*, but agreement between the measured and predicted values of T_{S0} and T_{SF} confirms the consistency of the experiment and theory.

4.5.2c Nonuniform duplex films covering water

In most studies of evaporation through duplex-oil films, little attention is paid to whether or not the film remains stable and of uniform thickness during the measurement. Here we address briefly the effect of isolated open areas in the film on evaporation rate. Consider a dewetted hole in a duplex film where the underlying water surface is exposed. Most likely, a monolayer (or two) of spreader covers the open hole and reduces evaporation to a certain extent. At most, water evaporates through the hole at the rate of a clean-water surface. Evaporation through a dewetted hole is strictly a two dimensional problem [108, 109]. We adopt a simple 1-D analysis. Water evaporative fluxes through the film-covered and open water surfaces obey the same rate law, but the resistances are different. In the duplex-film-covered surface outside of the dewetted hole, the total mass-transfer resistance is $R_I + R_F + R_m$. Above the dewetted surface, the resistance to evaporation is $R_I + R_m$. Thus, depending on the magnitude of R_F, water evaporates

faster through the clean surface, so that the overall evaporation rate increases even when the hole is small. Assuming independent 1-D concentration profiles and driving forces outlined in §4.2.1, the measured overall evaporation rate, J_{ov}, is predicted by

$$J_{ov} = \alpha_F J_F + (1-\alpha_F) J_0 \tag{28}$$

where α_F is the fraction of the total evaporating surface area covered by uniform duplex-oil film. Equations 14, 17, and 28 specify the measured overall evaporation reduction as

$$\frac{J_{ov}}{J_0} = \alpha_F \frac{R_m}{R_I + R_F + R_m}\phi + (1-\alpha_F)\frac{R_m}{R_I + R_m}\phi \tag{29}$$

The first term on the right of Equation 29 represents the evaporation reduction by the duplex-film-covered portion of the surface, whereas the second term gives the evaporation through the dewetted monolayer-covered regions.

As shown in §4.2.1, the driving force for evaporation is smaller through a clean surface due to evaporative cooling. In the case of a hole, however, the water-surface temperature is unlikely to be lowered to the wet-bulb temperature since the surrounding duplex-film-covered surface is warm. If we assume that the temperature of the water surface in the dewetted hole is close to that of the water/oil interface of the duplex film, then the concentration driving forces are the same for the dewetted hole and the oil-covered surface, and $\phi = 1$ in Equation 29.

Consider for simplicity, a water substrate with $\phi = 1$ covered by a uniform duplex-oil film such that $J_F/J_0 = 0.90$. If 5 % of the oil-film surface area dewets, Equation 29 predicts that $J_{ov}/J_0 = 0.91$, a minimal change. However, for a thicker oil film covering the water surface with $J_F/J_0 = 0.10$ and for the same 5 % extent of dewetting, Equation 29 predicts that $J_{ov}/J_0 = 0.15$. The same dewetted area now causes a 50% increase in measured evaporation ratio giving similar error in the duplex-film water permeability. Thus, the effect of oil-film nonuniformity in evaporation reduction is larger for more impermeable oil films, and can be significant. Langmuir and Schaefer [8] emphasized this effect in mixed monolayers of cetyl alcohol and the more permeable oleic acid. Archer and La Mer [110] documented a similar phenomenon. We later utilize these findings in interpretation of our experimental results.

4.6 Materials and methods

4.6.1 Materials

We measure evaporation reduction through two types of duplex-oil films. The first is an admixture of oxidized light mineral oil (MOx) (8042-47-5, Fisher Scientific, Fair Lawn, NJ) and bovine submaxillary mucin (BSM) (Worthington Biochemical Corp., Lakewood, NJ). We abbreviate this admixture as MOx/BSM. Mineral-oil oxidation was carried out following Blodgett [37]. Viscosity measurements of the oxidized mineral oil were performed on a Physica MCR301 rheometer (Anton-Paar, Ashland, VA) with a 25-mm diameter flat-plate geometry at shear rates between 1 and 10^3 s^{-1} and a 500-μm gap size, giving 63 and 25 mPa·s at 20 and 35 °C, respectively. With the viscosity known, the Siddiqi-Lucas correlation [111] predicts the diffusivity of water in this oil as $9x10^{-7}$ and $2x10^{-6}$ cm^2/s at these two temperatures. Duplex-oil films composed solely of MOx, however, dewet within seconds to minutes and are, thus, not long-lasting enough for measuring evaporation rates. Consequently, we follow the suggestion of Holly [38] and use MOx/BSM admixtures to extend duplex-oil-film lifetime.

To obtain the admixture, a small flake of dry BSM is wetted with a known volume of MOx before each experiment. Although it is difficult to control the exact weight of the BSM flake for each experiment, we set the mass of BSM at approximately 10 % of the oil-droplet

mass. Compared to films of MOx alone, films spread with BSM are noticeably more viscous, and when spread at the air/water interface retain uniformity and resist motion under a light breeze.

In addition to the MOx/BSM films, we employ films of bovine meibum (BM) in evaporation experiments. Whole bovine eyelids were obtained fresh from a local abattoir, transported in sealed bags to the laboratory, and placed into a water bath at 37 °C. Once warmed, bovine meibum is readily expressed from the glands following Nicolaides *et al.* [57]. Meibum from multiple lids was pooled and sealed in an amber glass jar for storage at -20 °C. Although bovine meibum spreads spontaneously on water above about 35 °C, spreading from a volatile, spreadable solvent results in more uniform films. Therefore, before spreading in all evaporation experiments, bovine meibum was first centrifuged, and the supernatant dissolved in a 5:1 (v:v) solution of toluene (108-88-3, >99.8 %, Fisher Scientific, Fair Lawn, NJ) and isopropanol (67-63-0, >99.9 %, EMD Chemicals, Philadelphia, PA). To ensure that solvent, storage process, and pooling play no role, evaporation was also measured through films of fresh, neat bovine meibum. No difference was found.

Human meibum (HM) from healthy human subjects was obtained by expressing the glands and scraping the lid margin with a metal spatula as described by Leiske *et al*. [112] and Rosenfeld *et al*. [83]. Collected material was transferred directly to a glass slide, which was then placed in a sealed amber jar and stored at -20 °C until use. Ethics approval was obtained for collection of human meibum; the procedure followed the guidelines of the Declaration of Helsinki.

The substrate consists of distilled/deionized water with 18.2-MΩ conductivity obtained from a MilliQ^{TM} filtering system (EMD Millipore, Billerica, MA) In some experiments, agarose (Fisher Scientific, Fair Lawn, NJ) and ultrapure water were used to synthesize a 0.5-wt% agarose gel that partially filled the evaporative trough and prevented free convection in the aqueous substrate. Several experiments were performed with various artificial-tear solutions containing salts, proteins, and mucins. Similar to Borchman *et al.* [13], no effect was seen on evaporation rates of pure-water or oil/lipid-covered surfaces.

A large number of chemicals was tested to find a suitable model-oil mixture including wax esters, fatty acids, triglycerides, phospholipids, oil-soluble surfactants, polymers, and oils. High-purity stearyl oleate (17673-49-3,~ 99 %), oleic acid (112-80-1, ~99 %), linseed oil (8001-26-1), dipalmitoyl phosphatidyl choline (DPPC) (63-89-8, >99 %), cholesteryl oleate (303-43-5, >98 %), Brij 30 surfactant (9002-92-0), and cholesterol (57-88-5, >99 %) were purchased from Sigma-Aldrich (St. Louis, MO). Commercial-grade extra virgin olive oil was from Filippo Berio, Italy. Stand oil (Winsor Newton, NJ) was purchased locally. Synthesized polyisobutylene (PIB) with molecular weight 145 kDa (PDI = 1.1) was obtained courtesy of N. Balsara of U.C. Berkeley (Berkeley, CA).

4.6.2 Apparatus

A schematic of the apparatus for measuring evaporation rates through duplex-oil films is shown in Figure 4.5. The system is a miniature Langmuir trough filled with water resting on an analytical balance. Evaporation rates with and without duplex-oil films were obtained gravimetrically by measuring the mass of water remaining in the trough over time.

The custom-built trough was constructed of black Delrin® with a fluid substrate surface area of 20 cm^2 (i.e., 4 x 5 cm) and a depth of 5 mm. Two Teflon® barriers allow compression and expansion of the surface area available to the oil film. The top surface of the trough is

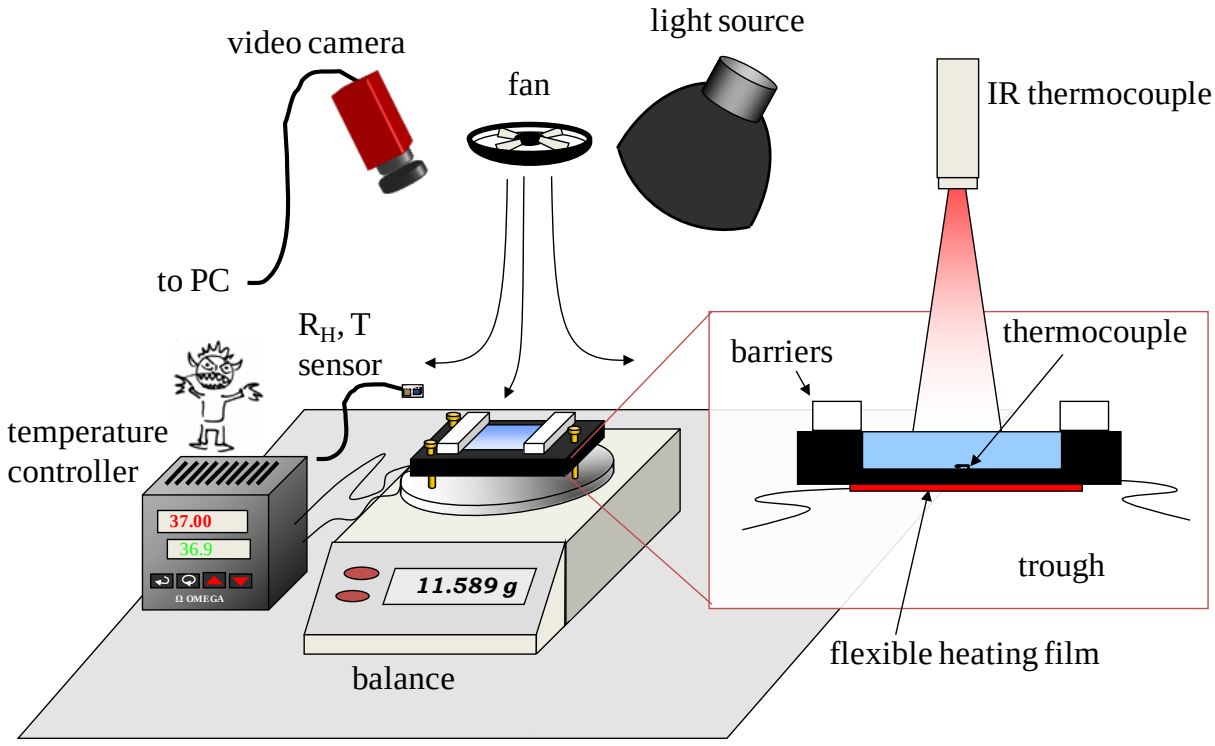

Figure 4.5: The evaporation-measurement apparatus. Process measurements and video-camera images are fed continuously to the computer. The entire apparatus is contained within an insulated box to minimize temperature and humidity fluctuations, and drafts (not shown).

rendered hydrophobic using Teflon® coating (86508-42-1, Dupont, Wilmington, DE). Three opposed screws enable leveling of the trough. A flexible heating film (KH-202/5, Omega Engineering Inc., Stamford, CT) adhered to the bottom of the trough provides heat to the water substrate. A thin, K-type thermocouple embedded in the bottom of the trough and coupled to a temperature controller (CN 733, Omega Engineering Inc., Stamford, CT) sets the temperature at the bottom of the water substrate. An infrared thermocouple (OS36-10K-80F, Omega Engineering Inc., Stamford, CT) gauged the average surface temperature of a spot 2 cm in diameter near the center of the water/air or oil/air interfaces.

The water surface is slightly colder in the center of the trough than near the edges, but the infrared thermocouple cannot view the entire gradient. Therefore, to account for the lateral-surface temperature distribution, we used a Merlin MW-IR thermal camera (FLIR Systems, Wilsonville, OR) to image the entire water surface and to provide an area-averaged temperature. The offset between the area-averaged surface temperature measured by the thermal camera and the local surface temperature from the infrared thermocouple corrected the infrared-thermocouple measurement. For experiments conducted without heating, the substrate consisted solely of water. When heating through the bottom, however, 4 mm of agarose gel was synthesized in the trough and covered with a 1-mm layer of water. The gel prevented buoyancy-driven thermal convection in the aqueous-substrate layer. Water-evaporation rates and oil-spreading dynamics were the same with and without the substrate gel present.

The trough rests on an analytical balance (MS 304S, Mettler-Toledo, Columbus, OH) with measurement accuracy of 0.1 mg, much less than the amount of mass lost during a typical experiment. A white light source and color CCD camera (AVT Marlin F131, Allied Vision Technologies, Newburyport, MA) positioned at near-normal incidence to the water surface provided white-light interferometric images of the films. The camera was attached to a computer, enabling continuous visualization of the spreading and uniformity of the duplex-oil films. In experiments with 1- to 2-mm thick oil films, a larger surface area was needed to register a mass loss significant enough to gauge reliably the small evaporative flux. In this case, a 10-cm diameter Pyrex® glass crystallizing dish replaced the Langmuir trough.

To obtain repeatable evaporation rates, careful control of the surrounding environment was necessary. Environment temperature (T_∞) and relative humidity (R_H) were maintained at 23-25 °C and 0.32-0.42, respectively, as measured with a Sensirion SHT75 sensor (Zurich, Switzerland). A 5-cm diameter, variable-speed electric fan (Sunon, Kaohsiung City, Taiwan) positioned above the trough directed an impinging jet of air at the interface. Fan speed, ω, was measured using a Strobotac 1531 strobe light (General Radio, Concord, MA). A fan speed of 3800 rpm, corresponding to a nominal velocity of 2.5 m/s (i.e., Reynolds number Re = 8000), set a repeatable mass-transfer coefficient without perturbing the film. Nevertheless, impinging airflow from the fan created fluctuations in the mass readings. Evaporation, however, was measured over 15 to 30 min, a long-enough time period to average fluctuations. A custom program written in LabView continuously recorded measurements from the infrared thermocouple, analytical balance, temperature/humidity sensor, and CCD camera.

4.6.3 Methods

4.6.3a Spreading experiments

Numerous spreading experiments were conducted to identify oily substances that might mimic the behavior of the tear-film lipid layer (TFLL). Figure 4.6 shows representative images of the *in-vivo* human TFLL after a blink in healthy subjects. The color interference patterns

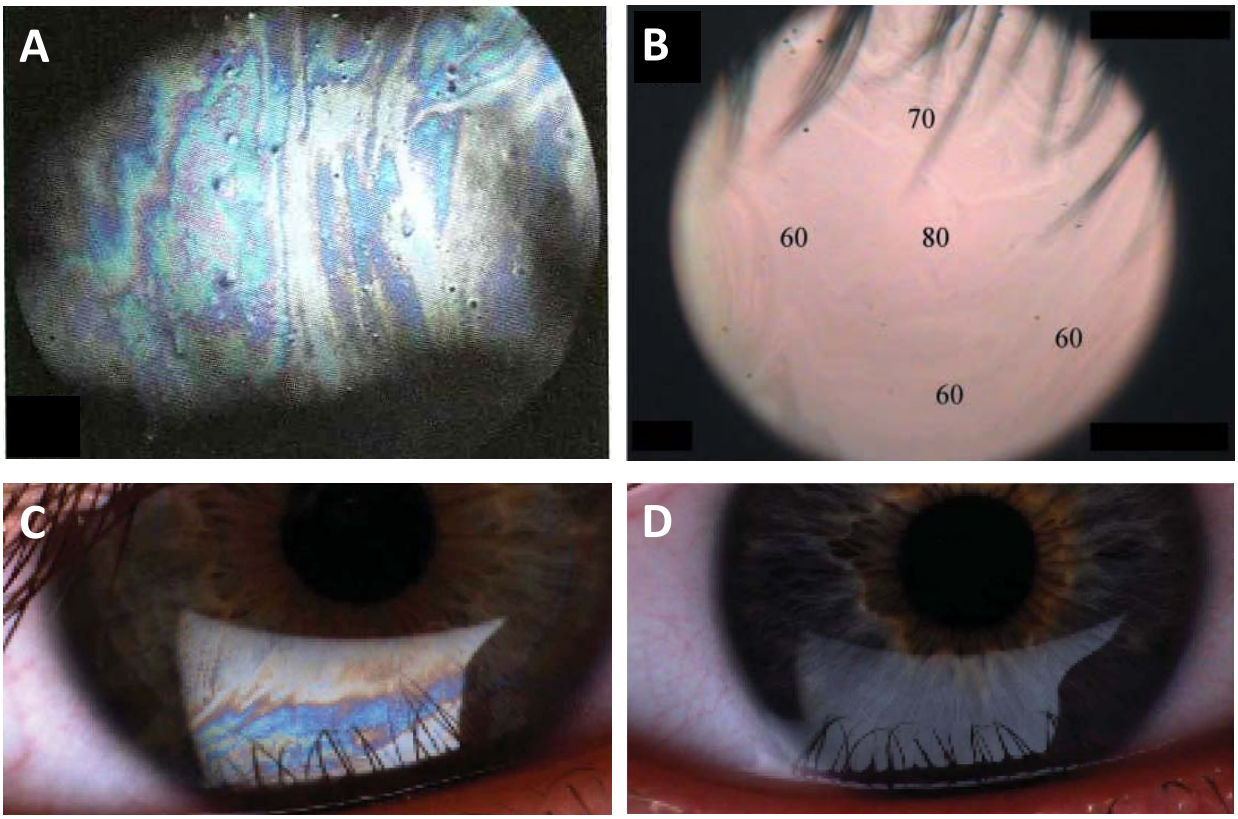

Figure 4.6: Interference patterns observed in healthy human lipid layer. (A) Color interference fringes observed in the TFLL [114]. (B) Lipid layer between 60 and 80 nm thick [78]. (C) Lipid interference patterns for films greater than 75 nm and (D) less than 60 nm [113].

indicate lipid-layer thicknesses ranging from 40 to well over 100 nm [78, 113, 114]. Successive frames in Figure 4.7 show color interference patterns in the TFLL of a single subject over the course of 6 blinks (approximately 5 s between blinks) [18]. Importantly, the color interferograms in Figure 4.7 repeat blink-to-blink with patterns re-emerging but eventually fading after several blinks. Chosen model-oil films must evidence this same phenomenon.

Our goal is to engineer films that spread uniformly at a thickness near 100 nm, that demonstrate repeatable color blink patterns as in Figure 4.7, and that resist dewetting long enough to measure evaporation rates. Although the human TFLL need only remain intact several seconds on the eye, we require a more stringent requirement of about 15 min to obtain an evaporation rate. To verify that our *in-vitro* films reflect the required characteristics of the TFLL, we visualized spreading/dewetting behavior of duplex-oil films for a large number of oils and spreaders. In the miniature Langmuir trough, the water surface was set level with the top of the trough sides, and a 0.5-μL droplet of the desired oil was deposited at the air/water interface in the center of the trough using a precision microliter syringe (701, Hamilton Co., Reno, NV). When using human or bovine meibum, the substrate was heated to 35 °C because these lipids spread minimally at ambient temperature. We then document whether or not the oil initially spread and whether or not it remained as a duplex film for at least 1 s. When an observable duplex-oil film occurred, the barrier was closed and opened once to mimic a blink, and the approximate breakup time (BUT) was recorded for visible holes to form in the film. We define BUT as the time taken for the first visible holes to appear in the film.

Figure 4.8 records representative behavior of the oils studied. In sequence A-B-C, a duplex film is formed (Panel B) that first forms visible rupture holes after about 5 s post-blink (i.e. BUT). In sequence A-E, the initially spreading drop rapidly dewets into lenses. No duplex-oil film forms. Panel D corresponds to a desposited oil droplet that immediately relaxes into a single lens.

4.6.3b Evaporation rates from a clean-water surface

Clean-surface evaporation experiments yield the evaporation rate J_0, as well as k_m, h, and UA_W at a given airflow rate (see Appendix 4C), which are properties of the evaporation apparatus. These values are necessary to determine oil-film water permeability via Equation 16. Pure-water evaporation measurements, therefore, serve to calibrate the apparatus.

Consequently, in each evaporation experiment, we first measured the evaporation rate from a clean-water surface. The unheated trough was filled about 2-3 mm above the brim with distilled/deionized water, the fan turned on, and data acquisition via LabView initiated. In the pure-water experiments, fan speed was varied from 3800 to 6300 rpm to investigate the behavior of the mass-transfer coefficient.

As water evaporates, with or without an oil film present, a steady wet-bulb temperature is reached where the mass of water in the trough decreases linearly in time. Attainment of steady state typically takes 30-40 min. Figure 4.9 graphs representative data for the area-averaged surface temperature of a clean water surface over time at a fan speed of 3800 rpm and no substrate heating. The temperature begins near ambient T_∞, eventually leveling off at the wet-bulb temperature, T_{S0}. For a typical R_H of 28.9 ± 6.9 % and a T_∞ of 23.6 ± 7 °C, T_{S0} is 17.2 ± 0.4 °C,which is just slightly higher than the wet-bulb temperature predicted from psychrometric charts of 17 °C [115]. Reported numbers are average ± standard deviation over at least 6 experiments.

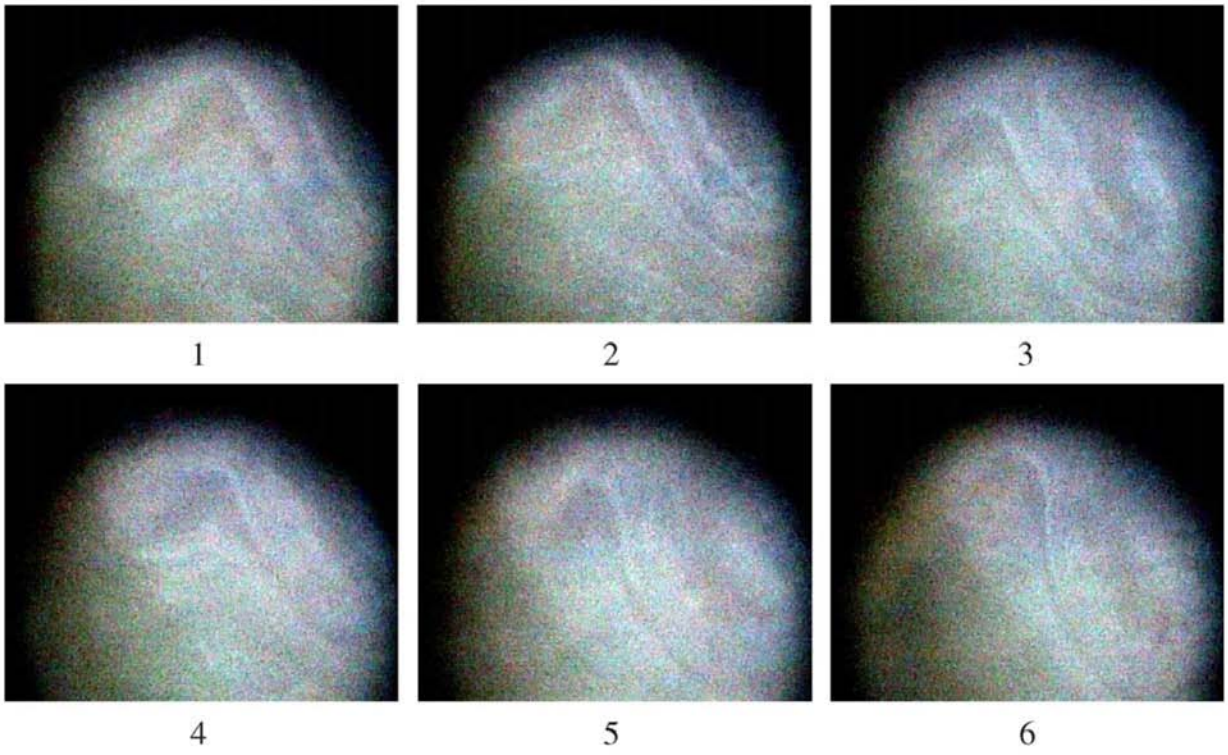

Figure 4.7: Repeated color interference patterns visualized in a human TFLL immediately after 6 successive blinks for the same human subject. The numbers under each panel indicate the blink number. From [18] with permission.

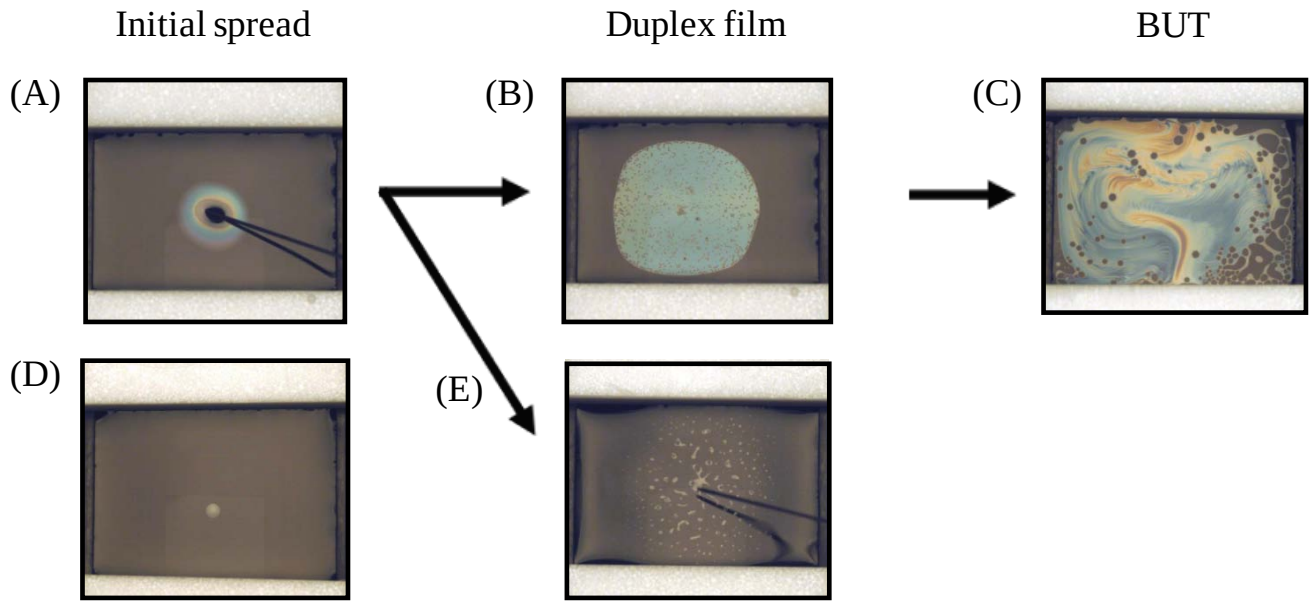

Figure 4.8: Color interference patterns documenting spreading behavior of 0.5-µL oil droplets deposited on water in the miniature Langmuir trough. Each column of images corresponds to a column from Table 4.1. After initial droplet deposition, the oil may spread (A, MOx) or remain as a lens (D, MO). Upon spreading, the oil may briefly form a visible uniform duplex film (B, MOx) or dewet instantaneously while spreading (E, OA). When a duplex film is formed, the trough barriers were blinked once, and the approximate duplex-film breakup time (BUT) is recorded (C, MOx).

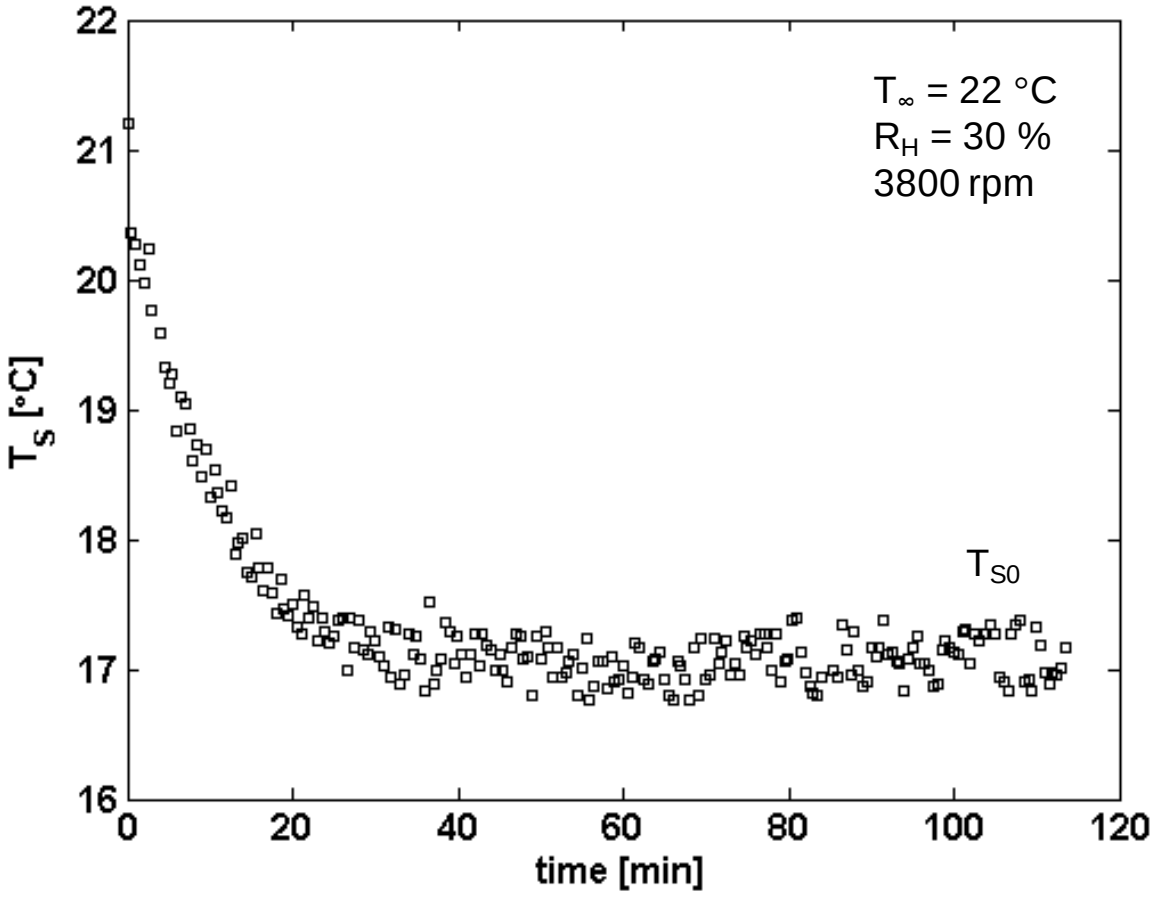

Figure 4.9: Surface temperature versus time for an evaporating clean-water surface at a fan speed of 3800 rpm, T_∞ = 22 °C, and R_H = 30 %. The temperature of the water surface drops from ambient temperature to a steady wet-bulb temperature T_{S0} of ~17 °C.

After about 15-20 min of steady evaporation at temperature T_{S0}, the water surface falls level with the top edge of the trough. Figure 4.10 shows representative results for the mass of water in the trough versus time for fan speeds of 3800, 5000, and 6300 rpm (*Re* = 8600, 11400, and 14300). Water mass decreases linearly in time indicating a constant evaporation rate. As the fan speed increases from 3800 to 6300 rpm, the mass-transfer coefficient and evaporation rate increase, mass loss is greater, and thus the slope of the line is steeper. Similar behavior is seen with a heated substrate. Evaporative mass flux, j_0 [g cm^{-2} s^{-1}], is obtained from the slope of the mass versus time at steady state after dividing by the trough surface area. For the ambient conditions described above and for 3800 rpm, j_0 is 1.16 ± 0.21x10^{-6} g/cm^2/s. Division by the molar mass of water, M, converts j_0 to the molar evaporation rate, J_0, used earlier. We report the measured mass fluxes, but it is implicit that they are converted to molar fluxes when inserted into the equations in §4.

Measurement of T_S, R_H, and T_∞ permits calculation of the water-vapor concentration difference between the air/water interface and the air far from the surface, $\Delta C_0 = C_w^{sat}(T_{S0}) - R_H C_w^{sat}(T_\infty)$. With the concentration driving force known and J_0 measured, we solve Equation 17 for k_m, which also yields $R_m = 1/k_m$. For typical measured J_0, T_{S0}, R_H, and T_∞, the mass-transfer coefficient in our apparatus is 1.34 ± 0.06 cm/s (average ± std. dev.) at a fan speed of 3800 rpm. For similar ambient conditions and fan speeds of 5000 and 6300 rpm, the respective k_m is 1.63 ± 0.05 and 1.80 ± 0.08 cm/s. From Equation B.7, h is calculated given the measured k_m value. Finally, we solve Equation C.5 to establish UA_W that accounts for heat transfer through the edges of the trough due to the small temperature difference between the water-surface center and the trough sides. With the transport properties established, evaporation measurements through the duplex-oil films are interpreted according to Equation 16 to establish Dk.

The experimental process is slightly more involved when the trough is heated from the bottom. Before adding water, warm agarose gel was poured into the trough to a depth of 4 mm and allowed to cool. After depositing a 1-mm layer of water over the gel, the temperature controller was activated at a set-point temperature for the bottom of the substrate, T_b. For a fan speed of 3800 rpm and the ambient conditions listed above, a set-point temperature of T_b = 45°C yields a surface temperature of T_{S0} = 35.4 ± 0.2 °C. The corresponding mass-evaporation rate was j_0 = 4.87 ± 0.27x10^{-5} g/cm^2/s. Calculation of k_m, h, and UA_W remains the same as that for the unheated surface except that we solve Equation 27 with modification described in Appendix 4C instead of Equation C.5.

4.6.3c Evaporation through duplex-oil films

Once the water surface evaporated level with the trough sides, a known volume of oil or solvent solution was deposited at the air/water interface using the precision microliter syringe. The known oil volume, V, and trough surface area, A, set the average film thickness, $L = V/A$. A 2-µL droplet of oil spread uniformly over the 20-cm^2 surface produces a film that is 1-µm thick. Film thickness was varied from 100 nm to 100 µm, except with bovine meibum, where the maximum film thickness was 10 µm. With bovine-meibum films 1-µm thick or less, meibum was typically dissolved in 50 µL of toluene/ispropanol solution (described earlier) before deposition. For thicker films, 200 µL of the same solvent was used with stepwise deposition to avoid overflow of the nonpolar solvent onto the hydrophobic trough edges or barriers. Although the chosen oils spread spontaneously, thin films less than 1-µm thick rarely cover the entire

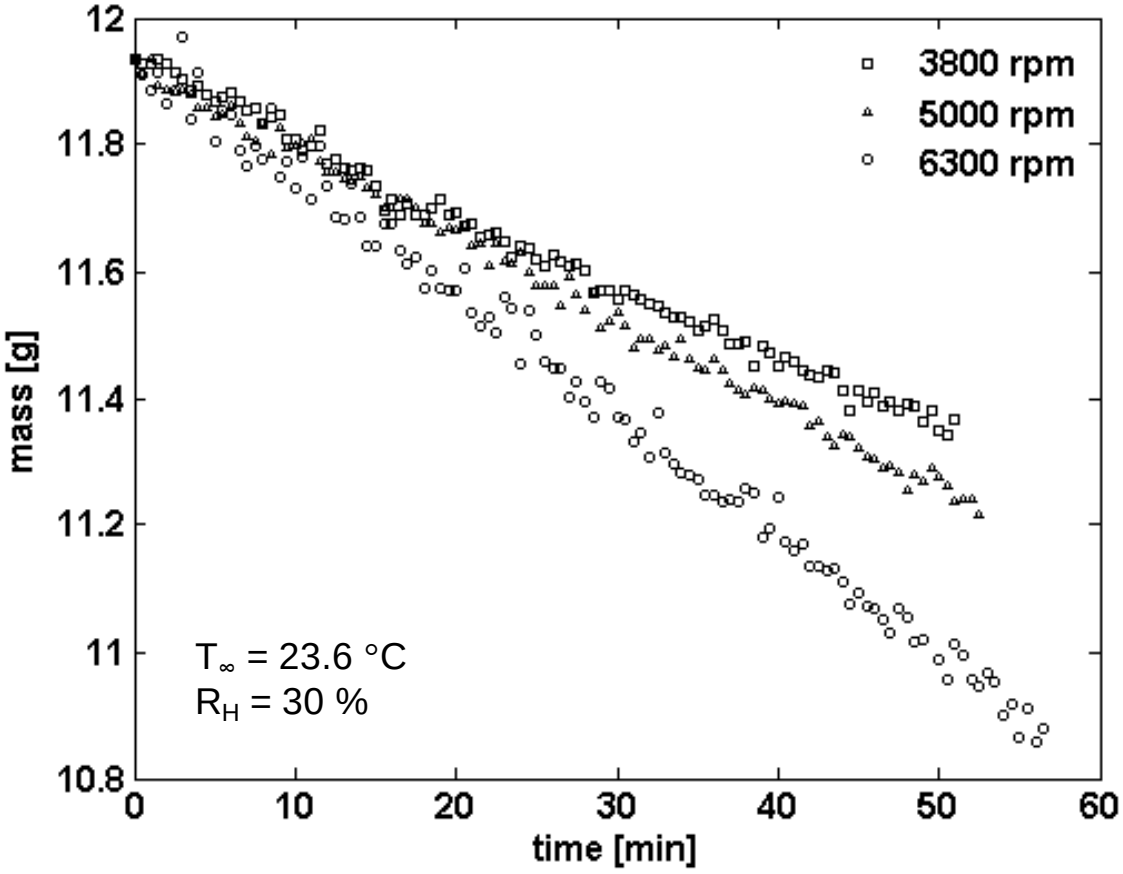

Figure 4.10: Mass of clean water in the unheated trough versus time for three different fan speeds: (□) 3800 rpm, (△) 5000 rpm, (○) 6300 rpm. Exact numerical values for each data set are shifted to give the same initial mass for all experiments.

water surface after initial deposition. To facilitate complete coverage, one barrier was brought across the surface until it almost contacted the other barrier and then returned to its original position, mechanically re-spreading the film. Holly refers to this process as "flexing" the film [38]. We coin this process as "blinking," as it mimics the action of an eyelid during a blink [116].

Figure 4.11 illustrates the water-surface temperature versus time in the unheated trough before and after the deposition of a 2.5-µm MOx/BSM layer at a fan speed of 3800 rpm. After coverage by the uniform duplex-oil film, the water temperature rises from T_{S0} = 18 °C to approach a new steady temperature, T_{SF}, and corresponding new constant evaporation rate, j_F, which depend on the oil-film thickness, among other things. Due to the thinness of duplex-oil films, there is no measurable difference between the two interface temperatures T_{wo} and T_{oa}; consequently, we refer to one measured surface temperature, T_{SF}, that substitutes for T_{wo} in Equations 14, 18, and 24 during data analysis. After reaching the film-covered steady-state temperature, mass-loss data are collected for at least another 15 min to ensure a reliable evaporation rate. During this time, the CCD camera records visual images every 5 min. If significant film dewetting occurs, the experiment is discarded.

Figure 4.12 shows typical relative evaporative mass loss versus time at a fan speed of 3800 rpm before and after the application of duplex MOx/BSM oil films ranging in thickness from 100 nm to 100 µm. Since the data are from multiple experiments, the absolute values of time and mass are shifted for convenience. Filled black squares from t = 0 to 47 min show mass loss from the calibrating clean-water surface. Subsequent mass-loss series correspond to water evaporation through films of increasing film thickness. As the film thickness increases, the oil-film diffusion resistance increases, and the evaporation rate decreases. Consequently, the slope of mass-versus-time, which gives the evaporative flux of water through the film-covered surface, j_F, decreases. Concurrent measurement of T_{SF}, R_H, and T_∞ allows calculation of the concentration driving force between the water/oil interface and the sub-saturated air: $\Delta C_F = C_w^{sat}(T_{SF}) - R_H C_w^{sat}(T_\infty)$. With j_F measured and ΔC_F established, Equation 14 is solved for the total mass-transfer resistance, R. Subtraction of the gas-phase mass-transfer resistance, R_m = $1/k_m$, (calculated from the pure-water evaporation rate as described in §4.2.1) from the total resistance R gives the mass-transfer resistance of the duplex-oil film, R-R_m, via Equation 16.

In Figure 4.13, we plot the measured film mass-transfer resistance (R-R_m) versus film thickness (L) for duplex-oil films of MOx/BSM and bovine meibum (BM). Without substrate heating (■), the average measured surface temperature, T_{SF}, is 20 °C; with heating (□, ○) it is 40 °C. Following Langmuir and Schaefer [8], we fit the film resistance-film thickness data with a straight line. According to Equation 16, the slope corresponds to the inverse of the water permeability in the oil film, $1/Dk$, and the intercept corresponds to the interfacial resistance, R_I. The intercept is approximately zero for all oil films studied, indicating that R_I is negligible in our systems. Above a 1-µm film thickness, film resistance no longer increases linearly with film thickness. This is likely a consequence of nonuniform film coverage. Inspection of the visual images shows that, even with thick films, the water surface is not completely covered near the edges of the trough, leaving 1 to 5 % of the surface area uncovered. As described in §4.2.3, small exposed areas have minimal effect on evaporation rate at small film thickness, but their impact can be pronounced at large film thickness. Accordingly, we use only the data up to 1-µm thickness in the linear fit to establish Dk.

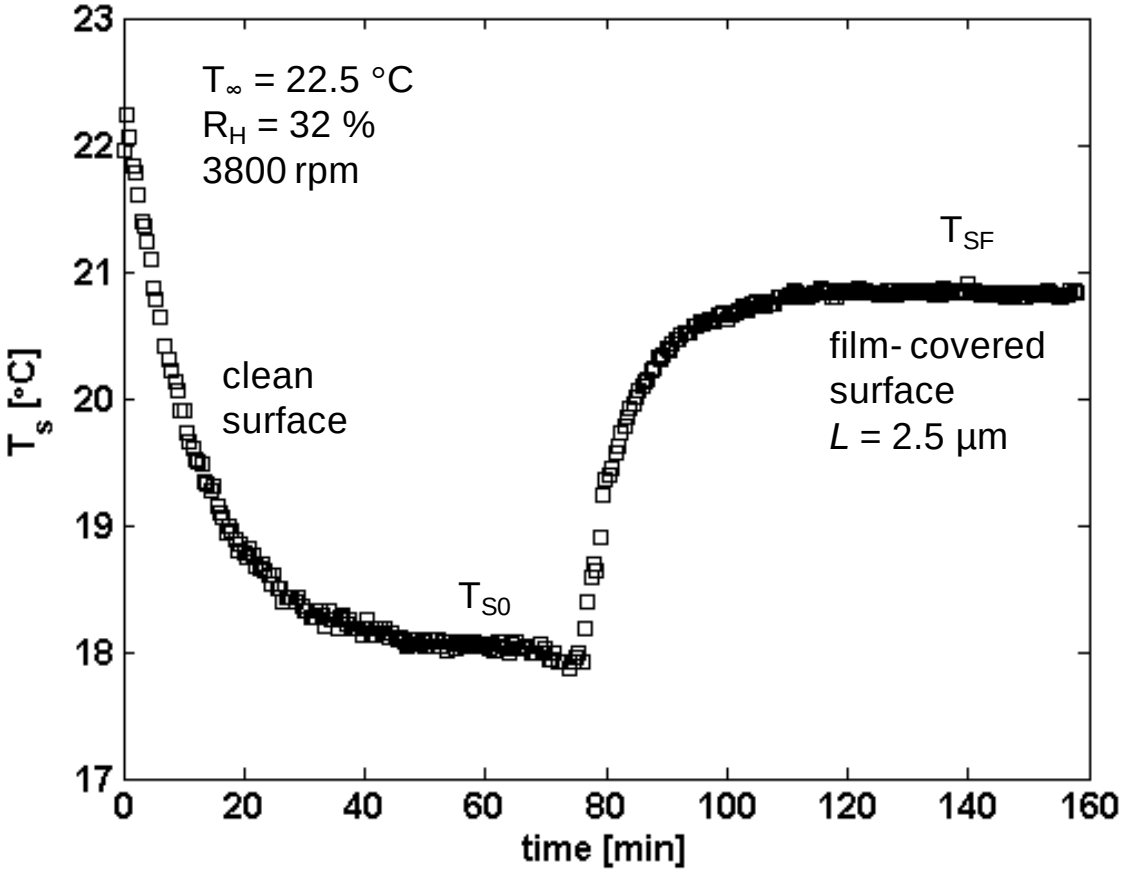

Figure 4.11: Surface temperature versus time before and after application of a 2.5-µm MOx/BSM duplex-oil film in an unheated trough. The temperature of the clean-water surface falls to a steady temperature T_{S0} of ~18 °C. After film deposition at t ~ 75 min, the temperature rises, eventually reaching a new steady-state temperature of T_{SF} = 20.7 °C.

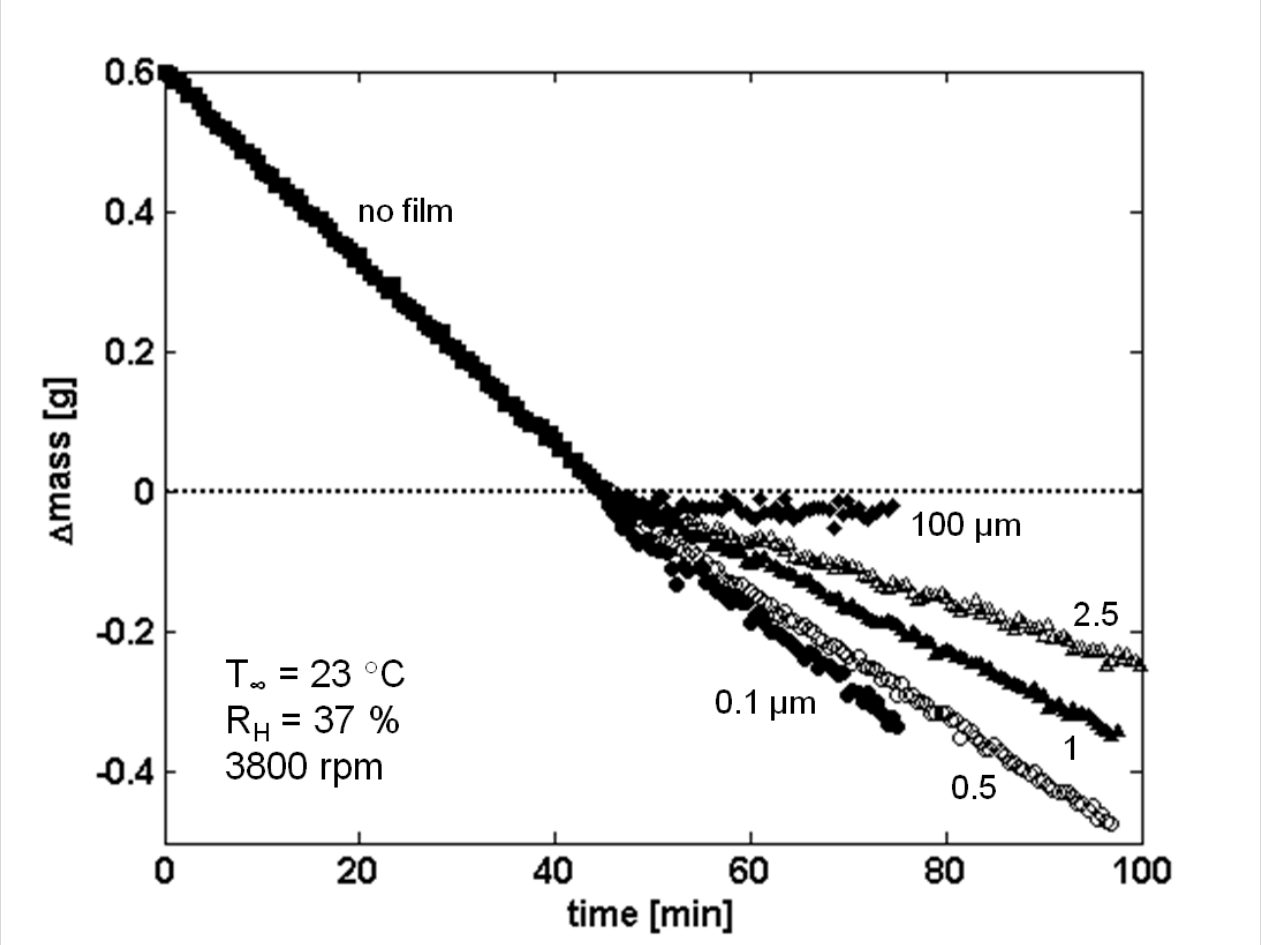

Figure 4.12: Relative mass of water in the trough versus time at a fan speed of 3800 rpm before and after application of MOx/BSM films of varying thickness in an unheated trough. The mass for each experiment is shown relative to the mass at which the film was applied. (■) clean water, (●) 0.1, (○) 0.5, (▲) 1, (△) 2.5, and (◆) 100-µm film.

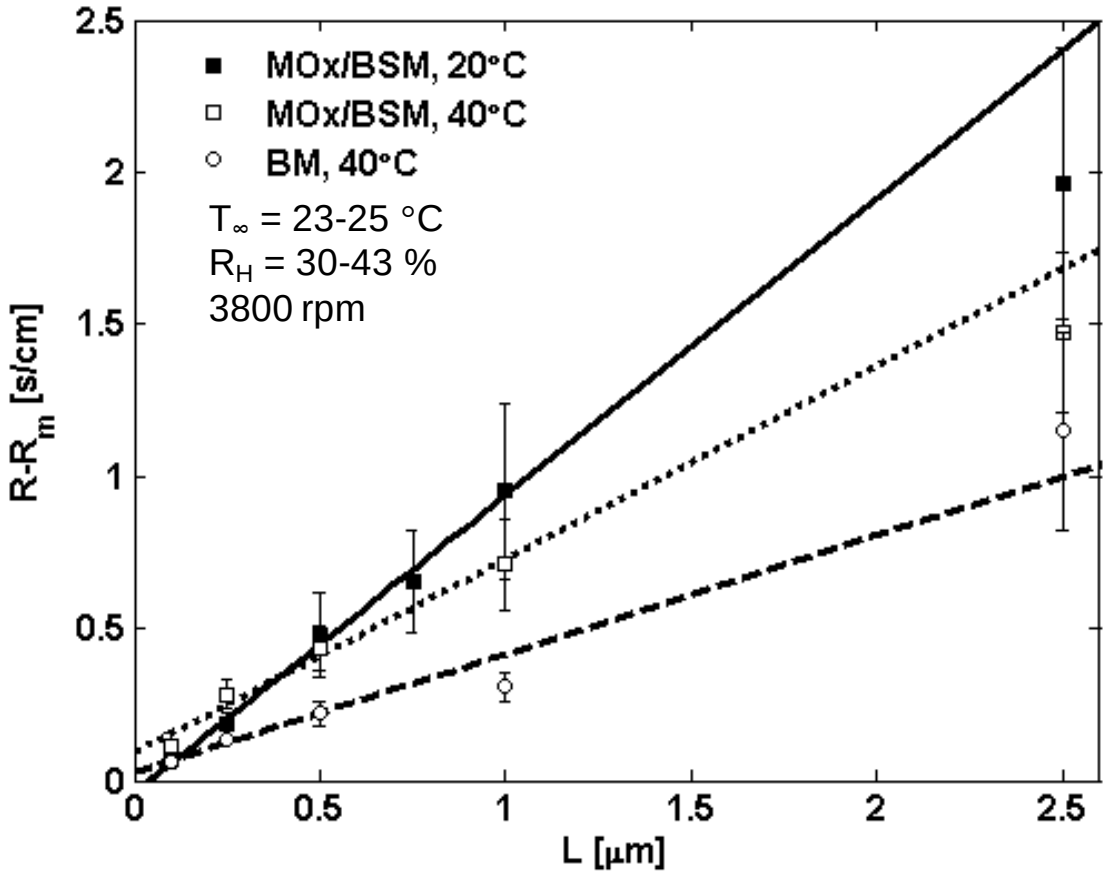

Figure 4.13: Film resistance, R-R_m, versus film thickness, L, for various oil films and temperatures. Squares represent MOx/BSM, and circles correspond to bovine meibum (BM). The average surface temperature for the filled symbols is T_{SF} = 20°C and for the open symbols is T_{SF} = 40°C. Best linear fits of the data up to 1 μm in thickness are shown.

To determine the water permeability of the oxidized mineral oil without admixed mucin, several experiments with much thicker films were conducted. Films as thick as 1 or 2 mm remained stable without added mucin. Because very little water mass is lost through such a thick oil film, special precautions were necessary. To maximize mass loss, most experiments were conducted in a glass crystallizing dish with a surface area of 79 cm^2. For the thicker films, fluctuations in mass from the applied airflow were no longer negligible, so the fan was not operated. Fortunately, such films are thick enough that the gas-phase mass-transfer resistance, R_m, is insignificant compared to the film resistance, R_F. Additionally, the substrate heater was not used because temperature fluctuations led to significant drift in mass readings from the electronic balance.

Distilled/deionized water was first added to the glass crystallizing dish and evaporated for 1 h to establish steady state, and to allow accurate determination of j_0. Next, an oil film approximately 5 to 8-mm thick was deposited slowly onto the water surface until gravity flattened the oil layer into a uniform bulk film. Then, using the microliter syringe, oil was withdrawn until the film reached the desired thickness (1.5 to 3 mm). For films of 1-mm thickness, the miniature Langmuir trough was used with only a 3-mm layer of water as the substrate, and the oil film was deposited directly onto the surface without overfill and siphoning of the oil. Once the oil film was in place, water was evaporated for up to 48 h to register significant mass losses. In one experiment, 5 wt% BSM was added to the film to ascertain the effect of mucin on the water permeability of the thick oil films.

4.6.3d Water uptake into oil

The partition coefficient, k, reflects the equilibrium uptake of water by the oil. To gauge k for our duplex-oil films, oil samples were equilibrated in dry and humid vapor environments. The resulting water uptake was measured by oil-sample mass change and by differential scanning calorimetry (DSC). Three 10-mg samples of oxidized mineral oil, consisting of 10 wt% BSM, and bovine meibum were placed in aluminum TA Tzero sample pans (TA Instruments, New Castle, DE) and weighed with an analytical balance. The open sample-containing pans were equilibrated for 48 h in a sealed glass container containing either pure water or anhydrous calcium-sulfate desiccant (Drierite, W.A. Hammond Drierite Co., Xenia, OH). The relative humidity in the sealed glass container was measured to be <5 % when containing desiccant and >90 % when containing pure water.

After removal from the glass chamber, each sample mass was recorded, and the pans were hermetically sealed with an aluminum lid. Each pan was placed into the DSC (TA Instruments DSC Q20, New Castle, DE), and cycled between 30 and -30 °C at a rate of 5 °C/min. From the measured heat released upon freezing/melting of any water present and the known heat of fusion, we establish the mass of water present in each sample.

4.7 Results

4.7.1 Film spreading and stability

To establish a model duplex-oil film that mimics evaporation studies through the human TFLL, we investigated the spreading and stability of a large number of oils in the miniature trough. Table 4.1 reports spreading behavior for 17 oil mixtures of 0.5-µL volume spread on the 20-cm^2 air/water interface. As illustrated in Figure 4.8, we recorded whether the various oils spread initially, whether the spreading film remained long enough to form a duplex-oil film, and how long the duplex film remained, as gauged by approximate BUT, after blinking action of the

Table 4.1: Oil spreading and dewetting on water.

Substance*	**Spreading behavior****		
	initial spread	**duplex film**	**BUT**
mineral oil (MO)	x	x	–
stearyl oleate (SO)	✓	x	–
oleic acid (OA)	✓	x	–
linseed oil (LS)	✓	✓	1 s
olive oil	✓	✓	< 1 s
MO + OA (0.5 wt%)	✓	✓	1 s
MO + DPPC (0.5 wt%)	✓	x	–
MO + $C_{12}E_4$ (0.5 wt%)	✓	x	–
MO, ChO, SO, Ch, DPPC (88, 5, 0.5, 6, 0.5 wt%)	✓	x	–
MO + ChO, Ch (0.4, 0.4 wt%)	✓	✓	5 s
Ch, ChO, SO (1:1:1)	✓	x	–
MO + stand oil (2 wt%)	✓	✓	5 s
oxidized MO (MOx)	✓	✓	5 s
MOx + 145K PIB (1 wt%)	✓	✓	10 s
MOx + BSM (10 wt%)	✓	✓	5 min
human meibum	✓	✓	> 30 min
bovine meibum	✓	✓	> 30 min

* DPPC = dipalmitoyl phosphatidyl choline, $C_{12}E_4$ = Brij 30, ChO = cholesteryl oleate, Ch = cholesterol, PIB = polyisobutylene.

**If 0.5 μL of oil spreads initially, the initial-spread entry is checked. If, in addition, it remains as a film long enough for a uniform duplex film to be visible, the duplex-film entry is checked. For oils that form duplex films, the barriers are blinked once and approximate breakup time is reported (BUT).

trough barriers. Tested substances fall into the categories of pure components, oil-soluble surfactant dissolved in mineral oil, meibomian-lipid mimics, and other mixtures including the MOx/BSM admixture. As expected, mineral oil, whose initial spreading coefficient is negative, does not spread. Pure surface-active lipids below their pK_a value, including oleic acid, stearyl oleate, and cholesteryl oleate, all spread initially. However, these lipid mimics subsequently dewet rapidly, and no metastable duplex film is observed. Olive oil and linseed oil, which are mixtures of plant-based lipids, spread initially but remain as duplex-oil films for only 1 s.

Mixtures of mineral oil and other surface-active substances exhibited varying results. Films spread from mineral oil mixed with 0.5-wt% oleic acid; 0.4-wt% cholesteryl oleate/0.4-wt% cholesterol; or 2-wt% stand oil persisted long enough to exhibit duplex-oil films (>1 s). Addition of DPPC to mineral oil in percentages above 0.5 wt% enabled initial spreading, but observable duplex-oil films did not form. Identical results emerged for mixtures of Brij 30 and mineral oil; cholesteryl oleate/stearly oleate/DPPC/ mineral oil; and cholesterol/cholesteryl oleate/stearyl oleate.

In agreement with others [8, 37, 38], oxidized mineral oil (MOx) spread at the air/water interface and remained uniform for approximately 5 s after blinking the trough barriers. Addition of PIB to the MOx increased the viscosity to 80 mPa·s and, thus, increased BUT to 10 s.

The most stable duplex-oil film resulted from the MOx/BSM admixture. In this system, the initial spreading rate is much slower than with the other mixtures because the BSM flakes disaggregate and dissolve into the oil and water. Once spreading is complete and the barriers are blinked, the 250-nm film resists dewetting for about 5 min. Thicker films resisted dewetting for much longer.

Figure 4.14 shows interference patterns visible under white light in spread MOx/BSM films after successive blinking of the trough barriers every 5 s. Color interference patterns repeat over several blinks, similar to the human-eye images in Figure 4.7 showing repeated blink patterns in the *in-vivo* human TFLL. Duplex-oil films of MOx alone also display repeated blink patterns. However, these films do not resist dewetting long enough to permit evaporation-rate measurements.

The most stable duplex films at the air/water interface were spread from samples of bovine (BM) and human meibum (HM). Both human and bovine meibum are waxy solids at room temperature [83]. Minor spreading occurred at 23 °C. Upon heating the water/air interface to 35 °C, both human and bovine meibum spread spontaneously. Upon blinking the films in the Langmuir trough, these films remained stable for well over 30 to 45 min without visible dewetting. Color interference patterns for bovine and human-meibum films (not shown) are similar both to those seen *in vivo* and those from MOx/BSM films. Our spreading studies focus on model MOx/BSM and meibum as candidate duplex-oil films for the evaporation experiments.

4.7.2 Evaporation reduction

4.7.2a Unheated substrate

A battery of 40 repeat experiments first measuring J_0 and T_{S0} followed by J_F and T_{SF} as a function of film thickness was conducted with MOx/BSM duplex films without substrate heating. Film thicknesses ranged from 100 nm to 100 µm. Experimental conditions and apparatus transport properties measured from the pure-water results are listed in Table 4.2. For the film-covered water surfaces, Dk was determined from the slope of film resistance, R-R_m, versus film thickness, L, as described in §4.3.3 and illustrated in Figure 4.13. Results are shown in the first row of Table 4.3 (i.e., $Dk = 1.1\text{x}10^{-4}$ cm^2/s).

Once Dk is known, Equations 18 and 24 permit simultaneous calculation of the evaporation ratio J_F/J_0 and surface temperature T_{SF} as a function of film thickness with no adjustable parameters. Comparison to the experimental data is made as solid lines in Figure 4.15 and Figure 4.16, respectively. Theory and data are in good agreement with minor discrepancy for the thickest films, which deviate from linearity in Figure 4.13. As expected, increasing film thickness slows evaporation, causing the surface temperature to rise. Quantitative prediction, however, demands the proposed dissolution-diffusion theory.

Two evaporation experiments were conducted with bovine meibum without substrate heating. At ambient temperature, bovine-meibum films do not readily spread; obtaining uniform film coverage was difficult even with the spreading solvent since bulk bovine meibum is a viscous, solid-like wax [83]. Due to the difficulty in obtaining uniform films, one film each was deposited at 100 and 500 nm. Evaporation reduction by bovine-meibum duplex films of 100 and 500-nm thickness was 36 and 81 %, respectively.

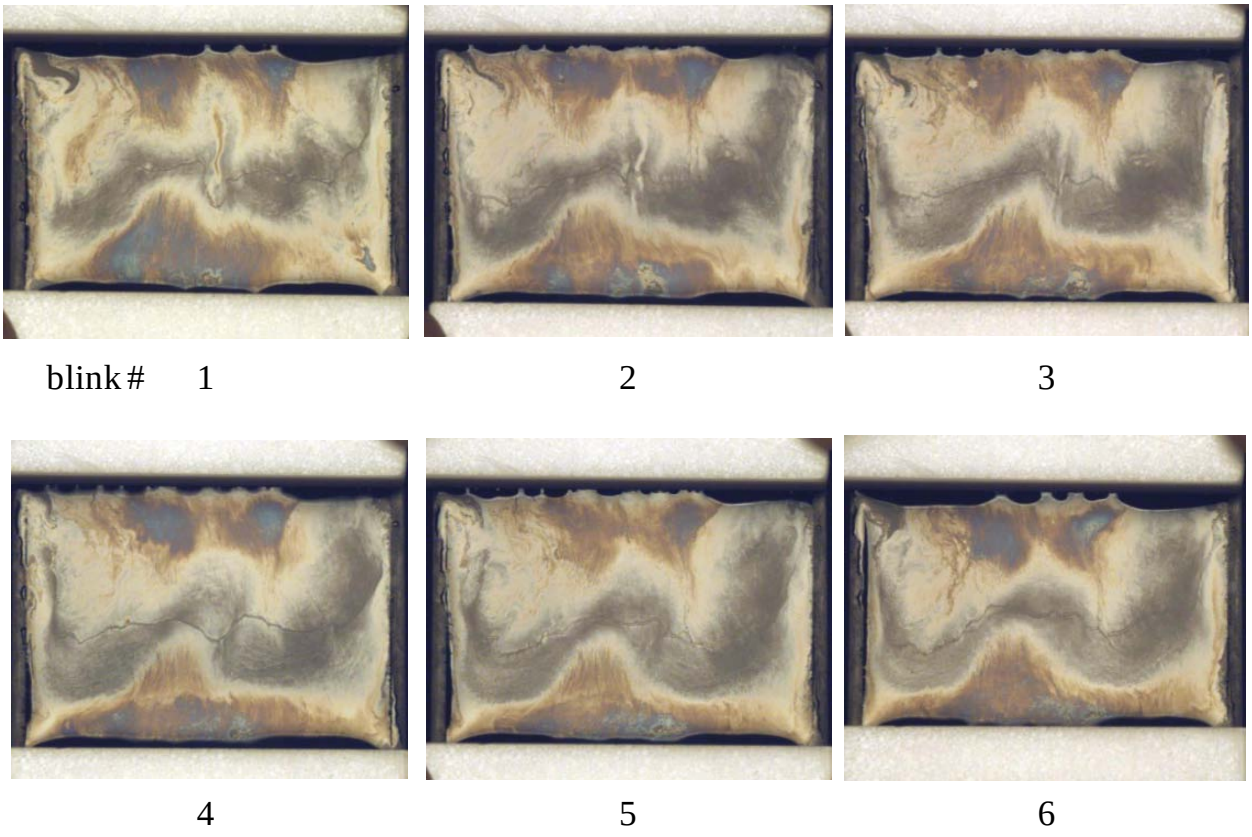

Figure 4.14: Color interference patterns observed in *in-vitro* duplex films of MOx/BSM in the miniature Langmuir trough immediately after 6 successive blinks. The deposited films are 100-nm thick. Each image is taken immediately after the blink number denoted below the frame. (Compare with Figure 4.7.)

Table 4.2: Evaporation rate from a clean-water surface for both heated and unheated substrate.†

Duplex-oil system:	**MOx/BSM**	**MOx/BSM**	**BM, HM**
Substrate heating:	none	T_b = 45 °C	T_b = 45 °C
j_0* [10^{-5} g/cm^2/s]	1.01 ± 0.18	5.41 ± 0.16	5.93 ± 0.24
T_{S0} [°C]	17.6 ± 0.4	37.2 ± 0.2	36.2 ± 0.3
T_∞ [°C]	22.9 ± 0.2	23.3 ± 0.2	25.0 ± 0.6
R_H [%]	36.7 ± 2.1	42.8 ± 2.5	31.9 ± 5.0
k_m‡ [cm/s]	1.34 ± 0.14	1.53 ± 0.11	1.71 ± 0.11
h [mW/cm^2/K]	1.44 ± 0.15	1.64 ± 0.12	1.83 ± 0.12
UA_W [mW/K]	63 ± 1	170 ± 10	140 ± 20

† Values are reported as average ± standard deviation over 40 measurements.

* Values for j_0, T_{S0}, T_∞, and R_H are measured directly.

‡ k_m, h, and UA_W are calculated as described in §4.3.2.

Table 4.3: Measured water permeability of duplex-oil films.

Substance	**Avg. T_{SF} [°C]**	**Dk [10^{-4} cm^2/s]**
MOx/BSM	20	1.1
MOx/BSM	40	1.6
BM	40	2.6

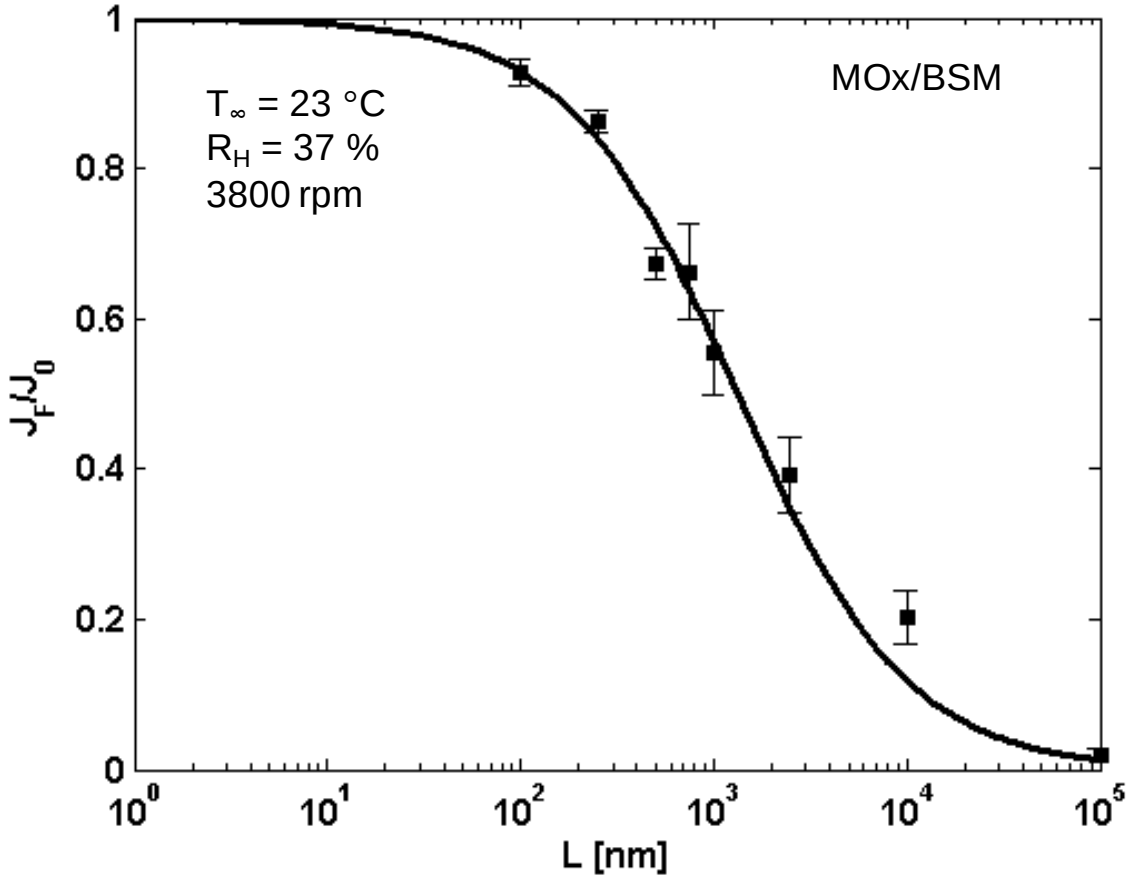

Figure 4.15: Evaporation ratio J_F/J_0 versus oil-film thickness L for MOx/BSM in an unheated trough. Filled squares represent the average experimental values. Error bars denote the standard deviations. Solid line corresponds to theory (Equation 18) with k_m = 1.34 cm/s and Dk = 1.1x10^{-4} cm^2/s, determined by the fit in Figure 4.13. Corresponding surface temperatures are given in Figure 4.16.

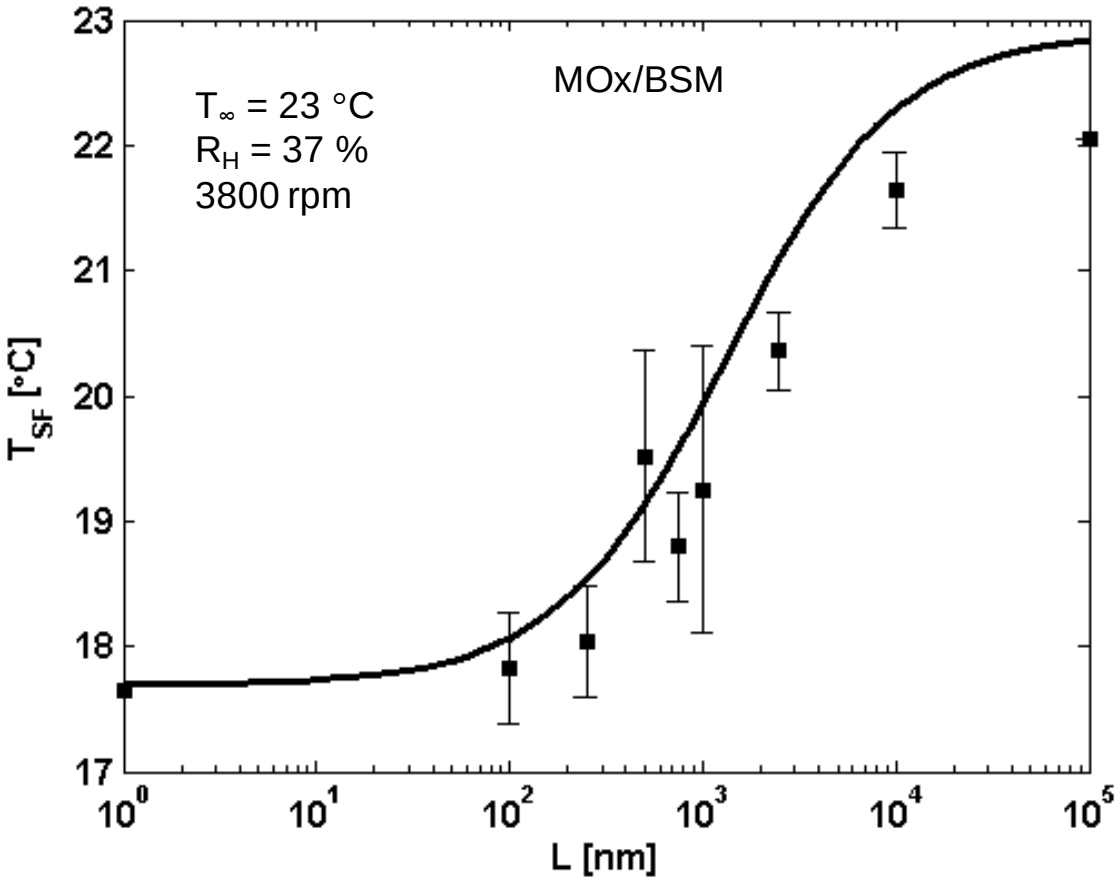

Figure 4.16: Surface temperature T_{SF} versus oil-film thickness L for MOx/BSM films in an unheated trough. Filled squares represent the average measured values. Error bars denote the standard deviation. Solid line corresponds to theory (Equation 24) with the same parameters as in Figure 4.15.

4.7.2b Heated substrate

Water evaporation through duplex films of MOx/BSM, bovine meibum (BM), and human meibum (HM) was likewise measured with a warmed substrate to facilitate meibum spreading and to reflect eye conditions. As with the unheated substrate, measurements of J_0 specified the apparatus transport properties reported in Table 4.2, and measurements of J_F and T_{SF} as functions of film thickness allowed determination of Dk from the slope of R-R_m versus L as reported in Table 4.3. Theory then predicts J_F/J_0 and T_{SF} as functions of L.

Comparison to experimental evaporation-reduction and surface-temperature data (T_b = 45 °C) at 3800-rpm fan speed is made in Figures 4.17 and 4.18. In these figures, filled squares correspond to MOx/BSM films and open circles correspond to BM films. Additionally, two samples of human meibum (HM) were obtained and tested, indicated in Figure 4.17 by inverted open triangles. The two lines in each figure correspond to the predictions of coupled Equations 18 and 24 with the corresponding Dk for each oil from Table 4.3: solid lines for MOx/BSM and dotted lines for BM. Ascertained permeabilities measured by R-versus-L data are 1.6 and $2.6\text{x}10^{-4}$ cm^2/s for MOx/BSM and BM duplex films, respectively, at an average T_{SF} = 40 °C. The limited sample amount of bovine meibum restricted the thickest bovine-meibum film studied to 10 μm and less. Excellent agreement is found between dissolution-diffusion theory and experiment, especially since no adjustable parameters are used in the theoretical predictions.

4.7.2c Evaporation through thick oil films

For oxidized-mineral-oil films between 1- and 5-mm thick deposited over water in a glass crystallizing dish, the measured water permeability, Dk, ranged from 2 to $3\text{x}10^{-5}$ cm^2/s, almost and order of magnitude smaller than that for MOx/BSM. For 2-mm thick films of MOx deposited in the miniature Langmuir trough, the calculated Dk ranged from 2.6 to $3.5\text{x}10^{-5}$ cm^2/s. In one experiment, a 1.9-mm thick layer of oxidized mineral oil was deposited in the miniature Langmuir trough: the calculated Dk was $3.2\text{x}10^{-5}$ cm^2/s. In another experiment, the same thickness film was deposited in the trough and 191 mg of BSM were gently contacted with the film. The BSM quickly settled into the film, and evaporation was measured over the course of 24 h. The calculated Dk was $5.6\text{x}10^{-4}$ cm^2/s. At the end of the experiment, large domains of water-containing BSM were visible throughout the oil film. Regions rich in BSM contained water droplets that appeared to rise through the oil film. Apparently, admixed water-liking mucin molecules imbibe water into the duplex-oil films.

4.7.2d Water uptake into oil

DSC measurements showed no measurable amount of water uptake into the samples of oxidized mineral oil. However, the samples of MOx/BSM and bovine meibum exhibited freezing and melting peaks corresponding to water phase transitions [83]. Integration of the heat-flow peaks shows that MOx/BSM and bovine meibum contain up to 10 and 4 wt% water, respectively, when equilibrated with water vapor at >90 % relative humidity. Detailed information on the DSC experiments is reported by Rosenfeld *et al*. [83].

4.8 Discussion

Not surprisingly, most oils deposited on water do not form persistent duplex films over a timescale useful for evaporation experiments. Three substances did so: MOx/BSM, human meibum, and bovine meibum. Similar to the results of Heymann and coworkers [5, 47], we find that addition of an interfacial structurant, BSM, imparts stability to duplex films of oxidized

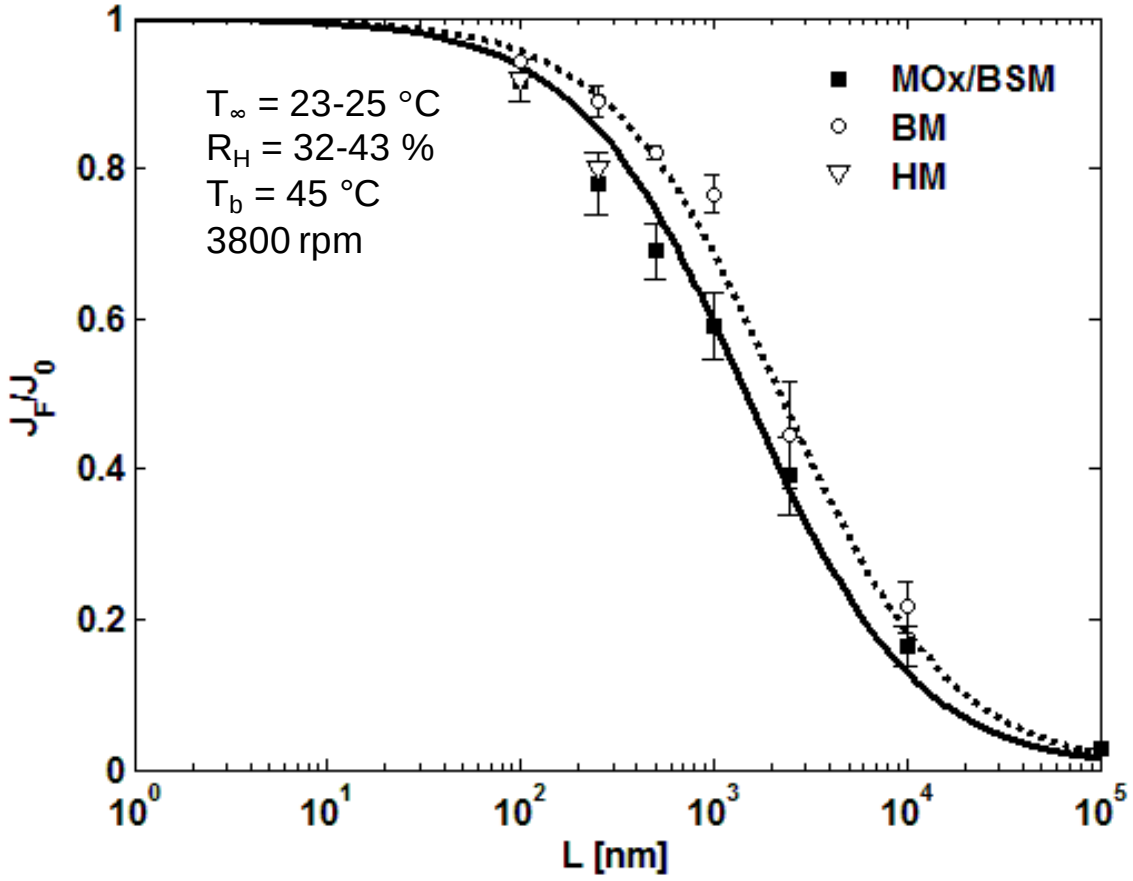

Figure 4.17: Evaporation ratio J_F/J_0 versus oil-film thickness L for MOx/BSM (■), bovine-meibum (○), and human-meibum (▽) films in a heated trough (T_b = 45 °C). Lines represent the theory in Equation 18 plotted for $Dk = 1.6 \times 10^{-4}$ (solid line, MOx/BSM) and 2.6×10^{-4} cm^2/s (dotted line, BM). Corresponding surface temperatures are shown in Figure 4.18.

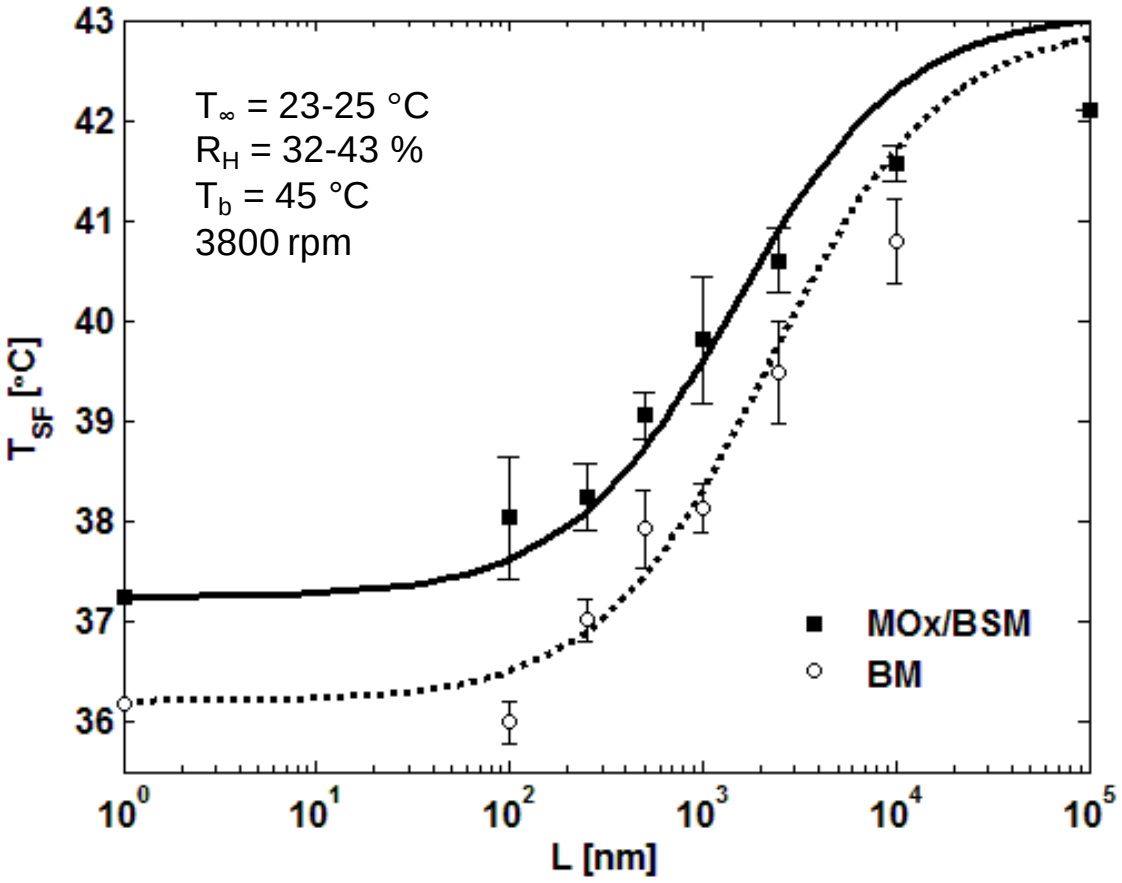

Figure 4.18: Surface temperature T_{SF} versus oil-film thickness L for MOx/BSM (■) and bovine-meibum (○) films in a heated trough (T_b = 45 °C). Lines correspond to theory (Equation 24) with the same parameters as in Figure 4.17 (solid line = MOx/BSM, dotted line = BM). T_{S0} is shown at L = 1 nm.

mineral oil. Although films of oxidized mineral oil alone form uniform duplex films, the resulting films are relatively fluid as seen by swirling and movement of the interference patterns. These films dewet well before the 15 min necessary to measure evaporative mass loss. In contrast, incorporation of BSM into mineral oil results in films that show little or no motion at the interface. Apparently, mucin forms gel-like networks at the water/oil and/or water/air interfaces.

Duplex-oil films spread from both human and bovine meibum were similarly stable at physiologic temperature. The viscosity of both human and bovine meibum is four orders of magnitude larger than that of water at 35 °C [83]. Large viscosity slows the dewetting process. Some films of meibum spread from samples stored for many months did indeed dewet in a fashion similar to mineral-oil mixtures. It is possible that decomposition of the meibomian lipids leads to a less-structured material that does not remain stable. There is evidence that the human TFLL indeed dewets *in vivo* in some, possibly unhealthy, individuals [82].

The duplex-oil films tested obey well the dissolution-diffusion mechanism of evaporation reduction outlined in §4.2, as shown by Figure 4.13 and Figures 4.15-4.18. The linear relationship between film resistance and film thickness, illustrated in Figure 4.13, confirms a constant *Dk*. In agreement with Langmuir and Schaefer [8], we do not find interfacial resistance in any of our duplex-oil films. Interfacial resistance apparently demands polymerized spreaders [47]. Figures 4.15-4.18 show the measured evaporation ratios and surface temperatures in comparison with dissolution-diffusion theory. Close agreement between data and theory in all of these figures indicates that heat and mass transfer in the films is well-characterized by our proposed 1-D model. Importantly, the fitted *Dk* value for each duplex-oil-film substance listed in Table 4.3 is a material property that describes water transport through the film. Without obtaining *Dk* from the raw evaporation data, quantitative comparison of evaporation reduction between different experimenters is not possible because measurements are apparatus and procedure sensitive.

Model and experiment do not agree as closely for the thickest films, which we attribute to inhomogeneous film coverage. The disagreement is most readily seen in Figure 4.13, where film resistance no longer increases linearly with film thickness above 1 μm. Gilby and Heymann [47] report a similar trend. They attribute this behavior to "an inhomogeneity of the duplex films below 10-μm thickness." Films at smaller thicknesses tend to dewet more readily. resulting in inhomogeneous coverage. However, the theory outlined in §4.2.3 predicts that the effect of dewetted holes on evaporation reduction decreases as the duplex-film thickness decreases. In fact, the effect of holes on evaporation is magnified in thicker films.

Duplex-oil-film water permeabilities calculated in §4.3.3 and shown in Table 4.3 for each film chemistry are higher than expected for an aliphatic hydrocarbon oil. Permeability is the product of the water diffusivity, *D*, and the partition coefficient, *k*, in the oil. Reported partition coefficients vary from about 3 for pure hexadecane or mineral oils [117] to 50 for vegetable oils [118]. Water diffusivities predicted in §4.1 give an expected permeability range of 0.3 to 5×10^{-5} cm^2/s at 20 °C and 0.6 to 10×10^{-5} cm^2/s at 40 °C. Experiments of Schatzberg [119] with pure hexadecane demonstrate water permeabilities of 7.3 and 8.5×10^{-5} cm^2/s at 20 and 40°C. Langmuir and Schaefer fitted their data to a water permeability of 2.1×10^{-5} cm^2/s for oxidized turbine oils [8]. Our values obtained for MOx/BSM and BM duplex films in Table 4.3 are significantly larger.

MOx/BSM films contain approximately 10 wt% bovine submaxillary mucin (BSM), a strongly water-liking glycoprotein. BSM molecules consist of hydrophilic carbohydrate moieties

extending from a polypeptide backbone [120, 121]. From the water-uptake experiments in §6.4, we find no measurable amounts of water present in pure oxidized mineral oil. However, the mucin-containing oxidized mineral oil contains as much as 10 wt% water. To confirm that the added mucin is indeed the cause of increased evaporation rate, we tested thicker MOx films above L_c that did not require mucin to remain stable. For 1.5 and 2-mm thick films of nascent oxidized mineral oil, the measured water permeability was 3×10^{-5} cm^2/s, close to that obtained by Langmuir and Schaefer for films of oxidized turbine oil [8]. When 10 wt% mucin was added to the same films, the permeability increased tenfold, and water visibly incorporated into the films. We conclude that admixed mucin increases the water permeability of MOx/BSM duplex-oil films.

High water permeability of bovine-meibum duplex films is more difficult to rationalize because no literature exists on the transport or water-uptake properties of bovine meibum. Only recently have data emerged on the structural and rheological properties of human and bovine meibum [83, 112, 122]. Bovine meibum is orders of magnitude more viscous than mineral oil [83] and is composed largely of waxy and cholesterol esters along with other lipids generally more polar than the hydrocarbons that constitute mineral oil [57]. Compared to oxidized mineral oil, the viscosity and polarity of bovine meibum are higher, leading to a lower D and a higher k. Bovine and human meibum are not amorphous fluids. Recent work shows that these substances are composed of structured lipid crystallites suspended within an amorphous continuous phase [83, 112]. It is possible that the continuous phase, through which water diffuses, consists of a noncrystallized lipid not much more viscous than is mineral oil. Thus, the expected diffusion coefficient corresponds not to an oil of 10^4 mPa·s, but instead a considerably lower viscosity. The absence of measured continuous-phase properties makes prediction of D in meibum difficult. DSC results presented here indicate that bovine meibum imbibes up to 4 wt% water, which suggests a high k of water in bovine meibum, but not as high as that of MOx/BSM. To explain fully the water permeability of meibum, more work is needed to understand its physicochemical structure.

In Figure 4.19, we compare our J_F/J_0 measurements at physiologic temperature for MOx/BSM, BM, and HM duplex films versus film thickness to data available in the literature. In the case of Langmuir and Schaefer [8], we used our 1-D dissolution-diffusion model to predict J_F/J_0 based on their reported Dk values and our measured heat and mass-transfer coefficients. This exercise permits comparison between the two data sets. For the data of Gilby and Heymann [47], we chose those experiments with a mass-transfer coefficient closest to ours. For the remaining literature data, we plot the values of J_F/J_0 reported by the authors.

Unlike previous work with meibum and tear-lipid mimics [13, 14, 33], our duplex-oil films reduce evaporation significantly as the film thickness increases, consonant with the dissolution-diffusion mechanism. The ability to spread and maintain uniform duplex-oil films explains our observation of significant evaporation reduction, whereas others do not [13, 14]. Nevertheless, bovine-meibum duplex films at physiological thickness, i.e., 100 nm, reduced water evaporation only by 6 %, which is much less than normally attributed to the human TFLL [21, 32]. Human-meibum duplex films in this study also reduced evaporation by only 8 % at 100-nm thickness.

In contrast to our *in-vitro* results, Mishima and Maurice report *in-vivo* evaporation reduction of 94 % by rabbit-meibum lipid films [21]. Unfortunately, the corresponding *in-vivo* measurement of evaporation reduction by the human TFLL is not available since most

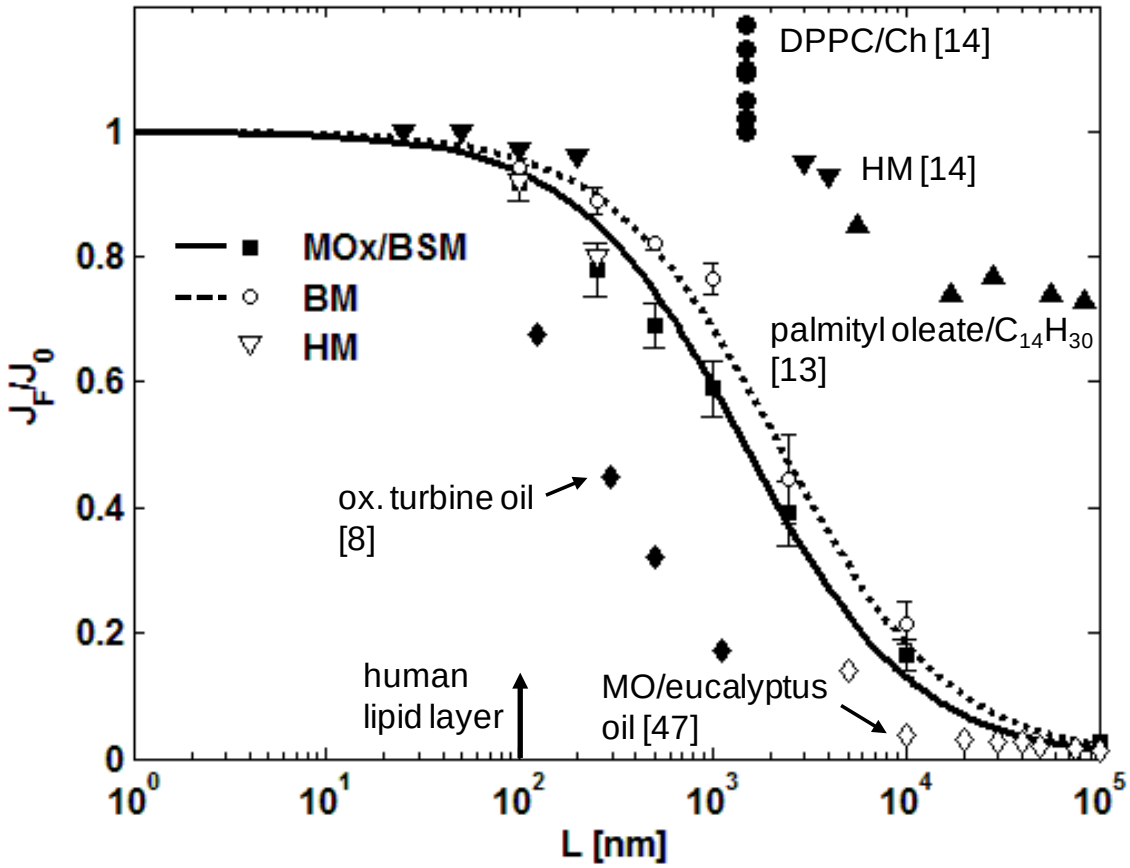

Figure 4.19: Evaporation ratio J_F/J_0 versus film thickness L for literature data and from theory and data from this study in the heated trough. The solid line and filled squares correspond to theory and data for heated MOx/BSM films. The dotted line and open circles correspond to theory and data for heated bovine-meibum films. Inverted open triangles are from human meibum experiments in this study. (●) and (▼) correspond to DPPC/Cholesterol and human-meibum films reported by [14]. (▲) are palmitoyl oleate/$C_{14}H_{30}$ films measured by Borchman *et al.* [13]. (◊) are films of MO:eucalyptus oil measured by [47]. (♦) are calculated values for evaporation reduction based on the *Dk* measured by Langmuir and Schaefer [8] for oxidized-turbine-oil duplex films assuming $\phi = 1$. A vertical arrow at 100 nm shows the approximate thickness of the human TFLL.

experiments can only detect j_F and not j_0. The range of clinically measured tear-evaporation rates from healthy subjects under various flow and environmental conditions is 0.002 to 6.3×10^{-6} g/cm^2/s. Most *in-vivo* tear-evaporation rates are measured without forced flow. The average evaporation rate measured under many different flow conditions is $j_F = 1.25 \times 10^{-6}$ g/cm^2/s at $T_S \approx$ 35 °C [123], $R_H \approx$ 30-40 %, and $T_\infty \approx$ 23-25 °C, similar environmental conditions to those in this study. Tomlinson *et al.* [70] measured the evaporation rate from pure water at 31 °C with the same device as used on eye. Comparison between the two measurements suggests an *in-vivo* evaporation reduction by the human TFLL of 25-45 %, much less than that of the rabbit. However, because j_F and j_0 are not measured under identical conditions, this estimate is not quantitative. Although the clinical evaporation rate is about 2-3 % of our *in-vitro* measurents, j_0 remains unknown for most clinical measurements, precluding direct calculation of the lipid-film mass-transfer resistance, R_F, or even evaporation reduction. Thus, it is possible that clinically reported evaporation reduction results primarily from a gas-phase mass-transfer resistance and not from the TFLL resistance.

To accentuate this point, quantitative analysis of evaporation rates requires an estimate of k_m, which depends on airflow and apparatus geometry. With a few exceptions, clinically measured evaporation rates are conducted in the absence of forced airflow. Tomlinson *et al.* discuss the details of the evaporation-rate-measurement methods [70]. Briefly, evaporation rates without forced flow are obtained either by measuring the relative-humidity gradient in front of the eye using a modified dermatological evaporimeter [71] or by measuring the transient relative-humidity increase in a sealed goggle placed over the eye [63, 72]. We estimate a reasonable range of k_m for these experiments as 0.05 to 1 cm/s. Due to the thinness of the human tear film, we assume that the tear-surface temperature remains constant regardless of the presence of a lipid film, so $T_{SF} = T_{S0}$. The clean-water evaporation rate for the *in-vivo* experiments then ranges from 1.6×10^{-6} to 3.1×10^{-5} g/cm^2/s at T_∞ = 23 °C and R_H = 40 %. Therefore, depending on the mass-transfer coefficient, the average clinically measured evaporation reduction varies from 20 to 96 %. Assuming a lipid-layer thickness of 100 nm, Equations 14 and 15 specify the possible range in lipid-layer water permeability for various values of the mass-transfer coefficient. Thus, for k_m = 1 cm/s, $Dk = 4.2 \times 10^{-7}$ cm^2/s; for k_m = 0.05 cm/s, $Dk = 2.0 \times 10^{-6}$ cm^2/s. At very small mass-transfer coefficient, however, estimation of Dk is extremely sensitive to changes in k_m. If k_m = 0.04 cm/s, the calculated Dk is 3.0×10^{-4} cm^2/s, close to that of this study: 2.6×10^{-4} cm^2/s. Importantly, without careful characterization of mass-transfer rates in clinical-evaporation measurements, it is not possible to estimate the effect of the TFLL on evaporation reduction.

Airflow and water permeability of the lipid layer control the evaporation rate through the TFLL. Figure 4.20 shows the calculated mass evaporation rate through a duplex film, j_F, as a function of film thickness, L, for various impinging air speeds, u, and two lipid-layer water permeabilities, Dk. We set $T_{S0} = T_{SF}$ = 35 °C, R_H = 40 %, and T_∞ = 23 °C to replicate physiological conditions. Solid, dotted, and dashed lines show theory results for u = 0.01, 0.1, and 1 m/s, representative of air speeds for nearly stagnant air, flow in a ventilated room, and walking, respectively [124]. The mass-transfer coefficient at each velocity is calculated by ratio with that measured in our experiments, assuming $k_m \sim u^{0.55}$ [105, 125]. Lines labeled with open squares and open circles correspond to $Dk = 2.6 \times 10^{-4}$ and 2.6×10^{-6} cm^2/s, respectively. Lower water permeability and slower air speed lead to lower evaporation rates. The ordinate intercept of each line corresponds to j_0, which increases significantly with increasing air speed. Greater evaporation reduction at any film thickness is effected by a smaller Dk for a given air speed or by

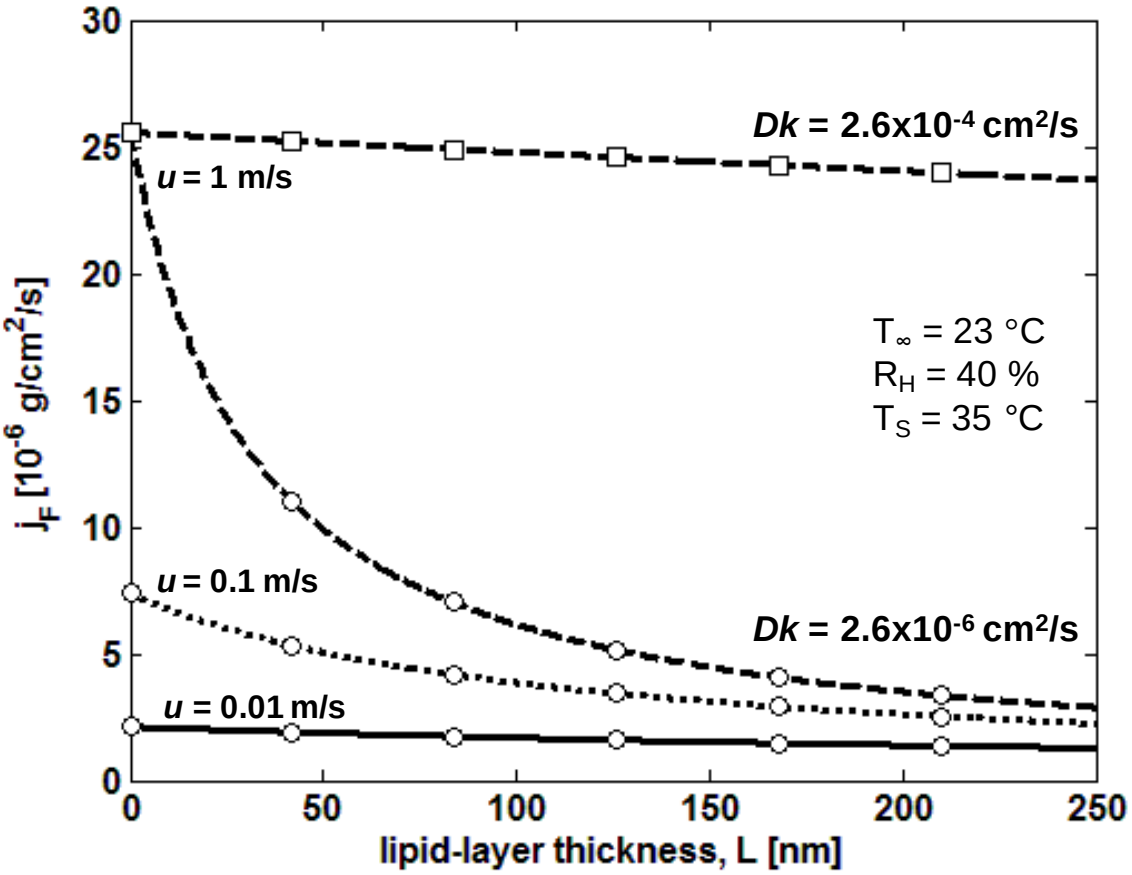

Figure 4.20: Calculated evaporation rate, j_F, versus lipid-layer thickness, L, for various impinging-air speeds, u, for two lipid-layer permeabilities. Open squares and circles on the lines correspond to Dk = 2.6x10^{-4} and 2.6x10^{-6} cm^2/s. Air speeds of 0.01, 0.1, and 1 m/s (corresponding to nearly stagnant air, ventilated-room air, and walking) are shown with solid, dotted, and dashed lines, respectively. For air speeds 0.01, 0.1, 1 m/s, the corresponding j_0 values are 2.1, 7.4, and 2.6x10^{-6} g/cm^2/s, respectively.

a larger air speed for a given *Dk*. There is no single evaporation rate or evaporation reduction. Thus, reporting a single number for the evaporation rate of the human TFLL is misleading. In addition to environmental R_H and *T*, evaporation rate and evaporation reduction depend strongly on airflow as well as on the thickness and water permeability of the lipid layer. At 100-nm thickness, little evaporation reduction is predicted except at the lowest *Dk* and the highest air speed. The importance of both controlling the experimental conditions and measuring k_m (i.e., j_0) cannot be overstated.

If we assume that $k_m > 0.05$ cm/s, then clinical evaporation measurements suggest that the water permeability of the human TFLL is ~10^{-6}-10^{-7} cm^2/s, which is at least an order of magnitude smaller than the most impermeable duplex-oil films measured by Langmuir and Schaefer [8], and two to three orders of magnitude lower than the *in-vitro* measurements from this study. We offer several reasons for this discrepancy.

First, recent measurements of meibum physical and structural properties show that human and bovine meibum undergo solidification phase transitions below 35 °C, turning into solid wax-like solids [83]. Eye temperature is close to this transition temperature, but all of our evaporations experiments were deliberately conducted well above this transition to avoid possible drastic changes in meibum properties at different film thicknesses and temperatures. Two evaporation measurements conducted with bovine meibum at 20 °C gave $Dk \sim 1x10^{-5}$ cm^2/s, which is about an order of magnitude less than that at 40 °C. Nevertheless, the *Dk* of bovine meibum well below tear-film temperature is still much higher than the purported clinical measurements [21, 32, 71].

Second, it is possible that our *in-vitro* substrate and duplex-oil films are fundamentally different from the *in-vivo* aqueous tear film and TFLL. The presence of salt, proteins, and mucins in the aqueous tear film is lacking in the most of our experiments. As mentioned in §4.1, however, addition of these components did not affect evaporation rates from either clean or film-covered water surfaces. This agrees with Borchman *et al.* [13] and Herok *et al.* [14], who show that human tear and salt buffers containing proteins evaporate at the same rate as pure water alone. The colligative effect of salt on the water-vapor pressure is minimal because tear salts make up less than 1 percent of the aqueous phase [24, 30, 126]. Lowering of the water chemical potential by dissolved protein is likewise negligible. Specific interaction between proteins and lipids adsorbed at the aqueous/lipid interface might lead to a structural change in the interface and lead to an interfacial resistance, R_I. However, we have no experimental evidence for such behavior.

Another possibility is that our sampling for bovine and human meibum results in exuded lipids with different chemical and physical properties than those in natural secretion. The physical state of meibum expressed from human meibomian glands depends on the pressure applied to the eyelid during collection [127]. At light pressures, typically less than 7 kPa (1 psia), liquid material exits the meibomian glands, but at higher pressures, the expressed material becomes solid-like. The bovine meibum collected from excised lids was done so at high pressures; human-meibum collection was not controlled for pressure application other than to avoid discomfort to the patients. Thus, it is possible that we obtained meibum not representative of that secreted under natural *in-vivo* conditions. We note, however, that the increased viscosity of solidified meibum usually exuded at high pressures likely exhibits lower *Dk* than liquid meibum deemed to be natural. Gentle expression of the glands results in a less viscous and larger water-permeable meibum that exhibits even less resistance to evaporation.

In our view, none of these potential explanations explains the apparent difference between the *in-vitro* evaporation rates in this study and clinical results on humans and rabbits. The human TFLL probably contributes insignificantly to water-evaporation reduction in the human tear film.

4.9 Conclusions

We review the available literature on water-evaporation reduction by duplex-oil films and outline the theoretical underpinnings of spreading and evaporation kinetics that govern behavior of these systems. The dissolution-diffusion model, wherein water dissolves in the duplex lipid film and subsequently diffuses through it and through an air boundary layer, unifies data reported in the literature and identifies dewetting of duplex films into nonuniform layers as a key challenge to obtaining significant evaporation reduction. We develop an improved apparatus for measuring evaporation reduction by duplex-oil films. New data reported in this study fit into the larger body of work conducted on water-evaporation by duplex-oil films. Duplex-oil films of MOx/BSM and bovine meibum reduce water evaporation by a dissolution-diffusion mechanism, as confirmed by agreement between the new measurements and theory. The water permeability of MOx/BSM duplex films agrees with those reported in the literature [8, 45, 119], after correction for the presence of bovine submaxillary mucin.

We find that duplex-oil films of bovine and human meibum at physiologic temperature reduce water evaporation only 6-8 % for a 100-nm film thickness pertinent to the human tear film. These numbers disagree with the 75-93 % reduction reported by *in-vivo* clinical measurements on evaporation reduction by rabbit lipid layers [21, 32]. Comparison to *in-vivo* human tear-evaporation measurements is inconclusive because evaporation from a clean-water surface is not measured and, accordingly, the mass-transfer resistance is not characterized. Without this characterization, evaporative resistances of the air and lipid layer cannot be decoupled. Theoretical estimation of j_0 gives evaporation reduction by the *in-vivo* human lipid layer of 20-96 %. Even at the smallest reduction, the calculated duplex-oil-film water permeability of the TFLL is significantly less than that reported in this study. To reconcile this difference, future *in-vivo* evaporation measurements must include calibration to characterize the mass-transfer coefficient and measurement of the evaporation rate from a clean-water surface.

4.10 Acknowledgments

This work was partially funded by Alcon Corporation under Contract 022466-003 to the University of California. The authors thank Yuzhang Li and Kevin Okimura for calibrating the IR camera and IR thermocouple, Gerald Fuller for use of the infrared camera, Nitash Balsara for the PIB samples, Rachel Segalman for use of the DSC, Eric Granlund for machining the miniature Langmuir trough, and David Chang for conducting many of the spreading experiments.

4.11 References

[1] Hedestrand G. On the influence of thin surface films on the evaporation of water. *J Phys Chem*. 1924;28:1245-52.

[2] Rideal EK. On the influence of thin surface films on the evaporation of water. *J Phys Chem*. 1925;29:1585-8.

[3] Barnes GT. The effects of monolayers on the evaporation of liquids. *Adv Colloid Interface Sci*. 1986;25:89-200.

[4] Harkins WD. A general thermodynamic theory of the spreading of liquids to form duplex films and of liquids or solids to form monolayers. *J Chem Phys*. 1941;9:552-68.

[5] Heymann E, Yoffe A. The stability of multimolecular films of hydrocarbon oils, containing spreaders, on water surfaces. *Trans Faraday Soc*. 1942;38:408-17.

[6] Langmuir I. Oil lenses on water and the nature of monomolecular expanded films. *J Chem Phys*. 1933;1:756-76.

[7] Sebba F, Briscoe HVA. The evaporation of water through unimolecular films. *J Chem Soc*. 1940;39:106-14.

[8] Langmuir I, Schaefer VJ. Rates of evaporation of water through compressed monolayers on water. *J Franklin Inst*. 1943;235:119-62.

[9] Docking AR, Heymann E, Kerley LF, Mortensen KN. Evaporation of water through multimolecular films. *Nature*. 1940;146:265.

[10] Bursztyn I. Evaporation Reduction of Water. Nature. 1966;211:521.

[11] Mansfield WW. Effect of Surface Films on the Evaporation of Water. *Nature*. 1953;172:1101.

[12] (No authors listed). The definition and classification of dry eye disease: report of the Definition and Classification Subcommittee of the International Dry Eye Workshop (2007). *Ocul Surf*. 2007;5:75-92.

[13] Borchman D, Foulks GN, Yappert MC, Mathews J, Leake K, Bell J. Factors affecting evaporation rates of tear film components measured in vitro. *Eye Contact Lens*. 2009;35:32-7.

[14] Herok GH, Mudgil P, Millar TJ. The effect of meibomian lipids and tear proteins on evaporation rate under controlled in vitro conditions. *Curr Eye Res*. 2009;34:589-97.

[15] (No authors listed). The epidemiology of dry eye disease: report of the Epidemiology Subcommittee of the International Dry Eye WorkShop (2007). *Ocul Surf*. 2007;5:93-107.

[16] King-Smith PE, Fink B, Hill R, Koelling K, Tiffany JM. The Thickness of the Tear Film. *Curr Eye Res*. 2004;29:357-68.

[17] Korb DR, Craig JP, Doughty M, Guillon J-P, Smith G, Tomlinson A. *The Tear Film: structure, function, and clinical examination*. Oxford: Butterworth-Heinemann; 2002.

[18] Bron AJ, Tiffany JM, Gouveia SM, Yokoi N, Voon LW. Functional aspects of the tear film lipid layer. *Exp Eye Res*. 2004;78:347-60.

[19] McDonald JE. Surface Phenomena of Tear Films. *Trans Am Ophthalmol Soc*. 1968;66:905-39.

[20] Craig JP, Tomlinson A. Importance of the lipid layer in human tear film stability and evaporation. *Optom Vis Sci*. 1997;74:8-13.

[21] Mishima S, Maurice DM. The oily layer of the tear film and evaporation from the corneal surface. *Exp Eye Res*. 1961;1:39-45.

[22] Wolff E. The muco-cutaneous junction of the lid-margin and th distribution of the tear fluid. *Trans Ophthalmol Soc U K*. 1946;66.

[23] Gilbard JP, Farris RL. Tear Osmolarity and Ocular Surface Disease in Keratoconjunctivitis Sicca. *Arch Ophthalmol*. 1979;97:1642-6.

[24] Gilbard JP, Farris RL, Santamaria J. Osmolarity of Tear Microvolumes in Keratoconjunctivitis Sicca. *Arch Ophthalmol*. 1978;96:677-81.

[25] Bron AJ, Yokoi Y, Gaffney EA, Tiffany JM. Predicted Phenotypes of Dry Eye: Proposed Consequences of Its Natural History. *Ocul Surf*. 2009;7:78-92.

[26] Baudouin C. The Pathology of Dry Eye. *Surv Ophthalmol*. 2001;45:S211-S20.

[27] Gilbard JP, Carter JB, Sang DN, Refojo MF, Hanninen LA, Kenyon KR. Morphological Effect of Hyperosmolarity on Rabbit Corneal Epithelium. *Ophthalmol*. 1984;91:1205-12.

[28] Khanal S, Tomlinson A, Diaper CJM. Tear Physiology of Aqueous Deficiency and Evaporative Dry Eye. *Optom Vis Sci*. 2009;86:1235-40.

[29] Khanal S, Tomlinson A, McFayden A, Diaper CJM, Ramaesh K. Dry Eye Diagnosis. *Invest Ophthalmol Vis Sci*. 2008;49:1407-14.

[30] Tomlinson A, Khanal S, Ramaesh K, Diaper CJM, McFayden A. Tear Film Osmolarity: Determination of a Referent for Dry Eye Diagnosis. *Invest Ophthalmol Vis Sci*. 2006;47:4309-15.

[31] Isreb MA, Greiner JV, Korb DR, Glonek T, Mody SS, Finnemore VM, et al. Correlation of lipid layer thickness measurements with fluorescein tear film break-up time and Schirmer's test. *Eye*. 2003;17:79-83.

[32] Iwata S, Lemp MA, Holly FJ, Dohlman CH. Evapoartion Rate of Water from the Precorneal Tear Film and Cornea in the Rabbit. *Invest Ophthalmol*. 1969;8:613-9.

[33] Brown SI, Dervichian DG. The oils of the meibomian glands: physical and surface characteristics. *Arch Ophthalmol*. 1969;82:537-40.

[34] Goto E, Shimazaki J, Monden Yu, Takano Y, Yagi Y, Shimmura S, et al. Low-concentration homogenized castor oil eye drops for noninflamed obstructive meibomian gland dysfunction. *Ophthalmol*. 2002;109:2030-5.

[35] Khanal S, Tomlinson A, Pearce EI, Simmons PA. Effect of an Oil-in-Water Emulsion on the Tear Physiology of Patients With Mild to Moderate Dry Eye. *Cornea*. 2007;26:175-81.

[36] Korb DR, Scaffidi RC, Greiner JV, Kenyon KR, Herman JP, Blackie CA, et al. The Effect of Two Novel Lubricant Eye Drops on Tear Film Lipid Layer Thickness in Subjects With Dry Eye Symptoms. *Optom Vis Sci*. 2005;82:594-601.

[37] Blodgett KB. Interference Colors in Oil Films on Water. J Opt Soc Am. 1934;24:313-5.

[38] Holly FJ. Surface chemistry of tear film component analogs. *J Colloid Interface Sci*. 1974;49:221-31.

[39] Langmuir I, Schaefer VJ. The effect of dissolved salts on insoluble monolayers. *J Am Chem Soc*. 1937;59:2400-14.

[40] Brown SI, Dervichi.Dg. Hydrodynamics of Blinking - In Vitro Study of the Interaction of the Superficial Oily Layer and the Tears. *Arch Ophthalmol*. 1969;82:541-7.

[41] Balsbaugh JC, Assaf AG, Pendleton WW. Mineral oil deterioration. *Ind Eng Chem*. 1941;33:1321-30.

[42] Hicks-Bruun MM, Ritz BL, Ledley RE, Bruun JH. Mineral oil oxidation. *Ind Eng Chem*. 1944;36:562-8.

[43] Zuidema HH. Oxidation of Lubricating Oils. *Chem Rev*. 1946;38:197-226.

[44] Lazzari M, Chiantore O. Drying and oxidative degradation of linseed oil. *Polym Degrad Stab*. 1999;65:303-13.

[45] Powell RW. The influence of surface films of oil on the evaporation of water. *Trans Faraday Soc*. 1943;39:311-8.

[46] Langmuir I, Langmuir DB. The effect of monomolecular films on the evaporation of ether solutions. *J Phys Chem*. 1927;31:1719-31.

[47] Gilby AR, Heymann E. The rate of evaporation of water through duplex films. *Aust J Sci Res A*. 1948;1:197-212.

[48] Fox RC. An Oil-Wax-Surfactant System for Retarding Evaporation of Water. *Nature*. 1965;205:1004.

[49] Ehlers N. The precorneal film: Biomicroscopical, histological and chemical investigations. *Acta Ophthalmol*. 1965:1-136.

[50] Butovich IA. Cholesteryl esters as a depot for very long chain fatty acids in human meibum. *J Lipid Res*. 2009;50:501-13.

[51] Butovich IA. The Meibomian Puzzle: Combining pieces together. *Prog Retin Eye Res*. 2009;28:483-98.

[52] Butovich IA. Lipidomics of human Meibomian gland secretions: Chemistry, biophysics, and physiological role of Meibomian lipids. *Prog Lipid Res*. 2011;50:278-301.

[53] Butovich IA, Millar TJ, Ham BM. Understanding and analyzing meibomian lipids - A review. *Curr Eye Res*. 2008;33:405-20.

[54] Butovich IA, Uchiyama E, McCulley JP. Lipids of human meibum: mass-spectrometric analysis and structural elucidation. *J Lipid Res*. 2007;48:2220-35.

[55] Butovich IA, Wojtowicz JC, Molai M. Human tear film and meibum. Very long chain wax esters and (O-acyl)-omega-hydroxy fatty acids of meibum. *J Lipid Res*. 2009;50:2471-85.

[56] Chen JZ, Green-Church KB, Nichols KK. Shotgun Lipidomic Analysis of Human Meibomian Gland Secretions with Electrospray Ionization Tandem Mass Spectrometry. *Invest Ophthalmol Vis Sci*. 2010;51:6220-31.

[57] Nicolaides N, Kaitaranta JK, Rawdah TN, Macy JI, Boswell FM, Smith RE. Meibomian Gland Studies - Comparison of Steer and Human Lipids. *Invest Ophthalmol Vis Sci*. 1981;20:522-36.

[58] Nicolaides N, Ruth EC. Unusual Fatty-Acids in the Lipids of Steer and Human Meibomian Gland Excreta. *Curr Eye Res*. 1982;2:93-8.

[59] Aronowicz JD, Shine WE, McCulley JP. Tear measurement in patients with keratoconjunctivitis sicca. *Invest Ophthalmol Vis Sci*. 2003;44:U640-U.

[60] Goto E, Endo K, Suzuki A, Fujikura Y, Matsumoto Y, Tsubota K. Tear evaporation dynamics in normal subjects and subjects with obstructive meibomian gland dysfunction. *Invest Ophthalmol Vis Sci*. 2003;44:533-9.

[61] Hamano H, Hori M, Kawabe H, Mitsunaga S, Ohnishi Y, Koma I. Modification of the superficial layer of the tear film by the secretion of the meibomian glands. *Folia Ophthalmol Japonica*. 1980;31:353-60.

[62] Mathers WD. Ocular evaporation in meibomian gland dysfunction and dry eye. *Ophthalmol*. 1993;100:347-51.

[63] Mathers WD, Binarao G, Petroll M. Ocular Water Evaporation and the Dry Eye - A New Measuring Device. *Cornea*. 1993;12:335-40.

[64] Mathers WD, Daley TE. Tear flow and evaporation in patients with and without dry eye. *Ophthalmol*. 1996;103:664-9.

[65] Mathers WD, Lane JA, Sutphin JE, Zimmerman MB. Model for ocular tear film function. *Cornea*. 1996;15:110-9.

[66] Rolando M, Refojo MF, Kenyon KR. Increased Tear Evaporation Rates in Eyes with Keratoconjunctivitis Sicca. *Arch Ophthalmol*. 1983;101:557-8.

[67] Shimazaki J, Sakata M, Tsubota K. Ocular Surface Changes and Discomfort in Patients with Meibomian Gland Dysfunction. *Arch Ophthalmol*. 1995;113:1266-70.

[68] Nichols JJ, Mitchell GJ, King-Smith PE. Thinning Rate of the Precorneal and Prelens Tear Films. *Invest Ophthalmol Vis Sci*. 2005;46:2353-61.

[69] Rolando M, Refojo MF. Tear evaporimeter for measuring water evaporation rate from the tear film under controlled conditions in humans. *Exp Eye Res*. 1983;36:25-33.

[70] Tomlinson A, Doane MG, McFayden A. Inputs and Outputs of the Lacrimal System: Review of Production and Evaporative Loss. *Ocul Surf*. 2009;7:186-98.

[71] Trees GR, Tomlinson A. Effect of Artificial Tear Solutions and Saline on Tear Film Evaporation. *Optom Vis Sci*. 1990;67:886-90.

[72] Tsubota K, Yamada M. Tear Evaporation from the Ocular Surface. *Invest Ophthalmol Vis Sci*. 1992;33:2942-50.

[73] Liu DTS, Di Pascuale MA, Sawai J, Gao YY, Tseng SCG. Tear film dynamics in floppy eyelid syndrome. *Invest Ophthalmol Vis Sci*. 2005;46:1188-94.

[74] Miano F, Calcara M, Giuliano F, Millar TJ, Enea V. Effect of meibomian lipid layer on evaporation of tears. *J Phys Condens Matter*. 2004;16:S2461-S7.

[75] Rantamaki AH, Javanainen M, Vattulainen I, Holopainen JM. Do Lipids Retard the Evaporation of the Tear Fluid? *Invest Ophthalmol Vis Sci*. 2012;53:6442-7.

[76] Doane MG. An Instrument for In Vivo Tear Film Interferometry. *Optom Vis Sci*. 1989;66:383-8.

[77] Fatt I, Weissman BA. *Physiology of the Eye: An Introduction to the Vegetative Functions*. 2nd ed. Stoneham, MA: Butterworth-Heinemann; 1992.

[78] Goto E, Dogru M, Kojima T, Tsubota K. Computer-synthesis of an interference color chart of human tear lipid layer, by a colorimetric approach. *Invest Ophthalmol Vis Sci*. 2003;44:4693-7.

[79] Guillon J-P. Tear film photography and contact lens wear. *Cont Lens Anterior Eye*. 1982;5:84-7.

[80] King-Smith PE, Hinel EA, Nichols JJ. Application of a novel interferometric method to investigate the relation between lipid layer thickness and tear film thinning. *Invest Ophthalmol Vis Sci*. 2010;51:2418-23.

[81] Korb DR, Greiner JV, Glonek T, Whalen A, Hearn SL, Esway JE, et al. Human and rabbit lipid layer and interference pattern observations. *Lacrimal Gland, Tear Film, and Dry Eye Syndromes 2: Basic Science and Clinical Relevance*. Vol. 438. New York: Plenum Press Div Plenum Publishing Corp; 1998. p. 305-8.

[82] King-Smith PE, Nichols JJ, Braun RJ, Nichols KK. High Resolution Microscopy of the Lipid Layer of the Tear Film. *Ocul Surf*. 2011;9:197-211.

[83] Rosenfeld L, Cerretani C, Leiske DL, Toney M, Radke CJ, Fuller GG. Structural and rheological properties of meibomian lipids. *Invest Ophthalmol Vis Sci*. 2013.

[84] Tiffany JM, Dart J. Normal and Abnormal Functions of the Meibomian Secretion. *R Soc Med Int Congr Symp Ser*. 1981;40:1061-4.

[85] Langmuir I. The constitution and fundamental properties of solids and liquids. II. Liquids. *J Am Chem Soc*. 1917;39:1848-906.

[86] Rowlinson J, Widom B. *Molecular Theory of Capillarity*. Oxford: Clarendon Press; 1982.

[87] Gibbs JW. *The Collected Works of J. Willard Gibbs. Vol. 1*. New York: Longmans; 1928. p. 258.

[88] Pomerantz P, Clinton WC, Zisman WA. Spreading Pressures and Coefficients, Interfacial Tensions, and Adhesion Energies of the Lower Alkanes, Alkenese, and Alkyl Benzenes on Water. *J Colloid Interface Sci*. 1967;24:16-28.

[89] Cerretani C, Radke CJ. Human tear lipid breaks up by dewetting. *6th International Conference on the Tear Film and Ocular Surface*. Florence, Italy2010.

[90] Brochard-Wyart F, Martin P, Redon C. Liquid/liquid dewetting. *Langmuir*. 1993;9:3682-90.

[91] Sharma A, Ruckenstein E. Dewetting of Solids by the Formation of Holes in Macroscopic Liquid Films. *J Colloid Interface Sci*. 1989;133:358-68.

[92] Martin P, Buguin A, Brochard-Wyart F. Bursting of a Liquid Film on a Liquid Substrate. *Europhys Lett*. 1994;28:421-6.

[93] Craster RV, Matar OK. Dynamics and stability of thin liquid films. *Rev Mod Phys*. 2009;81:1131-98.

[94] Lambooy P, Phelan KC, Haugg O, Krausch G. Dewetting at the liquid-liquid interface. *Phys Rev Lett*. 1996;76:1110-3.

[95] Hertz H. Ueber den Druck des gesättigten Quecksilberdampfes. *Ann Phys*. 1882;253:193-200.

[96] Knudsen M. Die maximale Verdampfungsgeschwindigkeit des Quecksilbers. *Ann Phys*. 1915;352:697-708.

[97] Alty T. The Reflection of Vapour Molecules at a Liquid Surface. *Proc R Soc Lond*. 1931;131:554-64.

[98] Cammenga HK. Evaporation Mechanisms of Liquids. In: Kaldis E, (editor). *Current Topics in Material Science. Vol. 4*: North Holland Publishing Company; 1980. p. 335-46.

[99] Schrage R. *A Theoretical Study of Interphase Mass Transfer*. New York: Columbia University Press; 1953.

[100] Bonacci J, Myers A, Nongbri G, Eagleton L. The Evaporation and Condensation Coefficient of Water, Ice, and Carbon Tetrachloride. *Chem Eng Sci*. 1976;31:609-17.

[101] Eames I, Marr N, Sabir H. The Evaporation Coefficient of Water: A Review. *Int J Heat Mass Transf*. 1997;40:2963-73.

[102] Bird R, Stewart W, Lightfoot E. *Transport Phenomena*. 2nd ed. New York: John Wiley & Sons, Inc.; 2002.

[103] Welty J, Wicks C, Wilson R, Rorrer G. *Fundamentals of Momentum, Heat, and Mass Transfer*. 4th ed. New York: John Wiley & Sons, Inc.; 2001.

[104] Green D, Perry R. *Perry's Chemical Engineer's Handbook*. 8th ed. New York: McGraw-Hill; 2008.

[105] Martin H. Heat and mass transfer between impinging gas jets and solid surfaces. In: James PH, Thomas FI, (editors). *Advances in Heat Transfer*. Vol. 13: Elsevier; 1977. p. 1-20.

[106] Bradley RS, Evans MG, Whytlaw-Gray RW. The Rate of Evaporation of Droplets. Evaporation and Diffusion Coefficients, and Vapour Pressures of Dibutyl Phthalate and Butyl Stearate. *Proc R Soc L A Math Phys Sci*. 1946;186:368-90.

[107] Fuchs N. Über die Verdampfungsgeschwindigkeit kleiner Tröpfchen in einer Gasatmosphäre. *Physikalische zeitschrift der Sowjetunion*. 1934;6:224-43.

[108] Assouline S, Narkis K, Or D. Evaporation suppression from water reservoirs: Efficiency considerations of partial covers. *Water Resour Res*. 2011;47.

[109] Stefan J. Ueber die Verdampfung aus einen kreisforming oder elliptisch begrenzten Becken. *Sitzungsberichte der Königlich Preussischen Akademie der Wissenschaften II*. 1881;83:943-54.

[110] Archer RJ, Lamer VK. The Rate of Evaporation of Water through Fatty Acid Monolayers. *J Phys Chem*. 1955;59:200-8.

[111] Siddiqi MA, Lucas K. Correlations for Prediction of Diffusion in Liquids. *Can J Chem Eng*. 1986;64:839-43.

[112] Leiske DL, Miller CE, Rosenfeld L, Cerretani C, Ayzner A, Lin B, et al. Molecular Structure of Interfacial Human Meibum Films. *Langmuir*. 2012;28:11858-65.

[113] Blackie CA, Solomon JD, Scaffidi RC, Greiner JV, Lemp MA, Korb DR. The Relationship Between Dry Eye Symptoms and Lipid Layer Thickness. *Cornea*. 2009;28:789-94.

[114] Josephson JE. Appearance of the Preocular Tear Film Lipid Layer. *Am J Optom Physiol Opt*. 1983;60:883-7.

[115] Felder R, Rousseau R. *Elementary Principles of Chemical Processes*. Third ed. New York, NY: John Wiley & Sons, Inc.; 2000.

[116] Doane MG. Interaction of Eyelids and Tears in Corneal Wetting and the Dynamics of the Normal Human Eyeblink. *Am J Ophthalmol*. 1980;89:507-16.

[117] Du Y, Mamishev AV, Lesieutre BC, Zahn M, Kang SH. Moisture solubility for differently conditioned transformer oils. *IEEE Trans Dielectr Electr Insul*. 2001;8:805-11.

[118] Hilder MH. Solubility of Water in Edible Oils and Fats. *J Am Oil Chem Soc*. 1968;45:703-7.

[119] Schatzberg P. Diffusion of water through hydrocarbon liquids. *Polym Rev*. 1965;10:87-92.

[120] Gum JR. Mucin Genes and the Proteins They Encode: Structure, Diversity, and Regulation. *Am J of Respiratory Cell Molec Biol*. 1992;7:557-64.

[121] Tsuji T, Osawa T. Carbohydrate structures of bovine submaxillary mucin. *Carbohydrate Res*. 1986;151:391-402.

[122] Leiske D, Leiske C, Leiske D, Toney M, Senchyna M, Ketelson H, et al. Temperature-induced transitions in the structure and interfacial rheology of human meibum. *Biophys J*. 2012;102:719-.

[123] Kamao T, Yamaguchi M, Kawasaki S, Mizoue S, Shiraishi A, Ohashi Y. Screening for Dry Eye With Newly Developed Ocular Surface Thermographer. *Am J Ophthalmol*. 2011;151:782-91.

[124] Baldwin PEJ, Maynard AD. A survey of wind speeds in indoor workplaces. *Ann Occ Hyg*. 1998;42:303-13.

[125] Chin DT, Tsang CH. Mass Transfer for an Impinging Jet Electrode. *J Electrochem Soc*. 1978;125:1461-70.

[126] Murube J. Tear Osmolarity. *Ocul Surf*. 2006;4:62-73.

[127] Korb DR, Blackie CA. Meibomian Gland Therapeutic Expression: Quantifying the Applied Pressure and the Limitation of Resulting Pain. *Eye Contact Lens*. 2011;37:298-301.

[128] Schlichting H, Gersten K. *Boundary-layer theory*. 8th ed. Berlin: Springer; 2000.

[129] Obot NT, Trabold TA. On the Rate Balance between Impingement Water Evaporation and Heat Transfer. *Int Comm Heat Mass Transf.* 1992;19:51-8.

Appendix 4A: Thermodynamic stability of duplex films

Equation 3 in §3.2 describes the free energy of hole formation in a thin duplex-oil film. Changes in surface energy and gravitational-potential energy are included in the analysis. Details are given here on the derivation of the gravity term ($\frac{1}{2}\tilde{\rho}gA_H L_0^2$) and on the calculation of areas A_1 and A_2.

The gravitational term in Equation 3 results from the difference in gravitational potential energy between a hole-containing film (Figure 4.2B) and that with a uniform film (Figure 4.2A). The gravitational-potential energy, *PE*, is that of the water substrate plus the oil film. The average potential energy in Figure 4.2A containing a uniform film of thickness L_0 resting on a substrate of thickness *d* is

$$\overline{PE}_{film} = m_w g\bar{z}_w + m_{oil} g\bar{z}_{oil} = \frac{1}{2}\rho_w A_0 g d^2 + \rho_{oil} A_0 g\left(L_0 d + \frac{L_0^2}{2}\right) \tag{A.1}$$

where subscripts *w* and *oil* indicate the water and oil phases, respectively, m_i is the mass of material in phase *i*, *g* is the gravitational constant (9.81 m/s^2), $\bar{z}_i$ is the average height of phase *i* above the reference point at the bottom of the trough, ρ_i is the mass density of phase *i*, and A_0 is the area of the water/oil and oil/air interfaces.

After dewetting and hole formation, the oil phase covers a smaller area, $A = A_0 - A_H$. Assuming that $r\text{-}r_1$ and $r\text{-}r_2$ are much smaller than the radius of the overall film, mass conservation of oil yields $A_0L_0 = AL$, and the resulting dewetted oil film thickens slightly. Buoyancy requires that the air/water interface in the hole rise a distance l' above the height of the water/oil interface in Figure 4.2A. When a hole forms in the film, the average potential energy in Figure 4.2B is:

$$\overline{PE}_{hole} = \frac{1}{2}\rho_w A_0 g\left(d - l_2 + l'\right) + \rho_w A_H l_2 g\left(d - \tfrac{1}{2}l_2 + l'\right) + \rho_{oil} AL\left(d - l_2 + l' + \tfrac{1}{2}L\right) \tag{A.2}$$

where all terms are defined in §3.2. Hydrostatics dictate that $l_2 = L\rho_{oil}/\rho_w$. Conservation of water mass relates l' and l_2:

$$l' = l_2\left(1 - \frac{A_H}{A}\right) \tag{A.3}$$

Upon combining Equations A.1-A.3 and the mass-conservation expressions for water and oil, the change in average gravitation potential energy between the film-with-hole and uniform-film states is

$$\Delta\overline{PE} = \overline{PE}_{hole} - \overline{PE}_{film} = \tfrac{1}{2}\rho_{oil} g A_0 \left\{\left(1 - \frac{A_H}{A}\right)\left[\frac{\rho_{oil}}{\rho_w}L^2\left(1 - \frac{A_H}{A}\right) + 2Ld\right] - \right.$$
$$\left. - \left(1 - \frac{A_H}{A_0}\right)\left[\frac{\rho_{oil}}{\rho_w}L^2 + 2Ld + L^2 + L^2\left(1 - \frac{A_H}{A_0}\right)\right]\right\} \tag{A.4}$$

In practice, the hole area is much smaller than the initial area such that $A \sim A_0$, and Equation A.4 simplifies to

$$\Delta\overline{PE} = \frac{1}{2}\rho_{oil}\left(1-\frac{\rho_{oil}}{\rho_w}\right)gL^2 A_H\left(1-\frac{A_H}{A_0}\right) \tag{A.5}$$

By assuming $L \sim L_0$, $A_H << A_0$, and by defining $\tilde{\rho} = \rho_{oil}\left(1-\rho_{oil}/\rho_w\right)$, Equation A.5 simplifies to the gravitational term in Equation 3 of the text:

$$\Delta\overline{PE} = \frac{1}{2}\tilde{\rho}gA_H L_0^2 \tag{A.6}$$

The water/oil and oil/air interface shapes in the region surrounding the hole determine the r_1, r_2, A_1, and A_2. We follow Sharma and Ruckenstein [91] and solve the Young-Laplace equation ignoring gravity for the shape of both interfaces and obtain expressions for the oil/air and oil/water profiles, $r_i(z)$. Evaluation of the profiles at l_1 and l_2 gives r_1 and r_2, respectively:

$$r_i = r_0\left[\cosh\left(\frac{l_i}{r_0\sin\alpha_i}\right)+\cos\alpha_i\sinh\left(\frac{l_i}{r_0\sin\alpha_i}\right)\right] \qquad i = 1,2 \tag{A.7}$$

where the subscript i = 1 or 2 for the top or bottom surface, respectively, and α_i is the contact angle in the oil between the water/air horizontal and the oil/water or oil/air interfaces. Neumann's triangle relates the three tensions, γ_w , γ_o , and γ_{ow} , to each contact angle. Areas are calculated by integrating the arc length from r_0 to r_1 or r_2. Given by Equation A.7, the result is

$$A_i = \frac{\pi}{2}r_0^2\left[(1+\cos^2\alpha_i)\sinh\left(\frac{l_i}{r_0\sin\alpha_i}\right)+2\cos\alpha_i\left(\cosh\left(\frac{l_i}{r_0\sin\alpha_i}\right)-1\right)+\frac{2l_i}{r_0}\sin\alpha_i\right] \quad i=1,2 \tag{A.8}$$

where again the subscript i denotes the areas of the top (1) or bottom (2) "shoulder" areas. Following Sharma and Ruckenstein [91], we assume that the profiles level at l_i for $r > r_i$, but since we ignore gravity in solving the Young-Laplace equation, the calculated profiles do not level smoothly.

Substitution of the expressions for r_i and A_i into Equation 3 and evaluation at $\Delta F=0$ gives the critical film thickness L_c, which depends on γ_o , γ_{ow} , α_1, α_2, and r_0. We numerically evaluate L_c. Similar to Equation 13 of Sharma and Ruckenstein [91], L_c is linear with r_0. For a reasonable range of mass densities and tensions applicable here, $f = L_c/r_0$ varies from about 0.2 to 0.8, corresponding to a total contact angle, $\alpha_1+\alpha_2$, of 20 to 90°.

Appendix 4B: Impinging-jet heat and mass transfer

The air-supply fan shown in Figure 4.6 directs an impinging jet of air perpendicular to the evaporating water surface in the miniature Langmuir trough. The resulting stagnation flow [128] at the water surface convects water vapor from the surface and heat to or from the surface, depending on whether the trough is heated. Equations 13 and 21 describe how water flux and heat flux from the trough into the air depend on the mass- and heat-transfer coefficients, k_m and h. As mentioned previously, k_m and h vary with the type and magnitude of the air flow as well as with the apparatus geometry. This dependence is reported in terms of the relationship between the Sherwood (*Sh*) and Nusselt (*Nu*) numbers, which characterize k_m and h, and the Reynolds (*Re*) number, which characterizes the air flow. For impinging-jet flow these dimensionless groups are

$$Sh = \frac{k_m D_{fan}}{D_{wa}} \tag{B.1}$$

$$Nu = \frac{hD_{fan}}{k_a} \tag{B.2}$$

$$Re = \frac{V_{fan}D_{fan}}{\nu} \tag{B.3}$$

where D_{fan} is the fan diameter, D_{wa} is the mass diffusivity [m^2/s] of water vapor in air, k_a is the thermal conductivity of air [W/m/K], V_{fan} is velocity of air exiting the fan [m/s], and ν is the momentum diffusivity of air [m^2/s]. V_{fan} is provided by the manufacturer via a linear calibration with fan speed, ω. Correlations for *Sh* and *Nu* at solid surfaces exposed to impinging-jet fluid flow are tabulated [105, 125]. Obot and Trabold [129] reported good agreement between the correlation proposed by Martin [105] and their measured values for water-evaporation data. For a single fan of diameter D_{fan} placed at a distance *H* above a surface, the integral-mean *Sh* and *Nu* at a radial distance *r* along on the evaporating surface from the stagnation point follow the forms

$$\frac{\overline{Sh}}{Sc^{0.42}} = \frac{\overline{Nu}}{Pr^{0.42}} = F\left(Re, r/D_{fan}\right)G\left(H/D_{fan}, r/D_{fan}\right) \tag{B.4}$$

where $\overline{Sh}$ and $\overline{Nu}$ are the integral-mean of *Sh* and *Nu* from $r = 0$ to *r* and *F* and *G* are functions shown graphically in Figure 9 of Martin [105]. Schmidt (*Sc*) and Prandtl (*Pr*) numbers are

$$Sc = \frac{\nu}{D_{wa}} \tag{B.5}$$

$$Pr = \frac{\nu}{\alpha} \tag{B.6}$$

where α is the thermal diffusivity of air [m^2/s]. For air at 25 °C, $Sc = 0.6$ and $Pr = 0.7$. Figure 9 in Martin [105] plots $\overline{Sh}/Sc^{0.42}$ and $\overline{Nu}/Pr^{0.42}$ versus *Re* for $H/D_{fan} = 7.5$ and various r/D_{fan}. For our experimental apparatus, $H/D = 8$ and $r/D_{fan} = 0.5$. The correlation in Martin [105] predicts that $\overline{Sh}$, $\overline{Nu} \sim Re^{0.54}$.

In our experiments, k_m is established from pure-water evaporation experiments using Equation 17. The rotational fan speed, ω, measured with a strobe light, sets the air exit velocity from the fan, V_{fan}, permitting calculation of *Re*. Figure 4B.1 shows measured log k_m versus log ω at two average surface temperatures: T_{S0} = 17.2 and 34.7 °C. There is little difference between k_m at the two temperatures, which is expected because the change in air physical properties is negligible over this range. Least-squares fitting calculates the slope of both lines to be 0.58, which is close to that reported in Martin [105] for similar systems. Mass and heat transfer in our system are, therefore, well described by impinging-jet flow. Any difference is most likely due to differences in fluid flow and geometry between our system and those reported in the literature, such as the presence of trough barriers which alter the airflow compared to that for a flat plate.

From the experimentally measured values of k_m, we calculate *h* using Equation B.4

$$h = k_m\left(\frac{k_a}{D_{wa}}\right)\left(\frac{Pr}{Sc}\right)^{0.42} \tag{B.7}$$

As the fan speed increases from 3800 to 6300, the predicted *h* increases from 1.4-1.9x10^{-3} W/cm^2/K at 18 °C and 1.5-2.0x10^{-3} W/cm^2/K at 35 °C. Thus, the pure-water evaporation experiments serve to establish both k_m and *h*, which are then used in the dissolution-diffusion model for predicting evaporation rate and surface temperature.

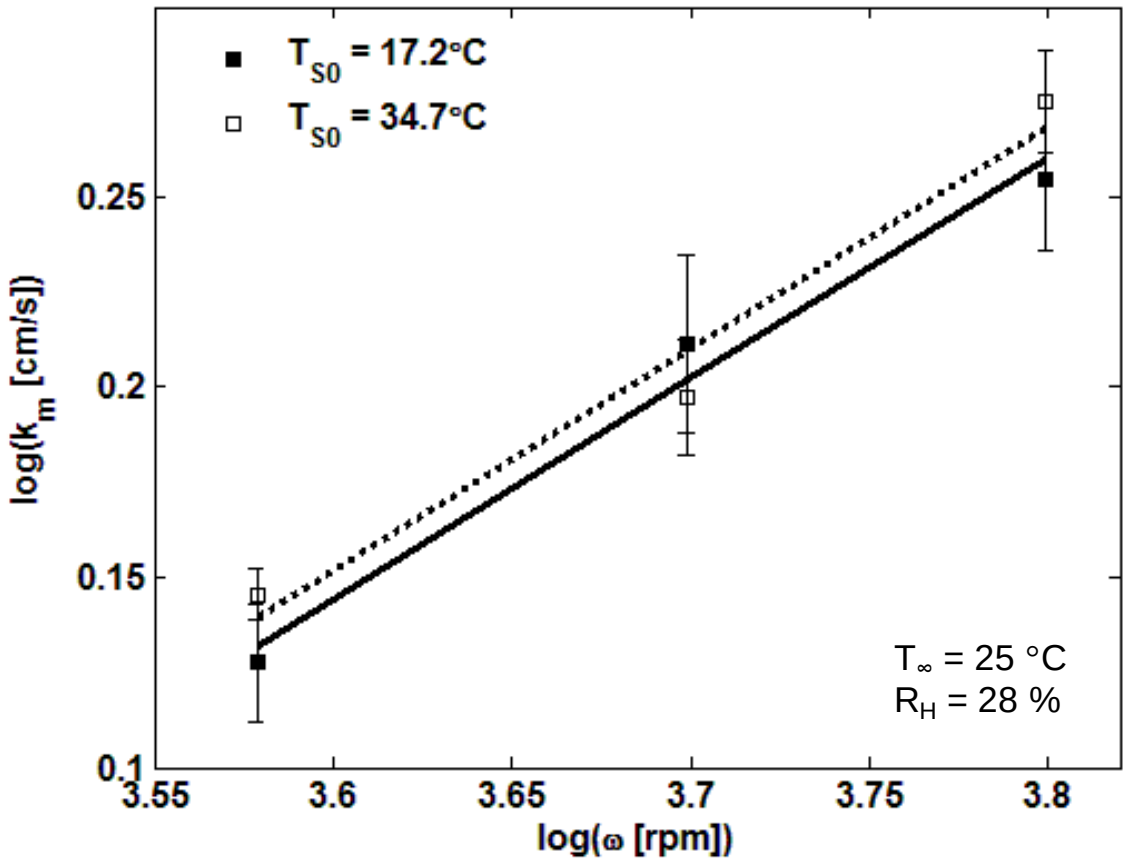

Figure 4B.1: Log-log plot of the measured mass-transfer coefficient [cm/s] versus fan speed [rpm]. Fan speeds used were 3800, 5000, and 6300 rpm. Error bars represent the standard deviation for each point, which was an average of 5 to 6 experiments. Filled and open squares correspond to data at T_{S0} of 17.2 and 34.7°C, respectively. The slope of both the solid and dotted best-fit lines is $m=0.58$. For the heated substrate, T_b = 43 °C.

Appendix 4C: Apparatus heat transfer

In §4.2, we developed a 1-D model to predict evaporation rates from and temperatures of an evaporating water surface including the effects of substrate heating and the presence of a spread duplex-oil film. The 1-D model requires modification to describe the behavior of the miniature Langmuir trough used in our experiments because the trough edges are not completely insulated and the temperature at the bottom of the substrate is not strictly uniform. As a result, the water-surface temperature is nonuniform. We use a pseudo-1-D heat-transfer model to account for heat flow from the trough walls, defined as $\dot{Q}_W$ [W], which is small but not negligible. Upon rewriting the energy balance at the water/oil interface in Equation 22 to include heat transfer from the walls, we find

$$0 = q_S A + \dot{Q}_W - q_F A - J_F \Delta\tilde{H}_s A \tag{C.1}$$

where A is the area of the evaporating surface, and all other variables are defined in §4.2.2. If the trough is not heated, then $q_S = 0$. In the absence of a film, J_0 replaces J_F in Equation C.1. $\dot{Q}_W$ is expressed in terms of a heat-transfer coefficient and a temperature driving force:

$$\dot{Q}_W = UA_W \left(T_{hot} - T_{wo}\right) \tag{C.2}$$

where U is the overall heat-transfer coefficient between the water surface and the heat source, A_W is the effective area over which heat transfer occurs, and T_{hot} is the hot temperature acting as a heat source. When the substrate is heated, $T_{hot} = T_b$, the temperature at the bottom of the trough. Without heating $T_{hot} = T_\infty$, the temperature of the ambient air. Neither U nor A_W can be obtained independently, but the product UA_W is a constant characteristic of the apparatus. Solution of Equations C.1 and 23 results in modified versions of Equations 24 and 27 that describe T_{SF} and T_{S0}. The difference is that U_W from Equation 25 is now redefined as

$$U_W = \frac{k_w}{H} + \frac{UA_W}{A} \tag{C.3}$$

Modified Equations 24 and 27 describe T_{SF} and T_{S0} when the water substrate is heated.

For experiments conducted without substrate heating, Equations 24 and 27 further simplify to

$$T_{SF} = T_\infty - \frac{J_F \Delta\tilde{H}_V}{U_F + UA_W / A} \tag{C.4}$$

and

$$T_{S0} = T_\infty - \frac{J_0 \Delta\tilde{H}_V}{h + UA_W / A} \tag{C.5}$$

In the pure-water evaporation experiments, all values in Equation C.5 are known or measured except UA_W. Therefore, the modified Equation 27 is solved to determine UA_W in the case where the trough is heated, and Equation C.5 is solved in the case where it is not heated. Results from all experiments show that UA_W is larger when the substrate is heated than when it is not and has a standard deviation of 10-17 %.

Appendix 4D: Experimental conditions and apparatus properties

Evaporation-reduction measurements were carried out over a 2-year span; hence, the environmental conditions were slightly different. There are three sets of data: MOx/BSM without substrate heating; MOx/BSM with substrate heating; and BM with substrate heating.

We outline the average conditions for each of these sets of data in Table 4.2. The measured quantities T_{S0}, T_{∞}, R_H, and j_0 are reported, followed by the calculated values for k_m, h, and UA_W. Reported values are averaged over the entire set of clean-water experiments that are conducted for a given oil system. Each data set contains over 30 to 40 measurements.

Chapter 5

Conclusions

The increasing global prevalence of dry-eye disease has renewed clinical and research interest in understanding this condition. Most cases of dry eye are attributed to evaporative dry eye (EDE) [1]. The current paradigm holds that a dysfunctional tear-film lipid layer (TFLL) leads to an increased tear-evaporation rate from the exposed ocular surface, which, in turn, causes tear hyperosmolarity. Chronic tear hyperosmolarity then triggers an inflammatory cascade that leads to clinical dry-eye disease [2-4]. However, a limited fundamental understanding of the role of the TFLL in dry eye impedes progress in developing care strategies. In an effort to advance knowledge in the field, this thesis focuses on tear evaporation in dry eye, on the structure and physical properties of tear lipid, and on the role of duplex-oil films in water-evaporation reduction.

The compartmentalized tear-dynamics model introduced in Chapter 2 describes the distribution of tear over the anterior ocular surface. The dependence of tear dynamics on tear-supply and tear-evaporation rates was investigated to understand dry-eye and normal behavior. Predicted tear osmolarity, tear volume, and tear-turnover rate all agree well with clinical observations of normal and dry-eye subjects. Tear-evaporation rate is the single most important driver of tear osmolarity and, therefore, plays a central role in dry eye. Osmotic water flow through the cornea and conjunctiva also play an important role in tear dynamics. For healthy tear-supply and tear-evaporation rates, osmotic flow contributes only 10 % of the total tear supply, but elevated tear osmolarity in dry-eye conditions augments the contribution to 50 % of the total tear supply. Inclusion of osmotic water flow enables our model predictions to agree better with clinical measurements at higher tear-evaporation rates and lower tear-supply rates than did previous models [5].

The tear-dynamics model is limited predominantly by the lack of reliable clinical measurements to set pertinent parameter values, especially evaporation rates. As mentioned in Chapter 4, measured *in-vivo* evaporation rates cover a wide range, and the choice of an appropriate evaporation rate is difficult. Importantly, inclusion of transmembrane osmotic water flow enables the predicted tear osmolarity to remain normal over a modest range of tear-evaporation rates.

The tear-dynamics model focuses on salt as a solute, but the mass balances are readily extended to include other solutes such as drugs or fluorescent tracers. Adaptation of the model to describe transient behavior enables prediction of drug bioavailability after ocular instillation. Also of interest are dry-eye care solutions that increase tear viscosity to improve tear residence

time on the eye. If the tear-drainage model were modified to incorporate tear viscosity, then the transient model could optimize the formulation of tear-thickening care solutions.

Structural and rheological examination of meibomian lipids in Chapter 3 provides a new understanding of the tear-film lipid layer (TFLL). Meibum is a structured, shear-thinning, and highly viscoelastic fluid. The complex rheology results from lamellar lipid crystalline solids suspended within a viscoelastic bulk liquid. Below 30 °C, meibum is essentially a solid wax. When heated above eye temperature, SAXS demonstrates that the crystalline material in meibum melts, causing a substantial change in rheological properties. Disappearance of crystalline lipids and the decrease of viscosity and viscoelasticity are accompanied by energy release observed with DSC and by loss of birefringence visualized with polarized-light microscopy. The current picture of the TFLL as a few ordered layers of stacked lipid molecules [6-8] fails to account for the behavior of the bulk liquid contained within the duplex film.

Our new findings have important implications for tear physiology. The melt transition of meibum suggests that meibum is liquid-like and easily expressible when expressed from the glands at 37 °C, but that the viscoelasticity increases as it cools down after spreading over the aqueous tear film, which could impart stability to the tear film. In addition, it is clear that chemical changes in meibum that affect its crystalline structure alter its rheology. Such compositional and structural changes observed in dry-eye disease [9-11] may explain why the TFLL is defective. Further research coupling compositional analysis with structural and rheological examination in healthy and dry-eye subjects could provide valuable insights into the origin of dry eye.

Despite the important new information obtained in Chapter 3, many questions still remain. Meibum is a complex mixture of lipids; we have not identified which specific molecules constitute the various crystalline populations. Future work measuring the structural and rheological properties of model meibomian-lipid components such as wax esters, cholesteryl esters, triacylglycerols, and phospholipids may pinpoint the contributions of each class of lipids to the overall properties. Characterization of the individual components could guide development of model meibum mixtures for evaporation-reduction studies, as in Chapter 4. Also, the surface and interfacial tensions of meibum that govern spreading behavior were not examined in this dissertation. Interfacial-tension measurements could provide information about the partitioning of polar lipid molecules at the lipid/water interface. Due to the relative scarcity of knowledge about the structure and physical properties of meibum, much remains to be discovered.

Experiments on water-evaporation reduction featured in Chapter 4 measure water-evaporation reduction by duplex films of model oil and meibomian lipids with careful attention to spreading and evaporation physics. By controlling relevant experimental parameters such as airflow, humidity, temperature, and duplex-film uniformity, the results are rigorous and apparatus independent. Uniform film coverage is critical, and duplex-film dewetting is a key challenge to obtaining reliable water-evaporation reduction. Duplex-oil films composed of oxidized mineral oil and mucin (MOx/BSM), bovine meibum, and human meibum all reduce water evaporation by a dissolution-diffusion mechanism. Application of the dissolution-diffusion theory allows calculation of water permeability, *Dk*, in the duplex-oil films, which is a material property of the oil.

Duplex-oil films studied in Chapter 4 reduced water-evaporation rates significantly at large thicknesses, in contrast to previous reports [12-14]. The water permeability of MOx/BSM films agrees with previously reported data after accounting for the presence of BSM [15, 16].

However, duplex films of bovine and human meibum spread at 100 nm in thickness reduced water evaporation by only about 10 %. This reduction is nowhere near the 90 % evaporation reduction for the eye reported by clinicians [17-19]. As described in Chapter 4, water-evaporation reduction depends on the gas-phase mass transfer and environmental conditions within the apparatus. Estimation of mass transfer in clinical goggle apparatus puts *in-vivo* water-evaporation reduction by the TFLL at 20 to 96 %, which is still more than that measured here.

The apparent disparity between *in-vivo* and *in-vitro* evaporation suppression by duplex films of meibomian lipid is obscured by the lack of mass-transfer characterization in clinical measurements. The implications of our results change depending on the role of the *in-vivo* TFLL in water-evaporation reduction, which is currently undetermined. If the actual evaporation reduction by the human TFLL is close to 20 %, then it is possible that our *in-vitro* results are in agreement. Although the TFLL is 100-nm thick near the center of the cornea, it thickens near the lid margins. Consequently, the average thickness of the healthy TFLL may be greater than 100 nm. A 250-nm thick duplex-lipid film of human meibum reduced water evaporation by 20 % in Chapter 4. Thus, small changes in assumptions about the TFLL might account for the perceived disparity. In this case, it is possible that the role of the TFLL is not primarily to reduce evaporation but instead to stabilize the aqueous tear layer against rupture and eventual dewetting [20, 21]. In fact, tear-film instability is thought to be another core mechanism of dry eye [4].

Conversely, if the human TFLL reduces tear-film evaporation by much more than 20 %, there is no clear explanation to reconcile the *in-vitro* reductions reported in Chapter 4. It is possible that our *in-vitro* experiments do not capture completely all aspects of the tear-film aqueous and lipid layers or their combined interaction in evaporation reduction. Chapter 4 details potential reasons for why our *in-vitro* system may not replicate that of the *in-vivo* tear film, but none is particularly compelling. *In-vivo* tear-evaporation measurements utilizing an evaporimeter with well-characterized mass transfer are required to address this inconsistency.

Altogether, the results obtained in this dissertation do not resolve the role of the TFLL in tear dynamics and in dry eye. Although we have learned a great deal about tear dynamics and the *in-vitro* properties of meibum, the implications of our findings are, unfortunately, ambiguous. The tear-dynamics model in Chapter 2 indicates that tear evaporation drives tear osmolarity. Specifically, increases in tear-evaporation rate measured in dry-eye subjects predict tear hyperosmolarity significant enough to initiate dry eye. However, the reliability of the clinical tear-evaporation measurements is called into question in Chapter 4. More importantly, *in-vitro* duplex films of bovine and human meibum do not reduce evaporation significantly at physiological TFLL thicknesses. Additional research is necessary to resolve the contradiction. Despite the present effort, our ultimate goal eludes us. Luckily, the thrill is in the chase.

5.1 References

[1] Lemp MA, Crews LA, Bron AJ, Foulks GN, Sullivan BD. Distribution of Aqueous-Deficient and Evaporative Dry Eye in a Clinic-Based Patient Cohort: A Retrospective Study. *Cornea*. 2012;31:472-8.

[2] Baudouin C. The Pathology of Dry Eye. *Surv Ophthalmol*. 2001;45:S211-S20.

[3] Bron AJ, Yokoi Y, Gaffney EA, Tiffany JM. Predicted Phenotypes of Dry Eye: Proposed Consequences of Its Natural History. *Ocul Surf*. 2009;7:78-92.

[4] (No authors listed). The definition and classification of dry eye disease: report of the Definition and Classification Subcommittee of the International Dry Eye Workshop (2007). *Ocul Surf*. 2007;5:75-92.

[5] Gaffney EA, Tiffany JM, Yokoi N, Bron AJ. A Mass and Solute Balance Model for Tear Volume and Osmolarity in the Normal and Dry Eye. *Prog Retin Eye Res*. 2010;29:59-78.

[6] Butovich IA, Millar TJ, Ham BM. Understanding and analyzing meibomian lipids - A review. *Curr Eye Res*. 2008;33:405-20.

[7] Green-Church KB, Butovich I, Willcox M, Borchman D, Paulsen F, Barabino S, et al. The International Workshop on Meibomian Gland Dysfunction: Report of the Subcommittee on Tear Film Lipids and Lipid-Protein Interactions in Health and Disease. *Invest Ophthalmol Vis Sci*. 2011;52:1979-93.

[8] Millar TJ, Tragoulias ST, Anderton PJ, Ball MS, Miano F, Dennis GR, et al. The surface activity of purified ocular mucin at the air-liquid interface and interactions with meibomian lipids. *Cornea*. 2006;25:91-100.

[9] Borchman D, Yappert MC, Foulks GN. Changes in human meibum lipid with meibomian gland dysfunction using principal component analysis. *Exp Eye Res*. 2010;91:246-56.

[10] Joffre C, Souchier M, Gregoire S, Viau S, Bretillon L, Acar N, et al. Differences in meibomian fatty acid composition in patients with meibomian gland dysfunction and aqueous-deficient dry eye. *Br J Ophthalmol*. 2008;92:116-9.

[11] Leiske DL. Understanding the Role of Lipids in Tear-Film Stability [Doctoral Thesis]: Stanford University; 2011.

[12] Borchman D, Foulks GN, Yappert MC, Mathews J, Leake K, Bell J. Factors affecting evaporation rates of tear film components measured in vitro. *Eye Contact Lens*. 2009;35:32-7.

[13] Brown SI, Dervichian DG. The oils of the meibomian glands: physical and surface characteristics. *Arch Ophthalmol*. 1969;82:537-40.